Super-resolution Control of Ultracold Dipolar Atoms on a 50-nm Scale

by

Li Du

B.S., Nanjing University (2016)

Submitted to the Department of Physics
in partial fulfillment of the requirements for the degree of

Doctor of Philosophy

at the

MASSACHUSETTS INSTITUTE OF TECHNOLOGY

May 2024

Author..
Department of Physics
May 15, 2024

Certified by..
Wolfgang Ketterle
John D. MacArthur Professor of Physics
Thesis Supervisor

Accepted by..
Lindley Winslow
Associate Department Head of Physics

Super-resolution Control of Ultracold Dipolar Atoms on a 50-nm Scale

by

Li Du

Submitted to the Department of Physics
on May 15, 2024, in partial fulfillment of the
requirements for the degree of
Doctor of Philosophy

Abstract

Degenerate quantum gases of magnetic atoms such as dysprosium (Dy) and erbium (Er) offer new opportunities to quantum simulation research due to their large spin degree of freedom and long-range dipole-dipole interactions. In this thesis, following an introduction to the fundamental properties of Dy, we introduce the design and construction of an experimental apparatus that is capable of producing Bose-Eintein codensates of more than 10^5 Dy atoms in every 10 seconds. In addition, we describe two experiments that advances the quantum control over the spin, the motion, the interaction, and the dynamics of ultracold dipolar gases.

In the first experiment, we introduce a super-resolution control scheme using a spin-dependent optical potential that localizes Dy atoms on a sub-50 nm scale, a distance that is more than 10 times shorter than the optical wavelength. With the interatomic distances shortened by a factor of 10, the interatomic dipole-dipole interaction is significantly enhanced. We will discuss how this strong and tunable long-range interaction enables the simulation of new classes of many-body Hamiltonians. We experimentally demonstrate the super-resolution technique by creating a bilayer of ultracold Dy atoms and mapping out the atomic density distribution with sub-10 nm resolution. The interlayer dipole-dipole interaction are detected via two out-of-equilibrium experiments.

In the second experiment, we study the suppression of dipolar relaxation, an inelastic process that limits the lifetime of higher spin states, using external optical confinements. By confining ultracold dysprosium atoms in ultrathin optical layers, the magnetic atoms can approach each other only side by side. The interatomic dipole-dipole repulsion provides a protective shield that stops the atoms from tunneling to short-range. We observe an order of magnitude suppression of inelastic dipolar relaxation losses in the presence of the dipolar shield. This scheme can extend the lifetime of quantum gases of spin mixtures, thereby offering more opportunities for exploring physics such as spin-orbit coupled Bose gases, dipolar spinor condensates, etc.

Thesis Supervisor: Wolfgang Ketterle
Title: John D. MacArthur Professor of Physics

Dedicated to my family.

Acknowledgments

Simplicity is the ultimate sophistication. I believe this sentence aptly describes all great discoveries in science, and Bose-Einstein condensation is certainly one of them. I have been fortunate to work on the design and construction of the first dysprosium Bose-Einstein condensation machine at MIT during my PhD. Despite the complex laser cooling apparatus, the extensive knowledge of atomic physics, and a great deal of hard work needed to achieve this goal, I continue to be fascinated by the simple yet striking effect of Bose-Einstein condensation every time I see it on the computer screen, even after all these years. Therefore, I dedicate this first paragraph to my advisor, Wolfgang Ketterle, for introducing me to the amazing field of ultracold atomic physics. Constructing a quantum gas machine from scratch was challenging, but Wolfgang always trusted and encouraged us along the way, providing enormous support whenever we faced difficulties. I treasure every day I spent as Wolfgang's student.

I would like to thank the members of the first-generation Dypole team: Michael, Alan, Pierre, and Will (known as Göreblaster). I began my PhD working with Michael on the new dysprosium machine, while Alan was a postdoc and Pierre was a visiting student. Together, we witnessed the machine's evolution from its inception. Görebläster joined our lab from BEC 5 in early 2017 as a senior PhD student. In addition to all the fancy electronics and software he brought to Dypole, I was deeply impressed by his passion for everthing he loves, such as his death metal band. I thank Görebläster not only for being an awesome labmate but also for introducing me to the world of electric guitar.

As the Dypole team expanded, more members came aboard. Julius is an excellent scientist who joined Dypole when we started the bilayer project in 2022. He thinks about physics deeply and clearly and has contributed many important ideas, insights, and nice Python simulations to this project. Moreover, he was a great source of stress relief when the hardships of experiments left me agitated. Having Julius on our team was a great fortune for my PhD.

Yu-Kun started his PhD in BEC 2. I remember the days we spent together setting up Görebläster's SoC analog channels before the pandemic. I was already impressed by how quickly Yu-Kun was able to learn things at that time and was happy when he decided to join Dypole several years later. Yu-Kun, I hope you become very successful in your academic career.

To the new members of the Dypole team—Jiahao, Yaashnaa, Hyo Son, and Gary—I hope you find joy in doing science in Dypole, have fun setting up the new machine, and enjoy your time at MIT. I'm sure you'll achieve fruitful results.

There are many others in the Ketterle group and in CUA who were important to my PhD. I would like to thank Jun-Ru for helping me integrate into the group when I first arrived at MIT. He has always been a scientific role model for me.

Timur and I shared the same office during the first few years before he graduated. He taught me how to program and compile Cicero, which was quite important for me to develop an overall understanding of our experiments. I still remember those weekends we spent together in the office during my first year, discussing various topics related to China. I also recall a time when he showed me some cigarettes and asked if I would like to take some when I was tired from working on problem sets.

I would like to express my gratitude to Martin and Dave. I was always captivated by Martin's enthusiasm during our physics discussions. Dave, with his broad and profound understanding of physics, never failed to intrigue me at the start of each semester.

Yicheng was a friend of mine in the Doyle group. He is passionate, generous, and is always willing to share his knowledge. I specifically want to thank him for three things: (1) informing us about the company Nichia which sells 421 nm laser diodes, (2) lending us a photonic-crystal fiber when we accidentally broke one, and (3) introducing the technology of phased-array acousto-optic deflectors to me for the bilayer project.

I would like to thank the rest of the Ketterle group for the collaborative culture and support I have enjoyed. In particular, I would like to thank Julie, Hyungmok, Tout, Hongyin, Boris, Furkan, Yair, Jinggang, Wenlan, Woo Chang, Jacob, Enid, Can-

8

dice, Cody, Colin, Niki, Jessie, Ivana, Hanzhen, Eunice, and Vitaly. I look forward to catching up with you in different corners of the world in the future. I also would like to thank many of my friends outside the lab, such as Zeyang, Guoqing, and Changhao.

Yian and Huating have been friends of mine for eighteen years since middle school. They provided enormous support during my PhD. I'm very happy to see Yian become a professor at Cornell. You always do a little better than me! Shiping has been a friend of mine since college and has also given me huge support during my PhD. I hope you can become a math professor soon. I apologize for not mentioning names of many other important friends. It is a great pleasure to share friendship with you all.

I would like to thank my girlfriend, Xinyi (Jessy). Before I met you, I always saw Boston as a place for studying. Now, I've started to consider it home.

Many teachers from before my graduate studies have contributed to my training and shaped my scientific outlook. I am particularly grateful to Professors Sihui Wang and Xiaopeng Hu from Nanjing University.

The last paragraph is dedicated to my family. I thank my parents, Suli Du and Yemei Lu, and especially my grandfather, Xingguo Du. I wouldn't have chosen physics as my field of study without the great intellectual freedom you provided since my early childhood. Without your understanding, unconditional support, and endless love, I might have given up halfway through. It's sad that my grandfather is not able to see my graduation.

Contents

List of Figures

List of Tables

Chapter 1

Introduction

Since the first realizations of Bose-Einstein condensates (BECs) in 1995 [30, 4], quantum gases of neutral atoms have become an ideal platform for creating, probing, and understanding interacting many-body systems. Despite the complex structures of their constituent electrons and nuclei, interactions among these dilute, ultracold atoms can be precisely described by only a handful of parameters, opening up numerous opportunities for constructing many-body Hamiltonians through a bottom-up approach [17]. The short-range contact interaction parameterized by the scattering length a has allowed for the investigation of topics such as the fundamental properties of superfluids and the physics of Hubbard Hamiltonians [16, 82]. The ability to tune the scattering length in ultracold atomic gases using Feshbach resonances has enabled the exploration of systems such as unitary Fermi gases [40], the anisotropic Heisenberg model [51], and Bose gases in lower dimensions [27]. These examples highlight the important role of precise control over atomic motion and interactions in advancing the study of many-body systems with ultracold atoms.

In addition to short-range contact interactions, quantum gases of magnetic atoms, polar molecules, Rydberg atoms, and optical cavity QED systems present long-range interactions that give rise to an even broader range of physics. This thesis will introduce one of these platforms based on ultracold gases of dysprosium (Dy), the most magnetic atom. Owing to its electronic configuration with a submerged open $4f$ shell, Dy has several special properties: a large ground-state spin, a large magnetic mo-

ment, strong long-range magnetic dipole-dipole interactions, dense Feshbach spectra and so on. These properties offer additional degrees of freedom and different types of inter-particle interactions, hence providing new opportunities for engineering, synthesizing, and investigating novel quantum systems.

In the following chapters of this thesis, I will introduce our effort in designing and constructing the experimental apparatus for creating BECs of Dy atoms and controlling their motion, spin states, and long-range dipole-dipole interaction using external fields including lasers, magnetic fields, and RF pulses. By using a new type of spin-dependent optical potential, we achieve the localization of two layers of Dy atoms in opposite spin states on a subwavelength scale of 50 nm. The super-resolution optical potential significantly enhances the strength of dipole-dipole interactions, enabling the observation of many-body effects arising from interlayer dipole-dipole couplings. By confining cold Dy gases in a tight quasi-2D optical potential, we observe a reduction in inelastic collisions due to dipole-dipole repulsion. These are the two principal experiments that I will describe in this thesis.

1.1 Bosonic Atoms at Ultralow Temperature: Bose-Einstein Condensates

Bose-Einstein condensation is a phenomenon arising from quantum statistics of identical bosons. It was predicted by Satyendra Nath Bose and Albert Einstein in 1924 [18, 35], and was first realized in ultracold dilute gases of rubidium [4] and sodium [30] in 1995. These interacting atomic gases exhibit superfluid behavior. Unlike conventional superfluid ^{4}He, which is in strongly-correlated liquid phase, weakly-interacting BECs of dilute atomic gases can be fully described by macroscopic wavefunctions that follow the Gross-Pitaevskii equation [17], making it a clean system for studying collective behaviors of superfluids such as vortex formation, sound propagation, and soliton physics. The BECs of dilute atomic gases are in the low-temperature and low-density thermodynamically forbidden regime [28] and can decay toward

chemical equilibrium (i.e., forming molecules) via three-body recombination. There-
fore, maintaining a low density is necessary for keeping the gases at metastable
kinetic equilibrium via two-body collisions.

Ideal Bose Gases

To understand the formation of BECs at ultracold temperatures, let's consider
non-interacting identical bosons confined in a volume V with single-particle energy
spectrum $\{E_i\}$. The partition function of a grand canonical ensemble that exchanges
energy and particles with a reservoir is given by

$$Z = \sum_{\{n_i\}} e^{-\sum_i n_i (E_i - \mu)/k_B T} = \prod_i \frac{1}{1 - e^{-(E_i - \mu)/k_B T}} \tag{1.1}$$

where the occupation n_i of each energy level E_i takes values between 0 and ∞ for
bosons. The average occupation of each state with energy E_i, known as the Bose-
Einstein distribution, is then

$$\langle n_i \rangle = k_B T \frac{\partial \ln Z}{\partial \mu} = \frac{1}{e^{(E_i - \mu)/k_B T} - 1} \tag{1.2}$$

For homogeneous confinement of a box potential, the single-particle energy spectrum
is $E(\mathbf{p}) = \mathbf{p}^2/2m$. Without macroscopic occupation of a single momentum state (i.e., no
Bose condensation), the total atom number in the box can be evaluated by integrating
over the momentum space

$$N = \sum_{\mathbf{p}} \langle n_{\mathbf{p}} \rangle = \sum_{\mathbf{p}} \frac{1}{e^{(\frac{\mathbf{p}^2}{2m} - \mu)/k_B T} - 1} \approx \frac{V}{\pi^3 \hbar^3} \int d\mathbf{p} \frac{1}{e^{(\frac{\mathbf{p}^2}{2m} - \mu)/k_B T} - 1}$$

$$= \frac{V}{2\pi^2 \hbar^3} \int_0^\infty dp \frac{p^2}{e^{(\frac{p^2}{2m} - \mu)/k_B T} - 1} \tag{1.3}$$

$$= \frac{V}{\lambda_{\mathrm{dB}}^3(T)} \mathrm{PolyLog}(\frac{3}{2}, e^{\mu/k_B T})$$

where the thermal de Broglie wavelength $\lambda_{\mathrm{dB}}(T) = \sqrt{\frac{2\pi\hbar^2}{m k_B T}}$ characterizes the size of
the matter wave at temperature T. Based on this expression, we define the phase-

space density as

$$\mathcal{D} = n\lambda_{\mathrm{dB}}^3(T) \tag{1.4}$$

which, under the assumption of no Bose condensation, is equal to $\mathrm{PolyLog}(\frac{3}{2}, e^{\mu/k_B T})$. However, this polylogarithm function saturates to a maximum value of $\zeta(3/2) \approx 2.61$ at $\mu \to 0$ with $\zeta(x)$ being the Riemann-Zeta function, indicating a *saturation of thermal states* [35]. A further increase of the phase-space density results in macroscopic particle occupation of the ground state $\mathbf{p} = 0$, leading to the phase transition of Bose-Einstein condensation.

We can therefore obtain the BEC transition temperature T_c from the maximum phase-space density of thermal particles

$$T_c = \frac{2\pi\hbar^2}{mk_B}\left(\frac{n}{\zeta(3/2)}\right)^{2/3} \tag{1.5}$$

When the temperature T is lower than T_c, the matter waves are so delocalized that their de Broglie wavelength λ_{dB} becomes comparable to the interparticle spacing $n^{-1/3}$, and a Bose condensate starts to form. In the limit of $\mu \to 0$, only the ground state with $\langle n_{\mathbf{p}=0} \rangle = \frac{1}{e^{\mu/k_B T}-1} \approx \frac{k_B T}{\mu}$ has macroscopic occupancy, in which case we have

$$\frac{N - N_0}{V}\lambda_{\mathrm{dB}}^3(T) = \frac{N}{V}\lambda_{\mathrm{dB}}^3(T_c) = \zeta\left(\frac{3}{2}\right) \tag{1.6}$$

where N_0 is the particle number of the Bose condensate. Hence the condensate fraction when $T < T_c$ is given by

$$\frac{N_0}{N} = 1 - \left(\frac{T}{T_c}\right)^{3/2}. \tag{1.7}$$

We can estimate, based on these results, that the critical temperature for liquid $^4\mathrm{He}$ with typical densities of 10^{22} cm^{-3} [47] is $T_c \sim 1.9$ K, which is similar to the λ-point at $T_\lambda = 2.2$ K for superfluid phase transition. For ultracold dilute gases with typical densities of 10^{13} to 10^{15} cm^{-3}, the typical BEC transition temperature T_c is in the $0.1\ \mu$K to $1\ \mu$K regime.

The above results of BEC transition temperature and the condensate fraction are based on the assumption of a homogeneous box potential. For harmonic confinements

that we use more frequently in ultracold atom experiments, the trap-averaged phase space density is $\mathcal{D} = n\lambda_{\text{dB}}^3(T) = N\left(\frac{\hbar\bar{\omega}}{k_B T}\right)^3$ with $\bar{\omega} = (\omega_x \omega_y \omega_z)^{1/3}$ being the geometric mean of trap frequencies. In this case, the transition temperature and condensate fraction become $T_c = \frac{\hbar\bar{\omega}}{k_B}\left(\frac{N}{\zeta(3)}\right)^{1/3}$ and $\frac{N_0}{N} = 1 - \left(\frac{T}{T_c}\right)^{1/3}$ [108], which have different power law dependences on particle number N and temperature T.

Interacting Bose Gases

From the analysis on the quantum statistic of ideal Bose gases, we see that particles forming a BEC occupy the same quantum state — they "march in lock step" [68]. Now let's consider interactions among particles. In ultracold dilute atomic gases, the inter-particle distances for typical densities around 10^{14} cm^{-3} are on the order of $n^{-1/3} \sim 200$ nm, much larger than the size of the atoms r_0. Therefore, on a time scale of a few seconds, we can neglect three-body recombination processes and only consider two-body elastic collisions. In addition, the de Broglie wavenumber k that is comparable to the inter-atomic distance for BECs satisfies $kr_0 \ll 1$. This means that we are in the low-energy regime where details of inter-atomic molecular potentials are not resolved during collisions. The effect of two-body collisions can be fully described by a phase shift of the inter-atomic wavefunction, which can be expressed in terms of a single universal value called the scattering length a.

These two conditions bring us into the dilute regime where the many-body problem is governed by the following Hamiltonian

$$H = \int d\mathbf{r}\, \hat{\psi}^\dagger(\mathbf{r})\left[-\frac{\hbar^2}{2m}\nabla^2 + V_{\text{ext}}(\mathbf{r})\right]\hat{\psi}(\mathbf{r}) + \frac{1}{2}\int d\mathbf{r}'\int d\mathbf{r}\, \hat{\psi}^\dagger(\mathbf{r})\hat{\psi}^\dagger(\mathbf{r}')V_{\text{int}}(\mathbf{r}',\mathbf{r})\hat{\psi}(\mathbf{r}')\hat{\psi}(\mathbf{r})$$

(1.8)

with $V_{\text{int}}(\mathbf{r}',\mathbf{r})$ being the two-body interaction potential and $\hat{\psi}^\dagger(\mathbf{r})$, $\hat{\psi}(\mathbf{r})$ being the field operators creating and annihilating a bosonic particle at position $\mathbf{r}$. This Hamiltonian was used to describe superfluid systems such as ^{4}He [39]. However, the theory is only a phenomenological description due to the high density of liquid helium. With ultracold dilute atomic gases, we have a physical system that is fully described by this many-body Hamiltonian. Under the mean-field approximation where

the field operators are replaced by a quantum fluctuation on top of a classical field $\hat{\psi}(\mathbf{r}, t) \rightarrow \langle \psi(\mathbf{r}, t) \rangle + \delta\psi(\mathbf{r}, t) \equiv \psi(\mathbf{r}, t) + \delta\psi(\mathbf{r}, t)$, we obtain the time-dependent Gross-Pitaevskii equation (GPE) for weakly-interacting BECs

$$i\hbar\frac{\partial}{\partial t}\psi(\mathbf{r}, t) = \left[-\frac{\hbar^2}{2m}\nabla^2 + V_{\text{ext}}(\mathbf{r}) + g|\psi(\mathbf{r}, t)|^2 + \int d\mathbf{r}' V_{\text{dd}}(\mathbf{r} - \mathbf{r}')|\psi(\mathbf{r}', t)|^2 \right]\psi(\mathbf{r}, t) \quad (1.9)$$

Here, the coupling strength g is related to the scattering length a as

$$g = \frac{4\pi\hbar^2}{m}a \tag{1.10}$$

, which characterizes the strength of the short-range contact interaction. In addition, we also include in the above equation a magnetic dipole-dipole interaction for spin-polarized atoms such as Dy, which has the following form of

$$V_{\text{dd}}(\mathbf{r}) = \frac{\mu_0\mu_m}{4\pi}\frac{1 - 3\cos^2\theta}{r^3} \tag{1.11}$$

with μ_m being the magnetic moment. We will discuss the properties of the dipole-dipole interaction potential in greater detail in Chapter 2. For convenience, we can characterize the strength of dipole-dipole interaction by defining the dipolar length as $a_{\text{dd}} = \frac{\mu_0\mu_m^2 m}{12\pi\hbar^2}$, which is approximately 7 nm for Dy, comparable to the s-wave scattering length of around 6 nm. Hence we expect that the dipolar superfluids of Dy can present many different behaviors compared to alkali superfluids where the short-range contact interaction plays the major role [27].

1.2   Quantum Gases of Magnetic Atoms

So far, three species of magnetic atoms have been Bose condensed: chromium (Cr) atoms with $\mu_m = 6\ \mu_B$ [41, 43], erbium (Er) atoms with $\mu_m = 8\ \mu_B$ [2], and Dy atoms with $\mu_m = 10\ \mu_B$ [73], where μ_B is the Bohr magneton. To motivate the experiments that will be introduced in the following chapters, we first summarize some recent advancements in the field of dipolar quantum gases.

1.2.1   Physics of Dipole-Dipole Interaction

The dipole-dipole interaction among magnetic atoms, due to its long-range, anisotropic, and non-integrability properties, has led to discoveries of new types of quantum matter in different optical confinements. Some examples are listed below.

Dipolar Superfluids and Supersolids

By fine-tuning the strength of contact interaction via Feshbach resonances, Dy BEC was discovered to present a droplet phase that resembles the Rosensweig instability of classical ferrofluid [53]. These quantum droplets can be self-bound without an external trapping potential [93] with lifetimes around 100 ms. The droplet phase is due to the instability of the Bogoliubov modes when the scattering length a is tuned to be smaller than the dipolar length a_{dd} such that the attractive dipolar interaction of head-to-tail dipoles kicks in and the BEC starts to collapse — this mechanism is known as the roton-maxon instability. The collapsing gases are stabilized due to the beyond mean-field repulsion that scales with density as $n^{3/2}$ known as the Lee-Huang-Yang (LHY) correction, leading to the formation of quantum droplets. The roton minimum of the Bogoliubov spectrum (i.e. the most unstable momentum k_{roton}) in an oblate optical confinement is set by the thickness l_z of the dipolar gas as $k_{\mathrm{roton}} \sim 1/l_z$ [89], hence, the droplet phase is in part a geometric effect.

As a quantum phase of matter arises from weakly-interacting supersolids and has spatial density modulation, a natural question is then "Is this matter a type of supersolid?" Supersoild is a special phase of matter that simultaneously breaks the internal gauge symmetry (leading to global phase coherence) and the spatial translational symmetry (leading to a crystalline density distribution). It was first claimed to be discovered in the liquid helium system [59], which later turned out to be a false claim [58, 8]. A stripe phase with supersolid properties was first reported in ultracold quantum gases in spin-orbit coupled systems and cavity QED systems [70, 64]. With dipolar quantum gases, it was shown that global phase coherence exists when the droplets have extensive spatial overlap [102, 26, 19], signifying the formation of dipolar supersolids. Two branches of low-energy Goldstone modes corresponding to

the breaking of two symmetries are observed in several experiments [101, 44, 84, 49].

Dipolar Physics in 1D: Quantum Thermalization

Another aspect of dipole-dipole interaction is its non-integrability. In 1D geometry, Bose gases with only short-range contact interaction are an integrable system described by the Lieb-Liniger Hamiltonian $H_{LLM} = -\sum_{\text{atoms}} \frac{\hbar^2}{2m} \frac{\partial^2}{\partial x^2} + \sum_{\text{pairs}} g_{1D} \delta(x)$ where the 1D coupling strength is defined as $g_{1D} = 2\hbar^2 a/ma_\perp^2$ with $a_\perp = \sqrt{\hbar/m\omega_\perp}$ being the oscillator length along the transverse direction. In the strong-coupling limit $g_{1D} \to +\infty$, collisions between two bosons lead to a total reflection of the incident wavefunction—these bosons are impenetrable. In this regime, the 1D Bose gas becomes a Tonk-Girardeau (TG) gas whose wavefunction is equal to the absolute value of its fermionic counterpart. The density anti-correlations become so strong that the mean-field description breaks down.

In a classical picture, particles in a TG gas experience elastic hard-ball collisions. Two particles exchange their velocities in each collision event. As such, the momentum distribution of the whole ensemble of particles is retained during time evolution. Hence, a TG gas is an integrable system that does not thermalize. This phenomenon was first observed with cesium atoms confined in 1D tubes [60]. Now with dipolar quantum gases, a tunable non-integrable component can be introduced into the system Hamiltonian in a controlled way, allowing the investigation of how quantum systems thermalize near the boundary of integrability [100].

Another interesting topic along this line of research is about super Tonks-Girardeau gases. By scanning through a Feshbach resonance and quenching the coupling strength g_{1D} of a TG gas from $+\infty$ to $-\infty$, stable 1D gases with positive stiffness are found [13, 25, 6, 46, 5], whereas such attractive gases typically collapse via three-body recombinations in 3D. The stabilization of such super-TG gases is due to the strong anti-bunching effect of the many-body state. With 1D quantum gas of Dy, it was discovered that the presence of dipole-dipole interaction leads to stronger correlations and further stabilizes the gas at all negative values of g_{1D} [54], which allowed for scanning through multiple Feshbach resonances and pumping the 1D gas into in-

creasingly excited many-body states caused by a quantum holonomy ($g_{1D} = ... \rightarrow 0 \rightarrow +\infty \rightarrow -\infty \rightarrow 0 \rightarrow ...$).

Quantum Simulation of Lattice Models

Beyond bulk experiments, lattice models, including the extended Bose-Hubbard Hamiltonian, can be studied by loading ultracold dipolar gases into 3D optical lattices. The anisotropic dipolar interaction was detected using spectroscopic methods and time-of-flight measurements with ultarcold Er gases [7]. A more recent experiment using a quantum gas microscope has led to the discovery of multiple stripe phases in a dipolar Bose-Hubbard quantum simulator with Er [98].

1.2.2 Physics of Large Spin

Besides the long-range dipole-dipole interaction, the additional degrees of freedom from the large spins of ground-state magnetic atoms open avenues to interesting physics.

Spinor Condensates

BECs with a spin degree of freedom can exhibit different spinor phases [95, 56]. Theoretical works have predicted diverse spinor condensate phases in magnetic atoms [71]. Phenomena like spin mixing dynamics and spontaneous demagnetization have been extensively studied in cold gases of Cr atoms. [65, 66, 87, 86].

Synthetic Dimension

The spin degree of freedom in dipolar atoms can also be treated as a synthetic spatial dimension. Introducing off-diagonal matrix elements through two-photon Raman couplings allows for the engineering of tunneling terms between these synthetic lattice sites. This has enabled the simulation of chiral edge states in a synthetic quantum Hall system [23].

1.2.3 More is Different

The electronic structures of dipolar atoms make their responses to external magnetic and laser fields different from those of alkali atoms. While this complexity affords greater flexibility in manipulating quantum gases, it also introduces bigger challenges in understanding the details of the interatomic molecular potentials that mediate the interactions among atoms.

Feshbach Resonance

Different from the Feshbach spectra of alkali atoms with mostly broad and sparse resonance features, magnetic atoms like Er and Dy exhibit much narrower and denser Feshbach resonances [38, 78]. Statistical analysis of the neighbouring energy spacings of these resonances reveals a Wigner-Dyson distribution with strong level repulsion for small energy spacings, indicating chaotic behavior of dipolar atoms during cold collisions.

Photoassociation

Although the interatomic interaction is dominated by two-body collisions in dilute gases of ultracold atoms, it might not be the case in the presence of optical confinements. Photons from laser beams can act as the "third body" and make two free atoms to form a molecular bound state, thereby converting the molecular binding energy into external kinetic energy. This process, known as photoassociation, can affect the metastability of Bose condensates.

Distinct resonance features have been detected on the red side of atomic lines in lanthanide atoms such as ytterbium (Yb) [99, 61, 105]. Yet, for magnetic atoms such as Er and Dy, no observation of discretized photoassociation features has been reported so far to the best of our knowledge. Our preliminary photoassociation spectroscopy experiments with Dy showed no discretized features within 1 GHz range on the red side of the 626 nm atomic line, nor within 100 MHz range on the red side of the 741 nm atomic line. The underlying physics of this observation needs further

investigation.

1.3   Thesis Outline

In this thesis, we summarize the design and construction of the Dy quantum gas apparatus in Professor Wolfgang Ketterle's research group at MIT. Additionally, we describe two experimental studies conducted with Bose gases of Dy [33, 11].

Chapter 2 provides an overview of the fundamental properties of Dy, including its electronic structure, optical transitions, and the dipole-dipole interaction Hamiltonian. In Chapter 3, we introduce the interactions between atoms and lasers via the electric-dipole Hamiltonian, with a focus on categorizing atom-light interactions into scalar, vector, and tensor components. Chapter 4 describes the design of our experimental apparatus, covering details of the Zeeman slower, magneto-optical trap, crossed optical-dipole trap, and RF control of spin states.

Chapter 5 details an experiment in which we achieved a bilayer configuration of Dy atoms with a 50 nm separation, enabling the observation of interlayer dipole-dipole interactions. This experiment paves the way for exploring novel many-body states that rely on strong long-range interactions.

In Chapter 6, we investigate the dynamics of dipolar relaxation, an inelastic collisional process that leads to heating in multi-component atomic gases. We explore the possibility of suppressing dipolar relaxation using the repulsive interaction of side-by-side dipoles under tight external confinement. This investigation offers new insights and possibilities for studying the physics of spin mixtures.

Chapter 2

Dysprosium

Dysprosium (Dy), a member of the lanthanide series, was first discovered from Holmium oxide by the French chemist Paul-Emile Lecoq de Boisbaudran in 1886. However, due to the similar chemical properties shared among the lanthanide elements (atom numbers 57-71), pure Dy was not isolated from other lanthanides until the advent of the ion-exchange technique in the 1950s. A single Dy atom possesses the largest total angular momentum ($J = 8$) among all atomic species in the periodic table, resulting in the strongest magnetic dipole momentum of 10 Bohr magnetons (μ_B). The periodic table in Fig. 2-1 uses a colormap to present different atomic species' relative dipole-dipole interaction strengths, which are proportional to the square of the magnetic dipole moments. With a magnetic dipole moment 10 times larger, Dy atoms exhibit interatomic dipole-dipole interactions 100 times stronger than those among alkali atoms, providing new opportunities for quantum simulation experiments.

This chapter will introduce several fundamental aspects of Dy atoms, including their electronic structure and optical transitions, interatomic interactions via the dipole-dipole interaction Hamiltonian, and the manipulation of internal spin states through the dressing of Dy atoms with RF photons.
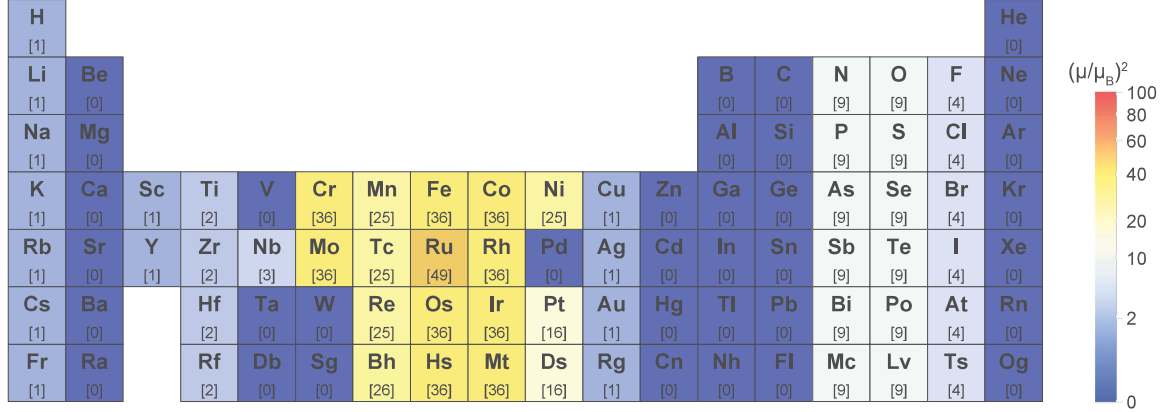
Figure 2-1 (Periodic table):

1	2	3	4	5	6	7	8	9	10	11	12	13	14	15	16	17	18
H [1]																	He [0]
Li [1]	Be [0]											B [0]	C [0]	N [9]	O [9]	F [4]	Ne [0]
Na [1]	Mg [0]											Al [0]	Si [0]	P [9]	S [9]	Cl [4]	Ar [0]
K [1]	Ca [0]	Sc [1]	Ti [2]	V [0]	Cr [36]	Mn [25]	Fe [36]	Co [36]	Ni [25]	Cu [1]	Zn [0]	Ga [0]	Ge [0]	As [9]	Se [9]	Br [4]	Kr [0]
Rb [1]	Sr [0]	Y [1]	Zr [2]	Nb [3]	Mo [36]	Tc [25]	Ru [49]	Rh [36]	Pd [0]	Ag [1]	Cd [0]	In [0]	Sn [0]	Sb [9]	Te [9]	I [4]	Xe [0]
Cs [1]	Ba [0]		Hf [2]	Ta [0]	W [0]	Re [25]	Os [36]	Ir [36]	Pt [16]	Au [1]	Hg [0]	Tl [0]	Pb [0]	Bi [9]	Po [9]	At [4]	Rn [0]
Fr [1]	Ra [0]		Rf [2]	Db [0]	Sg [0]	Bh [26]	Hs [36]	Mt [36]	Ds [16]	Rg [1]	Cn [0]	Nh [0]	Fl [0]	Mc [9]	Lv [9]	Ts [4]	Og [0]

La [1]	Ce [16]	Pr [11]	Nd [6]	Pm [1]	Sm [0]	Eu [49]	Gd [28]	Tb [100]	Dy [100]	Ho [81]	Er [49]	Tm [16]	Yb [0]	Lu [1]
Ac [1]	Th [2]	Pa [18]	U [18]	Np [11]	Pu [0]	Am [49]	Cm [28]	Bk [100]	Cf [100]	Es [83]	Fm [49]	Md [16]	No [0]	Lr [0]

$(\mu/\mu_B)^2$ — 100, 80, 60, 40, 20, 10, 2, 0

Figure 2-1: Periodic table showing the relative magnetic dipolar interaction strengths of different elements measured by $(\mu/\mu_B)^2$, where μ is the magnetic moment of the ground-state atom and μ_B is the Bohr magneton.

2.1 Electronic Structure

Dy, with an atomic number $Z = 66$, has a ground-state configuration of 66 electrons following the Madelung's rule, which is expressed as:

$$(1s^2 2s^2 2p^6 3s^2 3p^6 3d^{10} 4s^2 4p^6 4d^{10} 5s^2 5p^6) 4f^{10} 6s^2 \tag{2.1}$$

In addition to a xenon core denoted by the expression in the parentheses above, Dy has two outer orbitals: a fully-filled $6s$ orbital and a submerged partially-filled $4f$ orbitals. The ground-state quantum numbers S, L, and J are determined using Hund's rules as follows.

The First Hund's Rule. The first Hund's rule states that the lowest energy state corresponds to the one with the highest multiplicity $2S + 1$ in the open subshell. For Dy, the 10 electrons in the seven $4f$ orbitals with $m_L = -3... + 3$ add up to a maximum total spin of 2, resulting in a ground-state total spin $S = 2$. One of the explanations of the first Hund's rule can be understood by considering a simple system with two electrons in two orbitals $\psi_1(\mathbf{r})$ and $\psi_2(\mathbf{r})$. If the two electrons

form a spin singlet state with multiplicity of one, the spatial wavefunction has to be symmetric $\psi_S(\mathbf{r_1}, \mathbf{r_2}) \propto \psi_1(\mathbf{r_1})\psi_2(\mathbf{r_2}) + \psi_1(\mathbf{r_2})\psi_2(\mathbf{r_1})$; if the two electrons form a spin triplet state with multiplicity of three, the spatial wavefunction is antisymmetric $\psi_A(\mathbf{r_1}, \mathbf{r_2}) \propto \psi_1(\mathbf{r_1})\psi_2(\mathbf{r_2}) - \psi_1(\mathbf{r_2})\psi_2(\mathbf{r_1})$. In the triplet case, a node in the spatial wavefunction forms when two electrons come together, reducing the Coulomb repulsion. This simple model illustrates that the electronic structure with the lowest energy corresponds to the configuration of maximum S. There are more advanced discussions on the origin of the first Hund's rule in quantum chemistry related to the screening effects from the electrons, but the details of these topics are beyond the scope of this text.

The Second Hund's Rule. The second Hund's rule states that, for a given multiplicity, the electronic configuration that maximizes the total orbital angular momentum L has the lowest energy. This corresponds to the occupation of orbitals with $m_L = 0, +1, +2, +3$ by the unpaired electrons in the ground state of Dy, leading to $L = 6$. The second Hund's rule minimizes the Coulomb repulsion with respect to the orbital quantum numbers m_L of the electronic wavefunction.

The Third Hund's Rule. The first and second Hund's rules lock the valence electrons to the total spin eigenstate $S = 2$ and total orbital angular momentum eigenstate $L = 6$. The third Hund's rule accounts for the energy penalty due to spin-orbit couplings of electrons. The most general spin-orbit coupling Hamiltonian is written as $H_{\mathrm{SO}} = \sum_i \alpha_f^i \mathbf{S_i} \cdot \mathbf{L_i}$, which is approximated to first order as $H_{\mathrm{SO}} \approx \alpha_f \mathbf{S} \cdot \mathbf{L} = \frac{1}{2}\alpha_f(J^2 - L^2 - S^2)$. For the $4f$ shell that is more than half-filled, the state with the largest J corresponds to the lowest energy. Hence we have $J = |L + S| = 8$ for Dy.

Written in term symbol, the ground-state of Dy is a $^5I_8$ state. Thus, the ground-state of the most common bosonic isotopes ^{160}Dy, ^{162}Dy, and ^{164}Dy, with zero nuclear spins ($I = 0$), is composed of a $J = 8$ Zeeman manifold; the ground-state of the most common fermionic isotopes ^{161}Dy and ^{163}Dy, with nuclear spin $I = 5/2$, is composed of 6 Zeeman manifolds with $F = 11/2, 13/2, 15/2, 17/2, 19/2$, and $21/2$. As the focus of this thesis is on bosonics physics, we exclusively utilize the bosonic isotopes ^{162}Dy and ^{164}Dy.

2.2 Optical Transitions

Presented in Fig. 2-2 are the energy levels of Dy obtained from the NIST database [79, 62]. In this section, we are going to discuss several typical optical transitions that are particularly relevant to the experiments detailed in this thesis.
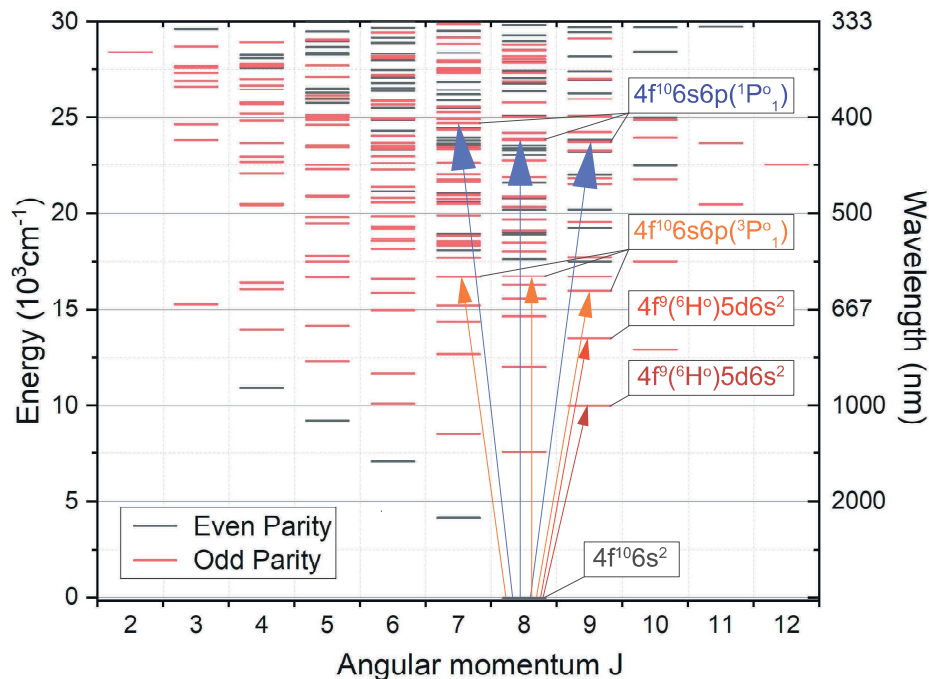
Figure 2-2: Energy levels of Dy. The ground-to-singlet transition associated with the two $6s$ electrons gives rise to the 421 nm line ($J = 8 \rightarrow J' = 9$), the 419 nm line ($J = 8 \rightarrow J' = 8$), and the 405 nm line ($J = 8 \rightarrow J' = 7$) marked in blue arrows; The ground-to-triplet transition associated with the two $6s$ electrons gives rise to the 626 nm line ($J = 8 \rightarrow J' = 9$), the 598 nm line ($J = 8 \rightarrow J' = 8$), and the 599 nm line ($J = 8 \rightarrow J' = 7$) marked in orange arrows. Two narrow transitions associated with the $4f$ electrons are marked in red arrows: the 741 nm line ($\Gamma = 2\pi \times 1.78$ kHz [74]) and the 1001 nm line ($\Gamma = 2\pi \times 11.5$ Hz [88]).

2.2.1 Outer Shell Transitions: Singlet and Triplet States

Let us first consider the optical transitions associated with the excitation of the two $6s$ electrons in the outer shell. The lowest excitations are then $6s^2 \rightarrow 6s6p$. If we disregard the couplings between the outer-shell and inner-shell electrons and treat the Coulomb repulsion between the two outer electrons as a perturbation,

the wavefunction of the two electrons in the atomic orbital basis can be expressed as $\psi(\mathbf{r_1}, \mathbf{r_2}) = a\psi_{6s}(\mathbf{r_1})\psi_{6p}(\mathbf{r_2}) + b\psi_{6s}(\mathbf{r_2})\psi_{6p}(\mathbf{r_1})$. Correspondingly, the Coulomb interaction Hamiltonian in degenerate perturbation theory is written as $H_{\text{Coulomb}} = \begin{pmatrix} J & K \\ K & J \end{pmatrix}$, where the direct interaction is $J = \frac{1}{4\pi\epsilon_0} \int d\mathbf{r_1} d\mathbf{r_2} |\psi_{6s}(\mathbf{r_1})|^2 \frac{e^2}{|\mathbf{r_1} - \mathbf{r_2}|} |\psi_{6p}(\mathbf{r_2})|^2$ and the exchange integral is $K = 4\pi\epsilon_0 \int d\mathbf{r_1} d\mathbf{r_2} \psi_{6s}^*(\mathbf{r_1})\psi_{6p}^*(\mathbf{r_2}) \frac{e^2}{|\mathbf{r_1} - \mathbf{r_2}|} \psi_{6s}(\mathbf{r_2})\psi_{6p}(\mathbf{r_1})$. Diagonalizing the Hamiltonian yields a symmetric spatial wavefunction $\psi_S(\mathbf{r_1}, \mathbf{r_2}) = \frac{1}{\sqrt{2}}(\psi_{6s}(\mathbf{r_1})\psi_{6p}(\mathbf{r_2}) + \psi_{6s}(\mathbf{r_2})\psi_{6p}(\mathbf{r_1}))$ with a higher eigen-energy of $J + K$, and an anti-symmetric spatial wavefunction $\psi_A(\mathbf{r_1}, \mathbf{r_2}) = \frac{1}{\sqrt{2}}(\psi_{6s}(\mathbf{r_1})\psi_{6p}(\mathbf{r_2}) - \psi_{6s}(\mathbf{r_2})\psi_{6p}(\mathbf{r_1}))$ with a lower eigen-energy of $J - K$. Without couplings to the inner-shell electrons, the total wavefunction for the two outer-shell electrons needs to be anti-symmetric. Hence, the spin part of $\psi_S(\mathbf{r_1}, \mathbf{r_2})$ is a singlet state $|S = 0\rangle = \frac{1}{\sqrt{2}}(|\uparrow\downarrow\rangle - |\downarrow\uparrow\rangle)$, whereas the spin parts of $\psi_A(\mathbf{r_1}, \mathbf{r_2})$ are triplet states $|S = 1, m_S = 1\rangle = |\uparrow\uparrow\rangle$, $|S = 1, m_S = 0\rangle = \frac{1}{\sqrt{2}}(|\uparrow\downarrow\rangle + |\downarrow\uparrow\rangle)$, and $|S = 1, m_S = -1\rangle = |\downarrow\downarrow\rangle$. In term symbol, the singlet state is denoted as $^1P_1$, and the three triplet states as $^3P_0$, $^3P_1$, and $^3P_2$.

It can be noticed that the ground-to-singlet transition is electric-dipole allowed, leading to Dy's strongest atomic lines around 400 nm with natural linewidths around $2\pi \times 30$ MHz. However, the ground-to-triplet transitions, which involve a flip in electron spins, are electric-dipole forbidden. The natural linewidths of the triplets states are given by the strength of spin-orbit interactions that couple electron spins with their orbital motions. For the $^1S_0 \rightarrow^3 P_1$ transitions, the wavelengths are around 600 nm and the natural linewidths are around 100 kHz (see Fig. 2-2).

In the above analysis, we have neglected the couplings between the outer-shell and inner-shell electrons. Under this assumption, their total angular momenta J_{outer} and J_{inner} remain good quantum numbers. Couplings between the inner- and outer-shell electrons lead to an energy shift of all $6p$ states due to quantum defect. Moreover, for the $^1P_1$ singlet excited state or the $^3P_1$ triplet excited state (both with $J_{\text{outer}} = 1$), adding in the inner-shell electrons with $J_{\text{inner}} = 8$ gives rise to 24 excited sublevels with $m_{J_{\text{inner}}} = -8, ..., +8$ and $m_{J_{\text{outer}}} = -1, 0, +1$. Now if we consider angular momentum couplings between inner- and outer-shell electrons in the form

of $H_{JJ} \approx \alpha_{JJ}\mathbf{J}_{outer}\cdot\mathbf{J}_{inner}$, the good quantum number now becomes $J = J_{inner} + J_{outer}$. This would split the $^1P_1$ and the $^3P_1$ states each into three excited-state manifolds with $J' = 7$, 8, and 9.

For the ground-to-singlet transition, the angular-momentum coupling gives rise to three blue lines at 421 nm ($J = 8 \rightarrow J' = 9$), 419 nm ($J = 8 \rightarrow J' = 8$), and 405 nm ($J = 8 \rightarrow J' = 7$). These are the three broadest optical transitions of Dy with theoretically predicted natural linewidths of $\Gamma = 2\pi \times 33$ MHz, $2\pi \times 34$ MHz, and $2\pi \times 33$ MHz [69]. The measured linewidth of the 421 nm is $2\pi \times 32.2$ MHz [77]. For the ground-to-triplet ($^3P_1$) transition, the angular-momentum coupling gives rise to three lines at 626 nm ($J = 8 \rightarrow J' = 9$), 598 nm ($J = 8 \rightarrow J' = 8$), and 599 nm ($J = 8 \rightarrow J' = 7$). The predicted natural linewidths of these transitions are $\Gamma = 2\pi \times 180$ kHz, $2\pi \times 160$ kHz, and $2\pi \times 210$ kHz [69]. The measured linewidth of the 626 nm is $2\pi \times 136$ kHz [77].

In laser cooling experiments, one need to use cycling optical transitions for persistent photon scattering. This can be achieved by choosing $J = 8 \rightarrow J' = 9$ atomic lines combined with circularly-polarized lasers. For our apparatus, we choose the 421 nm transition for Zeeman slowing, and the 626 nm transition for magneto-optical trapping. The 32.2 MHz fast photon scattering rate of the 421 nm transition provides a large light pressure, allowing us to decelerate hot Dy atoms to a stop in a shorter distance using the Zeeman slower. On the other hand, the 136 kHz narrow linewidth of the 626 nm transition provides a low Doppler temperature of $T_D = 3.3$ μK, allowing us to cool Dy atoms down to the 10 μK regime using the magneto-optical trap. We will cover the details of these two devices in Chapter 4.

2.2.2 Inner Shell Transitions

There are many optical transitions associated with the excitations of inner-shell electrons. Two of these transitions at 741 nm and 1001 nm are shown in Fig. 2-2. The inner shell transitions are usually narrow and more isolated. For example, the 741 nm transition has a narrow linewidth of $\Gamma = 2\pi \times 1.78$ kHz and couples to a single excited state $^5K_9$ [74, 29]. As we will discuss in Chapter 3, such isolated inner-shell transitions enables the implementation of optical potentials with strong spin-dependence,

strong Raman coupling strength, and negligible heating due to spontaneous photon scattering. The 1001 nm transition has an even narrower natural linewidth of 11.5 Hz [88], opening up new possibilities for precision measurements and multi-species quantum simulation experiments [88, 97].

2.3 Dipole-Dipole Interaction

The large angular momentum of ground-state Dy arising from the spin and orbital motions of electrons results in a large magnetic moment. For bosonic isotopes, the magnetic moment μ is related to the total angular momentum $\mathbf{J}$ as

$$\boldsymbol{\mu} = g_J \mu_B \mathbf{J} \tag{2.2}$$

where the Landé g-factor g_J is approximately 1.24 [77]. Therefore in the direction of a given quantization axis, the magnetic moment of a bosonic Dy atom in the $m_J = -8$ ground state is $|\boldsymbol{\mu}| = \langle J = 8, m_J = -8 | \mu_z | J = 8, m_J = -8 \rangle \approx -9.9 \mu_B$. This result is easily extended to fermionic isotopes by replacing $\boldsymbol{J}$ with $\boldsymbol{F}$. The corresponding Landé g-factor g_F is approximately 0.95 [77], leading to a magnetic momentum of fermionic Dy atoms in the stretched spin-state $m_F = -21/2$ of also $-9.9 \mu_B$. In the following parts of this section, we will introduce how the long-range dipole-dipole interaction Hamiltonian couples the motion of Dy atoms with large magnetic moments.

2.3.1 Coupling between Spin and Orbital Motion

The long-range dipole-dipole interaction is in the following form

$$U_{\mathrm{dd}}(\mathbf{r}) = \frac{\mu_0}{4\pi} (\mu_B g_J)^2 \frac{\mathbf{J}_1 \cdot \mathbf{J}_2 - 3(\mathbf{J}_1 \cdot \hat{\mathbf{r}})(\mathbf{J}_2 \cdot \hat{\mathbf{r}})}{r^3} \tag{2.3}$$

where $\mathbf{r} = \mathbf{r_1} - \mathbf{r_2}$ is the relative position operator between two magnetic dipoles, and $\mathbf{J}_1$ and $\mathbf{J}_2$ are the internal angular momenta of the Dy atoms. In the limit of classical point dipoles polarized in an external magnetic field, the dipole-dipole potential can
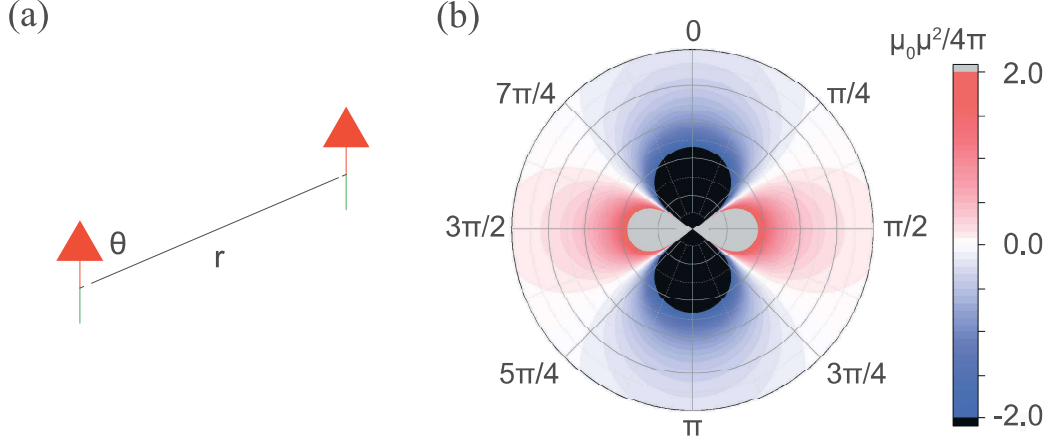
Figure 2-3: (a) Illustration of two polarized magnetic dipoles with relative distance r and relative orientation θ. (b) Dipole-dipole interaction strength as a function of (r, θ). The interaction is attractive in head-to-tail configuration, and is repulsive in side-by-side configuration.

be reduced to an algebraic form of $U_{\mathrm{dd}}(r, \theta) = \frac{\mu_0 \mu^2}{4\pi} \frac{1 - 3\cos^2\theta}{r^3}$. As plotted in Fig. 2-3, the interaction is attractive for head-to-tail configuration at $\theta = 0$, and is repulsive for side-by-side configuration at $\theta = 90°$. The interaction vanishes at the magic angle of $\theta \approx 55°$.

Now let's turn to quantum mechanical description and express the wavefunction of two Dy atoms as $|\psi(\mathbf{r})\rangle |m_{J1}, m_{J2}\rangle$. The relative position operator $\mathbf{r}$ acts on the spatial part $|\psi(\mathbf{r})\rangle$, and the angular momentum operators $\mathbf{J}_1$ and $\mathbf{J}_2$ act on the spin part $|m_{J1}, m_{J2}\rangle$. By introducing the spin-flip operators $J_{\pm} = J_x \pm i J_y$ and noticing the identity $\mathbf{J}_1 \cdot \mathbf{J}_2 = J_{1z} J_{2z} + \frac{1}{2}(J_{1+} J_{2-} + J_{1-} J_{2+})$, we can expand Eq. 2.3 as

$$
\begin{aligned}
U_{\mathrm{dd}}(\mathbf{r}) = \frac{\mu_0}{4\pi}(\mu_B g_J)^2 \frac{1}{r^3} \Big\{ & (1 - 3\cos^2\theta) J_{1z} J_{2z} \\
& - \frac{1}{4}(1 - 3\cos^2\theta)(J_{1-} J_{2+} + J_{1+} J_{2-}) \\
& - \frac{3}{2}\sin\theta\cos\theta \Big[e^{-i\phi}(J_{1z} J_{2+} + J_{1+} J_{2z}) + e^{+i\phi}(J_{1z} J_{2-} + J_{1-} J_{2z}) \Big] \\
& - \frac{3}{4}\sin^2\theta (e^{-2i\phi} J_{1+} J_{2+} + e^{+2i\phi} J_{1-} J_{2-}) \Big\}
\end{aligned}
$$

(2.4)

The above expression is divided into four parts. The angular dependence of each part can be expressed in terms of spherical harmonics $Y_{l,m}(\hat{\mathbf{r}})$. The first line propor-

tional to $Y_{2,0}(\hat{\mathbf{r}})J_{1z}J_{2z}$ is the classical part of the dipole-dipole interaction; The second line proportional to $Y_{2,0}(\hat{\mathbf{r}})(J_{1-}J_{2+}+J_{1+}J_{2-})$ is the spin-exchange coupling which couples the internal spins of two atoms; The third line proportional to $Y_{2,\mp1}(\hat{\mathbf{r}})(J_{1z}J_{2\pm} + J_{1\pm}J_{2z})$ converts one unit of the internal spin to the external orbital angular momentum (and vice versa); And the fourth line proportional to $Y_{2,\mp2}(\hat{\mathbf{r}})J_{1\pm}J_{2\pm}$ converts two units of the internal spin to the external orbital angular momentum (and vice versa). These couplings between the internal spins and external orbital motions due to the dipole-dipole interaction give rise to interesting physics of spin mixtures including dipolar relaxation (as we will introduce in Chapter 6), Einstein de Haas effect [55], new phases of spinor BECs [92], and so on.

2.3.2 Fourier Transform

From Eq. 2.4, we have already seen that the angular part of the dipole-dipole interaction Hamiltonian can be described by spherical harmonics. This becomes more evident if we factorize the spin and spatial operators as

$$U_{\text{dd}}(\mathbf{r}) = \frac{\mu_0}{4\pi}(\mu_B g_J)^2 \Big[\mathbf{J}_1 \cdot \mathbf{Q}(\mathbf{r}) \cdot \mathbf{J}_2\Big] \tag{2.5}$$

where the traceless rank-2 tensor $\mathbf{Q}(\mathbf{r})$ is defined as

$$
\mathbf{Q}(\mathbf{r}) = \frac{1}{r^3}(\mathbb{1} - 3\hat{\mathbf{r}}\hat{\mathbf{r}}) = -\nabla\nabla\frac{1}{r}
$$

$$
= \sqrt{\frac{6\pi}{5}}\frac{1}{r^3}
\begin{pmatrix}
\sqrt{\frac{2}{3}}Y_{2,0} - Y_{2,2} - Y_{2,-2} & i(Y_{2,2} - Y_{2,-2}) & Y_{2,1} - Y_{2,-1} \\
i(Y_{2,2} - Y_{2,-2}) & \sqrt{\frac{2}{3}}Y_{2,0} + Y_{2,2} + Y_{2,-2} & -i(Y_{2,1} + Y_{2,-1}) \\
Y_{2,1} - Y_{2,-1} & -i(Y_{2,1} + Y_{2,-1}) & -2\sqrt{\frac{2}{3}}Y_{2,0}
\end{pmatrix}
\tag{2.6}
$$

This is a particularly convenient form for some mathematical purposes such as evaluating the Fourier transform of $U_{\text{dd}}(\mathbf{r})$ in scattering theory, which can be done by noticing the following two properties of spherical harmonics.

Property 1. Spherical harmonics $Y_{lm}(\theta,\phi)$ are eigen-functions of Fourier transform

on a unit sphere, i.e.

$$\int_{\theta=0}^{\pi}\int_{\phi=0}^{2\pi} d\Omega\, e^{i\mathbf{k}\cdot\mathbf{r}} Y_{lm}(\hat{\mathbf{r}}) = 4\pi i^l j_l(kr) Y_{lm}(\hat{\mathbf{k}}) \tag{2.7}$$

Proof. Using the spherical harmonics addition theorem, we expand the plane wave into

$$e^{i\mathbf{k}\cdot\mathbf{r}} = 4\pi \sum_{l=0}^{+\infty} \sum_{m=-l}^{+l} i^l j_l(kr) Y_{lm}^*(\hat{\mathbf{r}}) Y_{lm}(\hat{\mathbf{k}}) \tag{2.8}$$

And the Fourier transform can be evaluated using the orthogonality of spherical harmonics

$$\int d\Omega\, e^{i\mathbf{k}\cdot\mathbf{r}} Y_{lm}(\hat{\mathbf{r}}) = 4\pi \sum_{l=0}^{+\infty} \sum_{m=-l}^{+l} i^l j_l(kr) Y_{lm}(\hat{\mathbf{k}}) \underbrace{\int d\Omega \left[Y_{l'm'}^*(\hat{\mathbf{r}}) Y_{lm}(\hat{\mathbf{r}}) \right]}_{\delta_{ll'}\delta_{mm'}}$$

$$= 4\pi i^l j_l(kr) Y_{lm}(\hat{\mathbf{k}}) \tag{2.9}$$

Property 2. The Fourier transform of $Y_{lm}(\hat{\mathbf{r}})/r^3$ preserves spherical harmonics symmetry in angular direction, but the radial $1/r^3$ dependence vanishes:

$$\int d^3\mathbf{r} \cdot e^{i\mathbf{k}\cdot\mathbf{r}} \frac{Y_{lm}(\hat{\mathbf{r}})}{r^3} = \pi^{3/2} i^l \frac{\Gamma(\frac{l}{2})}{\Gamma(\frac{3+l}{2})} Y_{lm}(\hat{\mathbf{k}}) \tag{2.10}$$

where $\Gamma(x)$ is the gamma function. Specifically, for spherical harmonics with $l = 2$, the right-hand-side gives $Y_{2m}(\hat{\mathbf{k}})/3$. This result can be proven using Property 1.

From Property 2, it becomes obvious that the matrix elements of the tensor $\mathbf{Q}(\mathbf{r})$ loses $1/r^3$ radial dependence, but the angular dependence is preserved after Fourier transform. Hence the Fourier transform of the dipole-dipole interaction Hamiltonian is

$$\tilde{U}_{\mathrm{dd}}(\mathbf{k}) = \int d^3\mathbf{r} \cdot e^{i\mathbf{k}\cdot\mathbf{r}} U_{\mathrm{dd}}(\mathbf{r}) = -\frac{1}{3}\mu_0(\mu_B g_J)^2 \left[\mathbf{J}_1\cdot\mathbf{J}_2 - 3(\mathbf{J}_1\cdot\hat{\mathbf{k}})(\mathbf{J}_2\cdot\hat{\mathbf{k}}) \right] \tag{2.11}$$

Chapter 3

Interaction between Atoms and Light

This chapter presents the theoretical framework that describes how lasers interact with Dy atoms via the electric-dipole interaction Hamiltonian. We will start with a scenario where only one ground state and one excited state are coupled by the laser, and show how the dissipative and conservative forces experienced by this two-level atom can be described by a complex polarizability. As more atomic states are involved in the ground- and excited-state manifolds, we will see that the polarizability of the atom becomes state-dependent: the interaction energy depends on the relative orientation between the atomic spin and the polarization of light. Such anisotropic interaction can be fully categorized into a scalar term, a vector term, and a tensor term. This categorization is essential for the optical trapping of Dy, or in general, atoms with large angular momentum studied in the following chapters.

3.1 Laser-Induced Electric Dipole Moment

An atom placed in the electric field of a laser beam $\mathbf{E_e}(t) = \mathbf{e}E\cos\omega t$ obtains a non-zero oscillating electric dipole moment $\langle \mathbf{d}(t) \rangle = \mathbf{e}d\left(u_{st}\cos\omega t + v_{st}\sin\omega t\right)$ due to the electric-dipole interaction via Hamiltonian $V = -\mathbf{d}\cdot\mathbf{E}$, here $\mathbf{e}$ is the polarization direction of the electric field, u_{st} and v_{st} denote the in-phase and in-quadrature compo-

nents of the induced electric dipole moment, the electric dipole operator $\mathbf{d}$ is related to the electron dipolar operators $\mathbf{r_i}$ as $\mathbf{d} = e \sum_i \mathbf{r_i}$. Since the operator $\mathbf{d}$ has odd parity, it only couples atomic eigenstates in opposite parities $\langle \psi_e(\mathbf{r_i}) | \mathbf{d} | \psi_o(\mathbf{r_i}) \rangle \neq 0$. Hence the mean electric dipole moment of an atom in energy eigenstates is zero, unless multiple different atomic orbitals in opposite parities are admixed by an electric field.

In complex notation, we can re-write the electric field and the dipole moment as

$$
\begin{cases}
\mathbf{E_e}(t) = \dfrac{1}{2}\mathbf{e}Ee^{-i\omega t} + c.c. \\
\langle \mathbf{d}(t) \rangle = \dfrac{1}{2}\mathbf{e}d(u_{st} + iv_{st})e^{-i\omega t} + c.c.
\end{cases}
\tag{3.1}
$$

and hence the complex amplitude d of the dipole moment can be related to the complex field amplitude E as

$$
d = \alpha E \tag{3.2}
$$

where we define $\alpha \propto (u_{st} + iv_{st})$ as the *complex polarizability*.

The induced oscillating electric dipole obtains a polarization energy in the laser field that is proportional to the real part of α

$$
U = -\frac{1}{2}\langle \mathbf{d} \cdot \mathbf{E} \rangle = -\frac{1}{2\epsilon_0 c}\mathrm{Re}(\alpha)I \tag{3.3}
$$

with the laser intensity $I = 1/2\epsilon_0 c|E|^2$. This is a conservative dipole force used for optical trapping of neutral atoms. On the other hand, the oscillating electric dipole also radiates photons dissipatively at the driving frequency ω — a process known as spontaneous scattering. The average power of the dipole radiation can be calculated as $P = -\langle \dot{\mathbf{d}} \cdot \mathbf{E} \rangle = -2\omega \mathrm{Im}(\alpha)E^2$, hence the spontaneous photon scattering rate is given by

$$
\Gamma_{sc} = -\frac{\langle \dot{\mathbf{d}} \cdot \mathbf{E} \rangle}{\hbar \omega} = -\frac{1}{\hbar \epsilon_0 c}\mathrm{Im}(\alpha)I \tag{3.4}
$$

which is proportional to the imaginary part of α.

To conclude, we see from the above analysis that the in-phase component of the induced electric dipole causes a conservative dipole potential, whereas the quadrature component causes spontaneous scattering. These two components are proportional

44

to the real and imaginary parts of the complex polarizability α, which is determined by the electronic structure of the atoms and the laser frequency, as will be discussed in the following sections.

3.2   Complex Polarizability of a Two-Level Atom

Here we consider a simple case where a two-level atom with a ground state $|g\rangle$ and an excited state $|e\rangle$ is coupled by an electric field via the electric-dipole interaction. The evolution of the density matrix $\rho = \begin{pmatrix} \rho_{gg} & \rho_{ge} \\ \rho_{eg} & \rho_{ee} \end{pmatrix}$ for the system is determined by the following equation of motion

$$\dot{\rho} = \frac{1}{i\hbar}[H,\rho] + \begin{pmatrix} \Gamma\rho_{ee} & -\frac{\Gamma}{2}\rho_{ge} \\ -\frac{\Gamma}{2}\rho_{ge} & \Gamma\rho_{ee} \end{pmatrix} \tag{3.5}$$

where the Hamiltonian in the rotating-wave approximation is $H = \frac{\hbar}{2}\begin{pmatrix} -\omega_0 & \Omega e^{+i\omega t} \\ \Omega e^{-i\omega t} & \omega_0 \end{pmatrix}$ with $\Omega = \langle e|\mathbf{d}\cdot\mathbf{E}|g\rangle/\hbar$ being the Rabi frequency, and $\hbar\omega_0 = E_e - E_g$ being the energy splitting between the ground and excited states. By defining the reduced density matrix $\tilde{\rho} = \begin{pmatrix} \tilde{\rho}_{gg} & \tilde{\rho}_{ge} \\ \tilde{\rho}_{eg} & \tilde{\rho}_{ee} \end{pmatrix} = \begin{pmatrix} \rho_{gg} & \rho_{ge}e^{-i\omega t} \\ \rho_{eg}e^{+i\omega t} & \rho_{ee} \end{pmatrix}$ co-rotating with the laser field, and introducing the Bloch vector $\mathbf{r} = (u,v,w)$ by decomposing $\tilde{\rho}$ using the Pauli matrices $\tilde{\rho} = \frac{1}{2}(I + \mathbf{r}\cdot\sigma) = \frac{1}{2}(I + u\sigma_x + v\sigma_y + w\sigma_z)$, the equation of motion can be re-written as

$$\dot{\mathbf{r}} = \begin{pmatrix} -\frac{\Gamma}{2} & \delta & 0 \\ -\delta & -\frac{\Gamma}{2} & \Omega \\ 0 & \Omega & -\Gamma \end{pmatrix}\mathbf{r} + \begin{pmatrix} 0 \\ 0 \\ -\Gamma/2 \end{pmatrix} \tag{3.6}$$

where $\delta = \omega_0 - \omega$ is the laser detuning, Γ is the natural linewidth of the excited state, and the three components of the Bloch vector are related to the density matrix elements as $u = \frac{1}{2}(\tilde{\rho}_{ab} + \tilde{\rho}_{ba})$, $v = \frac{1}{2i}(\tilde{\rho}_{ab} - \tilde{\rho}_{ba})$, and $w = \frac{1}{2}(\tilde{\rho}_{bb} - \tilde{\rho}_{aa})$. This is the optical Bloch equation (OBE) of a two-level system. From Eq. 3.6 we see that the detuning

δ controls the z-rotation of the Bloch vector, known as Lamor precesion; the Rabi frequency Ω controls the x-rotation of the Bloch vector, known as Rabi flopping; and the damping rate Γ controls the relaxation of the Bloch vector. By setting $\dot{\mathbf{r}} = 0$, we obtain the stationary solution of the OBE

$$
\begin{cases}
u_{\text{st}} = \dfrac{\Omega}{2} \dfrac{\delta}{\delta^2 + \Omega^2/2 + \Gamma^2/4} \\[2mm]
v_{\text{st}} = \dfrac{\Omega}{2} \dfrac{\Gamma/2}{\delta^2 + \Omega^2/2 + \Gamma^2/4} \\[2mm]
w_{\text{st}} = \dfrac{\Omega^2}{4} \dfrac{1}{\delta^2 + \Omega^2/2 + \Gamma^2/4} - \dfrac{1}{2}
\end{cases}
\tag{3.7}
$$

(a)

Im[α]

$\sim 1/\delta^2$

δ / Γ

(b)

Re[α]

$\sim 1/\delta$

δ / Γ
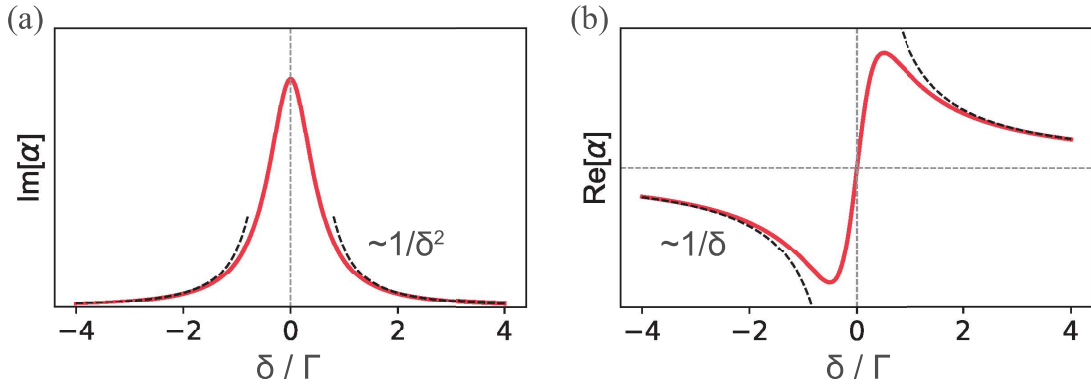
Figure 3-1: (a) Imaginary and (b) real parts of the complex polarizability α of a two-level atom. Dashed lines are weak-saturation limit where $\Omega \ll \Gamma, \delta$.

Using the density matrix description, the mean electric dipole moment is given by

$$
\begin{aligned}
\langle \mathbf{d}(t) \rangle = \text{Tr}(\rho \mathbf{d}) &= \langle e|\mathbf{d}|g\rangle \sum_{i=g,e} \langle i| \Big[\rho_{gg}|g\rangle\langle e| + \rho_{ee}|e\rangle\langle g| + \rho_{ge}|g\rangle\langle g| + \rho_{eg}|e\rangle\langle e| \Big] |i\rangle \\
&= \langle e|\mathbf{d}|g\rangle \left(\tilde{\rho}_{ge} e^{-i\omega t} + \tilde{\rho}_{eg} e^{+i\omega t} \right) \\
&= \langle e|\mathbf{d}|g\rangle \left[\left(\tilde{\rho}_{eg} + \tilde{\rho}_{ge} \right) \cos\omega t - i\left(\tilde{\rho}_{eg} - \tilde{\rho}_{ge} \right) \sin\omega t \right] \\
&= 2 \langle e|\mathbf{d}|g\rangle \left(u_{\text{st}} \cos\omega t - v_{\text{st}} \sin\omega t \right)
\end{aligned}
\tag{3.8}
$$

which is the sum of an in-phase and an in-quadrature component. (explain what is weak saturation limit with a plot) By expanding the dipole moment to the linear term of electric field E in the weak saturation limit $\Omega \ll \Gamma, \delta$, we obtain the complex

polarizability of the two-level system under rotating approximation

$$\alpha(\omega) = \frac{\Omega}{2} \frac{\delta + i\Gamma/2}{\delta^2 + \Omega^2/2 + \Gamma^2/4} \approx \frac{1}{2} \frac{|\langle e|\mathbf{d}\cdot\mathbf{e}|g\rangle|^2}{E_e - E_g - \hbar\omega - i\frac{\hbar\Gamma}{2}} \tag{3.9}$$

The real part of the expressions scales with $1/\delta$, whereas the imaginary part scales with $1/\delta^2$ in the far detuned limit (see Fig. 3-1). This enables the creation of conservative optical potentials $U \propto \mathrm{Im}(\alpha)$ with negligible spontaneous photon scattering rate $\Gamma_{\mathrm{sc}} \propto \mathrm{Re}(\alpha)$ using far-detuned high power lasers. This part of the light-atom interaction is used for techniques such as evaporative cooling, optical lattice, optical tweezers, etc. On the other hand, in the near-detuned regime where spontaneous scattering is dominant, lasers are used for cooling techniques such as Zeeman slowing, magneto-optical trapping, etc. The above result was based on rotating-wave approximation. Without dropping the counter-rotating term, the expression for the complex polarizability of a two-level atom can be extended to

$$\alpha(\omega) = \frac{|\langle e|\mathbf{d}\cdot\mathbf{e}|g\rangle|^2}{2} \left(\frac{1}{E_e - E_g - \hbar\omega - i\frac{\hbar\Gamma}{2}} + \frac{1}{E_e - E_g + \hbar\omega - i\frac{\hbar\Gamma}{2}} \right) \tag{3.10}$$

3.3 Anisotropic Polarizability

The two-level system we considered in the above section is a model with zero angular momentum. However, ideal two-level systems do not truly exist: S-to-S atomic transitions are electric-dipole forbidden. For atoms with angular momenta in the ground and excited states, their interaction with laser photons become anisotropic. The anisotropic nature of atom-light interaction is due to the addition of angular momenta of laser photons and atoms, as we will see in this section.

3.3.1 Near-Resonance Coupling: the Clebsch-Gordan Picture

To illustrate the anisotropic nature of atom-light interaction, here we consider a simple model where a ground-state manifold with angular momentum J is coupled to an excited-state manifold with angular momentum J'. Specifically for bosonic dyspro-

sium, the angular momentum carried by its ground state is $J = 8$, and that carried by the excited-state we study is $J' = 9$ (e.g. the dysprosium 741 nm line). Fig. 3-2 illustrates all possible couplings among 17 ground states and 19 excited states mediated by laser photons in different polarizations. Taking the Cartesian z axis as the quantization axis, we define spherical basis as

$$
\begin{cases}
\hat{\mathbf{e}}_{+1} = -\dfrac{1}{\sqrt{2}}\hat{\mathbf{e}}_x - \dfrac{i}{\sqrt{2}}\hat{\mathbf{e}}_y \\[2mm]
\hat{\mathbf{e}}_{-1} = +\dfrac{1}{\sqrt{2}}\hat{\mathbf{e}}_x - \dfrac{i}{\sqrt{2}}\hat{\mathbf{e}}_y \\[2mm]
\hat{\mathbf{e}}_0 = \hat{\mathbf{e}}_z
\end{cases}
\tag{3.11}
$$

Hence the electric field of the laser at the position of the atom can be written under the spherical basis as

$$
\mathbf{E}(t) = \sum_{\sigma=0,\pm 1} \hat{\mathbf{e}}_\sigma \left[E_\sigma^{(-)} e^{+i\omega t} + E_\sigma^{(+)} e^{-i\omega t} \right]
\tag{3.12}
$$

where amplitudes $E_\sigma^{(-)}$ and $E_\sigma^{(+)}$ are complex conjugates.

On the other hand, the electric-dipole operator can be written in terms of matrix elements $\langle g; J, m_J | \mathbf{d} | e; J', m'_J \rangle$ as

$$
\mathbf{d} = \sum_{m_J, m'_J} \langle g; J, m_J | \mathbf{d} | e; J', m'_J \rangle \left(\sigma_{m_J, m'_J} + \sigma^\dagger_{m_J, m'_J} \right)
\tag{3.13}
$$

where we define the operator $\sigma_{m_J, m'_J} = |g; J, m_J\rangle \langle e; J', m'_J|$. We can decompose the

m_J	-8	-7	-6	-5	-4	-3	-2	-1	0
$\|e\langle J'=9, m_J-1 \| \hat{\sigma}_- \cdot \mathbf{r} \| J=8, m_J\rangle\|^2$	1	$\frac{8}{9}$	$\frac{40}{51}$	$\frac{35}{51}$	$\frac{91}{153}$	$\frac{26}{51}$	$\frac{22}{51}$	$\frac{55}{153}$	$\frac{5}{17}$
$\|e\langle J'=9, m_J \| \hat{\pi} \cdot \mathbf{r} \| J=8, m_J\rangle\|^2$	$\frac{1}{9}$	$\frac{32}{153}$	$\frac{5}{17}$	$\frac{56}{153}$	$\frac{65}{153}$	$\frac{8}{17}$	$\frac{77}{153}$	$\frac{80}{153}$	$\frac{9}{17}$
$\|e\langle J'=9, m_J+1 \| \hat{\sigma}_+ \cdot \mathbf{r} \| J=8, m_J\rangle\|^2$	$\frac{1}{153}$	$\frac{1}{51}$	$\frac{2}{51}$	$\frac{10}{153}$	$\frac{5}{51}$	$\frac{7}{51}$	$\frac{28}{153}$	$\frac{4}{17}$	$\frac{5}{17}$

Table 3.1: Values of the relative strengths of the 741nm transitions between different Zeeman levels. Normalization is done with respect to the $m_J = -8 \to m_{J'} = -9$ transition.
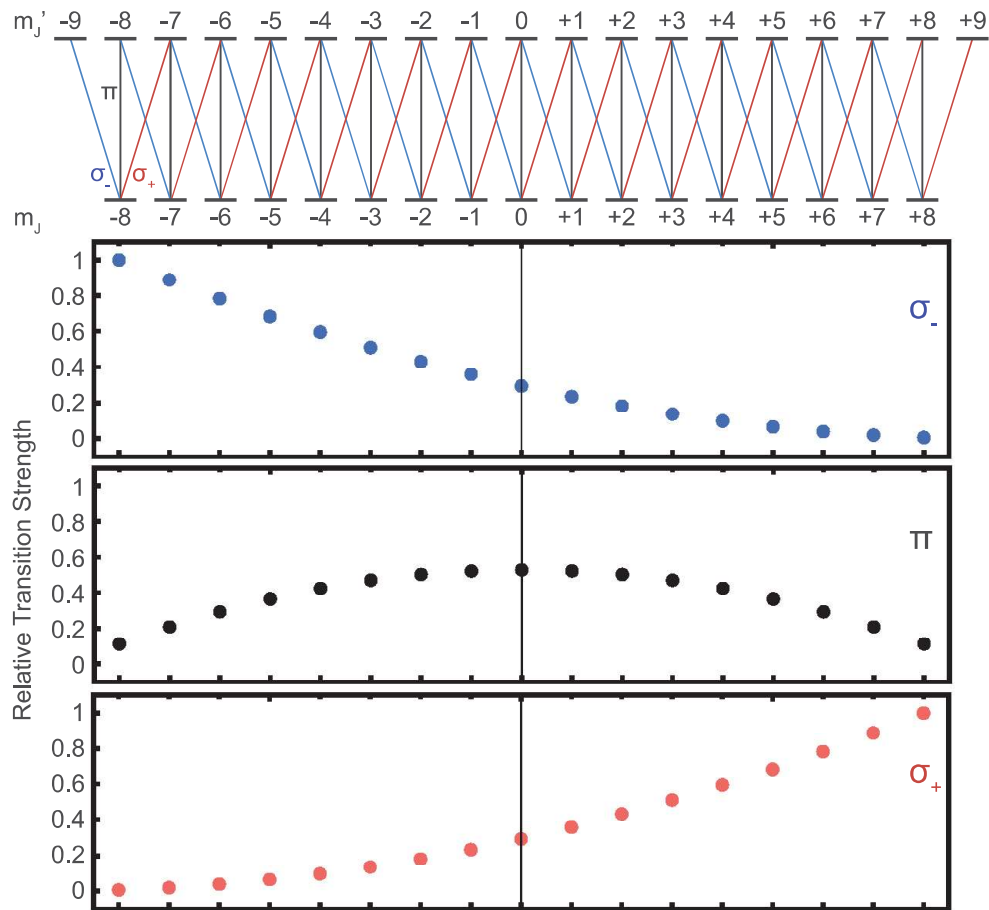
48

Figure 3-2: Possible couplings among the $J = 8$ ground-state manifold and the $J = 9$ excited-state manifold. Lasers with σ_- circular polarization causes couplings with $\Delta m_J = -1$ (blue); lasers with π circular polarization causes couplings with $\Delta m_J = 0$ (black); lasers with σ_+ circular polarization causes couplings with $\Delta m_J = +1$ (red).

operator $\mathbf{d} = e\sum_i \mathbf{r_i}$ under spherical basis as

$$\mathbf{d} = e\sum_i \mathbf{r_i} = e\sum_i \sum_{\sigma=0,\pm1} r_\sigma \hat{\mathbf{e}}_\sigma \tag{3.14}$$

with $r_{-1} = -(x-iy)/\sqrt{2}$, $r_{+1} = (x+iy)/\sqrt{2}$, and $r_0 = z$ being proportional to the three spherical harmonics $Y_{1,-1}$, $Y_{1,1}$, and $Y_{1,0}$. Since these operators d_σ rotate like spin-1 objects, we can factorize out the Clebsch-Gordan coefficients using the Wigner-Eckart theorem for the evaluation of the matrix elements:

$$\langle g; J, m_J | \mathbf{d} | e; J', m'_J \rangle \equiv \langle g; J || \mathbf{d} || e; J' \rangle \langle J, m_J; 1, \sigma | J', m'_J \rangle \tag{3.15}$$

This factorization gives rise to a part $\langle g; J || \mathbf{d} || e; J' \rangle$ in the electric-dipole interaction Hamiltonian that is independent of the internal spin state m_J, leaving the state-dependent part completely described by the Clebsch-Gordan coefficients $\langle J, m_J; 1, \sigma | J', m'_J \rangle$, as written in the following

$$V = -\mathbf{d} \cdot \mathbf{E}$$
$$= -\langle g; J || \mathbf{d} || e; J' \rangle \sum_{\sigma, m_J, m'_J} \langle J, m_J; 1, \sigma | J', m'_J \rangle \left[E_\sigma^{(-)}(z) e^{+i\omega t} + E_\sigma^{(+)}(z) e^{-i\omega t} \right] \left(\sigma_{m_J, m'_J} + \sigma^\dagger_{m_J, m'_J} \right) \tag{3.16}$$

In second-order perturbation theory, we see that relative transition strengths between the $|J, m_J\rangle$ ground state and the $|J', m'_J\rangle$ excited state of a spin-J atom is proportional to $|\langle J, m_J; 1, \sigma | J', m'_J \rangle|^2$. Therefore in contrast to a spinless two-level atom, the complex polarizability now depends on the relative orientation between the atomic spin and the laser polarization — the atom-light interaction is anisotropic. Listed in Table 3.1 are the relative transition strengths for dypsrosium $J = 8$ to $J = 9$ transitions. Remarkably, for the spin-polarized ground state $|J = 8, m_J = \pm 8\rangle$, the relative transition strength for $\sigma_\pm$ circular polarization is 153 stronger than for $\sigma_\mp$ polarization. This big contrast leads to a scenario where Dy atoms in the $|J = 8, m_J = -8\rangle$ spin state interact almost only with lasers in σ_- polarization, whereas Dy atoms in the $|J = 8, m_J = +8\rangle$ spin state interact almost only with lasers in σ_+ po-

50

larization. Such near-independent addressing of different atomic spin states with different polarizations of light enables the realization of bilayers system of Dy atoms with tunable interlayer spacings all the way down to a 50 nm scale, as will be introduced in the following chapters.

3.3.2 Scalar, Vector, and Tensor Polarizabilities

The previous section illustrated why atom-light interactions are generally anisotropic using a model with one ground-state manifold and one excited-state manifold. The complex polarizability of the ground-state atom that is proportional to the $\left(\text{matrix element}\right)^2$ of the $-\mathbf{d}\cdot\mathbf{E}$ Hamiltonian comes down to the square of the Clebsch-Gordan coefficient that corresponds to the conservation of angular momenta between the excited state $\left|J+1,m'_J\right\rangle$ and the ground state $\left|J,m_J\right\rangle$ with one unit of angular momentum contributed by the laser photon.
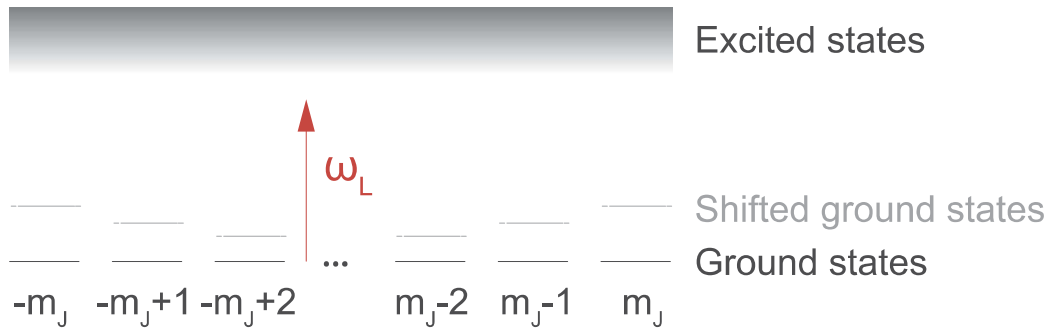
Figure 3-3: The ground state with angular momentum J is coupled to a bunch of excited states using a detuned laser field at frequency ω_L via the electric-dipole interaction Hamiltonian $V = -\mathbf{d}\cdot\mathbf{E}$, resulting in state-dependent level shifts in the ground-state manifold.

This section will introduce a more general approach for the categorization of anisotropic complex atomic polarizability, without assuming specific structures of the excited-state manifolds. We will show that, regardless of the electronic structure of the atom, its complex polarizability can always be categorized into a scalar term $\alpha^{(s)}$, a vector term $\alpha^{(v)}$, and a tensor term $\alpha^{(t)}$. The fundamental reason for this categorization is due to a maximum of $2\hbar$ angular-momentum change with two photons involved in the second-order perturbation theory.

In second-order perturbation theory, the energy shift of the ground-state atom with angular momentum J can be written as (see Fig. 3-3)

$$\Delta E(J, m_J; \omega) = \sum_{J', m'_J} \frac{\langle J, m_J | \mathbf{d} \cdot \mathbf{E} | J', m'_J \rangle \langle J', m'_J | \mathbf{d} \cdot \mathbf{E} | J, m_J \rangle}{\hbar(\omega_{J'J} - \omega)}$$

$$= \alpha_{\mu\nu}(J, m_J; \omega) E_\mu E_\nu \tag{3.17}$$

where the complex polarizability is expressed as

$$\alpha_{\mu\nu}(J, m_J; \omega) = \sum_{J'} \frac{\langle J, m_J | T_{\mu\nu} | J, m_J \rangle}{\hbar(\omega_{J'J} - \omega)} \tag{3.18}$$

with the dipole-product operator defined as

$$T_{\mu\nu} = \sum_{m'_J} d_\mu |J', m'_J \rangle \langle J', m'_J| d_\nu \tag{3.19}$$

The dipole-product operator is a Cartesian tensor of rank 2. It can be proven [96] that a rank-2 Cartesian tensor with 9 independent components can always be decomposed into three irreducible parts

$$T_{\mu\nu} = \frac{1}{3} T^{(0,0)} \delta_{\mu\nu} + \frac{1}{4} T_\sigma^{(1,0)} \epsilon_{\sigma\mu\nu} + T_{\mu\nu}^{(2,0)} \tag{3.20}$$

where the rank-0 tensor $T^{(0,0)} = \text{Tr}[\mathrm{T}_{\mu\nu}] = \mathrm{T}_{\mu\mu}$ is the trace of the original tensor operator $T_{\mu\nu}$ with 1 independent component, the rank-1 tensor $T_\mu^{(1,0)} = \epsilon_{\mu\alpha\beta}(T_{\alpha\beta} - T_{\beta\alpha})$ is the traceless asymmetric part of $T_{\mu\nu}$ with 3 independent components, and what is left over is a symmetric and traceless rank-2 tensor operator $T_{\mu\nu}^{(2,0)} = \frac{1}{2}(T_{\mu\nu} + T_{\nu\mu}) - \frac{1}{3} T_{\alpha\alpha} \delta_{\mu\nu}$ with 5 independent components. These irreducible tensors $T^{(k,q)}$ transform under rotations in the same way as the angular-momentum states $|J = k, m_J = q\rangle$ or spherical harmonics $Y_{k,q}(\theta, \phi)$, i.e. $R^\dagger T^{(k,q)} R = \sum_{q'} T^{(k,q)} D_{qq'}^{(k)}$, where $R = \exp\left(-i\theta \hat{\mathbf{n}} \cdot \mathbf{J}\right)$ is the rotation operator, and $D_{qq'}^{(k)}$ is the Wigner-D matrix. Hence they satisfy the angular-momentum addition rules $T^{(k,q)} = \sum_{q_1, q_2} T^{(k_1, q_1)} T^{(k_2, q_2)} \langle k_1, q_1; k_2, q_2 | k, q \rangle$. Based on the decomposition given by Eq. 3.20, we can categorize the complex polarizability expressed in Eq. 3.18 into a scalar part $\alpha^{(s)}$, a vector part $\alpha^{(v)}$, and a tensor part

$\alpha^{(t)}$. We can apply Wigner-Eckart theorem to the three irreducible spherical tensor operators

$$
\begin{cases}
\alpha^{(s)} \propto \langle J, m_J | T^{(0,0)} | J, m_J \rangle & \text{independent of } m_J \\[2mm]
\alpha^{(v)} \propto \langle J, m_J | T^{(1,0)} | J, m_J \rangle \propto \langle J, m_J | J, m_J; 1, 0 \rangle \propto m_J \\[2mm]
\alpha^{(t)} \propto \langle J, m_J | T^{(2,0)} | J, m_J \rangle \propto \langle J, m_J | J, m_J; 2, 0 \rangle \propto m_J^2
\end{cases}
\tag{3.21}
$$

and find that the scalar polarizability $\alpha^{(s)}$ contributes to state-independent level shifts, the vector polarizability $\alpha^{(v)}$ contributes to level shifts that is linear in m_J, and the tensor polarizability $\alpha^{(t)}$ contributes to level shifts that is quadratic in m_J. By using the above categorization, and contracting $\alpha_{\mu\nu}$ with the polarization vector $\mathbf{e}$ of the laser electric field, the complex polarizability can be expressed as [63]

$$
\alpha = \alpha^{(s)} - i\alpha^{(v)}\frac{(\mathbf{e}^* \times \mathbf{e}) \cdot \mathbf{J}}{2J} + \alpha_t \frac{3\left[(\mathbf{e}^* \cdot \mathbf{J})(\mathbf{e} \cdot \mathbf{J}) + (\mathbf{e} \cdot \mathbf{J})(\mathbf{e}^* \cdot \mathbf{J})\right] - 2\mathbf{J}^2}{2J(2J-1)}
\tag{3.22}
$$

As we see, the atom-light interaction associated with the vector polarizability $\alpha^{(v)}$ is completely analogous to the Zeeman interaction Hamiltonian $H_z = -\mu_B g_J \mathbf{B} \cdot \mathbf{J}$: a circular polarization of light acts as an effective magnetic field that provides a quantization axis perpendicular to the polarization vector $\mathbf{e}$, and thus gives rise to a level shift that is linear in m_J. This analogy between the vector light shift and an effective magnetic field provides an intuitive way for understanding the formation and the loading of the super-resolution optical potentials which will be introduced in the following chapter.

By using the properties of spherical tensor operators, we have already seen the m_J-dependence of each polarizability component. A complete calculation of the matrix elements in Eq. 3.18 gives the explicit forms of the three complex polarizabilities [63, 69]

$$
\begin{cases}
\alpha^{(s)} = \dfrac{1}{\sqrt{3(2J+1)}}\alpha^{(0)} \\[4mm]
\alpha^{(v)} = -\sqrt{\dfrac{2J}{(J+1)(2J+1)}}\alpha^{(1)} \\[4mm]
\alpha^{(t)} = -\sqrt{\dfrac{2J(2J-1)}{3(J+1)(2J+1)(2J+3)}}\alpha^{(2)}
\end{cases}
\tag{3.23}
$$

with

$$\alpha^{(K)}(\omega) = (-1)^{K+J+1}\sqrt{2K+1} \sum_{n',J'} (-1)^{J'} \begin{Bmatrix} 1 & K & 1 \\ J & J' & J \end{Bmatrix} \left| \langle g; J \| \mathbf{d} \| e; J' \rangle \right|^2$$

$$\left(\frac{1}{E_{e,J'} - E_{g,J} - \hbar\omega - i\frac{\hbar\Gamma_{e,J'}}{2}} + \frac{(-1)^K}{E_{e,J'} - E_{g,J} + \hbar\omega - i\frac{\hbar\Gamma_{e,J'}}{2}} \right) \tag{3.24}$$

where we have used the notation $\begin{Bmatrix} 1 & K & 1 \\ J & J' & J \end{Bmatrix}$ for the Wigner 6-j symbol. With the knowledge of the transition energies $(E_{e,J'} - E_{g,J})$, the atomic line strengths $\left| \langle g; J \| \mathbf{d} \| e; J' \rangle \right|^2$, the lifetimes of the excited states $\Gamma_{e,J'}$, and the angular momenta in ground and excited states J and J'[1], the complex polarizabilities of the ground-state ^{162}Dy atoms are plotted in Fig. 3-4 as functions of laser wavelength according to Eqs. 3.23 and 3.24.

3.3.3 The Blue Trio

From the result presented in Fig. 3-4, we see that each atomic line corresponds to a resonance feature in the ground-state complex polarizability, around which we obtain strong scalar, vector, and tensor components. In addition, it can be noticed that the scalar component $\alpha^{(s)}$ has a finite positive background value in the red-to-infrared regime due to the extension of three broad blue atomic lines centered at 421 nm, 419 nm, and 405 nm, whereas the vector and tensor components $\alpha^{(v)}$ and $\alpha^{(t)}$ are vanishingly small compared to $\alpha^{(s)}$. This behavior excludes the possibility of obtaining strongly spin-dependent optical potentials using far-detuned light. Here let's explore the underlying physics of such destructive cancellation of anisotropic polarizability components $\alpha^{(v)}$ and $\alpha^{(t)}$.

As illustrated in Fig. 3-5 (a), if we only consider the two $6s$ electrons in the outer shell, a blue laser coupling the $^1S_0$ ground state with angular momentum $J_{\mathrm{outer}} = 0$ and the $6s6p$ spin singlet excited state $^1P_1$ with angular momentum $J'_{\mathrm{outer}} = 1$ admixes the three excited states into the ground state, leading to a light shift U.

---

[1]Data provided by Maxence Lepers et al, authors of Ref. [69].
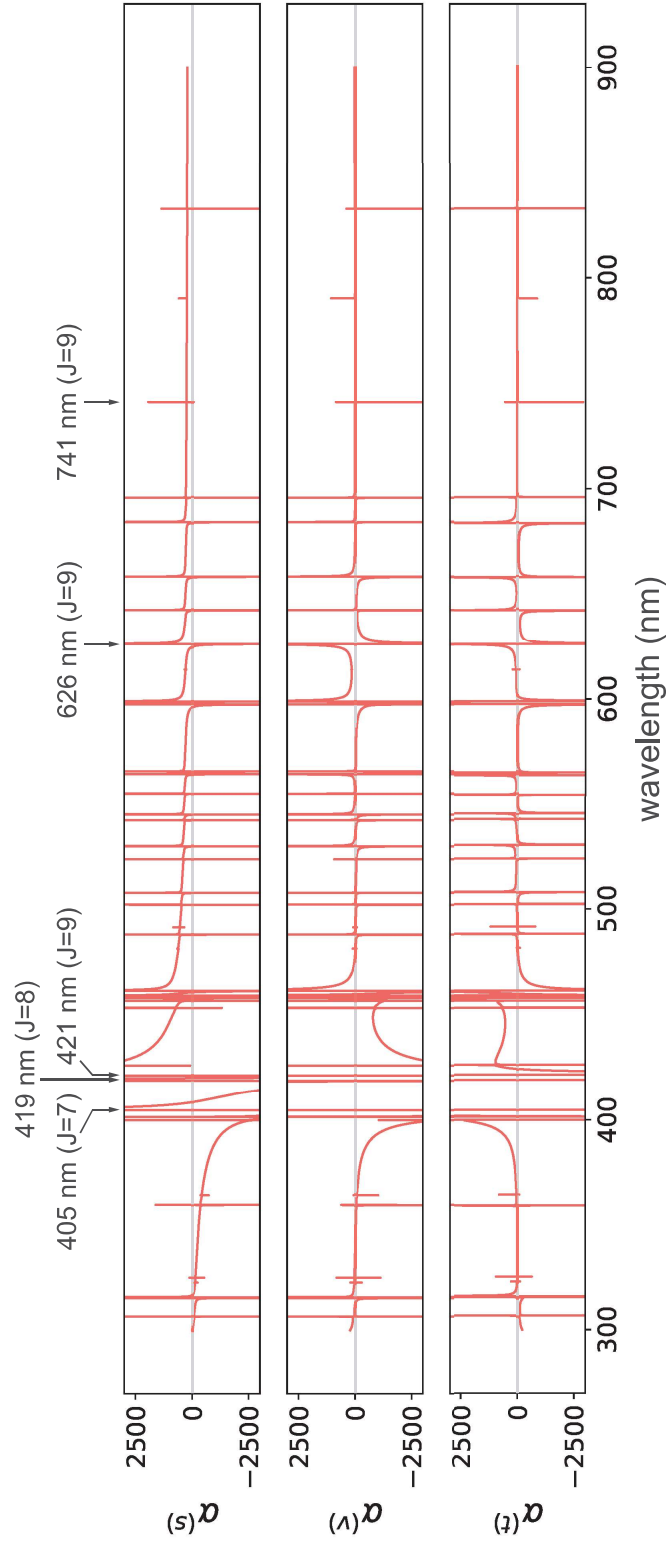
Figure 3-4: Dysprosium ground-state polarizabilities in atomic unit calculated based on the atomic line data provided by the authors of Ref. [69]. The ground-state scalar polarizability $\alpha^{(s)}$ in the infrared regime is mainly contributed by the 421 nm, 419 nm, and 405 nm triplets. The vector and tensor polarizabilities $\alpha^{(v)}$ and $\alpha^{(t)}$ are vanishingly small in the infrared, since the detunings from the strong triplets lines are much larger than the line splittings.

The coupling strength is independent of the polarization of light due to the identical Clebsch-Gordon coefficients $\langle 0,0;1,-1|1,-1\rangle = \langle 0,0;1,0|1,0\rangle = \langle 0,0;1,1|1,1\rangle = 1$. Therefore without angular-momentum coupling between the outer two electrons J_{outer} and the inner shell electrons J_{inner}, the ground-state light shifts are independent of laser polarization. In this case, only the scalar polarizability of the atom $\alpha^{(s)}$ is non-zero.

However, once the angular momentum coupling term $H_{JJ} = \alpha_{JJ}\mathbf{J}_{\text{outer}}\cdot\mathbf{J}_{\text{inner}}$ is introduced, the good quantum number becomes $J = J_{\text{outer}}+J_{\text{inner}}$. As shown in Fig. 3-5 (b), the three excited states with $m_{J\text{inner}} = -1$, 0, and +1 now branch into three manifolds with total angular momenta of $J' = 7$, 8, and 9, at wavelengths 405 nm, 419 nm, and 421 nm. With $\alpha_{JJ} \neq 0$, the splitting caused H_{JJ} modifies the admixture of the three excited-state manifolds in the ground state, and therefore the ground-state light shifts become polarization-dependent. In this case, the atom obtains the vector and the tensor polarizability components $\alpha^{(v)}$ and $\alpha^{(t)}$.

To further quantify the magnitudes of $\alpha^{(s)}$, $\alpha^{(v)}$, and $\alpha^{(t)}$ due to the contributions of the three blue lines, we re-write the energy shift Eq. 3.18 in terms of an operator form

$$\Delta E(J,m_J;\omega) = \langle J,m_J|\mathbf{d}\cdot\mathbf{E}\Big(P_e\frac{1}{H_{\text{atom}}}P_e\Big)\mathbf{d}\cdot\mathbf{E}|J,m_J\rangle \tag{3.25}$$

where $P_e = \sum_{J',m'_J}|J',m'_J\rangle\langle J',m'_J|$ is the projection operator onto the excite-state manifold, and $H_{\text{atom}}^{-1} = \Big(\hbar(\omega_{J'J}-\omega)+\alpha_{JJ}\mathbf{J}_{\text{outer}}\cdot\mathbf{J}_{\text{inner}}\Big)^{-1}P_e$ is the inverse of the many-body Hamiltonian for the bare atom in the rotating-frame. Under the assumption that the splittings Δ_1 and Δ_2 among the $J' = 7$, 8, and 9 excited-state manifolds are much smaller than the laser detuning $\omega_{J'J} - \omega$, we can do the following Taylor expansion

$$\frac{1}{H_{\text{atom}}} \approx \frac{1}{\hbar}\Big(\frac{1}{\omega_{J'J}-\omega} - \frac{\alpha_{JJ}\mathbf{J}_{\text{outer}}\cdot\mathbf{J}_{\text{inner}}}{(\omega_{J'J}-\omega)^2}\Big)P_e \tag{3.26}$$

From this expression we can conclude that under the rotating-wave approximation and in the limit where the laser detuning exceeds the excited-state splittings, the scalar polarizability scales with laser detuning as $\alpha^{(s)} \propto 1/(\omega_{J'J}-\omega)$, whereas the vector and tensor polarizabilities scale with laser detuning as $\alpha^{(v)}, \alpha^{(t)} \propto 1/(\omega_{J'J}-\omega)^2$.

This explains why in the red-to-infrared regime, the scalar polarizability of Dy is much larger than the vector and tensor components.

(a)

$^1P_1$ -1 0 +1   -1 0 +1   -1 0 +1

coupling to inner-shell elections

$^1S_0$

σ_+ π σ_-

$|^1S_0,m=0\rangle$ $|^1S_0,m=0\rangle$ $|^1S_0,m=0\rangle$
$+\epsilon|^1P_1,m=+1\rangle$ $+\epsilon|^1P_1,m=0\rangle$ $+\epsilon|^1P_1,m=-1\rangle$

(b)

405 nm line (J'=7)

419 nm line (J'=8)

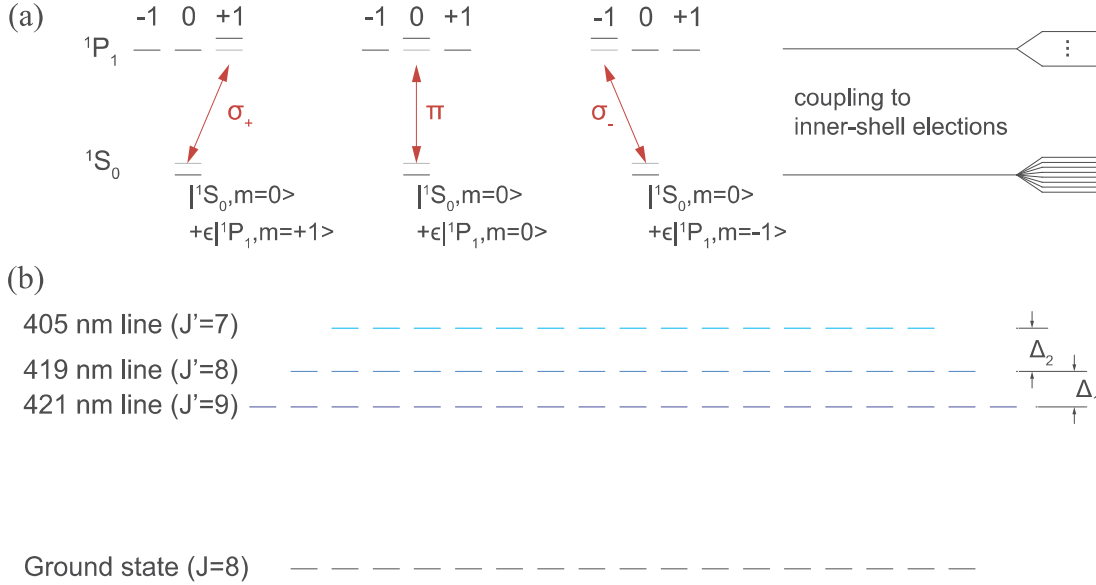421 nm line (J'=9)

Δ_2

Δ_1

Ground state (J=8)

Figure 3-5: (a) Level shifts under different polarizations of light addressing the ground-to-singlet transition $^1S_0 \rightarrow ^1P_1$ associated with the outer two electrons. The angular momenta of the ground and excited states are $J_{\text{outer}} = 0$ and $J'_{\text{outer}} = 1$. Excited states with different magnetic quantum numbers $m_J = 0, \pm 1$ are admixed into the ground-state wavefunction depending on the polarization of the laser. The ground-state manifold splits into 8 states, whereas the excited-state manifold splits into 24 states when the outer two electrons are coupled to the inner shell electrons with total angular momentum $J_{\text{inner}} = 8$. The $J-J$ coupling between the three admixed $^1P_1$ excited states and inner shell electrons gives rise to the spin dependence in the $J = 8$ ground state. (b) Due to the $J - J$ coupling between the inner-shell electrons and the outer two electrons, the total angular momentum of all electrons now become a good quantum number. Consequently, the excited state consists of three manifolds with total angular momenta of $J' = 9$, 8, and 7, corresponding to the Dy 421 nm, 419 nm, and 405 nm strong transitions. The splittings Δ_1 and Δ_2 among these three manifolds characterizes the strength of $J-J$ coupling. The level shifts in the $J = 8$ ground state is state-dependent only when the laser detuning is comparable or smaller than the $J - J$ coupling strengths, i.e. $\delta \lesssim \Delta_1, \Delta_2$. In the limit where the detuning is much larger than excited-state splittings $\delta \gg \Delta_1, \Delta_2$, the ground-state level shifts are almost identical. In this case, the complex polarizability of the atoms only has a scalar part $\alpha^{(s)}$. The vector and tensor components $\alpha^{(v)}$ and $\alpha^{(t)}$ are much smaller.

Chapter 4

Experimental Apparatus

This chapter will introduce the experimental apparatus we have been constructing since 2016 for producing, manipulating, and measuring quantum gases of Dy atoms. Existing techniques for alkali experiments, such as Zeeman slowing, magneto-optical trapping, and evaporative cooling, are employed in our apparatus. But due to many different properties of Dy, these techniques are not directly translated to our experiment. For example, the optical transition with a linewidth of 136 kHz used for our magneto-optical trap (MOT) is much narrower than the MHz transitions for alkali MOTs, leading to lower Doppler temperature, lower capture velocity, and a spin-polarized regime of the MOT; In addition, with a much higher oven temperature of around 1200°C, hot atoms effusing out of the oven nozzle travel at high thermal velocities of around 400 m/s, leading to reduction of flux due to transverse spreading of the atomic beam at the end of the Zeeman slower.

Aspects like these necessitate the development of new laser cooling techniques for better performance of the apparatus and to explore new physics underlying these techniques. We will describe in the following sections how our quantum gas apparatus is designed and characterized, and discuss how the performance of the machine can be further optimized for the next-generation experiments.

4.1 Effusive Oven

We use an effusive oven as our atomic beam source. The effusive oven manufactured by SVT Associates (Model SVTA-DF-2.75/4.5") heats up Dy metal powder to around 1150°C to 1250°C, temperatures that are below the melting point of 1412°C but high enough to build up vapor pressure inside the oven crucible. The Dy atoms then effuse from the nozzle of the crucible, forming a flow of hot gaseous atoms ejecting into the vacuum chamber. In the effusive regime where the mean free path of Dy atoms inside the crucible λ_{mf} is larger than the size of the orifice d, collisions among atoms can be neglected while emerging from the oven, leading to an atomic flux per solid angle $\mathrm{d}\Omega$ satisfying (see Fig. 4-1)

$$\frac{\mathrm{d}N\mathrm{d}\Omega}{\mathrm{d}t} = \frac{\mathrm{d}\Omega}{4\pi} nv \cos\theta A \tag{4.1}$$

where n is the density of Dy gas inside the crucible, A is the area of the orifice, and $\mathrm{d}\Omega = 2\pi \sin\theta \mathrm{d}\theta$. The velocity of the atoms $v = |\mathbf{v}|$ follows the 3D Maxwell Boltzmann distribution

$$f(v) = \left(\frac{m}{2\pi k_B T}\right)^{3/2} 4\pi v^2 \exp\left(-\frac{mv^2}{2k_B T}\right) \tag{4.2}$$

Integrating Eq. 4.1 over solid angle and averaging over velocity classes gives the total flux out of the oven in the effusive regime

$$\Phi = \frac{1}{4} n\bar{v} A \tag{4.3}$$

with $\bar{v} = \sqrt{8k_B T/\pi m}$ being the average velocity of the Maxwell-Boltzmann distribution.

From the analysis above, we see that the angular distribution of atomic flux follows a cosine pattern in the effusive regime, which is peaked in the forward direction with $\theta = 0°$ and is zero at $\theta = 90°$. Different from the effusive flow, a more collimated hydrodynamic flow can be achieved using special oven nozzles with micro-channel plates [94] such that the mean free paths of the atoms λ_{mf} are smaller than the characteristic size d of the nozzle, leading to more directional atomic fluxes.
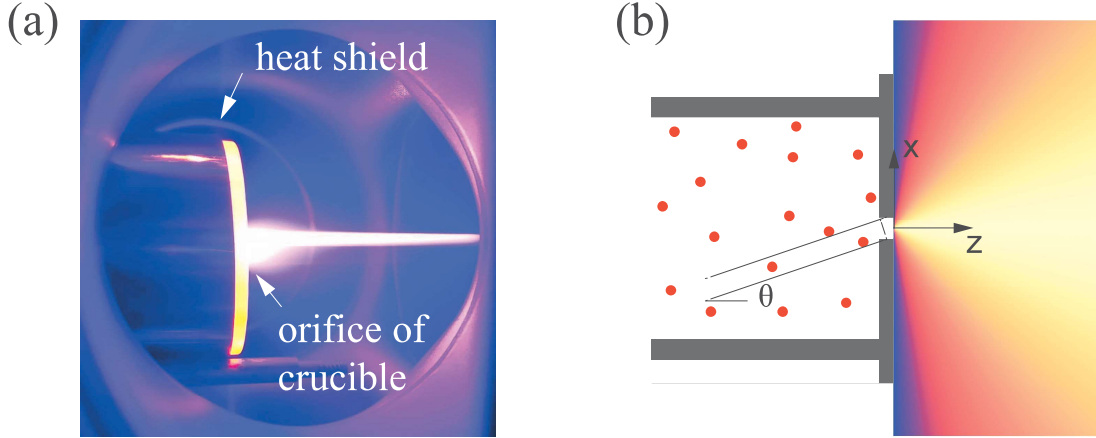
Figure 4-1: (a) A photo of the Dy effusive oven operating at 1250°C. Atom flux in the forward direction illuminated by the Zeeman slower laser beam fluoresces at 421 nm. (b) Schematics of the effusive oven with the colormap showing the angular distribution of the atom flux in the effusive regime (Eq. 4.1).

4.2 Zeeman Slower

An increasing-field Zeeman slower is used to reduce the linear velocity of the atomic beam from the effusive oven to around 40 m/s. This section will introduce the working principle of Zeeman slowers, revisit how our Zeeman slower was designed and characterized, and discuss how the performance of Zeeman slowers can be optimized.

4.2.1 Working Principle

The Zeeman slower is a solenoid that produces a spatially-varying magnetic field, such that the Zeeman shift due to the magnetic field compensates for the Doppler shift of the atoms undergoing constant deceleration. The circularly-polarized laser beam of the Zeeman slower addresses the Dy 421 nm transition, and optically pumps the atoms out of the effusive oven into the $|J = 8, m_J = -8\rangle \rightarrow |J = 9', m'_J = -9\rangle$ cycling transition. The detuning of the cycling transition is determined by (i) the bare laser detuning Δ, (ii) the differential Zeeman shift $\mu_B B(z)/\hbar$ between the ground state $|J = 8, m_J = -8\rangle$ and the excited state $|J = 9', m'_J = -9\rangle$ caused by the varying magnetic field $B(z)$, and (iii) the Doppler shift kv due to the motion of atoms inside the Zeeman slower. We select the bare laser detuning Δ such that the laser beam is res-

onant with the root-mean-square velocity $v_0 = \sqrt{3k_BT/m} = 484$ m/s of the Maxwell Boltmann distribution at 1250°C at the entrance of the Zeeman slower:

$$\Delta = -kv_0 + \frac{\mu_B B_{\text{bias}}}{\hbar} \tag{4.4}$$

Inside the Zeeman slower, the velocity class v_0 is designed to experience constant deceleration $v = \sqrt{v_0^2 - 2az}$ such that it comes to a stop at the exit of the Zeeman slower $z = L$, with L being the length of the slower. Hence we can write the nominal velocity profile as

$$v = v_0 \sqrt{1 - \frac{z}{L}} \tag{4.5}$$

To compensate for the varying Doppler shift due to such velocity profile, the following spatially-varying magnetic field profile is needed for the atoms to be on resonance with the laser beam during deceleration

$$B(z) = B_0 \left(1 - \sqrt{1 - \frac{z}{L}} \right) + B_{\text{bias}} \tag{4.6}$$

with the bias field B_{bias} determined by Eq. 4.4, and the Zeeman shift caused by $B_0 + B_{\text{bias}}$ at $z = L$ compensates for the bare detuning from the laser beam, i.e. $\mu_B(B_0 + B_{\text{bias}}) = \hbar\Delta$. The length of the slower L is determined by the deceleration a provided by the laser scattering force given by

$$a = -\frac{\hbar k}{m} \frac{\Gamma}{2} \frac{s_0}{1 + s_0 + \left[\frac{2}{\Gamma}(\Delta + kv - \frac{\mu_B B(z)}{\hbar}) \right]^2} = -\frac{\hbar k}{m} \frac{\Gamma}{2} \frac{s_0}{1 + s_0} \tag{4.7}$$

By selecting a saturation parameter $s_0 = 2\Omega^2/\Gamma^2$ based on the power budget of the laser, we can select the deceleration of the slower and hence the length of the slower L. For our experiment, with a saturation parameter of around 0.5, the length L is designed to be 42 cm for addressing the highest velocity class of $v_0 = 484$ m/s with the magnitude of the magnetic profile $B_0 = kv_0 = 822$ G.

In the above part, we have designed an ideal magnetic profile of the Zeeman slower which can slow the atoms in velocity class v_0 down to zero velocity. But what
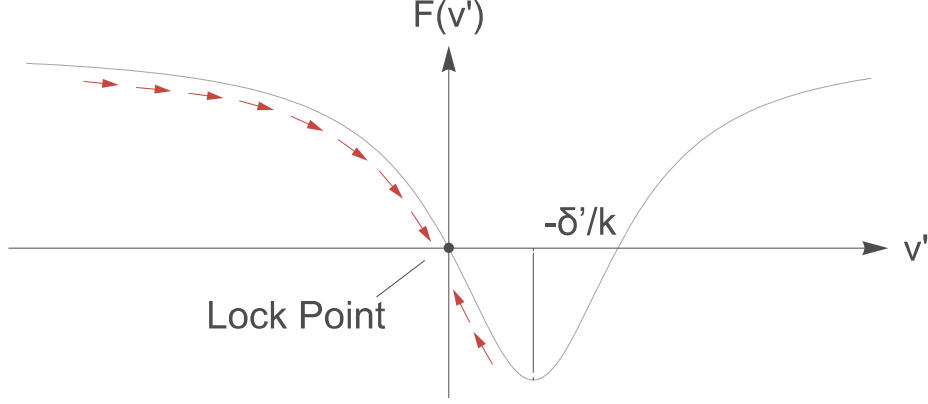
Figure 4-2: Force acting on the atoms in the non-inertial frame following the nominal velocity v (Eq. 4.5) with deceleration a in the Zeeman slower. With a negative deviation δ from the nominal laser detuning Δ, atoms with velocity deviation smaller than δ/k will be damped to the nominal velocity v, leading to slowed atomic beam at the exit of the Zeeman slower.

will happen if the actual magnetic field profile, laser detuning, and the initial velocity of the atoms deviate from the ideal case? Actually, Zeeman slowers are not only able to slow down one velocity class v_0, but are also able to slow down atoms with initial velocities below v_0. The performance of the Zeeman slower is also robust against small deviations in the laser detuning and magnetic field profile. These two aspects can be understood as the following. On top of the nominal velocity v in Eq. 4.5, we assume a relative deviation v' from the nominal velocity, and a deviation δ from the nominal laser detuning Δ. Transforming into the non-inertial reference frame with velocity v and deceleration a gives rise to an inertial force $F_{\mathrm{i}} = -ma$. Hence the total force that acts on the atoms in the non-inertial frame can be written as

$$F(v) = \hbar k \frac{\Gamma}{2}\left[-\frac{s_0}{1 + s_0 + \left(\frac{2(\delta + kv')^2}{\Gamma}\right)^2} + \frac{s_0}{1 + s_0 + \left(\frac{2\delta^2}{\Gamma}\right)^2}\right] \tag{4.8}$$

As plotted in Fig. 4-2, the combined effect of the photon scattering force and the inertial force act like a linear frictional force $f = -\alpha v'$ in the vicinity of $v' = 0$ which damps the relative velocity v' to zero. We can discuss the following three cases of laser detunings based on Eq. 4.8:

Nominal laser detuning ($\delta = 0$)

In this case, atoms traveling slower than the nominal velocity $v' < 0$ are subject to a damping force with negative slope, and thus are attracted to $v' = 0$. Therefore atoms with initial velocities below the threshold value v_0 can keep up with the the nominal velocity profile Eq. 4.5 and get decelerated as they travel through the Zeeman slower.

Laser detuning smaller than nominal value ($\delta < 0$)

This is the case plotted in Fig. 4-2. As we see, an attractor exists in the relative velocity space at $v' = 0$ for velocity classes with $v < v_0 + \delta/k$. However, the magnitude of the damping force in this case is smaller compared to $\delta = 0$, hence not all the atoms with $v < v_0 + \delta/k$ are guarenteed to keep up with the nominal velocity Eq. 4.5 within the finite time they spend inside the Zeeman slower.

Laser detuning larger than nominal value ($\delta > 0$)

When the laser detuning is larger than the designed value ($\delta > 0$), the attractor in the v' spapce is now at $v' = -\delta/k < 0$. In this case, atoms with initial velocity $v > v_0 - \delta/k$ are accelerated, whereas those with $v < v_0 - \delta/k$ are decelerated over time and eventually turned around in the long-time limit. What are delivered at the exist of the Zeeman slower are therefore atoms which don't have enough time to reach the attactor at $v' = -\delta/k$ due to the finite time they travel inside the slower.

4.2.2 Design and Characterization

The Zeeman slower of our apparatus is composed of three coil sets with independently controlled current sources: a bias coil for producing a uniform axial magnetic field B_{bias} inside the slower, a primary coil and a counterwind coil for producing the increasing part of the magnetic field $B_0\left(1 - \sqrt{1 - z/L}\right)$ and cancelling the reminant magnetic field at the center of the main chamber. These coils are wound using hollow-core square magnetic wires with an edge length of 3.68 mm. The bias and the primary coils were wound on a lathe around a brass tube (see Fig. 4-3 (e)). The counterwind coils were wound on a high density polyethylene (HDPE) substrate, and later attached to the end of the main and primary coils using epoxy (see Fig. 4-3 (b-

d)). The wires are water cooled when the machine is under operation.

The primary coil contains 16 layers. Each layer has a doubly-pitched region and a singly-pitched region. In order to produce a magnetic field that approximates the nominal magnetic field profile in Eq. 4.6, the starting points of the doubly-pitched and the singly-pitched regions were designed using a simulated annealing algorithm with 32 free parameters. The resulting configuration sketched in Fig. 4-3 (a) produces a magnetic field shown in Fig. 4-4, where the currents of primary and the counter-wind coils are set to be 26.3 A and 69.0 A, respectively. Tuning the bias current is equivalent to tuning the laser detuning, hence the bias coil is a convenient tool for tweaking the performance of the Zeeman slower when laser frequency needs to be fixed under some scenarios.

To characterize the performance the Zeeman slower, we did Doppler-sensitive spectroscopy by illuminating the atomic beam at the center of the main chamber with a laser beam at 45° addressing the Dy 626 nm transition. The 626 nm fluorescence was collected using a photomultiplier tube (PMT) with interference filters. By scanning the laser frequency and triggering the fluorescence signal on the scan voltage, the velocity distribution of the atomic beam can be detected. As we see in Fig. 4-4, a narrow peak centered at 40 m/s appears in the fluorescence signal as the Zeeman slower is switched on, indicating the detection of slowed atomic flux delivered by the Zeeman slower. However, not all the atmos below the threshold value $v_0 = 484$ m/s are piled up into the 40 m/s peak. This can be due to the inhomogeneous intensity of the Zeeman slower laser beam or the non-ideal magnetic field profile produced by the Zeeman slower.

It is worth noting that we were not able to decelerate the atoms below 40 m/s without losing population. As we tune the Zeeman slower parameters such that the atoms pile up at velocities below 40 m/s, the height of the peak also decreases. This can be explained by the transverse spreading of slowed atomic beam due to the extra distance between the exit of the Zeeman slower regime and the center of the main chamber. For our design, this distance $d = 22$ cm. Consider a transverse velocity v_{trans} that is 1% of the root-mean-square velocity of $v_0 = 484$ m/s, slowing down the
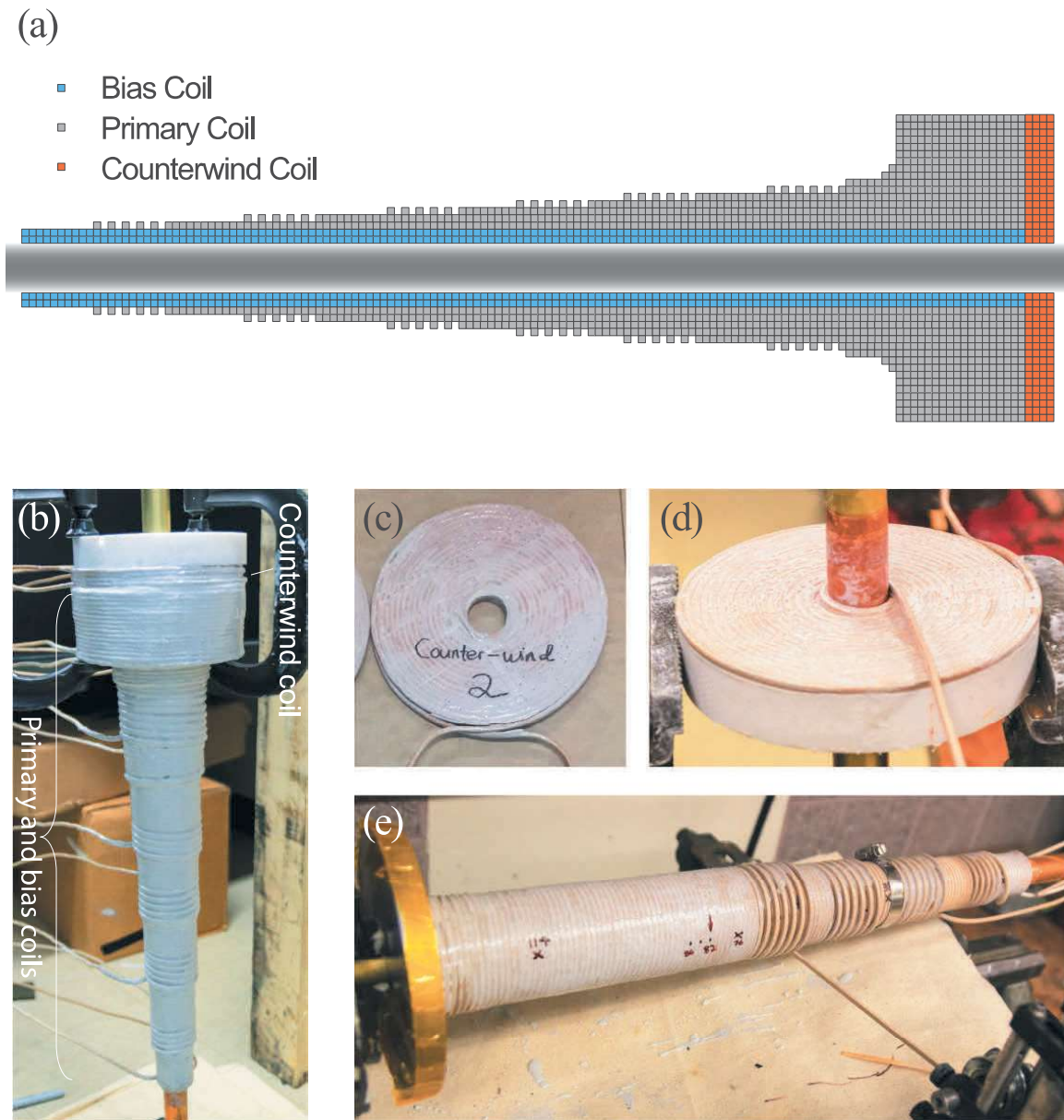
(a)

- Bias Coil
- Primary Coil
- Counterwind Coil

(b) Counterwind coil

Primary and bias coils

(c) Counter-wind 2

(d)

(e)

Figure 4-3: (a) Schematics of the Zeeman slower designed with a simulated annealing algorithm. The bias coil is used to produce the bias field B_{bias}, the primary and the counterwind coils with independently-controlled current are used to produce the increasing part of the magnetic field profile $B_0\left(1-\sqrt{1-\frac{z}{L}}\right)$ inside the Zeeman slower, as well as cancelling the residue magnetic field at the center of the main chamber. (b) The assembled Zeeman slower coils with epoxy being cured. (c) Photo of one of the two counterwind coils with two layers of magnetic wire in spiraled shape. (d) A counterwind coil being wound on an HDPE substrate. (e) The bias and the primary coils being wound layer by layer on a lathe.
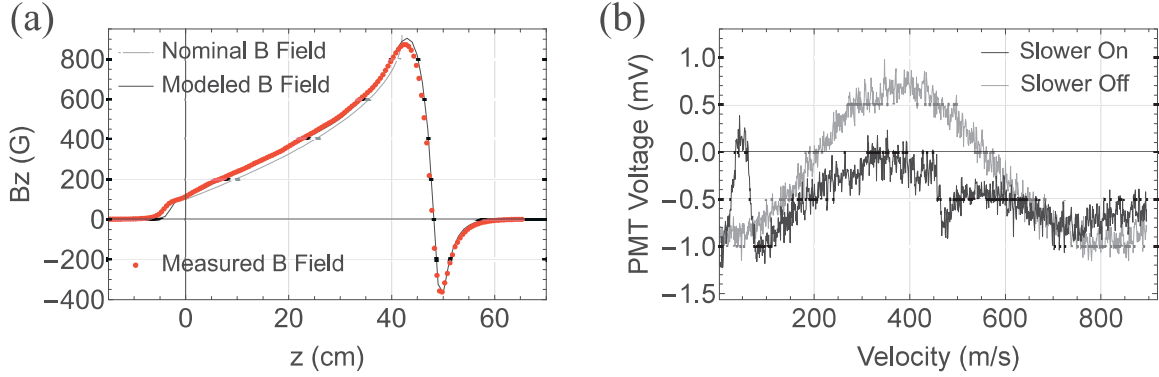
Figure 4-4: (a) Magnetic profile of the Zeeman slower. The gray dashed curve is the nominal profile given by Eq. 4.6, the black solid curve is the modeled profile optimized using simulated annealing algorithm, the red dots are measured magnetic fields using a gauss meter. (b) Doppler sensitive spectroscopy signals measured using a 626 nm laser beam at 45° at the center of the main chamber. The fluoresence signal is collected using a PMT. The signal is piled up at 50 m/s when the Zeeman slower is switched on.

atomic beam to the capture velocity of the MOT $v_{cap} = 8$ m/s (see next section) would lead to a transverse spreading of

$$\sigma = 2d \frac{v_{trans}}{v_{cap}} \approx 26 \text{ cm} \tag{4.9}$$

which significantly reduces the slowed atomic flux in the detection regime. To mitigate this issue for the loading of the narrow-line MOT, as we will see in the next section, we developed the angled slowing technique which enhances the capture velocity of the MOT, such that more atoms can be captured at higher terminal velocity out of the Zeeman slower.

4.2.3 How to Design an Optimal Zeeman Slower?

As a final discussion of this section, let's revisit why Zeeman slower is a useful tool for our Dy experiment. Although an ideal Zeeman slower can bring atoms with high initial velocities almost to a stand still, the long distance inside the Zeeman slower also leads to a reduction of solid angle and therefore a reduction of atomic flux. Setting aside technical issues such as geometry constrains of the vacuum chamber and

maintenance of ultra-high vacuum in the effusive oven section, whether a Zeeman slower can lead to an enhancement of slowed atom flux is therefore a question of whether the atoms piled up in the low-velocity region by the Zeeman slower can compensate for the reduction of solid-angle due to the presence of the Zeeman slower. To address this question, let's consider the following two simple models.
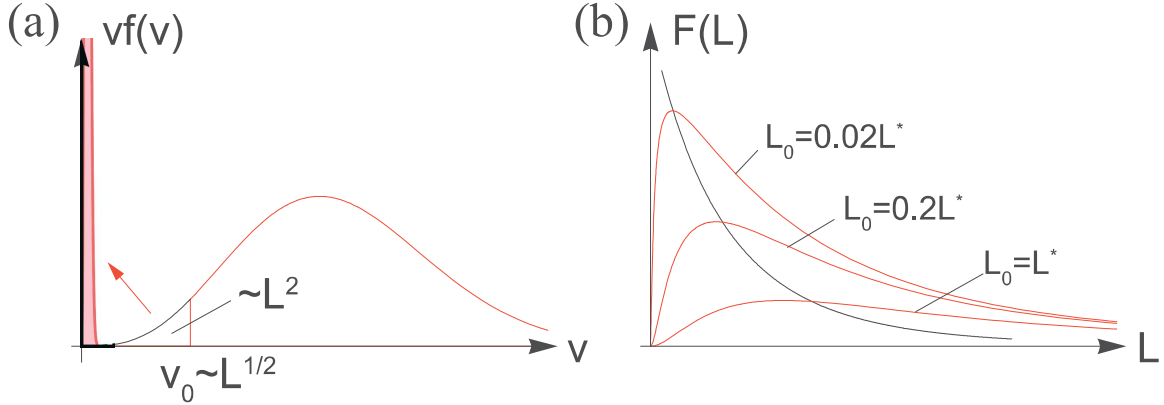

Figure 4-5: (a) The total slowed atomic flux scales as L^2 in the region where the threshold velocity v_0 is much smaller than the most probable velocity $v_p = \sqrt{2k_B T/m}$ of the Maxwell-Boltzmann distribution. (b) Offsetting the oven nozzle from the entrance of the Zeeman slower by distance L_0 leads to an optimal Zeeman slower length of $L \approx \sqrt{3L_0 L^*}$ (dashed line), where L^* is related to the most-probable velocity v_p as $L^* = v_p^2/2a$.

Zero Distance between Oven Nozzle and Zeeman Slower Entrance

In the first case, we assume that velocity of interest (e.g. the capture velocity of the MOT) is only the zero velocity class, and the threshold velocity v_0 in Eq. 4.5 is much smaller than the root-mean-square velocity of the Maxwell-Boltzmann distribution $v_0 \ll \sqrt{2k_B T/m}$. In this region, the Maxwell-Boltzmann distribution is quadratic, which can be expressed as

$$f(v) \approx \left(\frac{m}{2\pi k_B T}\right)^{3/2} 4\pi v^2 \propto v^2 \tag{4.10}$$

Since the maximum deceleration a provided by the Zeeman slower is determined by the available laser power according to Eq. 4.7, the threshold velocity v_0 addressed by the Zeeman slower is related to the length L by $v_0 = \sqrt{2aL}$. Therefore the number

of slowed atoms produced by the Zeeman slower per unit time can be calculated as (*Total Flux × Solid Angle*) (see Fig. 4-5 (a)), which scales with length L as

$$\frac{dN}{dt} = \frac{\Delta\Omega}{4\pi} \int_0^{v_0} dv f(v)v \propto \frac{\Delta\Omega}{4\pi} v_0^4 \propto \frac{1}{L^2}L^2 \sim \text{ independent of } L \qquad (4.11)$$

This indicates that a longer slower does not lead to a reduction of slowed atom flux. In fact, as the threshold velocity v_0 become comparable to $v_p = \sqrt{2k_BT/m}$, the total flux scales weaker than L^2, and cannot compensate for the $1/L^2$ scaling of solid angle. Thus the most optimal design is having no Zeeman slower and placing the oven nozzle in the front of the magneto-optical trap.

We notice some recent papers in which Dy apparatuses with no Zeeman slower are reported [52, 15]. By loading a 2D MOT in the front of the oven nozzle at a lower oven temperature of 800°C to 1000°C and subsequently transferring the atoms into a 3D MOT, they obtained MOT loading rates of 10^8 atoms/s.

Finite Distance between Oven Nozzle and Zeeman Slower Entrance

However, due to geometric constraints and other technical considerations, there is always a extra distance L_0 between the oven nozzle and the entrance of the Zeeman slower. In this case, the solid angle $\Delta\Omega$ scales as $1/(L_0+L)^2$. By defining a characteristic length related to the most-probable velocity of the Maxwell-Boltmann distribution $L^* = v_p^2/2a$ and evaluate the integral in Eq. 4.11 without assuming $v_0 \ll v_p$, the number of slowed atoms delivered per unit time now can be expressed as

$$\frac{dN}{dt} \propto \left(\frac{1}{l+l_0}\right)^2 - (l+1)\left(\frac{1}{l+l_0}\right)^2 e^{-l} \equiv F(l) \qquad (4.12)$$

with $l = L/L^*$ and $l_0 = L_0/L^*$. In the $l_0 \to 0$ limit, we find that $F(l)$ asymptotes to a constant as $l \to 0$, consistent with our analysis in the previous paragraph. For nonzero l_0, the maximum of $F(l)$ is determined by the equation $l^2 + (l_0+2)l + 2(1 - e^l) = 0$. In the $l = L/L^* \ll 1$ limit, the maximum of $F(l)$ can be approximated as $L \approx \sqrt{3L_0L^*}$ (see Fig. 4-5 (b)). This result indicates that the optimal length of the Zeeman slower is determined by the geometric mean of L_0 and L^*. For Dy oven at

69

1250°C, the most-probable velocity is around $v_p = 395$ m/s. With the acceleration provided 421 nm photon scattering with saturation parameter $s = 0.5$, the characteristic length $L^* \approx 40$ cm. For 50 cm separation between the oven nozzle and the Zeeman slower entrance, the optimal length of the Zeeman slower is around $\sqrt{3L_0L^*} \approx 77$ cm.

From these two simple cases, we can conclude that having a Zeeman slower is not always beneficial for the enhancement of slowed atomic flux. This is because that the total flux of slowed atoms produced by the Zeeman slower scales as L^2 in the $v_0 \ll v_p$ regime, which is compensated by the $1/L^2$ scaling of solid angle $\Delta\Omega$. A nonzero optimal length exists when the Zeeman slower is offset from the oven nozzle by distance L_0, so that we go to the tail of the $1/L^2$ function.

There are, of course, many other factors that could affect the optimal length of the Zeeman slower. For instance, we assumed that all velocity classes below the threshold value v_0 are slowed down by the Zeeman slower — this is usually not the case (see PMT signals in Fig. 4-4 (b)). Aspects like this make the scaling law of total flux even weaker than L^2. Therefore it is more preferential to have a shorter Zeeman slower. On the other hand, we have assumed that the solid angle $\Delta\Omega$ scales as $1/L^2$ — this is not the case if we consider the angular distribution of the atomic flux from the effusive oven. In the effusive regime, the angular distribution shown in Eq. 4.1 follows a cosine pattern, which leads to the scaling of $\Delta\Omega$ very close to $1/L^2$. Having an oven with special nozzles that is capable of producing much more collimated atomic beams [52, 94] will make the scaling law weaker than $1/L^2$. In these cases, it is preferential to have a longer Zeeman slower.

4.3 Narrow-Line Magneto-Optical Trapping (MOT)

Subsequent to Zeeman slowing, the atomic beam is captured and cooled by the 626 nm narrow-line MOT (see Fig. 4-6). The 136 kHz linewidth of the 626 nm optical transition leads to several special aspects of the MOT. First, different from the 421 nm transition with a linewidth of $\Gamma = 2\pi \times 32$ MHz and a Doppler temperature of $T_D =$
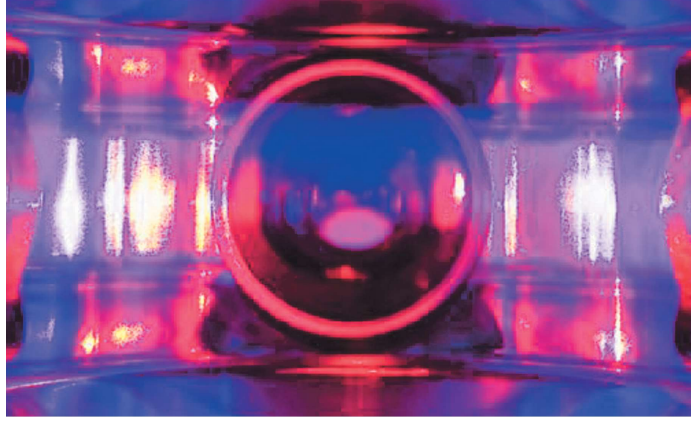
Figure 4-6: A picture of more than 3×10^8 dysprosium atoms confined in the 626 nm narrow-line magneto-optical trap inside the vacuum chamber.

0.77 mK, the 626 nm transition with T_D of $3.3 \mu K$ leads to much lower Doppler molasses temperatures. In addition, with properly adjusted laser detunings, atoms confined in the narrow-line MOT can be polarized in the lowest spin state $|J = 8, m_J = -8\rangle$ rather than being in mixed spin states [32]. This section will elaborate on the physics behind these aspects of the 626 nm narrow-line MOT.

Fig. 4-6 is a photo showing the red fluorescence from the atoms confined in the MOT. The setup consists of a quadrupole magnetic field produced by a set of anti-Helmholtz coils and three orthogonal pairs of counter-propagating laser beams. Each laser beam is circularly polarized[1], and has a $1/e^2$ diameter of $D = 2.3$ cm and a maximum power of 42 mW, corresponding to a saturation parameter of $s \approx 280$. In our experiments, We first perform a MOT loading step for capturing slowed atomic flux delivered by the Zeeman slower with a magnetic gradient of 2.5 G/cm along the strong direction. Subsequently, we perform a compression step by ramping the magnetic gradient to 1.75 G/cm, reducing the light power from 42 mW to 10 μW, turning off frequency dithering of MOT light (see following), and adjusting the laser detuning in 100 ms followed by a 200 ms hold. We obtain a spin-polarized atomic gases at 10 μK temperature at the end of compression.

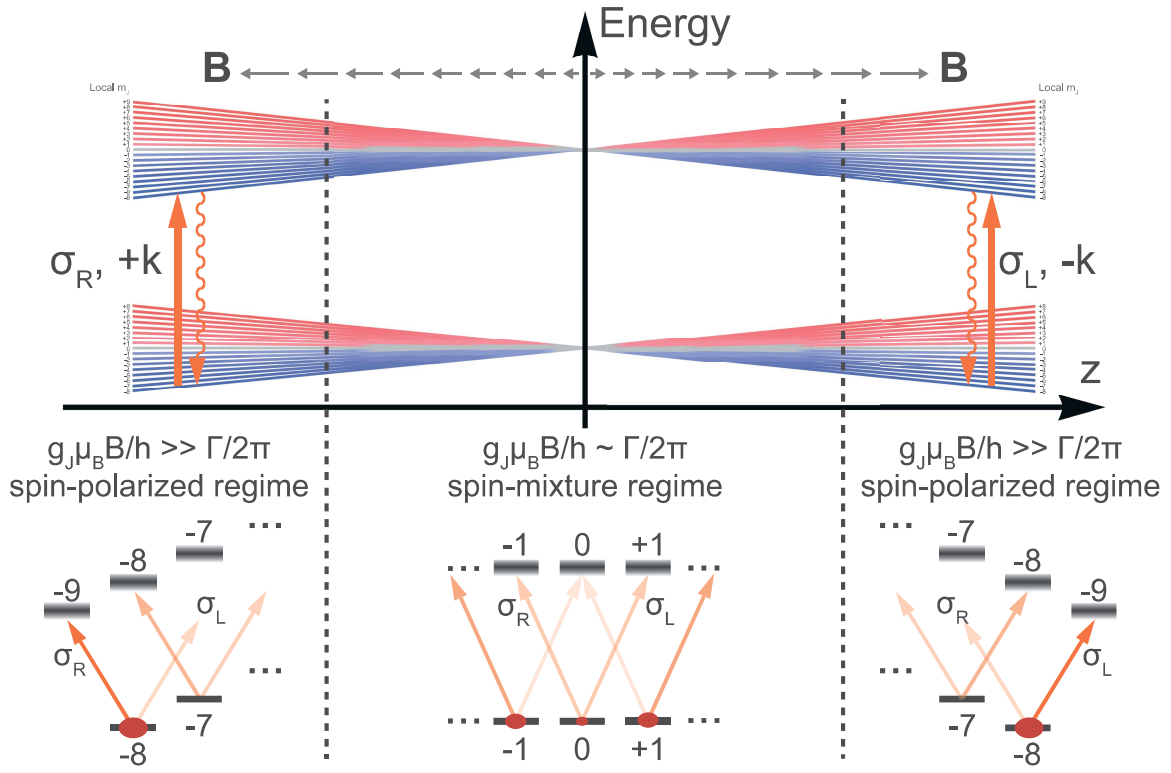[1]Refer to Fig. 4-7 for the polarizations of one of the beam pairs.

Figure 4-7: Energy levels of ground- and excited-state manifolds in the magnetic gradient of the 626 nm narrow-line MOT. With a natural linewidth of $\Gamma = 2\pi \times 136$ kHz for the 626 nm transition and a magnetic gradient of a few gauss per centimeter, the MOT region can be divided into a spin-mixture regime with $g_J \mu_B B/\hbar \sim \Gamma$ where different spin states are not resolved, and a spin-polarized regime with $g_J \mu_B B/\hbar \ll \Gamma$ where different spin states are resolved. Hence by selecting bare laser detunings of $\Delta \approx 8 g_J \mu_B B/\hbar \approx 10\Gamma$, we can create a spin-polarized MOT in the $|J = 8, m_J = -8\rangle \rightarrow |J' = 9, m'_J = -9\rangle$ cycling transition.

4.3.1 Spin-Polarized and Spin-Mixture Regimes

Fig. 4-7 illustrates the Zeeman levels of the $J = 8$ ground-state and the $J' = 9$ excited-state manifold addressed by the MOT beams. Under a magnetic gradient of 1.75 G/cm, each Zeeman level experiences a linear spatial energy shift. At 1 cm distance away from the center of the quadrupole field, the spacing between adjacent Zeeman levels $\Delta E = \mu_B g_J B$ is approximately 1.5 MHz. For broad optical transitions such as the 421 nm transition of Dy ($\Gamma = 2\pi \times 32$ MHz) and the 780 nm D2 transition of Rb ($\Gamma = 2\pi \times 6$ MHz), 1.5 MHz of Zeeman splitting is not large enough to resolve different spin states. However, the 136 kHz linewidth of the 626 nm narrow transition of Dy makes it possible to resolve the spin states within a few centimeter range of the MOT. We can hence divide the spatial region of the MOT into two parts according to the distance to the center of the quadrupole magnetic field: a spin-unresolved center region with $g_J \mu_B B/\hbar \sim \Gamma$, and a spin-resolved shell-shaped region with $g_J \mu_B B/\hbar \gg \Gamma$.

Spin-Polarized MOT ($\Delta \gg \Gamma$)

When the MOT detuning is larger than $8\Gamma \approx 1$ MHz, the cycling transition in the spin-resolved region between the $|J = 8, m_J = -8\rangle$ ground state and the $\left|J' = 9, m'_J = -9\right\rangle$ excited state becomes the most resonant with laser field (see Fig. 4-7). With optical transitions coupled by other polarization components detuned out of resonance by the local magnetic field, we obtain spin-polarized samples in the MOT which sags below the center of the quadrupole magnetic field due to gravity. In our experiment, the spin-polarized MOT is approximately 1 cm below the quadrupole center, and is produced with a laser detuning of 2.5 MHz.

Spin-Mixed MOT ($\Delta \ll \Gamma$)

When the detuning is smaller than $8\Gamma \approx 1$ MHz, atoms in the proximity of the quadrupole center become the most resonant with the laser (see Fig. 4-7). This is a spatial region where the internal spin states are not resolved by the laser linewidth, thus a spin mixture is obtained due to complicated optical pumping and Raman cou-

plings caused by multiple laser beams.

Atomic samples of spin mixtures are detrimental for evaporative cooling due to rapid inelastic losses caused by dipolar relaxations: atoms in higher spin states can collide and convert their internal Zeeman energy to external kinetic energy of orbital motions, leading to heating and population loss of the sample. Hence it is avoided in our experiment by characterizing the lifetime of the atomic gases after transferring into the 1064 nm crossed optical dipole trap (XODT).

4.3.2   Enhancement of Capture Velocity

The narrow linewidth of the 626 nm transition leads to atomic gases in the 10 μK temperature regime after MOT compression, which is a good starting point for evaporative cooling to Bose-Einstein condensates. However, it also leads to a smaller capture velocity and limits the number of atoms captured from the Zeeman slower during loading. The capture velocity of the MOT can be estimated as the maximum velocity of atoms that can be decelerated to a stop within the region of the laser beams. Assuming the atoms are in the fully saturated regime therefore experience the maximum deceleration rate of $a_{\max} = \hbar k \Gamma / 2m$ due to photon scattering, the capture velocity can be expressed as

$$v_{\mathrm{cap}} = \sqrt{\frac{\hbar k \Gamma}{m} D} \approx 9 \text{ m/s} \tag{4.13}$$

which is much smaller than the capture velocities of typical alkali MOTs. For example, with the same beam geometry, the capture velocity of a ^{87}Rb MOT using the 780 nm D2 transition is 71 m/s, an order of magnitude higher than the Dy narrowline MOT. This low capture velocity raises a more stringent requirement on how slow the atoms need to be decelerated by the Zeeman slower. But as we have discussed in the previous section, a low terminal velocity from the Zeeman slower leads to a significant reduction of the flux due to transverse spreading (see Eq. 4.9). To mitigate this issue, we operate the Zeeman slower at a slightly higher terminal velocity

of around 40 m/s, and use two techniques to enhance the capture velocity of the MOT.
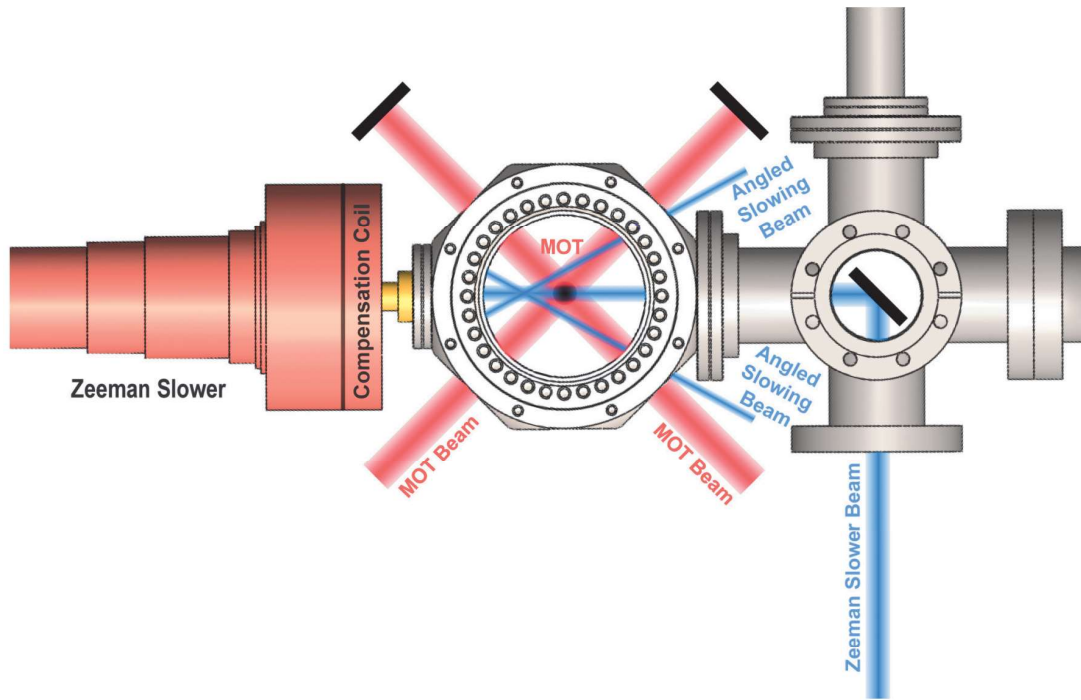

Figure 4-8: Setup of the Zeeman slowing beam, the angled slowing beams, and the horizontal MOT beams. The angle slowing beams intersect in front of the MOT which enhances the capture velocity of the 626 nm narrow-line MOT.

MOT Frequency Dithering

We dither the frequency of the MOT light during the loading stage at a frequency of 120 kHz and a depth of 1.3 MHz during loading. These parameters are chosen such that the effective saturation parameter is on the order of unity within each frequency bin, and that the time spent in each frequency bin during frequency modulation is long enough for scattering a photon. With the frequency dithering technique, we are able to enhance the MOT population by a factor of 3.

Angled Slowing

In addition to frequency dithering, we developed a technique named *angled slowing* which enhances the capture velocity of the MOT and leads to a factor of 20 enhancement in the MOT population [75]. As shown in Fig. 4-8, the angled slowing technique utilizes a pair of near-resonant angled beams addressing the Dy 421 nm

broad transition in the front of the MOT. Each of these two beams has a power below 10 mW and a $1/e^2$ beam size of $d_{AS} \approx 1$ cm. As atoms with linear velocities of $v_{ZS} \approx 40$ m/s travel through the angled slowing region, the number of 421 nm photons scattered by each atom is around $N_{AS} = \Gamma_{421} d_{AS}/v_{ZS} \sim 7500$, resulting in an average velocity change of $\Delta v = N_{AS} \hbar k/m \sim 40$ m/s and a velocity diffusion of $\sqrt{N_{AS}} \hbar k/m \sim 0.5$ m/s. Therefore although the Doppler limit of the 421 nm transition is not favorable, by combining a pair of angled 421 nm laser beam with the 626 nm narrow-line MOT, and giving atoms a strong kick right before loading, it is possible to achieve a narrow-line MOT with low Doppler temperature but high capture velocity at the cost of two extra low-power laser beams.
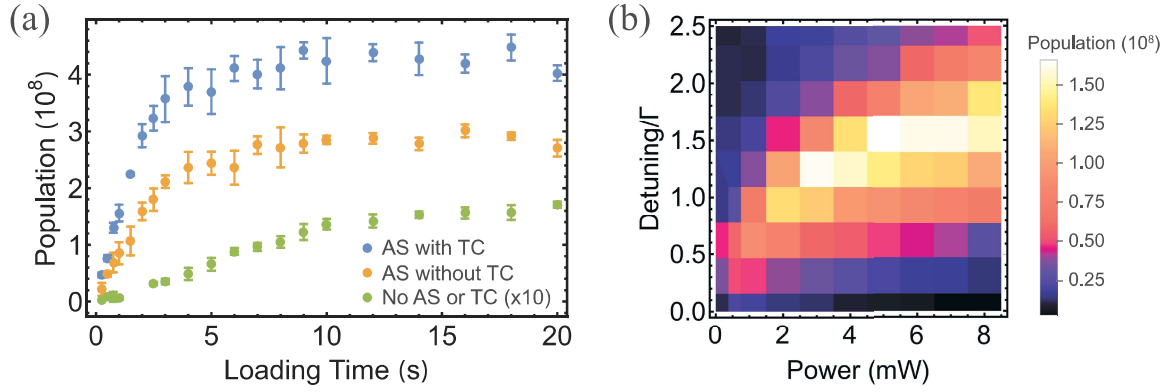

Figure 4-9: (a) MOT population as a function of loading time when both angled slowing and transverse cooling are on (blue), when angled slowing is on but transverse cooling is off (orange), and when neither angled slowing nor transverse cooling is on. The data for the last case is multiplied for a factor of 10 for visual clarity. The detuning and power for the angled slowing beam is $\delta = -50$ MHz and 7 mW per beam. (b) MOT population after a fixed amount of loading time as a function of angled-slowing power and detuning.

Fig. 4-9 (b) plots the population of the narrow-line MOT under different powers and detunings of the angled slowing beams. As we see, an optimal laser power exists for a fixed detuning. This can be explained by a simple model: At small power, more atoms are decelerated to below the capture velocity by the angled slowing beam, therefore the MOT population increases with power; At large power, however, atoms are turned around by the angled slowing beam, therefore the MOT population decreases due to reduction of flux. By parking the laser detuning and power at the

optimal point, we can load 3×10^8 [162]Dy atoms in 2 seconds, which is enhanced by a factor of 20 due to angled slowing (see Fig. 4-9 (a)).

4.4   Evaporative Cooling to Quantum Degeneracy

After MOT loading and compression, we perform evaporative cooling in a cross optical-dipole trap (XODT) to further lower the temperature of the atomic gases for producing BECs. Unlike alkali atoms, magnetic traps are not used for evaporative cooling of Dy for the reason that the low-field seeking states which are magnetically trappable, such as $|J = 8, m_J = +8\rangle$, are subject to dipolar relaxation losses[2].

Fig. 4-10 (a) illustrates the geometry of the XODT. We cross two focusing laser beams with a maximum power of 10 W per beam and a 100 μm of beam waist at an 8° angle in the horizontal plane, and the third laser beam with 3 W of power and 100 μm of beam waist at 90° with the two horizontal laser beams. Three laser beams at 1064 nm wavelength, detuned far away from Dy atomic transitions, create a conservative potential for the Dy atoms given by Eq. 3.3 — the shallow-angle ODT beams in the horizontal plane a big volume for capturing atoms from the MOT; the vertical ODT beam creates a dimple at the center of the conservative trap (see Fig. 4-10 (b)).

The XODT is switched on to maximum power during the 100 rm MOT compression step. The compressed MOT is then held for 200 ms, resulting in spin-polarized cold atoms at 12 μK loaded inside the XODT. We use a two-step evaporative cooling sequence. In step one, we ramp down the power of the two horizontal ODTs within around 1 second, such that most atoms are cooled into the dimple region created by the vertical ODT beam. The temperature of the atoms at this point is around 1 μK. In step two, we further ramp down the powers of all three laser beams to their final values within around 2 seconds, which leads to Bose-Einstein condensation of more

---

[2]We are able to observe magnetic trapping of Dy atoms by precisely placing atoms in the XODT in the $|J = 8, m_J = -8\rangle$ absolute ground state at the center of a quadrupole magnetic field that provides a magnetic force stronger than gravity, and quenching the atoms into higher spin states by quickly switching a few milligauss bias magnetic field. But the population of the magnetic trap is limited to a few thousand, and the lifetime of the trap is typically less than 100 ms.

than 10^5 atoms with a density of 10^{14} cm^{-3} (see Fig. 4-11). The presence of the dimple potential created by the vertical ODT beam speeds up thermalization at the end of evaporative cooling. We are also able to produce elongated BECs only with the two shallow-angle horizontal beams, but the evaporation takes a much longer time of 8 seconds.
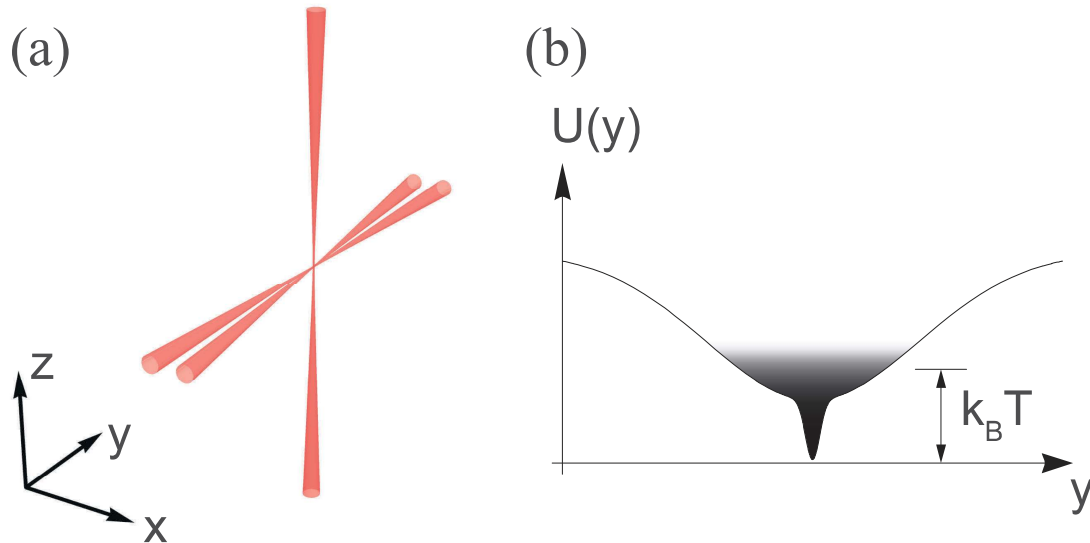

Figure 4-10: (a) Beam geometry of the 1064 nm XODT. Two horizontal beams are crossed at an 8° shallow angle. The third vertical beam is crossed with the horiontal beams at 90°. (b) The shallow angle trap formed by horizontal beams gives rise to a big trap volume for capturing cold atoms from the MOT at temperature T. The dimple at the center created by the vertical beam leads to a faster thermalization rate for evaporative cooling.

It took us more than a year from obtaining the first BEC signal (described in Will Lunden's thesis [75]) to being capable of producing stable BECs on an everyday basis. The essential aspects for achieving this goal are listed in the following. Once they are harnessed, obtaining Dy BECs is as straightforward as finding the final powers of the ODT beams, the total time of evaporation, and an optimal magnetic field by maximizing the remaining atom number after some time of evaporation to avoid inelastic collisions in the vicinity of Feshbach resonances.

Loading XODT from a spin-polarized MOT. Instead of using small values of final detunings and compressing the MOT close to the center of the quadrupole magnetic
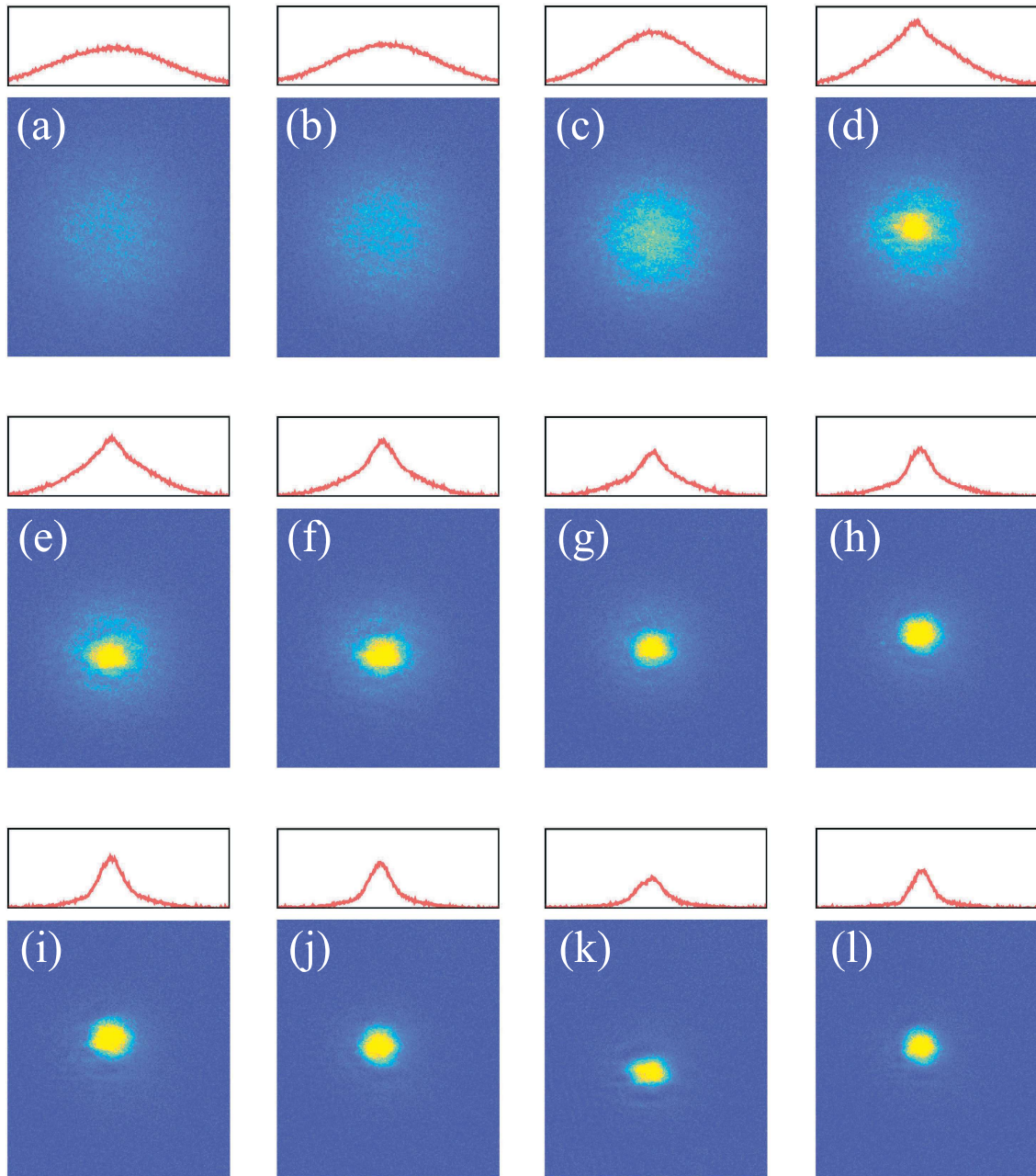
Figure 4-11: Time-of-flight absorption images taken at (a) 2.1 ms, (b) 2.2 ms, (c) 2.3 ms, (d) 2.4 ms, (e) 2.5 ms, (f)) 2.6 ms, (g) 2.7 ms, (h) 2.8 ms, (i) 2.9 ms, (j) 3.0 ms, (k) 3.1 ms, and (l) 3.2 ms into evaporative cooling with the colormap showing the optical densities of the absorption images, and the red traces showing the integrated signals along one direction. The momenta of atoms turn from thermal distributions to bimodal distributions, signaling the formation of Dy BECs with 10^5 atoms.

field to obtain more regular cloud shapes, we need to use large final detunings to avoid spin mixtures that experience inelastic dipolar relaxation losses after loading into the XODT. This corresponds to a sag of ~ 1 cm in the equilibrium position of the compressed MOT below the center of the quadrupole magnetic field.

Cooling atoms into the XODT with low MOT intensity. At the end of MOT compression, we cool the atoms into the XODT by maintaining a low final intensity of around 1 μW/cm^2 per beam for 200 ms, which corresponds to a saturation parameter $s \approx 0.02$. This extra holding step enables more atoms to be loaded into the dimple region of the XODT.

Eliminating laser noise. The Toptica laser system for delivering the 626 nm light needs to be parked in a mode-hop free region. This is done by tuning the diode current and the grating position of the ECDL seed while monitoring the error signal from the ULE cavity system. Whether or not stable BECs are obtained can be sensitive to the ripples of the error signal baseline.

4.5 Spin Control Using RF Pulses

After being able to produce Dy BECs in the absolute ground state $|J = 8, m_J = -8\rangle$, we can manipulate the internal spin states using RF photons. This section demonstrates how spin rotations can be implemented using resonance RF pulses, and detected with the Stern-Gerlach experiments. Since this thesis focuses on bosonic dysprosium, we do not consider RF couplings within different hyperfine manifolds of fermionic isotopes with GHz spacings. Hence the RF photons used here is in the MHz energy range.

4.5.1 Generating RF Pulses in the MHz Range

The RF signals are derived from the Rigol DG1022 arbitrary waveform function generator, amplified using a 30W Mini-Circuits RF amplifier LZY-22X+, and sent to a double-loop antenna placed on the top viewport that is approximately 2 cm away from the atoms impedance matched by the antenna tuner MFJ-993B. At the begin-

ning of each experimental cycle, the Rigol function generator is programmed with updated experimental parameters using SCPI commands via USB communication (see Fig. 4-13 for the software interface). The waveform is later triggered by digital control signals during experiment cycles.

By measuring the peak-to-peak voltage V_{pp} across a single-loop pickup antenna with area A, we characterize the peak-to-peak transverse magnetic field produced by the RF antenna at the position of the atoms to be around $B_{pp} = V_{pp}/(\omega_{RF}A) \approx$ 100 mG at RF frequencies above $\omega_{RF} = 2\pi \times 1$ MHz. With the impedance of the antenna matched to the rest of the circuit by the tuner, we observe sinusoidal voltage signals across the pickup antenna. However, the tuner we use only operates above 1 MHz, hence we need to bypass the tuner for RF applications below 1 MHz, in which cases we observe anharmonic RF signals across the pickup antenna probably due to nonlinear responses of the circuit in the presence of strong back reflections.

4.5.2 Stern-Gerlach Experiment

To demonstrate our spin control capability, we apply 5.3 MHz resonant RF pulses to the spin-polarized BECs prepared inside the XODT, with a vertical magnetic field of $B_z = 3.12$ G and a magnetic gradient of $dB_z/dz = 2.84$ G/cm. We subsequently switch off the XODT and perform time-of-flight measurements. The magnetic gradient is chosen such that the spin-polarized state $|J = 8, m_J = -8\rangle$ is levitated during time-of-flight, i.e. $mg = 8g_J\mu_B(dB_z/dz)$. Therefore the spin-dependent net force acting on the spin state with magnetic quantum number m_J can be written as $(m_J/8 + 1)mg$, which leads to flight distances of $\frac{1}{2}(\frac{m_J}{8}+1)gt^2$ that have quadratic dependence on m_J. This Stern-Gerlach technique enables us to resolve and analyze different spin-states during time-of-flight.

Fig. 4-12 shows the Stern-Gerlach signals we obtain during the first cycle of Rabi oscillation, in which we observe the spin of the BEC oscillates from $|J = 8, m_J = -8\rangle$ to $|J = 8, m_J = +8\rangle$ through all 15 spin states in between. The Rabi period of 14.20 μs corresponds to a Rabi frequency of $\Omega_R = 2\pi \times 70.4$ kHz. We are able to observe at least 70 cycles of Rabi oscillation before losing atomic signals due to dipolar relaxation.

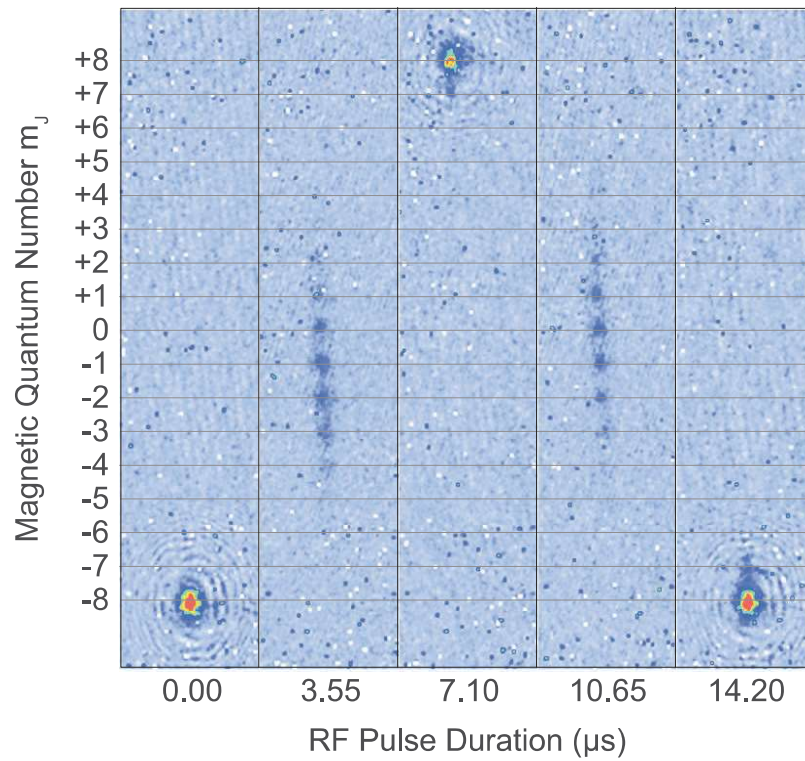Figure 4-12: Stern-Gerlach signal in a 2π Rabi cycle after applying resonant RF pulses for different amount of time. A magnetic gradient of 2.86 G/cm is applied to separate different spin states during time of flight.
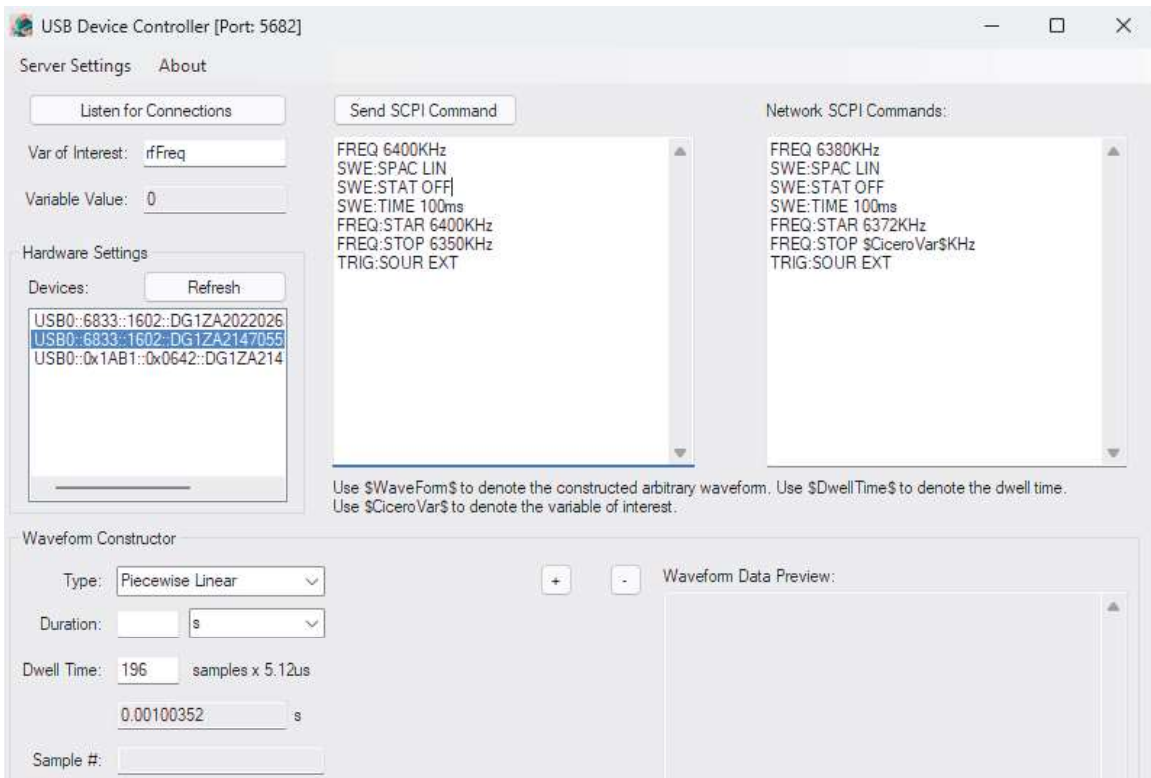
Figure 4-13: Software interface of the USB controller. SCPI commands with updated experimental parameters are sent to the function generator via USB at the beginning of each experimental cycle.

Chapter 5

Super-Resolution Control of Dipolar Atoms on 50 nm Scales

The interatomic distances for most ultracold atom experiments are on the order of hundreds of nanometers. For example, a typical quantum gas with $n = 10^{14}$ cm^{-3} density has an interatomic distance of around $n^{1/3} \approx 215$ nm. In lattice experiments, a square optical lattice formed by interfering counter-propagating laser beams with a wavelength of $\lambda = 1064$ nm corresponds to a distance between nearest lattice sites of $\lambda/2 = 532$ nm. Although being the atom with the largest magnetic moment of $10\mu_B$, the dipolar interaction strength between two head-to-tail Dy atoms in the polarized spin state separated by $d = 532$ nm is only $U_{\rm dd}/h = \mu_0 (10\mu_B)^2/(2\pi h d^3) \approx 17$ Hz, which is relatively weak compared to the typical energy scales in quantum simulation experiments. By using optical lattices with a shorter wavelength of 532 nm, the nearest-neighbour dipole-dipole interactions have been enhanced to around 100 Hz in extend Bose-Hubbard quantum simulators [7, 98], leading to the recent discovery of dipolar stripe phases [98].

In this chapter, we will introduce a super-resolution scheme which can localize Dy atoms to distances around 50 nm, more than 10 times shorter than the optical wavelength. Since the dipole-dipole interaction has a favorable scaling with distance as $1/r^3$, we obtain a maximum dipole-dipole interaction strength of 20 kHz. We apply this technique to the creation of a bilayer array of Dy atoms with tunable

interlayer distances, and observe the interlayer long-range interaction via two out-of-equilibrium experiments. The enhanced dipole-dipole interaction opens up new possibilities for exploring physics such as quantum thermalization, superradiance light scattering, interlayer pairing, exciton physics, etc. [9, 36]
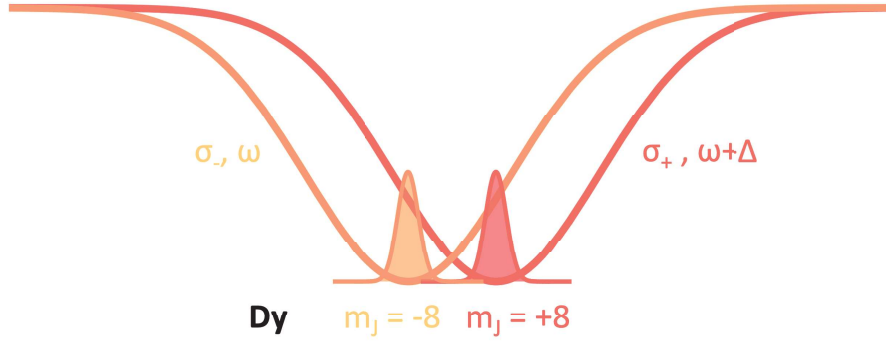

Figure 5-1: Illustration of the super-resolution control of Dy atoms. Two different types of atoms (Dy atoms in $m_J = \pm 8$ spin states) are indepdently controlled by two different types of light (near-resonant lasers in opposite circular polarizations offset by a frequency gap).

5.1   The Dual Frequency and Dual Polarization Scheme

Fig. 5-1 illustrates how the diffraction limit of light can be overcome using our super-resolution scheme. Two different types of atoms are each in the respective harmonic-oscillator ground states of the light potentials marked in red and orange. The root-mean-square size of the wavefunctions σ are related to the trap frequency ω as $\sigma = a_{HO}/\sqrt{2}$ with the oscillator length defined as $a_{HO} = \sqrt{\hbar/2m\omega}$. With a trap frequency of 100 kHz, the size σ is approximately 12 nm, much smaller than the diffraction limit of light. Hence by decoupling the red (orange) atom from the orange (red) light, we can localize the two atoms to tens of nanometer separation without contact.

In the super-resolution scheme we are going to introduce in this section, the two different atoms are Dy atoms in the opposite spin states with $m_J = \pm 8$, and the two different types of light are near-resonant 741 nm lasers in opposite circular polarization with a frequency offset around 300 MHz. The fundamental principle of this dual-frequency and dual polarization scheme is based on the anisotropic nature of

atom-light interaction introduced in Chapter 3. In the presence of vector and tensor polarizabilities in the ground state, Dy atoms experience different light shift under different laser polarizations. By tailoring the polarization and frequency of the light field, we can realize independent control of the two spin states $m_J = \pm 8$ of Dy atoms in the subwavelength regime.

To understand the super-resolution scheme, let's consider the electric-dipole interaction of Dy atoms exposed to two optical standing waves in opposite circular polarizations σ_+ and σ_-. The intensity maxima of the two standing waves are controlled by the relative phase ϕ. We will first study the diagonal part of the atom-light interaction and calculate the light shifts experienced by each spin state m_J, and then study the off-diagonal two-photon Raman couplings among different spin states.

Engineering the Diagonal Part

The electric fields of the two standing waves in σ_+ and σ_- circular polarizations can be written in the spherical basis as

$$
\begin{aligned}
\mathbf{E}_{\sigma\pm}(z,t) &= 2E_0 \cos(kz \pm \phi)\Big(\mathbf{e_x}\cos\omega t \pm \mathbf{e_y}\sin\omega t\Big) \\
&= E_0 \cos(kz \pm \phi)\Big[(\mathbf{e_x} \pm i\mathbf{e_y})e^{-i\omega t} + c.c.\Big]
\end{aligned}
\tag{5.1}
$$

which gives rise to the following light shift in the ground state

$$
\begin{aligned}
U(z) = &-2\alpha^{(0)}E_0^2\Big(1 + \cos 2kz \cos 2\phi\Big) \\
&+ 2\alpha^{(1)}E_0^2 \sin 2kz \sin 2\phi \frac{m_J}{J} \\
&+ \alpha^{(2)}E_0^2\Big(1 + \cos 2kz \cos 2\phi\Big)\frac{3m_J^2 - J(J+1)}{J(2J-1)}
\end{aligned}
\tag{5.2}
$$

As illustrated in Fig. 5-2, with only a scalar polarizability $\alpha^{(s)}$, the light shift is identical for all 17 spin states, which is proportional to the sum of intensities of the two standing waves. The vector polarizability $\alpha^{(v)}$ leads to light shifts that are linear in m_J, and can be regarded as Zeeman shifts caused by fictitious magnetic fields — the σ_+ and σ_- standing waves are analogous to magnetic fields along $+z$ and $-z$ directions with sinusoidal modulation which lift the degeneracy of 17 spin states besides

the points where the two magnetic fields cancel. As such, we obtain a spin-dependent optical potential that realizes independent control of the distance between two local ground states $|J = 8, m_J = -8\rangle$ and $|J = 8, m_J = +8\rangle$ with the relative phase ϕ.
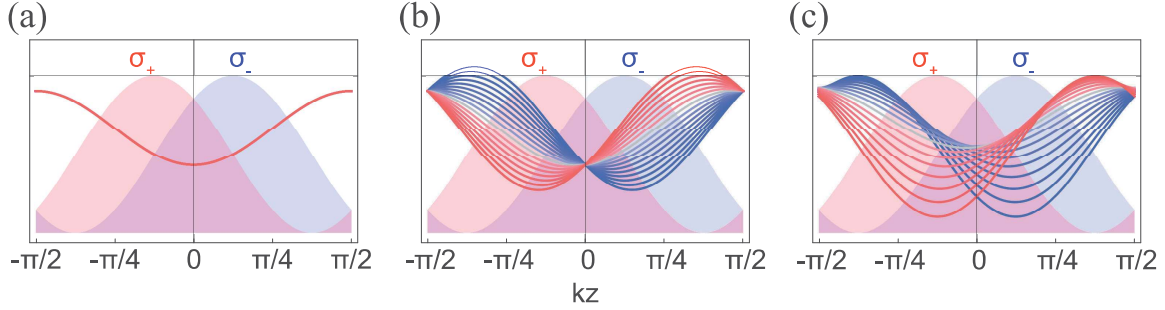

Figure 5-2: Contributions of (a) scalar polarizability $\alpha^{(s)}$, (b) vector polarizability $\alpha^{(v)}$, and (c) tensor polarizability $\alpha^{(t)}$ to the light shifts of $m_J = -8$ (blue) to $m_J = +8$ (red) spin states. The shaded regions refer to the intensities of lasers in two opposite circular polarizations.

However, due to the presence of the 17-fold degenerate point, off-diagonal couplings caused by e.g. a small transverse magnetic field B_x would create avoided crossings and lead to spin mixtures in the ground state. By adding in the contribution of tensor polarizability $\alpha^{(t)}$, we obtain tensorial light shifts that are proportional to m_J^2. Therefore the 17-fold degenerate points are lifted such that only spin states with the same $|m_J|$ cross in the middle. The presence of the tensor polarizability makes off-diagonal spin-flip couplings between $m_J = -8$ and $+8$ spin states higher-order processes, providing robustness of the super-resolution scheme

Engineering the Off-Diagonal Part

In addition to the diagonal part of the optical potential, we consider here the effects of two-photon Raman couplings contributed by the off-diagonal parts of vector and tensor polarizabilities [63]. In the presence of two opposite circular polarizations, the tensor polarizability $\alpha^{(t)}$ allows for Raman processes with $\Delta m_J = \pm 2$. As shown in Fig. 5-3, when the frequencies of the two lasers are the same, the off-diagonal Raman couplings weaken the adiabatic potential curves when the separation between the potential minima is smaller than $\lambda/10$, hence becoming a fundamental limitation of how close the atoms can be localized using the spin-dependent potential.
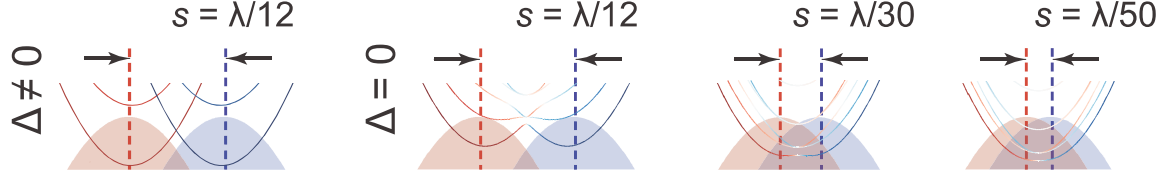
Figure 5-3: If the two laser beams have the same frequency $\Delta = 0$, the off-diagonal part of the tensor polarizability mixes spin states. As a result, the two minima merge into a single minimum for small separation s. This is avoided in our experiment by using two different frequencies for the $\sigma_\pm$ light. The color of the curves indicate the m_J character of the adiabatic eigenstates.

By introducing a big frequency gap Δ to the two laser beams, however, we can detune the two-photon Raman couplings out of resonance. In our experiment, the two-photon detuning $\Delta = 300$ MHz, much larger than the light shift and the energy spacings between adjacent vibrational levels. Hence the Raman couplings between different spin states and vibrational levels are negligible, leading to an isolated Hilbert space for $|J = 8, m_J = -8\rangle$ and $|J = 8, m_J = +8\rangle$.

By using extra laser beams with proper polarizations and detunings, it is possible to introduce Raman couplings that change vibrational quantum number. This could be used for Raman sideband cooling of atoms confined in the super-resolution potential.

5.2 A Bilayer System of Dipolar Atoms

Atoms loading in the ground state of the optical potential described in the above section form an array of bilayer systems with head-to-head magnetic dipoles. We will introduce in this section how such bilayer systems are created, loaded, and characterized.

5.2.1 Optical Setup

Fig. 5-4 illustrates the optical setup for producing the bilayer potential. Two lasers addressing the Dy 741 nm transition in different detunings and orthogonal linear polarizations are synthesized on the laser table using a single-passed acousto-optic

modulator (AOM) (Model ATM-2001A1) and a double-passed phased-array acousto-optic deflector (AOD) (Model ATD-801A6), and combined at a polarization beamsplitter (PBS). The two laser beams are coupled into a polarization-maintaining fiber whose fast and slow axes are adjusted to be aligned with the polarization directions of light. It is important to couple both lasers into a same fiber, rather than spatially combining two lasers on the machine table, to ensure precise overlap of the two transverse laser modes.

On the other side of the fiber, the laser beam with two frequency components along the two orthogonal linear polarizations is passed through an achromatic quarter waveplate (QWP) which converts linear polarizations into opposite circular polarizations. The beam is then focused onto the atoms and retro-reflected by a mirror on the other side of the vacuum chamber to form two optical standing waves. The intensity maxima of two standing waves are displaced at the position of atoms by a distance $s = L \cdot \Delta/f$, with Δ being the frequency gap between the two polarization components, f being the frequency of the laser, and L being the length of the retro path. By tuning the frequency gap Δ using the double-passed phased-array AOD, we can control the distance s between the two layers dynamically during experiments with a speed on the order to 10 μs. Before the achromatic QWP, the two polarization components of the laser are picked off by a 90-10 beamsplitter followed by a PBS, and detected by two photodiodes for intensity control and stabilization with PID electronics.

Below we would like to introduce two technical aspects of our optical design that are important for the realization of the bilayer potential. To achieve wide tunability of the interlayer distance s, we use a phased-array AOD that has high diffraction efficiency across 40 MHz of RF frequency. In addition, to produce high-quality circular polarizations, we used several tilted waveplats to compensate for the unwanted phase shifts introduced by optical elements such as dichroic mirrors.

Frequency Tuning with Phased-Array AOD

The tuning range of interlayer distance s is related to the laser frequency tuning
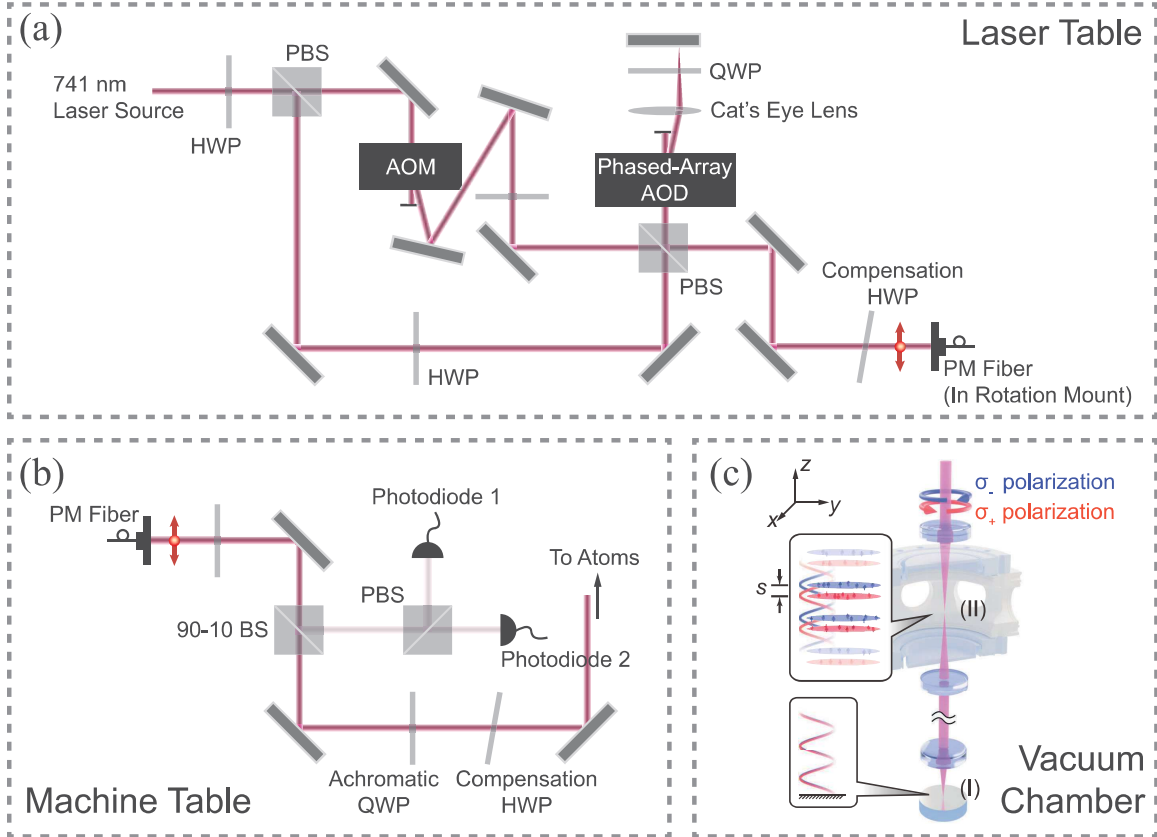
Figure 5-4: Optics setups for the bilayer potential. (a) Two 741 nm laser beams in orthogonal linear polarizations are produced by a single-passed AOM and a double-passed phased-array AOD, merged on a PBS, and coupled into a PM fiber. (b) On the machine table, the laser beam with two frequency components along two orthogonal linear polarizations are picked off by a 90-10 BS followed by a PBS for PID intensity control. An achromatic QWP converts the two linear polarization components into circular polarizations. The light is then sent into the vacuum chamber after a compensation HWP. (c) Two overlapping laser beams with opposite circular polarizations σ_+ and σ_- are retro-reflected by mirror (I) to form two optical standing waves. The two standing waves are displaced at the position of the atoms (II), controlled by the frequency offset Δ between the two laser beams. Dy atoms in this configuration form an array of pancake-shaped bilayers of head-to-head dipoles with adjustable interlayer distance s.

range as $\delta s = L \cdot \delta f / f$. For a retro-path length $L = 1.9$ m and a desired interlayer distance tuning range of $\lambda/2 \approx 370$ nm, the corresponding dynamic tuning range of laser frequency is around $\delta f = 79$ MHz. This tuning range is too large for ordinary AOMs. As illustrated in Fig. 5-5, the k-vectors of the zeroth order and the frequency-shifted first-order output of an ascouto-optical device have to satisfy the Bragg condition $\mathbf{k_0} + \mathbf{q} = \mathbf{k_{-1}}$, where $\mathbf{q}$ is the momentum provided by the acoustic phonon. As we tune the RF frequency, the magnitude of the vector $\mathbf{q}$ changes, therefore the crystal orientation needs to be adjusted to meet the Bragg condition in order.
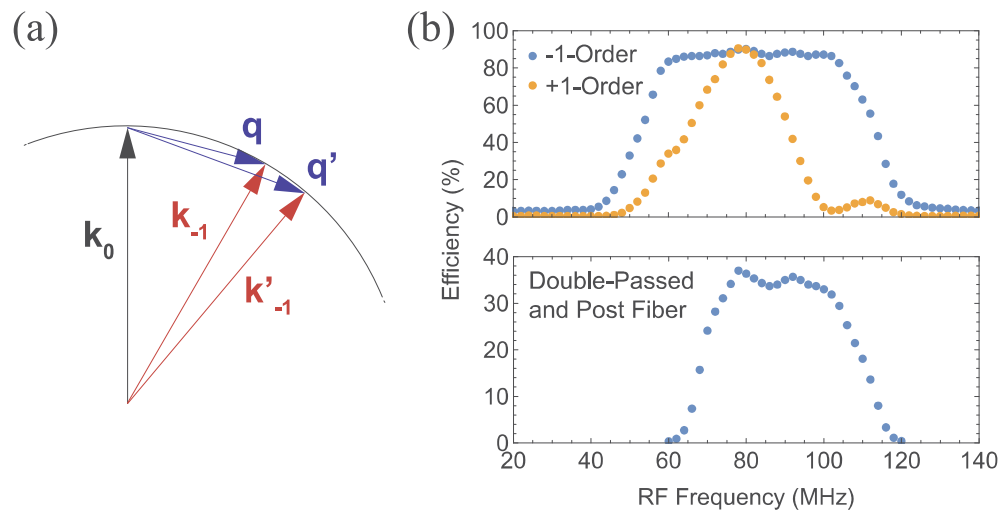

Figure 5-5: (a) Bragg condition between the zeroth-order photon momentum $\mathbf{k_0}$, the -1st-order photon momentum $\mathbf{k_{-1}}$, and the phonon momentum $\mathbf{q}$. When the RF frequency is changed, the direction of $\mathbf{q}$ also changes in order for the new Bragg condition to be satisfied. (b) Upper panel: Diffraction efficiency of the -1-order and the +1 order output with the orientation of the AOD being fixed; Lower panel: total efficiency after double-passing the phased-array AOD and fiber coupling.

In order to achieve high diffraction efficiency across a wide frequency range without changing the crystal orientation, we use a device called phased-array AOD manufactured by IntraAction Corp. The acousto-optic crystal inside such a phased-array AOD has a staircase-shaped edge, which is designed to shape the wavefront and automatically steer the orientation of the acoustic wave to meet the Bragg condition for the -1st order when the RF frequency is being changed. As shown in Fig. 5-5 (b), in contrast to diffraction orders such as the +1st order, the diffraction efficiency of the

-1st order has a flat region when the RF frequency is between 60 MHz and 100 MHz. After double passing and fiber coupling, we achieve 50 MHz frequency tunability in one of the laser beams with efficiency above 30%. This allows us to dynamically scan the bilayer array from interlaced configuration to overlapped configuration during each experimental cycle.

Phase Compensation with Tilted Waveplates

After reflecting off some optical elements at large incidence angles, especially when merging laser beams using dichroic mirrors, the circular polarizations of the optics beam can be significantly affected. We have seen that some dichroic mirros can lead to relative phase shifts of around $(n + 1/4)\lambda$ along vertical and horizontal directions, and convert circularly-polarized incident beams into linearly-polarized output beams. To compensate for these extra phase shifts, we insert a tilted half waveplate (HWP) whose fast and slow axes are along the horizontal and vertical directions (see Fig. 5-4). Since the optical elements in the path are angled along the axes that are perpendicular to the plane of optics rays, the resulting phase shifts can be undone by adjusting the tilt angle of the compensation HWP.

We characterize the quality of the circular polarization by passing the beam through a polarizer, and measure the maximum and minimum transmitted powers $I_{\max}$ and $I_{\min}$ as we rotate the polarizer. Using the tilted-waveplate technique, we are able to produce high quality circular polarizations at the position of the atoms with $I_{\min}/I_{\max} > 97\%$

5.2.2 Kapitza-Dirac Calibration of Interlayer Distance

We calibrate the interlayer distance s using a Kapitza-Dirac experiment [42] in which the diffraction patterns of atoms are used to reveal the structure of the pulsed optical standing waves. This is done with a BEC in the $m_J = -8$ Zeeman state polarized along the transverse direction **x** in a magnetic field of 1.3 G. After the preparation of the condensate, we simultaneously pulse on the two optical standing waves with the same intensity for $\tau = 5 \ \mu$s, such that most of the population is in the the first order of

the Kapitza-Dirac diffraction pattern. Since the transversely-polarized atomic spins see both circular polarizations as a superposition of $(\sigma_-, \pi, \sigma_+)$ light with weights of $(1, 2, 1)$, taking $\mathbf{x}$ as the quantization axis, the light-atom interaction Hamiltonian for the $m_J = -8$ state can be expressed as the superposition of two phase-shifted sinusoidal potentials of the same amplitudes $V_0(x, y)[\sin^2(kz) + \sin^2(kz + \phi)]$.

Fig. 5-6 shows the typical first-order Kapitza-Dirac signals in the short pulse limit $V_0(x, y)\tau/h \ll 1$. The result presents an oscillatory behavior as we vary the relative detuning Δ. When the bilayers are in an interlaced configuration ($\phi = \pi/2$), the first-order Kapitza-Dirac signal vanishes. When the bilayers are in an overlapped configuration ($\phi = 0$) the amplitude of the sinusoidal potential is maximized, corresponding to the strongest Kapitza-Dirac signal. The resulting oscillation period of the Kapitza-Dirac signal indicates the tuning sensitivity of the interlayer distance to be 4.7 nm/MHz with respect to the relative laser detuning Δ.
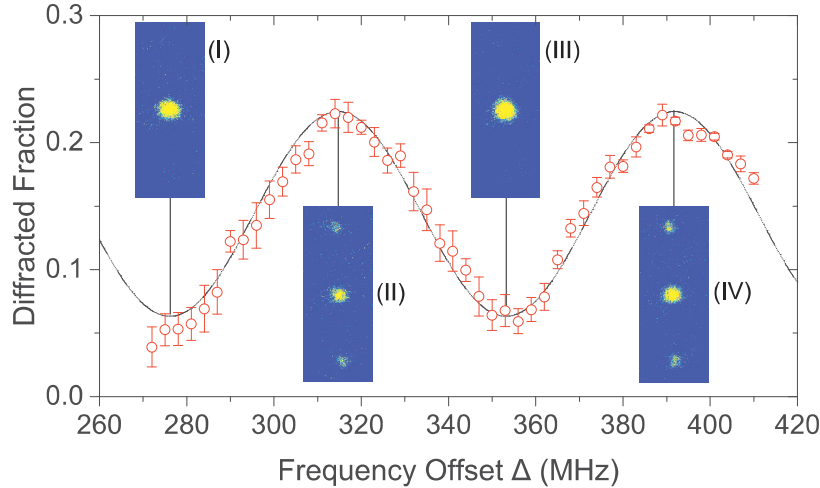
Figure 5-6: Characterization of the interlayer distance using Kapitza-Dirac diffraction. The 1st-order fraction of the Kapitza-Dirac signals N_{+1}/N_{tot} versus relative detuning Δ with $m_J = -8$ Bose-Einstein condensates polarized along the $\mathbf{x}$ direction. The Kaptiza-Dirac signal vanishes at interlaced bilayer configurations (I) and (III), whereas it is maximized for overlapped bilayer configurations (II) and (IV).

5.2.3 Adiabatic Loading

The ground state of the bilayer is loaded using an adiabatic transfer method, as depicted in Fig. 5-7. First, $m_J = -8$ atoms are prepared in a magnetic field with a transverse component $B_x = 200$ mG and an axial component B_z around 10 mG. We then ramp up the σ_+ and σ_- standing waves in the interlaced configuration (i.e. with $s = \lambda/4$) in 100 ms, loading all layers with atoms aligned with the x axis (Fig. 5-7. By ramping down the transverse magnetic component B_x in 15 ms, the potential depth increases while a bilayer array is formed with dipoles that are aligned head-to-head (Fig. 5-7. We ensure balanced loading by making sure that the energy offset between the minima of the σ_+ and σ_- potentials $\delta = U_+ - U_- + E_Z = 0$, where $U_\pm$ are the AC Starks shift of the layers, and the differential Zeeman energy is given by $E_Z = 16 g_J \mu_B B_z$. It is crucial that the atoms stay in their local ground state throughout the experiment to prevent losses and heating due to dipolar relaxation. Therefore, the Zeeman shifts caused by the external magnetic field B_z have to be smaller than the differential AC Stark shift between the $m_J = -8$ and $m_J = -7$ states.
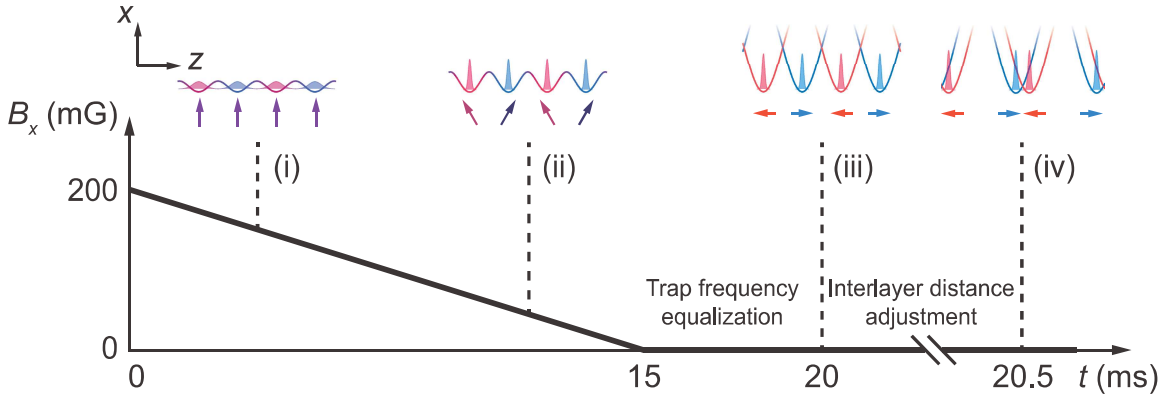
Figure 5-7: Adiabatic loading of the bilayer array. (i) Starting with the optical potential in the interlaced configuration in the presence of a dominating transverse magnetic field $B_x = 200$ mG, the atoms are initialized in the $m_J = -8$ spin state along the **x** direction. (ii) As B_x is ramped down in 15 ms, the light shift dominates over the Zeeman shift, thereby adiabatically loading the bilayer array. (iii) The power of the σ_+ and σ_- potentials are adjusted for identical trap frequencies. (iv) The interlayer distance is adjusted to designated values in 0.5 ms.

After loading a balanced bilayer array, the powers of the two optical standing

waves are ramped up, ensuring that the two layers have the same trap frequencies of typically $(\omega_x, \omega_y, \omega_z) = 2\pi \times (0.5, 0.5, 140)$ kHz. The strong axial confinement results in a harmonic oscillator length $a_{HO} = \sqrt{\hbar/m\omega_z}$ of 21.1 nm, where $\hbar = h/2\pi$ and m is the atomic mass. We load 4.2×10^4 ultracold ^{162}Dy atoms into an array of 42 bilayers, with a temperature of 1.7 μK determined from the cloud size after ballistic expansion (see Methods). Subsequently, the interlayer distance s is ramped from $\lambda/4$ to different designated values in 0.5 ms by changing the frequency of the σ_- standing wave. The interlayer distance s is calibrated with Kapitza-Dirac diffraction measurements (see Methods). At the end of each experimental sequence, the atoms are released from the bilayer array within 1 μs and are imaged after ballistic expansion. With the small axial magnetic field B_z serving as a guiding field, atoms remain in the $m_J = \pm 8$ states and are imaged by a spin-resolved absorption imaging technique. This method allows us to measure the population in each of the two layers simultaneously.

5.2.4 Spin-Resolved Imaging

Our spin-resolved absorption imaging system operates in the weak saturation limit of the 421 nm cyling transition. It utilizes the big contrast of photon scattering rates of atoms in the stretched $m_J = \pm 8$ Zeeman states for two opposite circular polarizations of light. The resonant imaging light addressing the 421 nm transition is linearly polarized along $\mathbf{x}$, and propagates along the axial direction $\mathbf{z}$. Taking $\mathbf{z}$ as the quantization axis, the imaging light contains equal amount of σ_- and σ_+ polarization components. Due to the big difference between the Clebsch–Gordan coefficients for the $|J = 8, m_J = -8\rangle \rightarrow |J' = 9, m'_J = -9\rangle$ and the $|J = 8, m_J = -8\rangle \rightarrow |J' = 9, m'_J = -7\rangle$ electric dipole transitions, the σ_+ photons are predominantly scattered by the atoms in the σ_+ layer, whereas the σ_- photons are predominantly scattered by the atoms in the σ_- layer. The two polarization components are then spatially separated by a 1° angle via a quarter-wave plate and a Wollaston prism (see Fig. 5-8), leading to two nearly-independent imaging channels for the σ_+ and the σ_- layers on the camera. The duration of the imaging pulse is adjusted to reduce optical pumping which would lead to crosstalk between the two imaging channels.
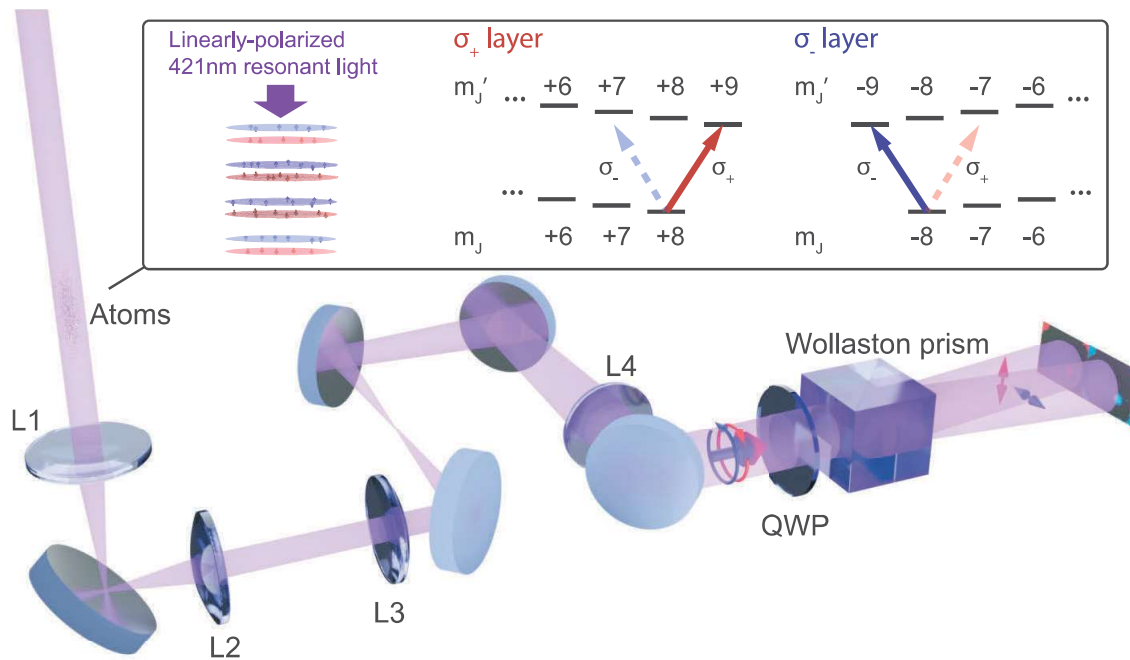
Figure 5-8: The spin-resolved absorption imaging scheme. The atoms are exposed to linearly polarized light that is co-propagating with the bilayer optical beams and that is resonant with the 421 nm transition. After the relay lenses ($L1$ and $L2$) and the magnification lenses ($L3$ and $L4$), the σ_+ and σ_- components of the imaging light are separated using a quarter-wave plate (QWP) and a Wollaston prism. The spatially separated images of the σ_+ and the σ_- layers are recorded by a CMOS camera.

Figure 5-9: A spin-resolved absorption image showing the time-of-flight signals of atoms in σ_+ and σ_- layers in two imaging channels.

5.2.5 Lifetime Measurement

We demonstrate the spatial control over the bilayer geometry to be better than 10 nm by scanning the two layers across each other, and measuring the lifetime of the atoms due to loss. As presented in Fig. 5-10, the loss rates are significantly enhanced when the two layers are fully overlapped. Assuming that loss processes occur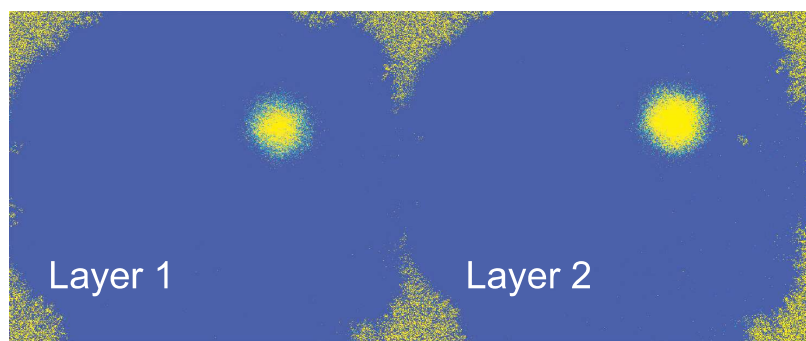 at short range, the sharp peak in the loss rate as a function of layer separation s is essentially the convolution between the density profiles of the two layers, from which we can extract the information of the thickness of each layer.
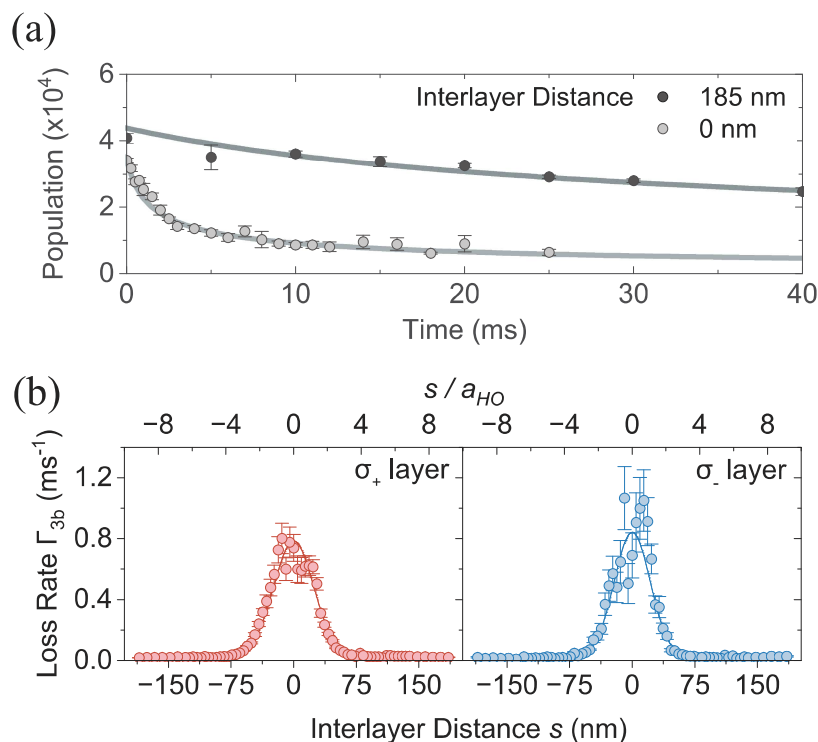
Figure 5-10: Demonstration of controlling the interlayer distance on a 10 nm scale by recording atom loss as a function of layer separation. (a) Evolution of the population in σ_+ layers at two different interlayer distances $s = 185$ nm and 0 nm. The loss is much faster when the layers are overlapped. Initial loss rates Γ_{3b} are obtained from the fits to the decay curves. (b) Gaussian fits of the initial loss rates Γ_{3b} to the interlayer distances s according to Eq. 5.4 (solid lines) provide a value of $\sigma_z = 18.6$ nm for the layer thickness.

Due to the partial condensation of the cloud and technical heating during the loading, we assume a Gaussian distribution in the transverse direction such that the

atomic density is

$$n_{i,\mathrm{3D}}^{(\pm)}(\rho,z) = n_{0,\mathrm{3D}}\,e^{-\frac{1}{2}\left(i\frac{\lambda}{2\sigma_{\mathrm{ODT}}}\right)^2}\,e^{-\frac{1}{2}\left(\frac{\rho}{\sigma_\perp}\right)^2}\,e^{-\frac{1}{2}\left(\frac{z\pm s/2}{\sigma_z}\right)^2} \tag{5.3}$$

where $n_{0,\mathrm{3D}}$ is the peak local density, $i = 0, \pm 1, \pm 2, \ldots$ is the index of the bilayer, $\sigma_\perp$ and σ_z are the RMS widths of each layer along transverse and axial directions, and the superscript $(\pm)$ denotes the σ_+ or σ_- layer. By integrating along x, y, z, and summing over index i, we obtain the relation between the peak density and the total atom number of the $\sigma_\pm$ layers $n_{0,\mathrm{3D}} = 3N_{\mathrm{tot}}^{(\pm)}/V_{\mathrm{eff}}$, with the effective volume defined as $V_{\mathrm{eff}} = 12\pi^2\sigma_\perp^2\sigma_z(2\sigma_{\mathrm{ODT}}/\lambda)$.

Since two-body inelastic collisions such as dipolar relaxation between $m_J = -8$ and $+8$ states require higher-order couplings, we assume the interlayer inelastic losses to be three-body processes. Taking into account the intralayer and interlayer three-body losses and assume balanced bilayers $n^{(+)} = n^{(-)} = n$, we can write the loss equation for local density as $\frac{dn}{dt} = -\beta_{\mathrm{intra}}n^3 - \beta_{\mathrm{inter}}n^3 e^{-\frac{1}{3}\left(\frac{s}{\sigma_z}\right)^2}$. Integrating the rate equation over space and summing over layer index i gives rise to the following rate equation for total atom numbers

$$\Gamma_{\mathrm{3b}} = \Gamma_{\mathrm{intra}} + \Gamma_{\mathrm{inter}}e^{-\frac{1}{3}\left(\frac{s}{\sigma_z}\right)^2} = \frac{\dot{N}_{\mathrm{tot}}}{N_{\mathrm{tot}}} \tag{5.4}$$

where $\Gamma_{\mathrm{intra}} = \beta_{\mathrm{intra}}(N_{\mathrm{tot}}/V_{\mathrm{eff}})^2$, and $\Gamma_{\mathrm{inter}} = \beta_{\mathrm{inter}}(N_{\mathrm{tot}}/V_{\mathrm{eff}})^2$. For spin-independent three-body collisions and thermal clouds, we expect $\Gamma_{\mathrm{intra}} = \Gamma_{\mathrm{inter}}$. Unexpectedly, we observed about a fiftyfold increase in loss rate when the two layers are overlapped, which implies that three-body recombination involving mixed spin states is much faster than recombination of three atoms all in the same spin state. This strongly-enhanced loss feature serves as a highly sensitive monitor for the density overlap between the two layers, while fitting the loss curve determines the thickness of each layer $\sigma_z = 18.6$ nm. This is slightly larger than the RMS size of the harmonic oscillator ground state $a_{\mathrm{HO}}/\sqrt{2} = 14.3$ nm, and can be explained by a small fraction of atoms in excited states of the axial potential [1]. The observed losses in the two layers

---

[1] By taking into account thermal excitation into the higher axial vibrational levels due to finite

are almost equal, implying equal loss rates for three-body collisions involving one spin-up and two spin-down atoms, or vice versa. With this technique of scanning two layers across each other, we have mapped out an atomic density distribution with a resolution much better than 10 nm.

We conclude from the loss measurement that for $s \gtrsim 50$ nm we can regard the layers as coupled only by long-range dipolar forces. The dipolar energy U_{dd}/h between two Dy atoms with opposite spins at this separation is 20 kHz. This geometry now allows us to study dipolar physics in new regimes. In the following, we present two out-of-equilibrium experiments which demonstrate strong interlayer dipole-dipole interactions.

5.3 Detection of Interlayer Dipole-Dipole Interaction

5.3.1 Interlayer Thermalization

One novel experiment is energy-transfer via dipolar interactions, or sympathetic cooling between two atomic systems separated by vacuum [90, 24]. Each layer is heated up by the fluctuating magnetic field created by the dipoles in the other layer. For equal temperatures, in detailed balance, the heat flows cancel. For unequal temperatures, the dipolar fluctuations cause thermalization. Fig. 5-11 (b) shows the experimental results.

We can estimate the interlayer collision rate as $n_{\mathrm{2D}}\sigma_{\mathrm{dd}}v_{\mathrm{rel}}$, where n_{2D} is the 2D density distribution, and σ_{dd} is the cross section for two dipolar atoms passing each other at the separation s. Using the Born approximation, we calculate the elastic cross section between two atoms in thin layers separated by a distance s, and the

---

temperature $T = 5.5$ μK, the thickness of each layer is estimated to be $\sigma_z = \sqrt{\frac{\sum_{n=0}^{\infty}(2n+1)e^{-n\hbar\omega_z/k_B T}}{\sum_{n=0}^{\infty}e^{-n\hbar\omega_z/k_B T}}} \frac{a_{\mathrm{HO}}}{\sqrt{2}} \approx$ $1.31 a_{\mathrm{HO}}/\sqrt{2} \approx 18.8$ nm. Note that the data in Fig. 5-10 were taken at higher temperature than the other data.
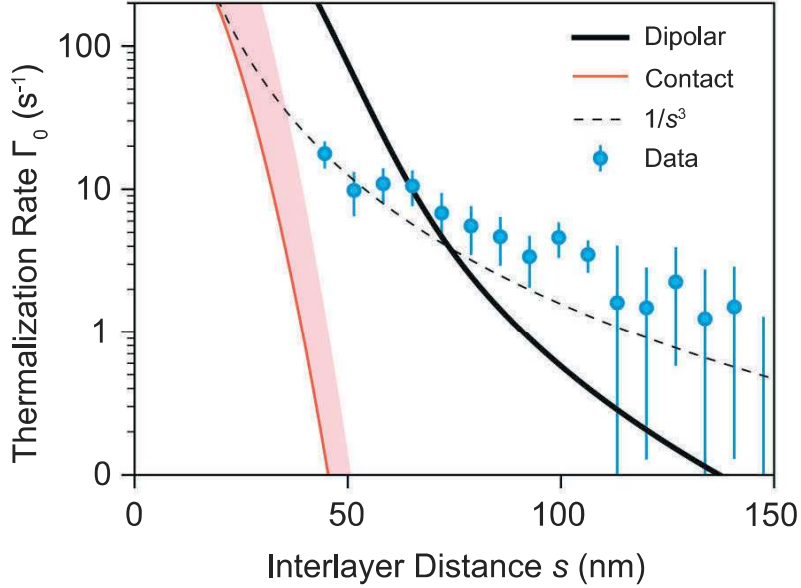
Figure 5-11: Observation of interlayer thermalization. (a) Interlayer elastic scattering cross sections as functions of separation s calculated using the Born approximation. The grey curves correspond to dipolar cross sections for infinitely-thin $\sigma_z = 0$ layers (thin grey) along with its large interlayer distance limit $ks \gg 1$ (dashed, following Eq. 5.5, and for layers with finite thickness $\sigma_z = 14.9$ nm (quasi 2D, solid grey). The red curve is for simple contact interactions at the background scattering length (red, quasi 2D), and the shaded area corresponds to a 10 times enhanced cross section. (b) Observed thermalization rates Γ_0 obtained from the pseudo-exponential fits. The black and red solid lines show the expected thermalization rate from dipolar and contact interactions (see Methods). The dotted line is for reference and is proportional to $1/s^3$.

analytic large-s limit is

$$\sigma_{\mathrm{dd}}^{(2D)} = a_{\mathrm{dd}}^2 \frac{\pi}{k^2 s^3} \tag{5.5}$$

Here, $a_{\mathrm{dd}} = 10.2$ nm is the dipolar length and k is the relative momentum between the colliding particles. For $s = 75$ nm, the quasi-2D cross section $\sigma_{\mathrm{dd}} = 0.38$ nm (see Fig. 5-11 (a)). With a typical 2D peak density of $n_{2D} \approx 1.3 \times 10^9$ cm^{-2} and a thermal velocity of 2.1 cm/s one obtains an interlayer collision rate of 100 s^{-1}. The observed thermalization times are much slower, around 160 ms (rate of 6 s^{-1}). This can be fully accounted for by the anisotropy of dipolar scattering, which is peaked in the forward direction and reduces the effective cross section by a factor of 6, and by multiple averaging arising from the inhomogeneity of our sample (see Methods). In Fig. 5-11 (b), we compare the observed thermalization rates to calculations. They don't have any adjustable parameters and fully take into account the momentum and angular dependence of dipolar scattering and the finite thickness of the layer. The calculations are in semi-quantitative agreement with the observations. The drop-off of the thermalization rate is much weaker than the steep exponential decrease in density overlap, and therefore in the contact interactions between the two layers. This is clear evidence for purely dipolar collisions in the range of 50 to 100 nm interlayer distances.

The observed dependence on s roughly follows a $1/s^3$ dependence which is less steep than predicted. This is possibly due to the assumptions of the theory based on purely dipolar binary collisions. For small s, there can be an interference term with s-wave contact interactions and a contribution from non-universal short-range dipolar s-wave scattering [91] which is not included in the Born approximation. The largest separations s studied are comparable to the interparticle separation and the binary collision approximation may no longer be accurate, i.e. there are now more then two particles interacting with each other.

5.3.2 Coupled Oscillation

In the second experiment, we look for coupled collective oscillations of the bilayer system. Several theoretical papers [81, 50] predicted the coupling of transverse oscillations by the mean dipolar field between the layers. Indeed, when we excite transverse oscillations in one layer, we find that they cause oscillations of the other layer (Fig. 5-12). Experimentally, after loading a balanced bilayer array and adjusting the interlayer distance to a designated value in 0.5 ms, we adiabatically displace the σ_+ layer along the transverse direction **y** in 10 ms using an extra laser beam with σ_+ polarization. This beam, blue-detuned from the 626 nm transition by 458 MHz, is misaligned from the atoms by about one beam waist, and almost only displaces the atoms in the σ_+ layer. A sudden switch-off of the displacement beam hence creates a center-of-mass oscillation of the σ_+ layer at the transverse trap frequency of 500 Hz with an adjustable amplitude ranging from 0 to 8 μm depending on the final power of the beam. As a function of hold time, the in-trap velocity of each layer is obtained from time-of-flight images to reveal how momentum is transferred between layers. The displacement beam also displaces the σ_- layer due to crosstalk, but 100 times less. The crosstalk could be observed only at much larger oscillation amplitudes than shown in Fig. 5-12.
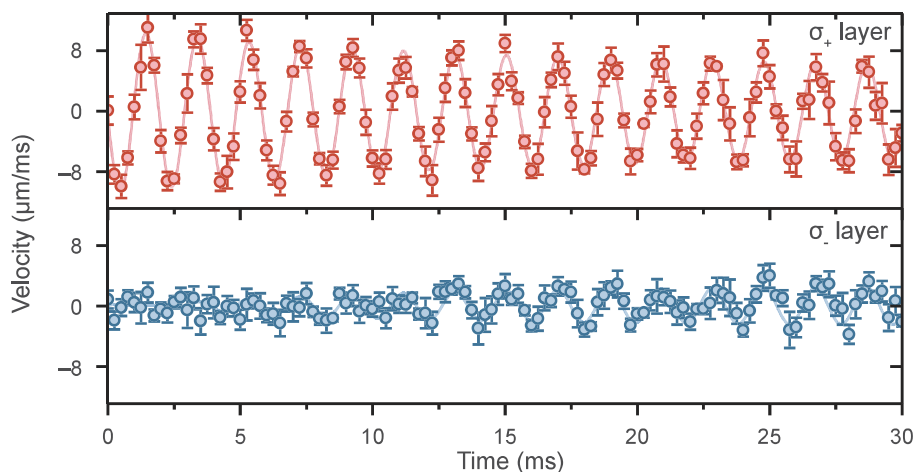

Figure 5-12: Observation of coupled oscillations of the two layers at 62 nm interlayer distance. The center-of-mass oscillation of the σ_+ layer is excited by suddenly switching off a displacement force. The σ_- layer oscillates due to dipolar coupling.

Fig. 5-12 shows the time evolution of the velocity of each layer as obtained from ballistic expansion images. The harmonic oscillation of the σ_+ layer shows damping whereas the σ_- layer starts at rest and shows a growing in-phase oscillation. Our observation is in contrast to the theoretical treatments [81, 50], where the mean-field coupling potential would cause a beat note, which is initially an oscillation 90 degrees out of phase. Furthermore, the predicted mean-field coupling [81, 50] results in a normal-mode splitting of less than 1 Hz, which is too slow to be observed on the experimental time scale. Our observation is fully consistent with a friction force caused by dipolar collisions. First, frictional coupling between harmonic oscillators causes an in-phase oscillation of the driven oscillator. Second, the time-constant for the damping of the relative motion between the two layers of 25 ms is similar to the observed interlayer thermalization times. These observations establish dipolar coupling between two layers which are completely physically separated.

When we explored the coupled oscillations for longer times and for larger amplitudes and separations, we found that the observations depended critically on a precise matching of the potentials of the two bilayers. Non-isotropic radial confinement could cause two-dimensional motion of the layers and Lissajous figure type orbits. Nevertheless, all observations showed an initial in-phase oscillation of the σ_- layer consistent with a frictional force.

Chapter 6

Control of Dipolar Relaxation

Quantum gas experiments with ultracold atoms and molecules are often limited by inelastic processes. In ultracold molecule experiments, inelastic collisions due to complex chemical reactions have hampered the creation of degenerate gases of cold molecules. Similarly, in experiments with ultracold magnetic atoms such as Dy, Er, and Cr, atoms in different spin states undergo inelastic dipolar relaxation. This inelastic collision process converts internal Zeeman energy into the external kinetic energy of atoms, thereby severely limiting the lifetime of ultracold Bose gases that are not in the ground spin state — the lifetime of a typical Dy BEC in the highest spin state $|J = 8, m_J = +8\rangle$ with density of 10^{14} cm^{-3} is only on the order of milliseconds [11, 21].

In cold molecule experiments, suppressing short-range chemical reactions using microwave shielding effect [3] or dipolar shielding effect in external quasi-2D confinement [80] have been proven to be the most effective technique for producing degenerate gases of polar molecules so far. Efforts along this technical path have led to the recent successful creation of Bose-Einstein condensates [14] and degenerate Fermi gases [106] of ground-state polar molecules. On the other hand, suppressing inelastic dipolar relaxation of magnetic atoms using dipolar repulsion is a more challenging task: the strength of dipolar repulsion among magnetic atoms is three orders of magnitudes weaker compared to that of polar molecules.

This chapter introduces our result [12] of controlling dipolar relaxations of Dy

atoms using an external quasi-2D optical confinement. The optical potential is pro-
duced by a blue-detuned 741 nm optical standing wave providing tight axial con-
finement with trap frequency ω_z greater than 200 kHz, and a high-power 1064 nm
optical dipole potential providing transverse confinement with trap frequency around
200 Hz. We observe one order of magnetude suppression of dipolar relaxation rate
with Dy atoms in the highest spin state $m_J = +8$ in such a quasi-2D geometry.

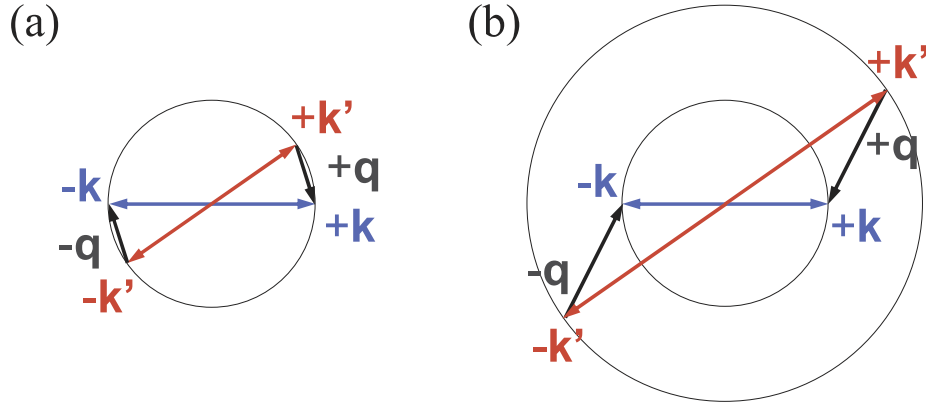## 6.1   Elastic and Inelastic Collisions in 3D

Figure 6-1: Illustration of (a) elastic (on-shell) scattering and (b) inelastic (off-shell)
scattering with the initial incident momentum denoted as $\mathbf{k}$ and the final momentum
denoted as $\mathbf{k}'$. The momentum change is defined as $\mathbf{q} = \mathbf{k} - \mathbf{k}'$. The internal spin
states of the atoms $|m_{J1}, m_{J2}\rangle$ are unchanged before and after an elastic scattering
event, hence the kinetic energy is conserved. On the contrary, spin flip happens
before and after an inelastic scattering event, converting internal Zeeman energy
into external kinetic energy of the two atoms.

   We start by discussing quantum collision theory between two Dy atoms. For sim-
plicity of analysis, we assume in this chapter that the two incoming atoms are in
the same initial spin state, hence the spin part of the two-body wavefunction can be
written as $|m_J, m_J\rangle$. After scattering off the dipole-dipole potential Eq. 2.4, as dis-
cussed in Chapter 2, the initial spin state is coupled to three channels of final sym-
metric spin states: $\left|S^{(0)}\right\rangle = |m_J, m_J\rangle$, $\left|S^{(1)}\right\rangle = \frac{1}{\sqrt{2}}\big(|m_J, m_J - 1\rangle + |m_J - 1, m_J\rangle\big)$, and
$\left|S^{(2)}\right\rangle = |m_J - 1, m_J - 1\rangle$. These three channels correspond to scattering processes
with 0, 1, and 2 units of spin flip — the first being elastic collision, and the latter two

being inelastic dipolar relaxations.

Fig. 6-1 illustrates the relation between incident momentum $\mathbf{k}$ and final momentum $\mathbf{k}'$ during elastic and inelastic scattering processes. For elastic scattering where spin-flip is not involved, the kinetic energy is conserved, hence $k = k'$. For inelastic scattering where spin states of the atoms are changed, the internal energy is converted into external kinetic energy. Therefore we have $\frac{\hbar^2 k'^2}{m} - \frac{\hbar^2 k^2}{m} = \Delta E$, which leads to

$$\frac{k'}{k} = \sqrt{1 + \frac{m \Delta E}{\hbar^2 k^2}} \tag{6.1}$$

where the released energy ΔE is given by 0 for zero unit of spin flip, $\mu_B g_J B$ for one unit of spin flip, and $2\mu_B g_J B$ for two units of spin flip.

6.1.1 Born Approximation

In this section, we study the 3D dipolar collision processes using Born approximation. The two-body wavefunction in the center-of-mass frame involves an incident plane wave and a scattered spherical wave:

$$\left| \psi^{(i)}(\mathbf{r}) \right\rangle = \left(1 - \frac{|\epsilon|}{2} \right) \left\{ \left(e^{i\mathbf{k}\cdot\mathbf{r}} + \epsilon e^{-i\mathbf{k}\cdot\mathbf{r}} \right) \left| S^{(0)} \right\rangle + \left[f^{(i)}(\mathbf{k}',\mathbf{k}) + \epsilon f^{(i)}(-\mathbf{k}',\mathbf{k}) \right] \frac{e^{ik'r}}{r} \left| S^{(i)} \right\rangle \right\} \tag{6.2}$$

where $\epsilon = +1$ for bosons and -1 for fermions, $i = 0, 1, 2$ corresponds to different units of spin flip, and $f^{(i)}(\mathbf{k}',\mathbf{k})$ corresponds to the respective scattering amplitude. Using the first Born approximation, the scattering amplitude can be written as the Fourier transform of the dipole-dipole interaction potential [21, 48]:

$$\begin{aligned} f^{(i)}(\mathbf{k}',\mathbf{k}) &= -\frac{m}{4\pi\hbar^2} \int d\mathbf{r} e^{i\mathbf{q}\cdot\mathbf{r}} \left\langle S^{(i)} \middle| U_{dd}(\mathbf{r}) \middle| S^{(0)} \right\rangle \\ &= \frac{a_{dd}}{J^2} \left\langle S^{(i)} \middle| \mathbf{J_1} \cdot \mathbf{J_2} - 3(\mathbf{J_1} \cdot \hat{\mathbf{q}})(\mathbf{J_2} \cdot \hat{\mathbf{q}}) \middle| S^{(0)} \right\rangle \end{aligned} \tag{6.3}$$

where $\mathbf{q} = \mathbf{k} - \mathbf{k}'$ is the momentum change during a scattering event, and $a_{dd} = \frac{m}{12\pi\hbar^2} \mu_0 (\mu_B g_J J)^2$ is defined as the dipolar length. For Dy atoms in the highest Zeeman level $|8, +8\rangle$, we have $a_{dd} \approx 6.82$ nm. The corresponding matrix elements are

listed in the following (see Chapter 2):

$$\begin{cases} \left\langle S^{(0)} \middle| \mathbf{J_1} \cdot \mathbf{J_2} - 3(\mathbf{J_1} \cdot \hat{\mathbf{q}})(\mathbf{J_2} \cdot \hat{\mathbf{q}}) \middle| S^{(0)} \right\rangle = J^2(1 - 3\cos^2\theta_{\mathbf{q}}) \\ \left\langle S^{(1)} \middle| \mathbf{J_1} \cdot \mathbf{J_2} - 3(\mathbf{J_1} \cdot \hat{\mathbf{q}})(\mathbf{J_2} \cdot \hat{\mathbf{q}}) \middle| S^{(0)} \right\rangle = -3J^{3/2} e^{+i\phi} \sin\theta_{\mathbf{q}} \cos\theta_{\mathbf{q}} \\ \left\langle S^{(2)} \middle| \mathbf{J_1} \cdot \mathbf{J_2} - 3(\mathbf{J_1} \cdot \hat{\mathbf{q}})(\mathbf{J_2} \cdot \hat{\mathbf{q}}) \middle| S^{(0)} \right\rangle = -\frac{3}{2} J e^{+2i\phi} \sin^2\theta_{\mathbf{q}} \end{cases} \qquad (6.4)$$

with $\theta_{\mathbf{q}}$ being the angle between $\mathbf{q}$ and the external magnetic field $\mathbf{B}$. Here we see that the momentum components $\mathbf{q}$ provided by the dipole-dipole potential possess d-wave patterns, and that the magnitudes of the three matrix elements differ by factors of $\sqrt{J}$. Since the scattering cross-section scales as the square of the matrix element (as will be introduced in the following paragraph), we expect, for bosonic Dy atoms with $J = 8$, that the elastic scattering rate is an order of magnitude faster than the dipolar relaxation rate with $\Delta L = 1$, which is another order of magnitude faster than the dipolar relaxation rate with $\Delta L = 2$.
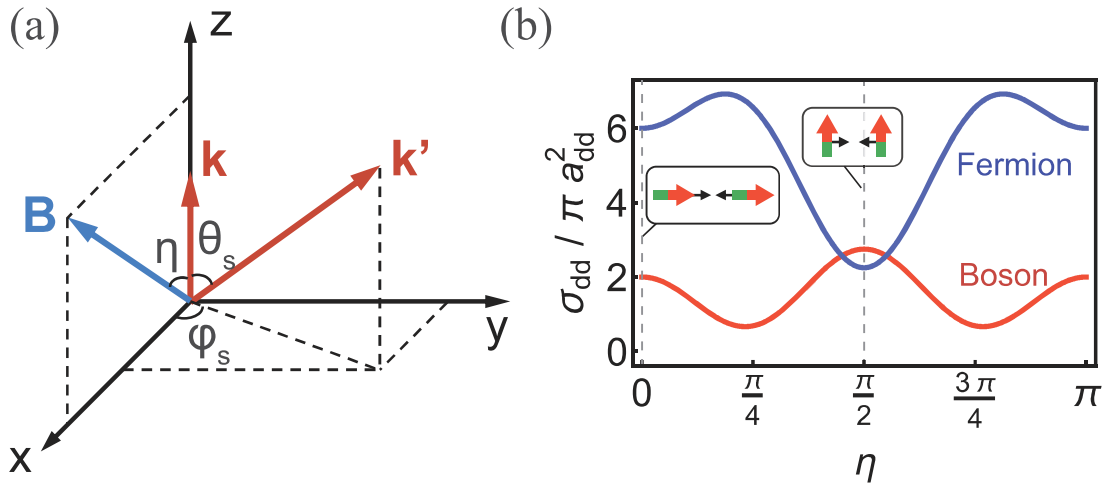

Figure 6-2: (a) The coordinate system under which collisional cross-sections are solved using the Born approximation. The incident $\mathbf{k}$ are chosen to align with the z axis, the guiding magnetic field $\mathbf{B}$ is chosen to lie within the XOZ plane, and the outgoing momentum $\mathbf{k}'$ is scattered into all directions. Angles η, φ_s, and θ_s are as indicated in the figure. (b) Elastic cross-section of bosonic and fermionic Dy atoms as functions of incident angle η. $\eta = 0°$ corresponds to head-to-tail collisions, and $\eta = 90°$ corresponds to side-by-side collisions.

In the coordinate system defined in Fig. 6-2, we express the quantization axis, the

incident momentum, and the outgoing momentum as

$$
\begin{cases}
\hat{\mathbf{B}} = (\sin\eta, 0, \cos\eta) \\[2mm]
\mathbf{k} = k(0,0,1) \\[2mm]
\mathbf{k}' = k'(\sin\theta_s \cos\varphi_s, \sin\theta_s \sin\varphi_s, \cos\theta_s)
\end{cases}
\tag{6.5}
$$

And therefore $\theta_{\mathbf{q}}$ can be expressed as

$$
\cos^2\theta_{\mathbf{q}} = \left(\frac{(\mathbf{k}-\mathbf{k}')\cdot\hat{\mathbf{B}}}{|\mathbf{k}-\mathbf{k}'|} \right)^2 = \frac{\left[\cos\eta(1 - \frac{k'}{k}\cos\theta_s) - \frac{k'}{k}\sin\eta\sin\theta_s\cos\varphi_s \right]^2}{1 + \left(\frac{k'}{k}\right)^2 - 2\frac{k'}{k}\cos\theta_s}
\tag{6.6}
$$

Using the expressions for the scattering amplitudes Eq. 6.3, the total cross-sections of the three scattering channels can be evaluated as the integral of the differential cross-sections over the whole solid angle in $\mathbf{k}'$ space:

$$
\sigma^{(i)} = \int d\Omega_{\mathbf{k}'} \left(\frac{d\sigma}{d\Omega_{\mathbf{k}'}} \right) = \left(1 - \frac{|\epsilon|}{2} \right) \int_0^{2\pi} d\varphi_s \int_0^\pi d\theta_s \sin\theta_s \left| f^{(i)}(\mathbf{k}',\mathbf{k}) + \epsilon f^{(i)}(-\mathbf{k}',\mathbf{k}) \right|^2
\tag{6.7}
$$

6.1.2 Elastic Cross-Section of Dipolar Collisions

The elastic collisions of neutral atoms due to contact interaction in the low-energy regime is usually characterized by the scattering length a which can be interpreted as the phase shift of the asymptotic wavefunction at the short range [57]. For bosonic atoms, the elastic cross section due to s-wave contact interaction is $\sigma_B = 8\pi a_s^2$ with a_s being the s-wave scattering length. For identical fermionic atoms, however, the elastic cross section σ_F vanishes in the low-energy regime due to Pauli exclusion, or due to the presence of the p-wave centrifugal barrier. This vanishing elastic cross-section necessitates the use of sympathetic cooling method [45] or employing fermionic atoms in different hyperfine states [31] for producing degenerate Fermi gases of alkali atoms.

The presence of magnetic dipole-dipole interaction among Dy atoms modifies the above conclusions. The elastic cross-section contributed by the dipole-dipole inter-action given an incident momentum $\mathbf{k}$, according to Eq. 6.3, Eq. 6.4, and Eq. 6.5,

is

$$\sigma_{B,F}^{(0)} = \frac{a_{dd}^2}{2}\left(1 - \frac{|\epsilon|}{2}\right)\int_0^{2\pi} d\varphi_s \int_0^\pi d\theta_s \sin\theta_s$$

$$\left[(1 - 3\cos^2\theta_{\mathbf{k}-\mathbf{k}'})^2 + (1 - 3\cos^2\theta_{\mathbf{k}+\mathbf{k}'})^2 + 2\epsilon(1 - 3\cos^2\theta_{\mathbf{k}-\mathbf{k}'})(1 - 3\cos^2\theta_{\mathbf{k}+\mathbf{k}'})\right]$$

(6.8)

Using the expressions of $\theta_{\mathbf{k}-\mathbf{k}'}$ and $\theta_{\mathbf{k}+\mathbf{k}'}$ given by Eq. 6.6 and assuming $k = k'$ for elastic scattering, we obtain the dipolar elastic cross-section for bosons and fermions

$$\sigma_{B,F}^{(0)} = \frac{\pi}{4}a_{dd}^2 \begin{cases} 11 - 30\cos^2\eta + 27\cos^4\eta & \text{(bosons)} \\ 9 + 54\cos^2\eta - 39\cos^4\eta & \text{(fermions)} \end{cases}$$

(6.9)

which are both anisotropic and depend on the angle between the incident momentum $\mathbf{k}$ and the quantization axis $\hat{\mathbf{B}}$ defined by the external magnetic field. The angular dependence of the elastic cross-sections are plotted in Fig. 6-2 (b). By integrating over all incident directions $\int_{-1}^{+1} d(\cos\eta)\sigma_{B,F}^{(0)} / \int_{-1}^{+1} d(\cos\eta)$, the averaged elastic dipolar cross-sections for bosons and fermions can be obtained

$$\begin{cases} \langle \sigma_B^{(0)} \rangle_{\mathbf{k}} = \frac{8}{5}\pi a_{dd}^2 + 8\pi a_s^2 \\ \langle \sigma_F^{(0)} \rangle_{\mathbf{k}} = \frac{24}{5}\pi a_{dd}^2 \end{cases}$$

(6.10)

The above expressions also include the contribution of s-wave contact interaction, and neglect the interference term between the s-wave and dipolar scattering amplitudes. For bosons, the presence of dipole-dipole interaction leads to a correction term to the elastic cross-section on top of the s-wave contact interaction (consistent with the result shown in Chapter 3 of Ref. [77]). For fermions, the effect of dipole-dipole interaction is more significant: it leads to a non-zero universal elastic cross-section in the low-energy regime and enables evaporative cooling of single-component fermionic gases to quantum degeneracy. This has been first demonstrated by Francesca Ferlaino's group in Ref. [1].

6.1.3 Inelastic Cross-Sections of Dipolar Relaxations

The above integrals can be extended to the calculation inelastic dipolar cross-sections averaged over all incident directions. Here we list the results for scattering processes with $\Delta L = 0$, 1, and 2

$$
\begin{cases}
\langle \sigma_{B,F}^{(0)} \rangle_{\mathbf{k}} = \dfrac{16}{5} \pi a_{dd}^2 \left[1 + \epsilon h(1) \right] \\[2ex]
\langle \sigma_{B,F}^{(1)} \rangle_{\mathbf{k}} = \dfrac{24}{5} \pi a_{dd}^2 \dfrac{1}{J} \left[1 + \epsilon h(k'/k) \right] \dfrac{k'}{k} \\[2ex]
\langle \sigma_{B,F}^{(2)} \rangle_{\mathbf{k}} = \dfrac{24}{5} \pi a_{dd}^2 \dfrac{1}{J^2} \left[1 + \epsilon h(k'/k) \right] \dfrac{k'}{k}
\end{cases}
\tag{6.11}
$$

where $h(x) = -\frac{1}{2} - \frac{3}{8} \frac{(1-x^2)^2}{x(1+x^2)} \ln\left(\frac{1-x^2}{1+x^2} \right)$ is a monotonically increasing function. In the limit where the Zeeman energy is much larger than the incident kinetic energy $\Delta E \gg \hbar^2 k^2/m$, the dimensionless variable $x = k'/k \approx \sqrt{m \Delta E}/\hbar k$ asymptotes to infinity (see Eq. 6.1) and the function $h(x)$ asymptotes to $1 - 4/x^2$. Therefore we conclude that the inelastic cross-sections scale as $\sqrt{B}$ for bosons, and as $1/\sqrt{B}$ for fermions in the large-B limit, i.e. dipolar relaxation is enhanced with increasing magnetic field for bosons, whereas is suppressed by a larger magnetic field for fermions [72].
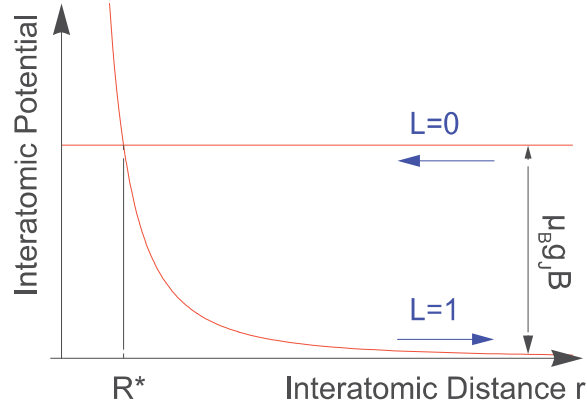
Figure 6-3: The interatomic potential for the incoming channel with $L = 0$ and the outgoing channel with $L = 1$. Two channels cross at $r = R^*$ where dipolar relaxation of two bosonic atoms happens [85].

The scaling laws of the magnetic-field dependences of dipolar relaxation rates for bosons and fermions can also be understood from the Fermi's golden rule perspective. This is discussed in great details in P. Barral's thesis [10] and by B. Pasquiou *et al.*

in Ref. [85].

In essence, for the case of bosons, two Dy atoms in the s-wave channel with $L = 0$ are scattered into the $L = 1$ and the $L = 2$ channels through the dipole-dipole interaction. In 3D, the reaction resonantly happens at a specific interatomic distance R^*, known as the *Condon point*, where the potential curves of the incoming and the outgoing channels form a cross. For the dominant dipolar relaxation with $\Delta L = 1$, the position of the Condon point R^* is approximately given by the Zeeman energy $\mu_B g_J B$ and the centrifugal barrier $\hbar^2 L(L+1)/mr^2$ of the $L = 1$ channel (see Fig. 6-3), leading to $R^* \approx \hbar \sqrt{\frac{2}{m\mu_B g_J B}} \propto 1/\sqrt{B}$. Hence a larger magnetic field would push the Condon point to a shorter range.

In the vicinity of the Condon point, the incoming radial wavefunction is proportional to the zeroth-order spherical Bessel function $\psi_{\text{in}}(r) \propto j_0(kr) \to 1$ which asymptotes to a constant in the low-energy and short-range limit $kr \ll 1$. On the other hand, the outgoing wavefunction ψ_{out} is highly oscillatory due to the released kinetic energy. Therefore the matrix element that enters the Fermi's golden rule is proportional to the amplitude of incoming wavefunction evaluated at R^* upon integrating out ψ_{out}, i.e. $|\langle \psi_{\text{out}} | U_{\text{dd}} | \psi_{\text{in}} \rangle|^2 \propto |\psi_{\text{in}}(R^*)|^2 \sim \text{const}$.

In addition, two atoms after collision are scattered into a continuum of momentum states with an energy given by the released Zeeman energy $\mu_B g_J B$. This corresponds to a 3D density of states $\rho(\Delta E) \propto \sqrt{\Delta E} \propto \sqrt{B}$. Thus we conclude that the dipolar relaxation rate scales as $\sqrt{B}$ for bosonic Dy according to the Fermi's golden rule.

On the other hand, two fermionic atoms in the same initial spin state $m_J = +8$ only approach in the p-wave channel with $L = 1$ due to the anti-symmetrized total wavefunction. The incoming radial wavefunction in this case is given by the first-order spherical Bessel function which, due to the presence of the centrifugal barrier, has a node at $r = 0$. At short range, the incoming wavefunction linearly asymptotes to zero, i.e. $\psi_{\text{in}}(r) \propto j_0(kr) \to \frac{1}{3}kr$ as $kr \to 0$. Therefore the square of the matrix element in the fermionic case follows $|\langle \psi_{\text{out}} | U_{\text{dd}} | \psi_{\text{in}} \rangle|^2 \propto |\psi_{\text{in}}(R^*)|^2 \propto R^{*2} \propto 1/B$. Combined with the B-field dependence of density of states, we conclude that the

dipolar relaxation rate scales as $1/\sqrt{B}$ for fermions.

The scaling laws of dipolar relaxation rates with magnetic field obtained from the Fermi's golden rule are fully consistent with those obtained from the Born approximation [85]. Moreover, we see from the Fermi's golden rule analysis that by reducing the amplitude of the incoming wavefunction at short range, or in other words, by shielding the Condon point using a repulsive potential, any general inelastic processes which happen at short range should be suppressed.

Besides the p-wave centrifugal barrier for identical fermions, repulsive barriers have been achieved, for example, by addressing different rotational states of cold molecules using microwave photons [3], and by utilizing dipolar repulsion in tight quasi-2D confinements [80]. But most of these techniques are used for suppressing inelastic losses (or chemical reactions) in cold molecule experiments, which have clear short-range characteristics.

6.2 Dipolar Relaxation in a Quasi-2D Confinement

Motivated by the above analysis, we study below how dipolar relaxation of Dy atoms in the $m_J = +8$ spin state can be suppressed using dipolar repulsion in a tight-2D confinement. Different from typical polar molecule experiments where long-range repulsive forces are used to suppress short-range inelastic losses, here we attempt to suppress the inelastic part of the magnetic dipole-dipole interaction (3rd and 4th lines of Eq. 2.4) using its elastic part (1st line of Eq. 2.4). We observe that, despite the similar long-range behaviors of the elastic and the inelastic potentials, the dipolar relaxation rate can be suppressed by an order of magnitude under a tight axial confinement with a trap frequency of 200 kHz.

6.2.1 Introduction to Dipolar Shielding

The concept of dipolar shielding was developed by several theoretical papers [20, 104, 103]. Let's understand this concept by considering two dipolar particles confined in a harmonic oscillator with a trap frequency of ω_z along the z direction. The two-

particle wavefunction can be factorized into a center-of-mass part and a relative part by transforming into the following coordinates

$$
\begin{cases}
\mathbf{R} = \dfrac{1}{2}(\mathbf{r}_1 + \mathbf{r}_2) \\
\mathbf{r} = \mathbf{r}_1 - \mathbf{r}_2
\end{cases}
;
\qquad
\begin{cases}
\mathbf{P} = \mathbf{p}_1 + \mathbf{p}_2 \\
\mathbf{p} = \dfrac{1}{2}(\mathbf{p}_1 - \mathbf{p}_2)
\end{cases}
\tag{6.12}
$$

where $\mathbf{R}$ and $\mathbf{P}$ are the center-of-mass coordinate and momentum, and $\mathbf{r}$ and $\mathbf{p}$ are the relative position and momentum. By using this definition, the two-body Hamiltonian (neglecting the Zeeman energy and the inelastic parts of dipole-dipole interaction) can be re-written in terms of a center-of-mass part and a relative part

$$
H = \underbrace{\frac{1}{2}\left(\frac{\mathbf{P}^2}{2m} + 2m\omega_z^2 Z^2\right)}_{\text{center-of-mass part}} + \underbrace{2\left(\frac{\mathbf{p}^2}{2m} + \frac{1}{8}m\omega_z^2 z^2\right) + \frac{\mu_0}{4\pi}(\mu_B g_J J)^2 \frac{1 - 3\cos^2\theta}{r^3}}_{\text{relative part}}
\tag{6.13}
$$

with the corresponding Schrodinger equations written as

$$
\begin{cases}
\dfrac{1}{2}\left(\dfrac{\mathbf{P}^2}{2m} + 2m\omega_z^2 Z^2\right)\Psi(\mathbf{R}) = E\Psi(\mathbf{R}) \\[2mm]
\left[\dfrac{\mathbf{p}^2}{m} + \dfrac{1}{4}m\omega_z^2 z^2 + \dfrac{\mu_0}{4\pi}(\mu_B g_J J)^2 \dfrac{1 - 3\cos^2\theta}{r^3}\right]\psi(\mathbf{r}) = \epsilon\psi(\mathbf{r})
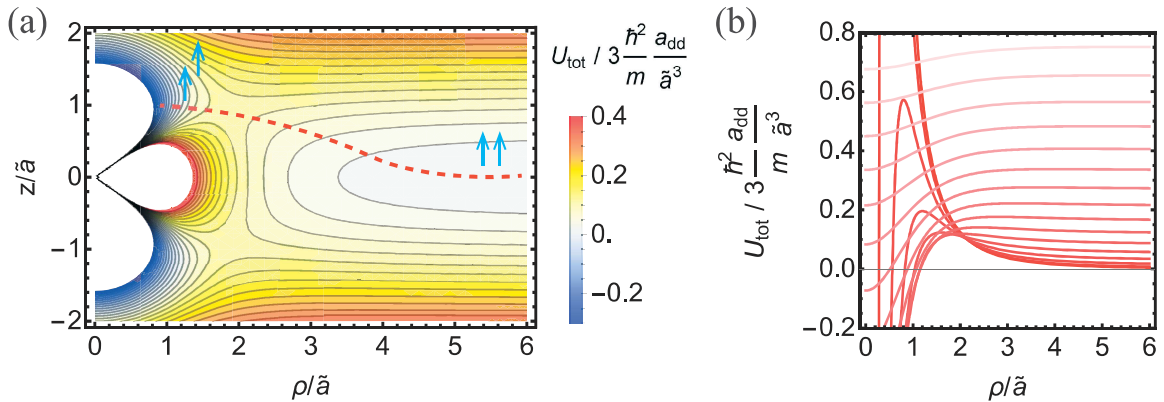\end{cases}
\tag{6.14}
$$

Figure 6-4: (a) Contour plot of the dipole-dipole potential with an axial harmonic confinement (Eq. 6.15). A saddle point exists at $\rho \approx 1.83\tilde{a}$ and $z \approx 0.92\tilde{a}$. As Dy atoms move across the saddle point from ($z = 0, \rho = \infty$), their dipolar interaction turn from repulsive to attractive. (b) 1D cuts of $U_{\text{tot}}(\rho, z)$ from $z = 0.0$ to $z = 3.0\tilde{a}$ (dark red to light red) with a step of $\Delta z = 0.2\tilde{a}$. The dipolar barrier vanishes as z increases.

Combining the harmonic confinement and the elastic dipole-dipole interaction, we define the total potential as the following

$$
\begin{aligned}
U_{\text{tot}}(\rho,z) &= \frac{\mu_0}{4\pi}(\mu_B g_J J)^2 \frac{1-3(\frac{z}{r})^2}{r^3} + \frac{1}{4}m\omega_z^2 z^2 \\
&= 3\frac{\hbar^2}{m}\frac{a_{\text{dd}}}{\tilde{a}^3}\left[\frac{\tilde{a}^3}{(\rho^2+z^2)^{3/2}} - 3\frac{z^2\tilde{a}^3}{(\rho^2+z^2)^{5/2}} + \frac{1}{12}\frac{z^2}{\tilde{a}^2}\right]
\end{aligned}
\tag{6.15}
$$

where $a_{\text{dd}} = \frac{m}{12\pi\hbar^2}\mu_0(\mu_B g_J J)^2$ and $\tilde{a} = \left(a_{\text{HO}}^4 a_{\text{dd}}\right)^{1/5}$ with the axial oscillator length $a_{\text{HO}} = \sqrt{\hbar/m\omega_z}$. The total potential with two saddle points locating at ($\rho \approx 1.83\tilde{a}, z \approx \pm 0.92\tilde{a}$) is plotted in Fig. 6-4 (also see Ref. [20]). As we see, a dipolar barrier exists when $|z| < 0.92\tilde{a}$ and vanishes when $|z| > 0.92\tilde{a}$. Hence, we expect that when the axial confinement is so tight that the oscillator length a_{HO} becomes comparable to the dipolar length a_{dd}, the incoming wavefunction needs to penetrate through a barrier before reaching the short range, leading to an exponential suppression of short-range inelastic processes. This is the basic concept of dipolar shielding.

For the case of 3D dipolar relaxation, the Condon point at which dipolar relaxation resonantly happens can be tuned to shorter range with increasing magnetic field. For the quasi-2D geometry, on the other hand, the concept of Condon point is more complicated with more vibrational channels and Zeeman channels coming into play. The full discussion on this matter is included in P. Barral's thesis [10]. In the following parts, we focus on introducing the experimental setups for implementing the suppression of dipolar relaxations in a quasi-2D confinement.

6.2.2 Experimental Protocol

The main experimental challenges for measuring dipolar relaxation rates come from the following two aspects: (1) achieving tight axial confinement without increasing atomic density too much to avoid strong three-body losses, and (2) adjusting the magnetic field to designated values quickly so that dipolar relaxation processes, which typically occur on millisecond timescales, can be measured under constant magnetic fields.

Blue-Detuned Optical Lattice

To create tight axial confinement while keeping the atomic density low, we use a blue-detuned circularly-polarized optical standing wave with a beam waist of approximately 50 μm addressing the 741 nm narrow-line transition of Dy. The blue-detuned standing wave produces axial confinements at the intensity minima with a trap frequency of ω_z. However, it also produces a transverse repulsive potential proportional to the gradient of the axial zero-point energy, i.e. $U_\perp(\rho) = -\hbar \nabla \omega_z$. To compensate for this repulsion, we add a coaxial high-power (up to 8 W) 1064 nm circularly-polarized laser beam with a beam waist of 64 μm for transverse confinement (see Fig. 6-5).
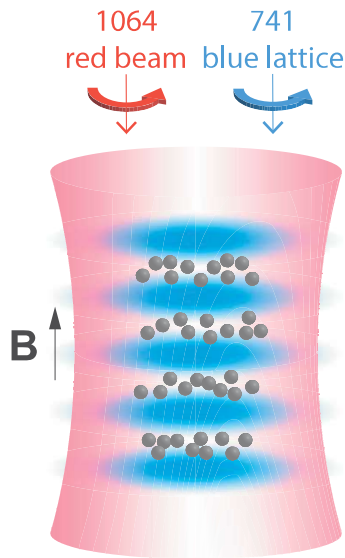

Figure 6-5: Illustration of the trap geometry. A blue-detuned 741 nm optical standing wave is used for producing tight axial confinement. A 1064 nm beam is used for transverse confinement.

We experimentally determine the required power for the 1064 nm compensation beam by imaging the atoms in situ using off-resonant 421 nm light and ensuring that the atomic clouds are not fragmented in the transverse direction. The resulting powers are typically much higher than the values estimated from the zero-point energy gradient. This can be attributed to the imperfect contrast of the optical standing wave when the powers of the intro- and the retro-beams are not balanced, and to aberrations of the intro- and the retro-beams.

Zeroing of Magnetic Field

To measure dipolar relaxation rates in an external magnetic field on a milligauss level, we need to zero the transverse magnetic field with high precision. This is accomplished using two calibration methods: (1) measuring absorption imaging signals with circularly-polarized imaging light, and (2) measuring Kapitza-Dirac signals by pulsing on a circularly-polarized optical lattice. Both methods are based on the same principle that the strength of the $m_J = -8 \rightarrow -9$ transition is 153 times larger than that of the $m_J = -8 \rightarrow -7$ transition due to the ratio of the corresponding Clebsch-Gordan coefficients. When the transverse magnetic field is perfectly zeroed, the absorption imaging signal or the Kapitza-Dirac diffraction signal should experience a drastic change when the axial magnetic field B_z is scanned through zero. By maximizing the steepness of the step functions (see Fig. 6-6), we achieve zero transverse magnetic field with an accuracy higher than 10 mG.
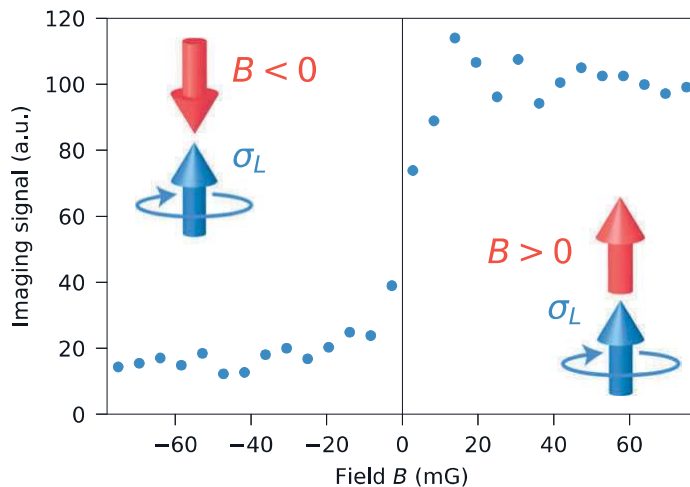

Figure 6-6: Transverse magnetic field is zeroed utilizing the high-contrast absorption imaging signals of the $m_J = -8 \rightarrow -9$ and the $m_J = -8 \rightarrow -7$ transitions. The absorption imaging beam is prepared with high-quality circular polarization. The transverse magnetic field is adjusted to produce a step-like change in the imaging signal when the axial magnetic field B_z is scanned through zero.

The calibrations based on the absorption imaging method and the Kapitza-Dirac diffraction method give a consistent magnetic zero point. We used the former method for the dipolar relaxation experiment and the latter for the bilayer experiment introduced in Chapter 5.

Fast Adjustment of Magnetic Field

The dipolar relaxation of the $m_J = +8$ state occurs on a millisecond timescale, with a typical atomic density of 10^{14} to 10^{15} cm^{-3}. To measure atom losses and temperature increases on this timescale under different magnetic field strengths, we need to adjust the magnetic field faster than the millisecond timescale immediately after preparing the atoms in the $m_J = +8$ spin state.

To address this issue, we generate a total magnetic field of 3.5 G along the z direction using two Helmholtz coil pairs, referred to as pairs A and B. Pair A produces the designated field, B_z, for measuring dipolar relaxation, while pair B provides the remaining field to ensure the total field is consistently 3.5 G at the beginning. We then transfer the atoms from the $m_J = -8$ state to the $m_J = +8$ state using a linear Landau-Zener sweep. The adiabaticity of the spin flip is verified by performing a reverse sweep and ensuring that the lifetime of the resulting atomic cloud is consistent with that of the original cloud in the $m_J = -8$ state. After the spin transfer, we open the solid-state relay controlling coil pair B. The current in coil pair B is then dissipated by the varistor connected in parallel within 50 μs. This procedure of adjusting magnetic field by switching off coils allows us to change the magnitude of the axial magnetic field much faster than the millisecond timescale.

6.2.3   Measurement of Dipolar Relaxation Rates

Loaded from a thermal cloud with a temperature of $T = 150$ nK and the root-mean-square axial extension of $\sigma_{\text{ODT}} \approx 4.7$ μm, we populate around $4\sqrt{\pi}\sigma_{\text{ODT}}/\lambda \approx 45$ copies of pancake-shaped gases with an initial transverse temperature of 1 μK. Following the above experimental procedures, we measure the evolution of total population and temperature of the quasi-2D gases in the $m_J = +8$ spin state under different values of axial trap frequencies and magnetic fields. We extract the dipolar relaxation rates β_{3D} from these measurements based on the local rate equation $\frac{\text{d}n_{\text{3D}}}{\text{d}t} = -\beta_{\text{3D}}n_{\text{3D}}^2$. The full analysis involves the calculation of averaged atomic densities according to the effective trap volume that takes into account inhomogeneous density distributions within each pancake and across different pancakes, which is described in P. Barral's

and M. Cantara's thesis [10, 22] and in Ref. [12]. Here we directly present the results in Fig. 6-7.
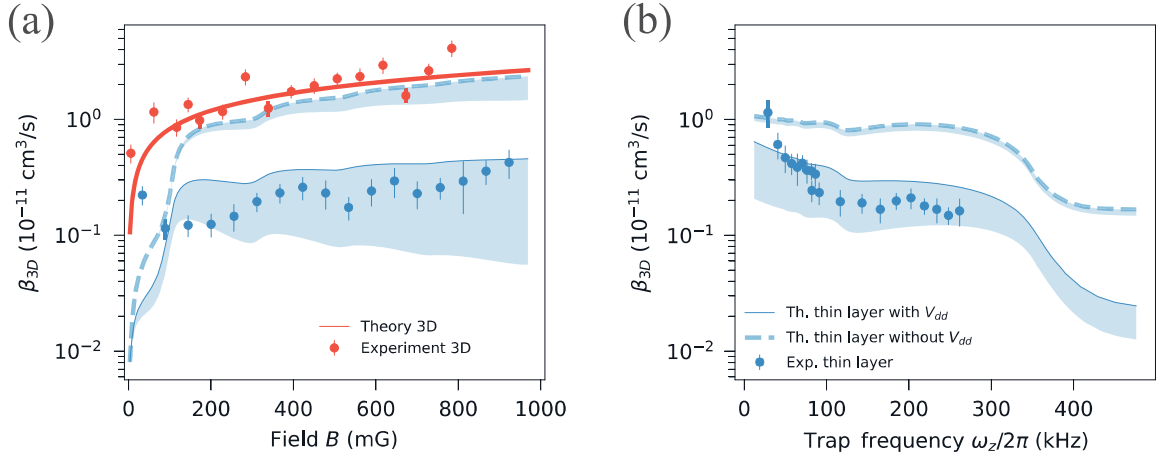

Figure 6-7: (a) Experimentally measured dipolar relaxation rates in 3D (red points) and in a quasi-2D confinement with an axial trap frequency of $\omega_z = 2\pi \times 185$ kHz (blue points). The red and blue solid curves are the corresponding theoretical curves; The dashed blue curve is a theory curve for non-shielded atoms in the same quasi-2D confinement [10] (same for (b)). (b) Measured dipolar relaxation rates in quasi-2D confinements with different axial trap frequencies in an external magnetic field of $B_z = 200$ mG.

We see from Fig.6-7(a) that, with an axial trap frequency of $\omega_z = 2\pi \times 185$kHz, the dipolar relaxation rates of quasi-2D gases are reduced to the 10^{-12}cm^3/s regime, which is an order magnitude slower than those of 3D gases confined in a XODT. Under such a tight quasi-2D confinement, more axial vibrational channels open up with increasing magnetic field, thereby shifting dipolar relaxation processes to larger distances and weakening the dipolar shielding effect.

Fig.6-7(b) shows the measured dipolar relaxation rates in an axial magnetic field of 200mG. As the axial trap frequency reaches 260 kHz, we observe an order of magnitude suppression in the dipolar relaxation rate coefficient β_{3D}. The extrapolation of the theoretical curve suggests that another order of magnitude suppression is achievable when the axial trap frequency exceeds 500 kHz. This would be comparable to the lowest dipolar relaxation rate obtained with fermions through Pauli suppression, as reported in Ref.[21]. The theoretical curves presented in Fig.6-7 contain no free parameters and agree well with the experimental results. The dashed curves repre-

sent the calculated dipolar relaxation rate with the dipolar barrier removed from the Hamiltonian (see Refs. [10] and [12] for details).

Chapter 7

The Future, At Present

This thesis explored several aspects of using ultracold Dy atoms as fundamental building blocks to assemble and study interesting quantum systems. The unique electronic structure of Dy gives rise to many distinctive atomic properties, such as a large angular momentum in the ground state, a large magnetic moment that leads to strong long-range dipole-dipole interactions, and optical transitions that differ from those of typical alkali atoms. We introduced the experimental apparatus for producing Bose-Einstein condensates of Dy atoms and for controlling their internal spin states. Based on this, we conducted two experiments with ultracold Dy atoms.

Utilizing the large ground-state angular momentum, we developed a dual-frequency and dual-polarization super-resolution optical potential capable of bringing two layers of Dy atoms in opposite spin states $m_J = \pm 8$ to a separation of 50 nm. Such close proximity significantly enhances the interlayer dipolar interaction strength by three orders of magnitude and allowed us to observe motional couplings between the two layers arising purely from the long-range effect.

By confining Dy atoms in tight quasi-2D geometries, we realized dipolar shielding in the ultracold regime and observed an order of magnitude suppression of inelastic dipolar relaxation processes in Dy atoms in the $m_J = +8$ spin state. This opens up possibilities for studying physics of spin mixtures that would otherwise be short-lived due to inelastic collisions.

While the story of this thesis concludes here, the exploration of intriguing physics

continues in the lab. On the technical front, with the new lab 'Dypole II' ramping up, alternative slowed-atom sources, such as a 2D MOT and a 3D moving molasses, can be implemented to deliver the cold flux of Dy. These techniques could make the new apparatus more compact compared to the old Zeeman slower design. Moreover, by integrating a glass cell and a high-N.A. objective into the apparatus, a quantum gas microscope with single-site imaging and potential projection capabilities can be implemented. Such technical advances and upgrades could elevate the quantum gas machine to a new level for experiments with dipolar gases of Dy.

On the scientific front, there is still much to understand about Dy atoms and their interactions with laser photons. As mentioned in Chapter 1, no discretized photoassociation features have yet been discovered in Dy Bose-Einstein condensates (BECs) or thermal gases, to the best of our knowledge. This topic can be more systematically investigated using well-prepared Mott insulators in optical lattices.

In addition, all experiments discussed in this thesis utilized the bosonic isotopes ^{162}Dy and ^{164}Dy. There are also intriguing topics to explore with the fermionic isotopes ^{161}Dy and ^{163}Dy, such as p-wave superfluidity [107], dipolar pairing [37], and more. Unlike bosons, for fermions, the Fermi energy E_F, which characterizes the kinetic energy due to Pauli exclusion, scales with $n^{2/3}$ where n is the density of the Fermi gas. But the strength of the dipolar interaction, inversely proportional to the cubic power of the interparticle spacing, scales with n. Therefore, one needs to reach a high-density regime for significant dipolar effects to occur in fermions. For single-component Fermi gases in 3D, this would require an inter-atomic distance $n^{-1/3}$ that is comparable to the dipolar length $a_{\mathrm{dd}} \approx 7$ nm, which is not feasible for Dy. However, this can be achieved either by confining two fermionic atoms at each site of an optical lattice, or by reducing the effective kinetic energy of atoms using flat energy band in an optical kagome lattice [67] or in a twist bilayer optical lattice [83].

Finally, the super-resolution technique introduced in this thesis can open up many research directions. By adding extra transverse optical potentials, it is possible to study 1D tubes or 2D lattices separated by 50 nm with strong proximity dipolar couplings. Applying this technique to optical tweezer arrays enables the im-

plementation of two-qubit quantum gates at kilohertz speeds driven by magnetic dipolar interactions. By moving one set of tweezers back and forth, a 1D chain of dipolar atoms with full connectivity can be implemented. Additionally, if degenerate gases of bosonic and fermionic isotopes can be co-trapped, subwavelength independent control using two lasers at tune-out wavelengths can be realized, allowing for the implementation of a head-to-tail dipole configuration in a bilayer. Many of these new research directions are described in Ref. [34] (also see Appendix C).

Appendix A

Calculation of magnetic field

The design of magnetic coils of the machine requires accurate calculations of magnetic fields based on the geometries of the coils. This appendix introduces the approach for modeling the spatial distribution of magnetic field given the winding pattern and the cross-sectional shape of the magnetic wires.
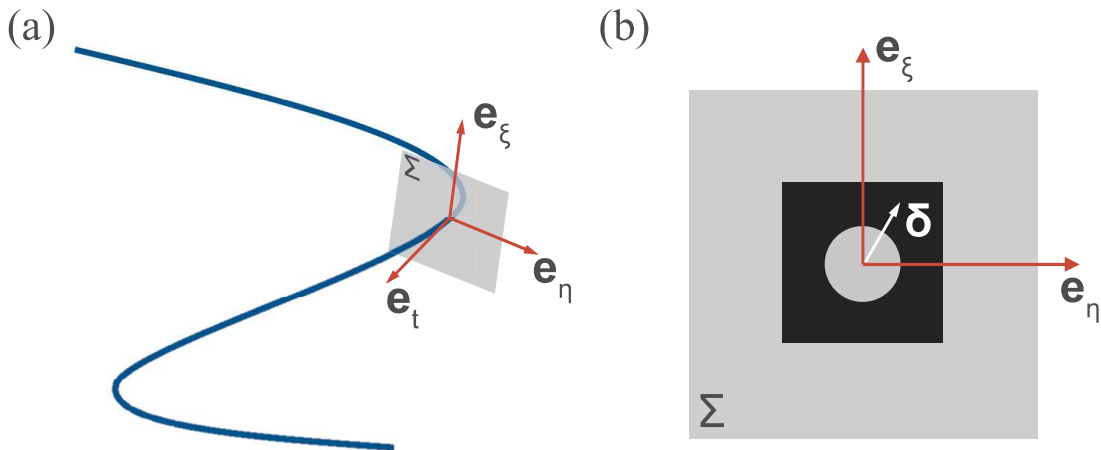

Figure A-1: (a) Local coordinate system where $\mathbf{e_t}$ is the unit vector along the tangential direction of the center line, $\mathbf{e}_\xi$ and $\mathbf{e}_\eta$ are orthogonal unit vectors perpendicular to $\mathbf{e_t}$. (b) The cross section of the wire is described by vector $\boldsymbol{\delta}$ in the 2D space spanned by $\mathbf{e}_\xi$ and $\mathbf{e}_\eta$.

We describe the current distribution $\mathbf{j}(\mathbf{r_0})$ inside the magnetic wire as a perturba-

tion $\boldsymbol{\delta}$ around its center line $\mathbf{r_c}$:

$$\mathbf{j}(\mathbf{r_0}) = \mathbf{j}(\mathbf{r_c} + \boldsymbol{\delta}) \tag{A.1}$$

where we define $\boldsymbol{\delta}(\xi, \eta) = \xi \mathbf{e}_\xi + \eta \mathbf{e}_\eta$ to be the local right-handed coordinate describing the cross section of the wire with $\mathbf{e}_\xi$ and $\mathbf{e}_\eta$ being the local Cartesian basis, and $\mathbf{r_0}(\theta) = x(\theta)\mathbf{e_x} + y(\theta)\mathbf{e_y} + z(\theta)\mathbf{e_z}$ to be the coordinate of the center line of the magnetic wire parameterized by θ (see Fig. A-1). The local tangential basis, analogous to the velocity vector moving along the magnetic wire, can be expressed in terms of the derivative of the local coordinate as

$$\mathbf{e_t} = \frac{\mathbf{r'_0}}{|\mathbf{r'_0}|} = \frac{1}{|\mathbf{r'_0}|}\left[\mathbf{r'_c}(\theta) + \xi \mathbf{e'}_\xi + \eta \mathbf{e'}_\eta\right] \tag{A.2}$$

Thus the current density can be written as $\mathbf{j}(\mathbf{r_0}) = j\mathbf{e_t}$. Under the local coordinate spanned by basis $\{\mathbf{e}_\xi, \mathbf{e}_\eta, \mathbf{e_t}\}$, a Jacobi determinant appears in volume integrals

$$dV_0 = dx_0 dy_0 dz_0 = \begin{vmatrix} (\mathbf{r'_0} \cdot \mathbf{e_x}) & (\mathbf{r'_0} \cdot \mathbf{e_y}) & (\mathbf{r'_0} \cdot \mathbf{e_z}) \\ (\mathbf{e}_\xi \cdot \mathbf{e_x}) & (\mathbf{e}_\xi \cdot \mathbf{e_y}) & (\mathbf{e}_\xi \cdot \mathbf{e_z}) \\ (\mathbf{e}_\eta \cdot \mathbf{e_x}) & (\mathbf{e}_\eta \cdot \mathbf{e_y}) & (\mathbf{e}_\eta \cdot \mathbf{e_z}) \end{vmatrix} d\theta d\xi d\eta = (\mathbf{r'_0} \cdot \mathbf{e_t}) d\theta d\xi d\eta \tag{A.3}$$

By using the Biot-Savart law, the vector potential in the Coulomb gauge due to the current inside magnetic wires can be derived as

$$\mathbf{A}(\mathbf{r}) = \frac{\mu_0}{4\pi} \int_{V_0} dV_0 \frac{\mathbf{j}(\mathbf{r_0})}{|\mathbf{r} - \mathbf{r_0}|} = \frac{\mu_0 j}{4\pi} \int d\theta d\xi d\eta \cdot (\cos\gamma \cdot \mathbf{r'_0}) \frac{1}{|\mathbf{r} - \mathbf{r_0}|} \tag{A.4}$$

where $\cos\gamma = (\mathbf{r'_0} \cdot \mathbf{r'_c})/|\mathbf{r'_0}||\mathbf{r'_c}|$ denote the angle between the local tangential vector and the tangential vector of the center line. To summarize, by parameterizing the shape of the center line and the cross section of the magnetic wire, one can calculate the spatial magnetic field distribution $\mathbf{B} = \nabla_{\mathbf{r}} \times \mathbf{A}$ based on Eq. A.4.

Under the approximation that $|\boldsymbol{\delta}| \ll |\mathbf{r_c}|$ and $|\mathbf{r}|$, we can do far-field expansion and factorize out the integral with respect to ξ and η in Eq. A.4. This is done by expanding

the propagator $1/|\mathbf{r}-\mathbf{r_0}|$ as

$$
\begin{aligned}
\frac{1}{|\mathbf{r}-\mathbf{r_0}|} &\approx \frac{1}{|\mathbf{r}-\mathbf{r_c}|} - (\boldsymbol{\delta}\cdot\nabla)\frac{1}{|\mathbf{r}-\mathbf{r_c}|} + \frac{1}{2}(\boldsymbol{\delta}\cdot\nabla)^2\frac{1}{|\mathbf{r}-\mathbf{r_c}|} + \ldots \\
&= \frac{1}{|\mathbf{r}-\mathbf{r_c}|} + \frac{\boldsymbol{\delta}\cdot(\mathbf{r}-\mathbf{r_c})}{|\mathbf{r}-\mathbf{r_c}|^3} + \frac{1}{2}(3\boldsymbol{\delta}\boldsymbol{\delta}-\boldsymbol{\delta}^2\mathbb{1}):\frac{(\mathbf{r}-\mathbf{r_c})(\mathbf{r}-\mathbf{r_c})}{|\mathbf{r}-\mathbf{r_c}|^5} + \ldots
\end{aligned}
\tag{A.5}
$$

where the column operator is defined for vectors as $\mathbf{ab}:\mathbf{cd} = (\mathbf{a}\cdot\mathbf{d})(\mathbf{b}\cdot\mathbf{c})$. By also noticing the expansion of $\cos\gamma$ in Eq. A.4, we can organize the terms of the vector potential $\mathbf{A}(\mathbf{r})$ according to different orders in $\boldsymbol{\delta}$ as

$$
\begin{cases}
\mathbf{A}^{(0)}(\mathbf{r}) = \dfrac{\mu_0 j}{4\pi}\displaystyle\int_{(\xi,\eta)}\mathrm{d}\xi\mathrm{d}\eta\int_\theta\frac{\mathbf{r'_c}}{|\mathbf{r}-\mathbf{r_c}|}\mathrm{d}\theta \\[12pt]
\mathbf{A}^{(1)}(\mathbf{r}) = \dfrac{\mu_0 j}{4\pi}\displaystyle\int_{(\xi,\eta)}\boldsymbol{\delta}'\mathrm{d}\xi\mathrm{d}\eta\int_\theta\frac{1}{|\mathbf{r}-\mathbf{r_c}|}\mathrm{d}\theta + \dfrac{\mu_0 j}{4\pi}\int_{(\xi,\eta)}\boldsymbol{\delta}\cdot\mathrm{d}\xi\mathrm{d}\eta\int_\theta\frac{(\mathbf{r}-\mathbf{r_c})}{|\mathbf{r}-\mathbf{r_c}|}\mathbf{r'_c}\mathrm{d}\theta \\[12pt]
\mathbf{A}^{(2)}(\mathbf{r}) = \dfrac{\mu_0 j}{4\pi}\displaystyle\int_{(\xi,\eta)}\frac{1}{2}(\boldsymbol{\delta}'\boldsymbol{\delta}'-\boldsymbol{\delta}'^2\mathbb{1})\mathrm{d}\xi\mathrm{d}\eta:\int_\theta\frac{\mathbf{r'_c}\mathbf{r'_c}}{\mathbf{r'^4_c}}\frac{\mathbf{r'_c}}{|\mathbf{r}-\mathbf{r_c}|}\mathrm{d}\theta + \dfrac{\mu_0 j}{4\pi}\int_{(\xi,\eta)}\boldsymbol{\delta}'\boldsymbol{\delta}\cdot\mathrm{d}\xi\mathrm{d}\eta\int_\theta\frac{\mathbf{r}-\mathbf{r_c}}{|\mathbf{r}-\mathbf{r_c}|^3}\mathrm{d}\theta \\[12pt]
\qquad + \dfrac{\mu_0 j}{4\pi}\displaystyle\int_{(\xi,\eta)}\frac{1}{2}(3\boldsymbol{\delta}\boldsymbol{\delta}-\boldsymbol{\delta}^2\mathbb{1})\mathrm{d}\xi\mathrm{d}\eta:\int_\theta\left((\mathbf{r}-\mathbf{r_c})(\mathbf{r}-\mathbf{r_c})\right)\frac{\mathbf{r'_c}}{|\mathbf{r}-\mathbf{r_c}|^5}\mathrm{d}\theta
\end{cases}
\tag{A.6}
$$

where $\mathbf{A}^{(1)}(\mathbf{r})$ is related to the first moment of the cross section, and $\mathbf{A}^{(2)}(\mathbf{r})$ is related to the second moments of the cross section. For the commonly-used magnetic wires with square or round cross sections, the first moments are zero hence $\mathbf{A}^{(1)}(\mathbf{r})$ vanishes. The lowest-correction term in addition to the vector potential $\mathbf{A}^{(0)}(\mathbf{r})$ caused by zero-thickness magnetic wires is then $\mathbf{A}^{(2)}(\mathbf{r})$. By modeling the magnetic wires in terms of the parametric equations for $\{\mathbf{r_c}(\theta), \mathbf{e}_\xi(\theta), \mathbf{e}_\eta(\theta)\}$ and evaluating the matrix elements in Eq. A.6, the vector potential induced by the magnetic wire can be calculated.

Attached to the end of this appendix is the code for evaluating $\mathbf{A}^{(0)}(\mathbf{r})$ and $\mathbf{A}^{(2)}(\mathbf{r})$ written in Mathematica. As an example, we calculate the magnetic field from a solenoid wound using a square wire with an edge length of the cross section $a = 0.5$ cm. The solenoid has a diameter of 6 cm, and a length of 50 cm. The zeroth order term and the second order correction to the magnetic field distribution of the solenoid is plotted in Fig. A-2. The zeroth order term is consistent with the result obtained simply from the Ampere's law $B/I = \mu_0/a = 2.51$ G/A. Since the second-order

127

correction is 4 orders of magnitudes smaller than the zeroth-order term, we neglect this correction for all the coil-design applications.
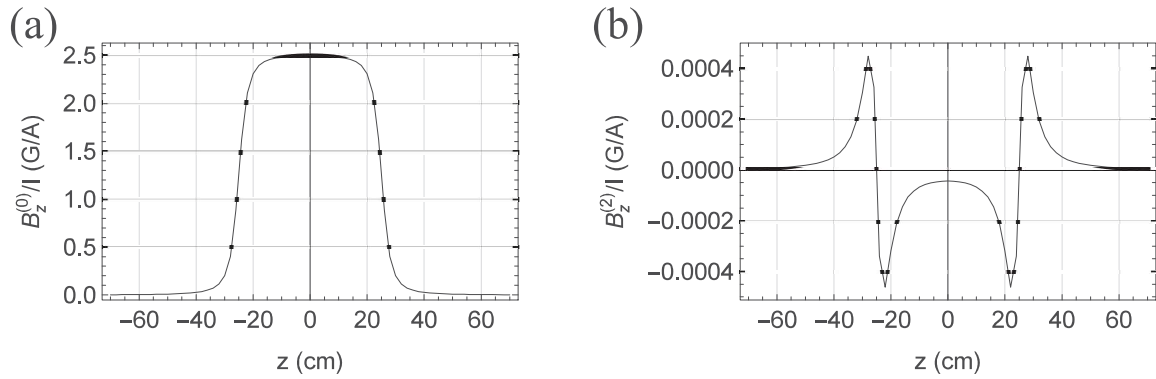
(a)

(b)

Figure A-2: (a) The axial zeroth-order magnetic field $B_z^{(0)}(z)$ from a solenoid made by a tightly-wound square wire with edge length of 6 cm. The length of the solenoid is 50 cm. (b) The second-order correction to the magnetic field $B_z^{(2)}(z)$ from the same solenoid, taking the finite cross-section of the wire into consideration.

Magnetic Field Calculation

Zeroth-order Magnetic Field (BField0 Module)

The *BField0* module is for calculating the magnetic field caused by an electric wire to the zeroth order. The shape of the center line of the wire is describe by the parametric equation $\{x_c(\theta), y_c(\theta), z_c(\theta)\}$.

Format:
Magnetic Field at location (x,y,z) = BField0 $[x, y, z, \theta_{min}, \theta_{max}, x_c, y_c, z_c]$;

```
BField0[x00_, y00_, z00_, θmin0_, θmax0_, xc0_, yc0_, zc0_] := Module[
   {xfield = x00, yfield = y00, zfield = z00, θmin = θmin0,
    θmax = θmax0, xc = xc0, yc = yc0, zc = zc0, I0, rc, dB, B, x, y, z, μ0, θ0},
   I0 = 1; (*A*)
   μ0 = 4 * Pi * 10^(-7); (*H/m*)
   rc[θ0_] := {xc[θ0], yc[θ0], zc[θ0]};
   (* B-field calculation *)
   100 * 10 000 * μ0 * I0 / (4 * Pi) *
    NIntegrate[Cross[D[rc[θ0], θ0], ({xfield, yfield, zfield} - rc[θ0])] /
      Norm[rc[θ0] - {xfield, yfield, zfield}]^3, {θ0, θmin, θmax}]
 ]
```

Second-order Magnetic Field (BField2 Module)

The *BField2* module for calculating the second-order residue of the magnetic field. The shape of the center line of the wire is describe by the parametric equation $\{x_c(\theta), y_c(\theta), z_c(\theta)\}$. The two orthonormal basis $\{e_\xi, e_\eta\}$ are also parameterized by θ, illustrating how the wire is twisted. To specify the size effect of the cross-section, the second-moment integral defined as $\frac{1}{2}\int(\xi^2+\eta^2)d\xi d\eta / \int d\xi d\eta$ also needs to be specified.

Format:
Second-order residue at location (x,y,z) = BField2 $[x, y, z, \theta_{min}, \theta_{max}, \text{Integral}, x_c, y_c, z_c, e_\xi, e_\eta]$;

```
BFieldℤ[x00_, y00_, z00_, θmin0_,
   θmax0_, itg0_, xc0_, yc0_, zc0_, eξ0_, eη0_] := Module[
   {xfield = x00, yfield = y00, θmin = θmin0, θmax = θmax0, zfield = z00,
    itg = itg0, xc = xc0, yc = yc0, zc = zc0, eξ = eξ0, eη = eη0, I0, rc,
    δ, δδ, δδI, δδppI, δδpp, δδp, m1, m2, m3, dB, B, x, y, z, μ0, θ0},
   I0 = 1; (*A*)
   μ0 = 4 * Pi * 10 ^ (-7); (*H/m*)
   rc[θ0_] := {xc[θ0], yc[θ0], zc[θ0]};
   δ[ξ_, η_, θ0_] := ξ * eξ[θ0] + η * eη[θ0];
   (* matrix elements *)
   δδ[θ0_] :=
    itg * Table[eξ[θ0]〚i〛 * eξ[θ0]〚j〛 + eη[θ0]〚i〛 * eη[θ0]〚j〛, {i, 1, 3}, {j, 1, 3}];
   δδI[θ0_] := itg * Norm[eξ[θ0] + eη[θ0]] ^ 2 * {{1, 0, 0}, {0, 1, 0}, {0, 0, 1}};
   δδppI[θ0_] := itg * Norm[eξ'[θ0] + eη'[θ0]] ^ 2 * {{1, 0, 0}, {0, 1, 0}, {0, 0, 1}};
   δδpp[θ0_] := itg *
     Table[eξ'[θ0]〚i〛 * eξ'[θ0]〚j〛 + eη'[θ0]〚i〛 * eη'[θ0]〚j〛, {i, 1, 3}, {j, 1, 3}];
   δδp[θ0_] :=
    itg * Table[eξ'[θ0]〚i〛 * eξ[θ0]〚j〛 + eη'[θ0]〚i〛 * eη[θ0]〚j〛, {i, 1, 3}, {j, 1, 3}];

   m1[θ0_, x_, y_, z_] := Sum[(δδppI[θ0] - δδpp[θ0])〚i, j〛 * rc'[θ0]〚j〛 * rc'[θ0]〚i〛,
      {i, 1, 3}, {j, 1, 3}] / Norm[rc'[θ0]] ^ 4;
   m2[θ0_, x_, y_, z_] :=
    Sum[Transpose[δδp[θ0]]〚i〛 * ({x, y, z} - rc[θ0])〚i〛, {i, 1, 3}];
   (*problem maybe exists here!*)
   m3[θ0_, x_, y_, z_] :=
    Sum[(3 * δδ[θ0] - δδI[θ0])〚i, j〛 * ({x, y, z} - rc[θ0])〚j〛 * ({x, y, z} - rc[θ0])〚i〛,
      {i, 1, 3}, {j, 1, 3}] / Norm[{x, y, z} - rc[θ0]] ^ 5;
   (* B-field calculation *)
   dB[θ0_, x0_, y0_, z0_] := ComplexExpand[
      Curl[100 (*cm → m*) * 10 000 (*Tesla → Gauss*) * μ0 * I0 / (4 * Pi) * (
         -1 / 2 * m1[θ0, x, y, z] * rc'[θ0] / Norm[{x, y, z} - rc[θ0]]
          + m2[θ0, x, y, z] / Norm[{x, y, z} - rc[θ0]] ^ 3
          + 1 / 2 * m3[θ0, x, y, z] * rc'[θ0]
         )
       , {x, y, z}]] /. {x → x0, y → y0, z → z0};
   Re[
    NIntegrate[(dB[θ0, xfield, yfield, zfield]), {θ0, θmin, θmax}]
   ]
  ]
```

Example

Here we present an example to evaluate the zeroth order and the second-order residue of the magnetic field induced by a spiral wire.

```
Off[NIntegrate::ncvb];
Off[NIntegrate::slwcon];
d = 6; (*cm*)
a = 0.5; (*cm*)
L = 50; (*cm*)
ϕ = 0.2; (*cm*)
(* 2nd moment *)
itg = 2 * a^2 / 3 / 8;
(* center line *)
xc[θ0_] := (d / 2 + a / 2) * Cos[θ0];
yc[θ0_] := (d / 2 + a / 2) * Sin[θ0];
zc[θ0_] := a / (2 * Pi) * θ0;
(* local basis *)
eξ[θ0_] := {Cos[θ0], Sin[θ0], 0};
eη[θ0_] := 1 / (Sqrt[(d / 2 + a / 2)^2 + (a / (2 * Pi))^2]) *
    {-(a / (2 * Pi)) * Sin[θ0], (a / (2 * Pi)) * Cos[θ0], -(d / 2 + a / 2)};

Dynamic[z]
BAxial =
  Table[BField0[0, 0, z, -Pi * L / a, Pi * L / a, xc, yc, zc][[3]], {z, -70, 70, 2}];
BAxialRes = Table[BField2[0, 0, z, -Pi * L / a, Pi * L / a, itg, xc, yc, zc, eξ, eη][[3]],
    {z, -70, 70, 2}];
ListPlot[BAxial, Joined → True, PlotRange → All, PlotStyle → {Blue, Thick},
  Frame → True, FrameLabel → {"z (cm)", "Bz/I (G/A)"},
  FrameStyle → Directive[Black, 12], ImageSize → 200]
ListPlot[BAxialRes, Joined → True, PlotRange → All,
  PlotStyle → {Blue, Thick}, Frame → True, FrameLabel → {"z (cm)", "Bz/I (G/A)"},
  FrameStyle → Directive[Black, 12], ImageSize → 200]
```

z

Appendix B

Enhancing the Capture Velocity of a Dy Magneto-Optical Trap with Two-Stage Slowing

This appendix contains a reprint of Ref. [76]: William Lunden, Li Du, Michael Cantara, Pierre Barral, Alan O. Jamison, and Wolfgang Ketterle, *Enhancing the capture velocity of a Dy magneto-optical trap with two-stage slowing* Physical Review A, 101(6), 063403.

Enhancing the capture velocity of a Dy magneto-optical trap with two-stage slowing

William Lunden [ID], Li Du [ID], Michael Cantara, Pierre Barral, Alan O. Jamison, and Wolfgang Ketterle

Research Laboratory of Electronics, MIT-Harvard Center for Ultracold Atoms, Department of Physics,
Massachusetts Institute of Technology, Cambridge, Massachusetts 02139, USA

Magneto-optical traps (MOTs) based on the 626-nm, 136-kHz-wide intercombination line of Dy, which has an attractively low Doppler temperature of 3.3 μK, have been implemented in a growing number of experiments over the last several years. A challenge in loading these MOTs comes from their low capture velocities. Slowed atomic beams can spread out significantly during free flight from the Zeeman slower to the MOT position, reducing the fraction of the beam captured by the MOT. Here we apply a scheme for enhancing the loading rate of the MOT wherein atoms are Zeeman slowed to a final velocity larger than the MOT's capture velocity and then undergo a final stage of slowing by a pair of near-detuned beams addressing the 421-nm transition directly in front of the MOT. By reducing the free-flight time of the Zeeman-slowed atomic beam, we greatly enhance the slowed flux delivered to the MOT, leading to more than an order-of-magnitude enhancement in the final MOT population.

I. INTRODUCTION

Dysprosium, which possesses the largest magnetic moment ($\mu \approx 10\mu_B$) of any atomic species, has grown in popularity in the ultracold quantum gas community over the last decade [1–11]. The large magnetic moment, as well as several other useful properties, arises from its [Xe] $4f^{10}6s^2$ electronic configuration. The two $6s$ electrons give rise to a heliumlike excitation spectrum, including a strong transition at 421 nm and a weak, intercombination transition at 626 nm. The unfilled $4f$ shell gives rise to narrow clocklike transitions. It also leads to spin-orbit coupling in the ground state, which is useful for many quantum simulations, including simulating gauge fields [11,12].

The narrow linewidth of the 626-nm transition in Dy corresponds to a low Doppler temperature of 3.3 μK, making it an attractive option for magneto-optical trapping (MOT). The downside of using a narrow transition is that the capture velocity of the MOT is lower than for a broader transition. Slowing an atomic beam to within a low capture velocity can lead to a situation where the slowed beam transversely spreads out so much that many slowed atoms miss the MOT. Cooling the transverse degrees of freedom of the atomic beam and increasing the capture velocity of the MOT by frequency dithering the MOT light are two measures which are typically employed to mitigate this limitation [2–6,13], but their effectiveness can be limited.

In the present work, we add an approach which we refer to as "angled slowing," which applies a second stage of slowing to the atomic beam with a pair of low-power beams that intersect directly in front of the MOT. This allows us to choose a sufficiently large final velocity for the first stage of slowing (i.e., Zeeman slowing) where atoms do not spread out appreciably before reaching the MOT. This approach was introduced in a Yb experiment, where it gave a small

enhancement to the MOT loading rate [14]. The Yb experiment has recently explored the approach in more detail [15]. In our experiment, angled slowing enhances the MOT population by more than a factor of 20. Compared to other methods which have been employed to increase the capture velocity of narrow-line MOTs—such as the two-stage MOT [1] and the core-shell MOT [16]—the angled slowing approach requires fewer beams and less laser power.

In Sec. II we briefly describe the aspects of our experiment that are similar to those previously reported by other experiments. In Sec. III, the idea behind angled slowing and how it is particularly applicable to experiments with narrow-line MOTs is discussed. In Sec. IV, we describe how we optimized the performance of angled slowing with respect to beam pointing, laser power, and frequency. In Sec. V, the compression and detection sequence that follows the loading of our MOT is described, and the temperature and phase-space density of the compressed MOT are reported.

II. EXPERIMENTAL SETUP

Due to the recent explosion in popularity of dysprosium, several groups have developed similar cooling and trapping protocols in parallel [2–6,13]. Here we briefly describe our approach and give references to more detailed explanations of similar systems.

Our atomic beam of Dy is generated by a commercial molecular beam epitaxy oven [17] heated to 1250 °C. The dysprosium vapor is collimated into an atomic beam by a 7-nm-diameter nozzle, which is 90 mm from the opening of the oven, followed by a 10-cm-long, 7-mm-diameter differential pumping tube that starts 19 cm from the nozzle.

We use 421-nm laser light for Zeeman slowing, transverse cooling, and absorption imaging. This light is gener-
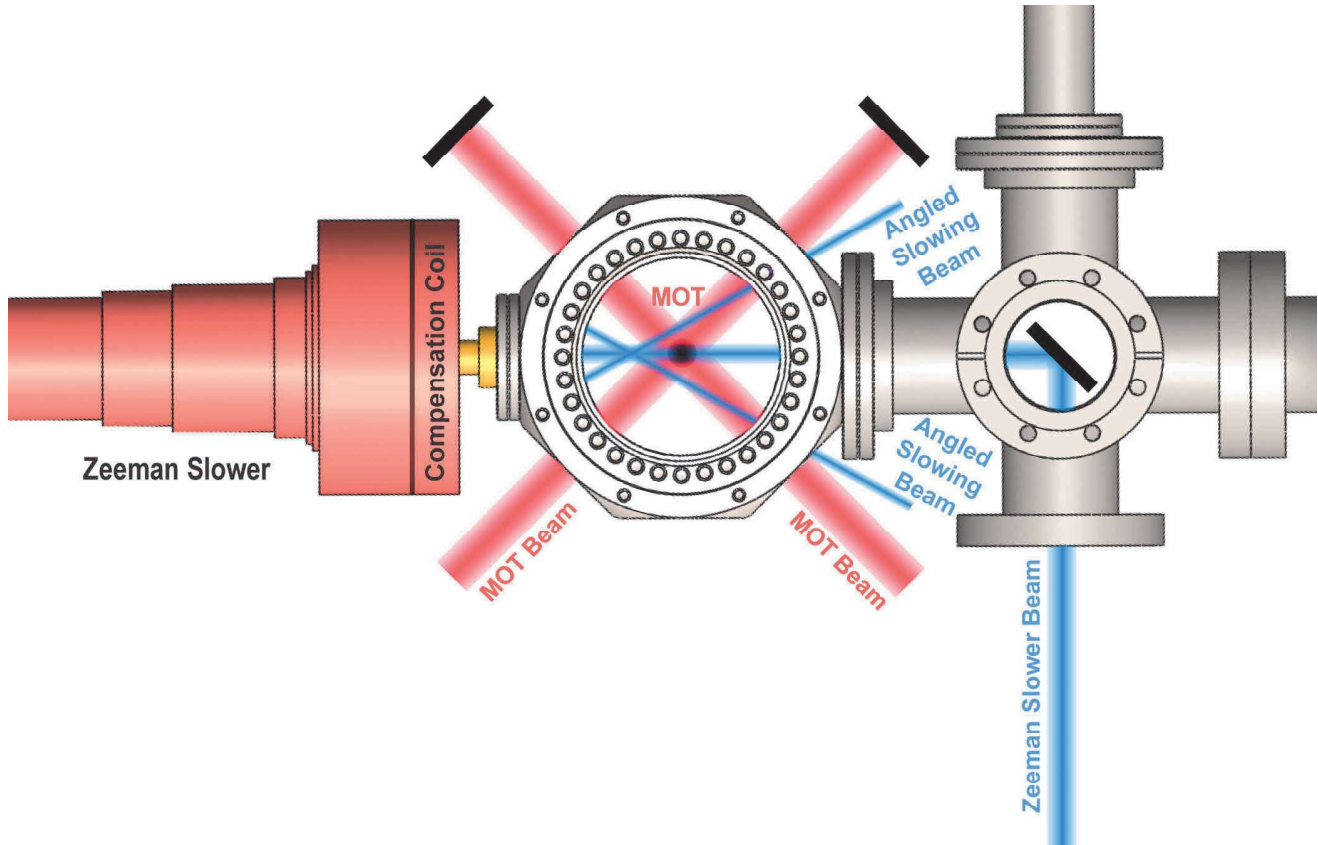
FIG. 1. Geometry of our Zeeman slowing, MOT, and angled slowing beams. The vertical MOT beam pair is not shown in this top view of the machine. The angled slowing beams enter through the same viewports as the MOT beams and are aligned such that they intersect the atomic beam without hitting the MOT (indicated by the dark circle in the center of the chamber).

ated using an M-squared Ti:sapphire laser and an ECD-X fixed-frequency second-harmonic generation cavity (1.6 W total output), as well as two injection-locked laser diodes (90 mW total output each). The frequency of the Ti:sapphire laser is stabilized by measuring the frequency of the doubled light with a HighFinesse WLM-7 wavemeter, and feeding back on a piezo-actuated mirror in the laser cavity using an Arduino Due. The wavemeter lock drifts by a few megahertz (verified at multiple wavelengths with lasers locked to atomic references) over the course of a few days if the wavemeter is not physically moved or perturbed. We periodically adjust for drifts in the calibration of the wavemeter (which are typically a few megahertz per day) by checking the resonance frequency of the 421-nm transition via absorption imaging. A Toptica TA-SHG system (700 mW total output) generates the 626-nm light for the MOT. For frequency stabilization of this laser, we shift the light by about +1 GHz and employ a modulation transfer spectroscopy scheme to lock the laser frequency to a transition in a room-temperature iodine cell. We stabilize our laser frequency to at least the few-hundred-kHz level with this setup.

In the present work we slow the bosonic isotope ^{162}Dy, which has 25.5% natural abundance [18]. Our Zeeman slow-ing light consists of 300 mW of light addressing the 421-nm transition ($\Gamma_{421} = 32.2$ MHz), which comes to a focus at the position of the oven. Light enters the vacuum chamber

with a beam diameter of about 2 cm, bouncing off of a 45-degree in-vacuum mirror as shown in Fig. 1. This scheme was implemented so the entrance window for the slowing light does not get coated by the Dy atomic beam.

To minimize the effect of the Zeeman slower light on atoms trapped in our MOT, we use an increasing-field Zeeman slower design. This allows us to employ a larger detuning in our slowing beam, which reduces the losses due to scattering in the MOT. A counterwound segment of coils at the end of the slower cancels the fringing magnetic field from the slowing coils at the position of the MOT. We use light de-tuned about 1.1 GHz from the zero-velocity transition, which resonantly addresses atoms moving at 480 m/s (close to the most probable velocity of the atoms emitted from the oven). We have an additional, uniformly wound bias coil running the length of the Zeeman slower, which creates a constant offset magnetic field inside the slowing region. This allows adjustment of the effective detuning of the Zeeman slower beam by up to several hundred megahertz without needing to employ an acousto-optic modulator (AOM).

Our MOT is formed by three retroreflected 626-nm beams. Each beam has a $1/e^2$ diameter of 2.3 cm and a total power of 42 mW ($\pm 5\%$), corresponding to a (peak) saturation pa-rameter of $s \approx 280$. The quadrupole field's gradient along the strong direction is approximately 2.5 G/cm. To improve the capture velocity of the MOT, we dither the frequency

of the MOT light using a double-passed AOM. The dithering occurs at a frequency of 120 kHz and broadens the laser linewidth to 2.6 MHz ($30\Gamma_{626}$). Three pairs of rectangular coils in Helmholtz configuration allow us to cancel background magnetic fields and will also allow us to employ feedback- and feedforward-based magnetic field stabilization schemes during future experiments.

III. ANGLED SLOWING

Atoms that have been slowed by a Zeeman slower must travel some nonzero distance at their final, slowed velocity from the end of the Zeeman slower to the position of the MOT. During this period of free flight, the transverse velocity distribution of the beam causes the atomic beam to spread out. If the free-flight time is sufficiently long, then the atoms can spread out far enough that they are not captured by the MOT.

While this is not typically a limiting factor in experiments, the combination of an increasing-field slower and the narrow linewidth of the MOT transition creates a situation in which the transverse spread plays a significant role. To clarify this point, we compare Dy to the more common alkali MOTs.

The capture velocity of a MOT can be estimated by calculating the largest velocity that can possibly be slowed to a stop within the profile of the MOT beams. Assuming that the atoms scatter photons at the maximum possible rate $\frac{\Gamma}{2}$ across an entire beam diameter D, an expression for the capture velocity is given by

$$v_{\text{cap}} = \sqrt{2\frac{\hbar k \Gamma}{2m}D}, \qquad (1)$$

where m is the atomic mass and $k = \frac{2\pi}{\lambda}$ is the wave number of the MOT light.

The spatial spread σ of the atomic beam can be estimated as

$$\sigma \approx 2d\frac{v_{\text{trans}}}{v_{\text{long}}}, \qquad (2)$$

where d is the free-flight distance, v_{trans} is the rms transverse speed, and v_{long} is the average longitudinal speed. Collimation of the atomic beam by one or more apertures typically leads to a transverse velocity distribution with an rms speed around 1% of the average (unslowed) longitudinal velocity [19].

Let us compare the case of a ^{87}Rb MOT to a ^{162}Dy MOT, taking typical values of $D = 2$ cm for the MOT beam diameters. For Rb, $\lambda = 780$ nm, $m = 87$ amu, and $\Gamma = 2\pi \times 6$ MHz. This corresponds to a capture velocity of 67 m/s, although due to the large Doppler shift at this velocity, a more realistic [20] capture velocity is about 43 m/s [21]. A typical initial most-probable velocity for atoms effusing from a Rb oven is about 330 m/s, and so 3.3 m/s is a reasonable estimate of the rms transverse speed of the atoms. If we consider an atomic beam slowed to the capture velocity value and an example free-flight distance of 10 cm we can estimate the spread of the atomic beam to be

$$\sigma_{\text{Rb}} \approx 1.5 \text{ cm}, \qquad (3)$$

which is smaller than or comparable to the size of the MOT beams.

For a Dy MOT, $\lambda = 626$ nm, $m = 162$ amu, and $\Gamma_{626} = 2\pi \times 136$ kHz. This gives a capture velocity of (no more than) 8 m/s. The most probable velocity of the Dy atoms effusing from our oven is about 480 m/s, so 4.8 m/s is a reasonable estimate of the average transverse speed. For a free-flight distance of 10 cm, we estimate the spread of the atomic beam to be

$$\sigma_{\text{Dy}} \approx 12 \text{ cm}, \qquad (4)$$

which is much larger than the size of the MOT beams. We thus see that the narrow linewidth of the 626-nm transition already leads to a significantly larger spreading of the atomic beam than in a typical alkali MOT.

Employing an increasing-field slower, while effective in reducing scattering losses in the MOT due to the larger Zeeman slower laser detuning, further exacerbates the transverse spreading problem. One reason is that the larger detuning reduces the amount of off-resonant slowing that occurs during the free-flight distance. The more off-resonant slowing that occurs during the free flight, the larger the initial exit velocity from the Zeeman slowing region can be. We can estimate the typical effect of off-resonant slowing in a Dy experiment: a typical Zeeman slower beam detuning in a spin-flip slower is around $-18\Gamma_{421}$, with (resonant) saturation parameters of $s_0 \approx 1$ [2]. If we assume that the slowed atoms scatter at a (detuned) saturation parameter of $s = \frac{s_0}{1+4\Delta^2/\Gamma^2} \approx 7.7 \times 10^{-4}$ over a 10-cm free-flight distance, then we can estimate that atoms with exit velocities as high as 13 m/s will be decelerated to within the capture velocity of the MOT.

A second reason is the increased free-flight distance due to the need for field-canceling coils near the MOT. In an increasing-field Zeeman slower, the largest numbers of windings are closest to the MOT. As a result, it is necessary to compensate for the large fringing fields with an oppositely wound compensation coil so that the total residual magnetic field and field curvature at the position of the MOT is close to zero. Slowed atoms must thus travel an extra distance of several centimeters compared to the travel distance in spin-flip Zeeman slowers. In our experiment, the free-flight distance is 16 cm.

The purpose of the angled slowing scheme is to reduce the free-flight time by allowing atoms to exit the Zeeman slower at velocities well above the MOT's capture velocity. A few centimeters before the MOT, two beams with red detuning on the order of Γ_{421} intersect the atomic beam to provide a net longitudinal slowing force, slowing the atomic beam to within the capture velocity of the MOT. The transverse components of the two beams' scattering forces are oppositely oriented and thus cancel. In effect, the addition of the angled slowing beams increases the capture velocity of the MOT.

The advantage of using a pair of angled beams over a single beam colinear with the main Zeeman slower light, or adding a near-resonant sideband to the Zeeman slower, is that scattering losses in the MOT are avoided. Angled slowing also requires fewer beams and less laser power than the recently reported core-shell MOTs for alkaline-earth-like atoms [16]. The setup for the angled slowing beams is depicted in Fig. 1.

Without employing angled slowing, optimization of our Zeeman slowing parameters led to a steady-state MOT
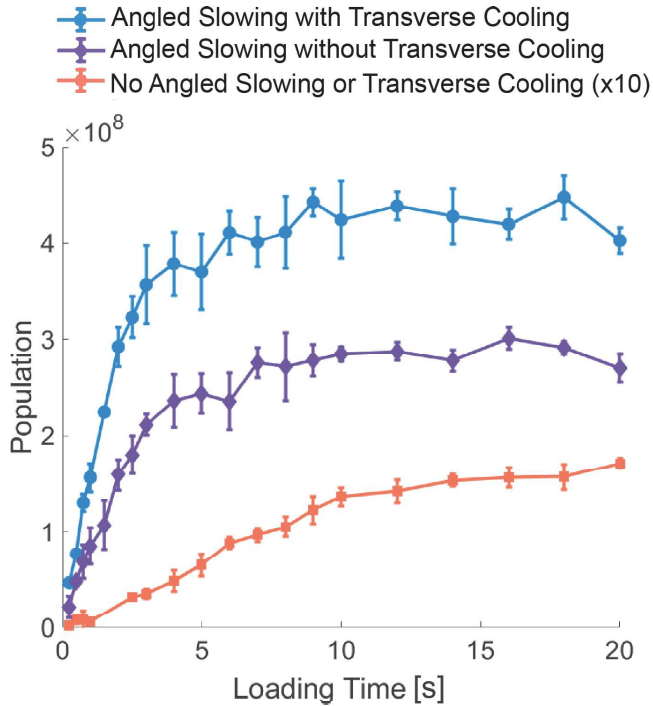
FIG. 2. Population of the MOT as a function of loading time. The blue curve (circles) shows the population when both transverse cooling and angled slowing with the optimal parameters of $\delta = -50$ MHz and 7 mW per beam are employed. The purple curve (diamonds) shows the population when angled slowing with the same optimal parameters is employed but the transverse cooling beams are turned off. The orange curve (squares) shows the population when both the transverse cooling and angled slowing beams are turned off, multiplied by a factor of ten for visual clarity.
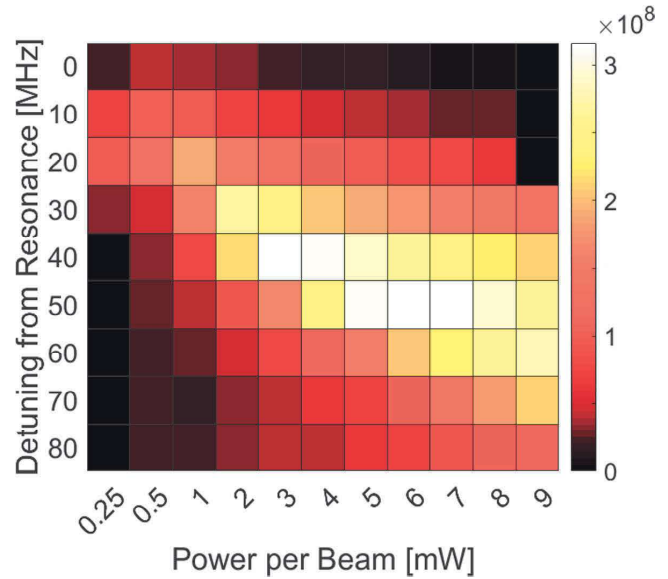

FIG. 3. Optimizing angled slowing. Dependence of the MOT population on the detuning and power of the angled slowing beams. A fixed loading time and compression sequence were employed for all of the data shown. The powers in the two beams were balanced to within 15%. The detuning from the 421-nm resonance was known to within ± 2 MHz.

population of about 10^7 atoms. We observe more than a factor of 20 gain in the final population of our MOT when using angled slowing. As described in the next section, we found optimal angled slowing performance with only 7 mW per beam and a detuning of -50 MHz ($-1.6\Gamma_{421}$). The beam diameters are about 5 mm, putting us far below the saturation regime ($I_{\mathrm{sat}} = 56$ mW/cm^2). Figure 2 shows the population with and without angled slowing as a function of MOT loading time. As shown in the figure, the improvement in MOT population we see due to transverse Doppler cooling is approximately a factor of 1.4, limited by laser power. This factor is independent of whether or not angled slowing is employed.

IV. OPTIMIZATION OF ANGLED SLOWING

We determined the optimal alignment of our angled slowing beams by maximizing the steady-state MOT population as measured by the integrated 626-nm fluorescence scattered by the MOT. While σ^- light is used to pump and cycle atoms that are being slowed by our Zeeman slower, the magnetic field magnitude and direction at the position where the angled slowing beams intersect the atomic beam are not easily known, so we varied the polarization of the angled slowing beams to maximize the MOT population after the pointing had been optimized.

The angled slowing light is prepared by frequency shifting light from our 421-nm master laser with a 500-MHz AOM in a double-pass configuration and then splitting the shifted light into two separate fibers. With more than 200 mW of input power to this frequency shifting setup, thermal lensing in the AOM causes sensitively power-dependent variations in the spatial mode of the beams reaching the fibers, greatly reducing the fiber coupling efficiency. To avoid thermal lensing (and allow for more controlled variation of the angled slowing power via the rf power), we keep the power going to this AOM low, resulting in a maximum power of about 10 mW per beam in our angled slowing light.

Given this power constraint, we looked for an optimal combination of power and detuning for the angled slowing beams. Figure 3 shows the population after a fixed load time and fixed compression sequence (see the following section) as a function of both detuning (always red) and power per beam. The uncertainty in our beam power was at most $\pm 15\%$, and the uncertainty in our frequency was about ± 2 MHz, with the latter uncertainty arising from drifts in our wavemeter.

The general trends are explained by a simple physical picture: At small detunings, a small amount of power kicks some of the slowed flux to below the capture velocity of the MOT, but increasing power causes significant additional scattering in the nearly-zero-velocity atoms and causes them to turn around. At intermediate detunings, more flux is kicked out of the broad, slowed distribution to velocities below the capture velocity. Eventually, with enough power, off-resonant slowing begins to turn the atoms around again. At large detunings, the majority of the slowed flux is only addressed off-resonantly by the angled slowing beams. Eventually, atoms will also

be turned around off-resonantly, and thus there should be an optimal power for any given detuning.

At each detuning, we scanned the constant offset field in the slower, which is equivalent to scanning the Zeeman slower laser frequency and hence the final velocity. We found that the optimal bias field was the same for all detunings to within the step size we explored (steps of $1 \text{ A} \approx \frac{\Gamma_{421}}{2}$ of effective Zeeman slower detuning). We also found that the same bias field was optimal when loading a MOT without angled slowing. Together, these observations suggest that the final velocity distribution of the Zeeman-slowed atoms is broad compared to Γ_{421}. If the final velocity distribution were narrow, we would expect the optimum to vary with the choice of angled slowing detuning.

V. COMPRESSION AND DETECTION

We load about 3×10^8 atoms in 2 s with our optimized angled slowing parameters. To prepare the captured atoms to be loaded into an optical dipole trap (ODT) for evaporation, we compress the cloud over 50 ms and let the compressed cloud equilibrate for at least 300 ms. Compression consists of switching off the dithering of the MOT light frequency and ramping the frequency from the initial detuning to within about a few linewidths of resonance. To minimize losses due to light-assisted collisions and to reach the lowest final temperature of the cloud, the MOT beams are ramped down to a final power of 22 μW per arm. We also reduce the magnetic field gradient from 2.5 to 1.75 G/cm in order to further minimize losses. At the end of the compression, the MOT is approximately $400 \times 800 \times 800$ μm (dimensions of the optically dense region). We lose up to half of our atoms during the 300 ms of postcompression equilibration but obtain a net gain in phase-space density due to the simultaneous reduction in temperature.

To detect the number of atoms captured in our trap, we perform absorption imaging using light resonant with the 421-nm transition. We expect a high degree of spin polarization in the $m_J = -8$ spin state as a result of the force of gravity on our narrow-line MOT as discussed in [4], and so we image using σ^- light to address the $m_J = -8 \rightarrow m_J' = -9$ transition, which has a Clebsch-Gordon coefficient of nearly unity [22]. We let the cloud expand freely for between 10 and 30 ms before shining a 100-μs imaging light pulse. We have verified that we have a high degree of spin polarization by using σ^+ light instead of σ^- light and observe that the optical depth was reduced by more than an order of magnitude.

We measure the temperature of our cloud after compression by loading successive MOTs with identical parameters

and varying the time-of-flight (TOF) after turning off the MOT beams and quadrupole. By fitting the cloud size as a function of the TOF, we can observe the mean speed of the cloud and hence the temperature. We observe faster expansion along the vertical direction than along the horizontal direction, corresponding to a "vertical temperature" of 8.8 μK and a "transverse temperature" of 12.7 μK [23].

To obtain the optimal phase-space density, $n\lambda_T^3$, we varied the MOT frequency, detuning, and gradient during the compression sequence. We used the size in large TOF (20–25 ms) as a proxy for velocity (and therefore temperature), which in combination with the measured number allowed for single-shot estimation of the phase-space density. We optimized the phase-space density both through manual parameter scans and by automating the search using a simple genetic algorithm. We obtained similar results from both approaches and measured an optimal phase-space density of 10^{-5} after 10 s of loading.

VI. CONCLUSION

In conclusion, we used the described angled slowing technique to reduce the effect of transverse atomic beam spreading on our MOT loading, effectively increasing the capture velocity of our narrow-line MOT. We observe more than an order-of-magnitude increase in the number of atoms captured in the MOT when the angled slowing is operated with optimal parameters, allowing us to load MOTs in the 10^8 regime in a few seconds. In our experiment, the combination of a narrow cooling transition, long free-flight distance, and reduced off-resonant slowing means that the free-flight time is particularly long; we believe that angled slowing can be of use in similarly designed experiments using species with narrow cooling transitions (such as Dy, Er, or Yb). Even in experiments where transverse spread can be avoided by employing other techniques, such as transverse Doppler cooling or the core-shell MOT configuration, the low power requirements and simple geometry of the angled slowing scheme may make it a comparatively attractive option.

[1] M. Lu, N. Q. Burdick, S. H. Youn, and B. L. Lev, Strongly Dipolar Bose-Einstein Condensate of Dysprosium, Phys. Rev. Lett. **107**, 190401 (2011).

[2] T. Maier, M. S. H. Kadau, A. Griesmaier, and T. Pfau, Narrow-line magneto-optical trap for dysprosium atoms, Opt. Lett. **39**, 3138 (2014).

[3] E. Lucioni, G. Masella, A. Fregosi, C. Gabbanini, S. Gozzini, A. Fioretti, L. Del Bino, J. Catani, G. Modugno, and M. Inguscio, A new setup for experiments with ultracold dysprosium atoms, Eur. Phys. J.: Spec. Top. **226**, 2775 (2017).

[4] D. Dreon, L. A. Sidorenkov, C. Bouazza, W. Maineult, J. Dalibard, and S. Nascimbene, Optical cooling and trapping of highly magnetic atoms: The benefits of a spontaneous spin polarization, J. Phys. B: At., Mol. Opt. Phys. **50**, 065005 (2017).

[5] F. Mühlbauer, N. Petersen, C. Baumgärtner, L. Maske, and P. Windpassinger, Systematic optimization of laser cooling of dysprosium, Appl. Phys. B **124**, 120 (2018).

[6] P. Ilzhöfer, G. Durastante, A. Patscheider, A. Trautmann, M. J. Mark, and F. Ferlaino, Two-species five-beam magneto-optical trap for erbium and dysprosium, Phys. Rev. A **97**, 023633 (2018).

[7] L. Chomaz, D. Petter, P. Ilzhöfer, G. Natale, A. Trautmann, C. Politi, G. Durastante, R. M. W. van Bijnen, A. Patscheider, M. Sohmen, M. J. Mark, and F. Ferlaino, Long-Lived and Transient Supersolid Behaviors in Dipolar Quantum Gases, Phys. Rev. X **9**, 021012 (2019).

[8] L. Tanzi, E. Lucioni, F. Famà, J. Catani, A. Fioretti, C. Gabbanini, R. N. Bisset, L. Santos, and G. Modugno, Observation of a Dipolar Quantum Gas with Metastable Supersolid Properties, Phys. Rev. Lett. **122**, 130405 (2019).

[9] I. Ferrier-Barbut, H. Kadau, M. Schmitt, M. Wenzel, and T. Pfau, Observation of Quantum Droplets in a Strongly Dipolar Bose Gas, Phys. Rev. Lett. **116**, 215301 (2016).

[10] F. Böttcher, J.-N. Schmidt, M. Wenzel, J. Hertkorn, M. Guo, T. Langen, and T. Pfau, Transient Supersolid Properties in an Array of Dipolar Quantum Droplets, Phys. Rev. X **9**, 011051 (2019).

[11] N. Q. Burdick, Y. Tang, and B. L. Lev, Long-Lived Spin-Orbit-Coupled Degenerate Dipolar Fermi Gas, Phys. Rev. X **6**, 031022 (2016).

[12] X. Cui, B. Lian, T.-L. Ho, B. L. Lev, and H. Zhai, Synthetic gauge field with highly magnetic lanthanide atoms, Phys. Rev. A **88**, 011601(R) (2013).

[13] S. H. Youn, M. Lu, U. Ray, and B. L. Lev, Dysprosium magneto-optical traps, Phys. Rev. A **82**, 043425 (2010).

[14] B. T. Plotkin-Swing, Large momentum separation matter wave interferometry, Ph.D. thesis, University of Washington, 2018.

[15] B. Plotkin-Swing, A. Wirth, D. Gochnauer, T. Rahman, K. E. McAlpine, and S. Gupta, arXiv:2004.10298 [physics.atom-ph] (2020).

[16] J. Lee, J. H. Lee, J. Noh, and J. Mun, Core-shell magneto-optical trap for alkaline-earth-metal-like atoms, Phys. Rev. A **91**, 053405 (2015).

[17] SVT Associates model SVTA-DF-20-450.

[18] T. Maier, Interactions in a quantum gas of dysprosium atoms, Ph.D. thesis, Universität Stuttgart, 2015.

[19] When transverse Doppler cooling of the atomic beam is employed prior to Zeeman slowing, the transverse velocity distribution can become much narrower; however, the light scattering during Zeeman slowing causes the transverse velocity distribution to rebroaden.

[20] The Doppler shift at 67 m/s is about 14 linewidths, but the Zeeman shift across the MOT for a typical gradient of 20 G/cm is about 9 linewidths. At around 43 m/s, the Zeeman shift across the MOT can compensate for the Doppler shift.

[21] E. W. Streed, A. P. Chikkatur, T. L. Gustavson, M. Boyd, Y. Torii, D. Schneble, G. K. Campbell, D. E. Pritchard, and W. Ketterle, Large atom number Bose-Einstein condensate machines, Rev. Sci. Instrum. **77**, 023106 (2006).

[22] M. Lu, Quantum Bose and Fermi gases of dysprosium: Production and initial study, Ph.D. thesis, Stanford University, 2014.

[23] We attribute the anisotropy to laser power imbalance in our MOT beams, which gives rise to different scattering-induced heating rates along the three MOT axes and hence different steady-state temperatures. This imbalance has been subsequently corrected.

Appendix C

Atomic Physics on a 50-nm Scale: Realization of a Bilayer System of Dipolar Atoms

This appendix contains a reprint of Ref. [34]: Li Du, Pierre Barral, Michael Cantara, Julius de Hond, Yu-Kun Lu, and Wolfgang Ketterle, *Atomic physics on a 50-nm scale: Realization of a bilayer system of dipolar atoms* Science, 2024, 384(6695): 546-551.

ATOMIC PHYSICS

Atomic physics on a 50-nm scale: Realization of a bilayer system of dipolar atoms

Li Du*†, Pierre Barral†‡, Michael Cantara†§, Julius de Hond¶, Yu-Kun Lu, Wolfgang Ketterle

Controlling ultracold atoms with laser light has greatly advanced quantum science. The wavelength of light sets a typical length scale for most experiments to the order of 500 nanometers (nm) or greater. In this work, we implemented a super-resolution technique that localizes and arranges atoms on a sub–50-nm scale, without any fundamental limit in resolution. We demonstrate this technique by creating a bilayer of dysprosium atoms and observing dipolar interactions between two physically separated layers through interlayer sympathetic cooling and coupled collective excitations. At 50-nm distance, dipolar interactions are 1000 times stronger than at 500 nm. For two atoms in optical tweezers, this should enable purely magnetic dipolar gates with kilohertz speed.

A major frontier in many-body physics is the realization and study of strongly correlated quantum phases (1–3). In ultracold atomic systems, the typical short-range contact interaction has led to the creation of a variety of exotic quantum phases (3, 4). However, a wide range of quantum phenomena require long-range dipolar interactions (5–7). But even for the most magnetic atoms such as chromium, erbium, and dysprosium (Dy), the magnetic dipole-dipole interaction is rather weak. For Dy, with a magnetic dipole moment of 10 Bohr magneton (μ_B), the dipolar interaction at 500-nm distance is only $h \times 20$ Hz, where h is Planck's constant. Although such weak interactions could be observed (8, 9), and supersolidity and other forms of matter could be realized with magnetic atoms (5), there are major efforts to harness the much stronger interactions of polar molecules (10, 11) and Rydberg atoms (12). The electric dipolar interaction of molecules (at 3 D) can be 1000 times stronger than the magnetic dipolar interaction (at 10 μ_B). In this work, we show how this factor of 1000 can be compensated for by decreasing the distance between two magnetic atoms to 50 nm. Studying dipolar physics with neutral atoms has major advantages: It is simpler to cool atoms to quantum degeneracy, and atoms have more favorable collisional properties.

It has been a long-standing goal to create optical potentials with subwavelength components to enhance tunneling and interaction strengths. Early works on atom lithography achieved deposition of metal structures with spatial periods one-eighth the size of optical wavelengths (13, 14) and feature sizes of tens of nanometers (15) using state-dependent potentials. With ultracold atoms, many schemes have been suggested (16–20), and methods such as dark states (21, 22), radio frequency–photon dressing (23), stroboscopic techniques (24), and multiphoton processes through Raman transitions between hyperfine states (13, 25, 26) have been demonstrated. Challenges, such as additional heating, limited coherence time, and limited reduction of atomic spacing, have hindered a wide adoption of these methods. In this work, we introduce a method that has no fundamental limit. It is based on the key concept of optical super-resolution microscopy: One can determine the center of a diffraction-limited Airy disk with a precision that exceeds the diffraction limit. Similarly, a deep optical lattice or a strong tweezer beam can localize an atom to 10 nm (15, 27, 28), limited only by available power and heating from spontaneous light scattering. In a typical super-resolution microscopy experiment, molecules are imaged sequentially, whereas for trapping atoms, simultaneous confinement on a subwavelength scale is required. One possible solution is to trap two different kinds of atoms with two different colors of light. But, usually, for quantum science, one needs identical atoms. The strategy we implemented was to use two opposite spin states of Dy and two different polarizations of light at different frequencies—a dual-polarization and dual-frequency super-resolution scheme. Unlike spin-1/2 and alkali atoms, ground-state Dy has a strong tensor polarizability (29). It can cause detrimental two-photon Raman couplings between spin states with different m_J quantum numbers, which are suppressed by the frequency offset between the two optical potentials. The remaining diagonal part of the tensor couplings makes our scheme much more robust because it creates, for ^{162}Dy, an isolated two-state Hilbert space for $m_J = \pm 8$ spin states with a big energy gap to all the other 15 spin states.

Spin-dependent potentials have been realized with rubidium (30–34) and cesium (27, 35). In contrast to alkali atoms (36), very deep s̲ dependent potentials can be realized with D̲y with negligible spontaneous emission as a result of Dy's electronic orbital angular momentum in the ground state. Furthermore, with a magnetic dipole moment of only 1 μ_B, the dipolar interaction for alkali atoms is 100 times weaker than for Dy. Therefore, previous work on alkalis has used spin-dependent forces to control the overlap between sites with spin up and down (27, 33) but not to study interactions between nonoverlapping sites.

The subwavelength scheme

An illustration of the experimental scheme is shown in Fig. 1B, which demonstrates a bilayer potential created by two optical standing waves of σ_+ and σ_- polarizations with a small spatial displacement s. This illustration also applies to the case of spin-dependent optical tweezers. The figure shows the adiabatic potentials of all 17 spin states (quantized along the z direction in the lab frame), with different polarizability components taken into account. With only a scalar polarizability α_s, the ac Stark shifts are the same for all 17 m_J states, so there is only one potential minimum. The vector polarizability α_v leads to ac Stark shifts that are linear in m_J and therefore can be regarded as a Zeeman shift caused by a fictitious sinusoidal magnetic field—it lifts the degeneracy except for points where the fictitious magnetic fields from the σ_+ and the σ_- standing waves cancel. This creates a double-well potential even for an arbitrarily small displacement of the standing waves. However, small transverse magnetic fields would couple the degenerate states, leading to mixing among different m_J states. This is where the tensor polarizability α_t makes a qualitative difference. The diagonal part of the tensor light-atom interaction (which has an m_J^2 dependence) partially lifts the degeneracy. The $m_J = \pm 8$ ground states are separated from all other states by a large gap and are coupled by transverse fields only in 16th order. Note that the $m_J = \pm 8$ states are the local ground states of the $\sigma_\pm$ potential minima, and therefore inelastic two-body losses are prevented in each of the layers.

Although the tensor polarizability α_t provides robustness against transverse magnetic fields, it allows for two-photon Raman processes with $\Delta m_J = \pm 2$ using one σ_+ and one σ_- photon. Figure 1C shows the effect of the resonant Raman process caused by off-diagonal tensor couplings when both polarization components have the same frequency. This is the situation when the σ_+ and the σ_- standing waves are created by retroreflecting a single beam with rotated linear polarization, as often used for alkalis [e.g., see (30, 31, 33)]. For Dy, the Raman couplings weaken the potential minima for separations smaller than $\lambda/10$, where λ is the wavelength of the light. For

MIT-Harvard Center for Ultracold Atoms, Research Laboratory of Electronics, Department of Physics, Massachusetts Institute of Technology, Cambridge, MA 02139, USA.
*Corresponding author. Email: lidu@mit.edu
†These authors contributed equally to this work.
‡Present address: Amazon Web Services, Boston, MA, USA.
§Present address: Oracle Cloud Infrastructure, Boston, MA, USA
¶Present address: PASQAL SAS, Fred. Roeskestraat 100, Amsterdam, Netherlands.
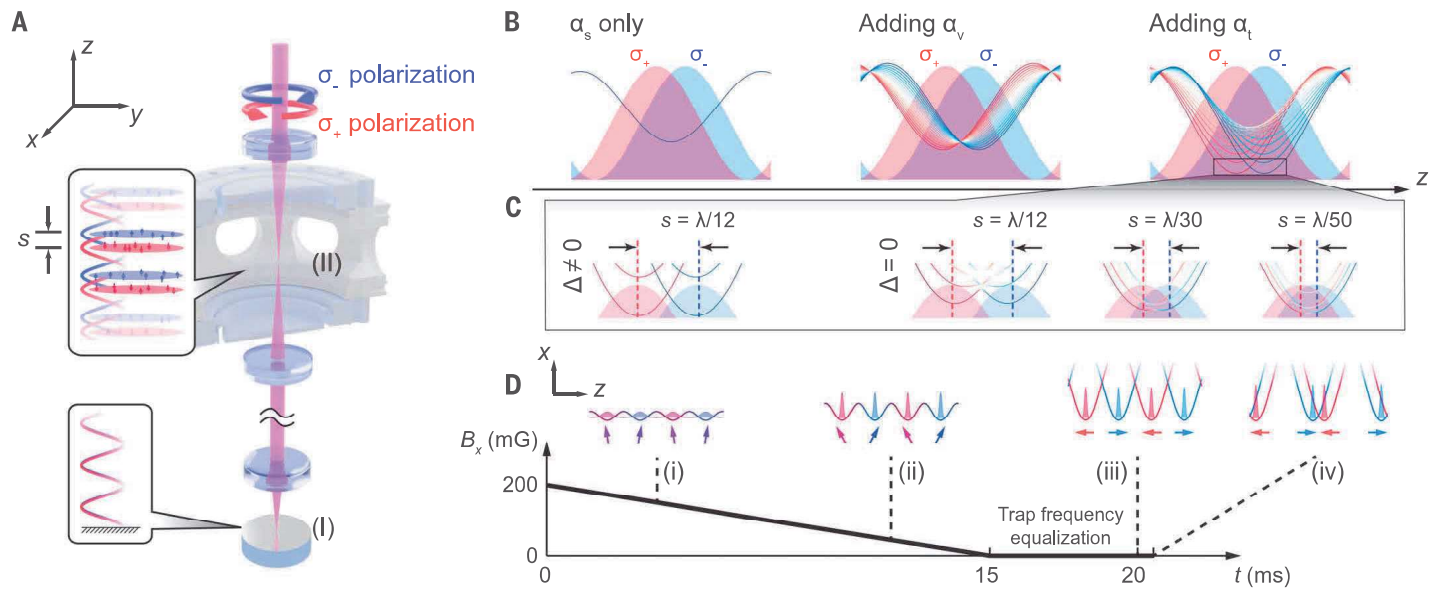
Fig. 1. Creation of the subwavelength bilayer array. (**A**) Experimental setup. Two overlapping laser beams with opposite circular polarizations σ_+ and σ_- are retroreflected by a mirror (I) to form two optical standing waves. The two standing waves are displaced at the position of the atoms (II), which is controlled by the frequency offset Δ between the two laser beams. Dy atoms in this configuration form an array of pancake-shaped bilayers of head-to-head dipoles with adjustable interlayer distance s. (**B**) Contributions of different polarizability components. Solid lines denote adiabatic potential curves for different m_J states ($-8 \leq m_J \leq 8$, represented by dark blue to dark red, assuming red detuning), and the shaded regions refer to the intensities of the $\sigma_\pm$ light for a particular interlayer separation. (**C**) If the two laser beams have the same frequency $\Delta = 0$, the off-diagonal part of the tensor polarizability mixes spin states. As a result, the two minima merge into a single minimum for a small separation s. This is avoided in our experiment by using two different frequencies for the $\sigma_\pm$ light. The color of the curves indicate the m_J character of the adiabatic eigenstates. (**D**) Adiabatic loading of the bilayer array. (i) Starting with the optical potential in the interlaced configuration in the presence of a dominating transverse magnetic field $B_x = 200$ mG, the atoms are initialized in the $m_J = -8$ spin state along the x direction. (ii) As B_x is ramped down in 15 ms, the light shift dominates over the Zeeman shift, thereby adiabatically loading the bilayer array. (iii) The power of the σ_+ and σ_- potentials is adjusted for identical trap frequencies. (iv) The interlayer distance is adjusted to designated values in 0.5 ms.

displacements of the standing waves of less than $\lambda/30$, the double minima have merged. We eliminated the Raman coupling by offsetting the frequencies for the σ_+ and σ_- optical standing waves by more than 300 MHz, much larger than the ac Stark shifts, which makes the two-photon Raman process off-resonant (*37*). The conclusion is that the dual-polarization and dual-frequency scheme isolates the Hilbert space for the $m_J = \pm 8$ spin states and creates a double-minimum potential that is not flattened out even for very small separations of the two minima.

Dy, with its high angular momentum of $J = 8$ in the ground state, is the ideal atom for this scheme. For a $J = 8 \rightarrow J' = 9$ transition, the $m_J = 8$ state has a transition strength ratio of 153 between the σ_+ and σ_- transitions (*38*). For atoms with $J = 1$ (2), the ratio is only 6 (15). Therefore, this stretched transition in Dy is very similar to a hypothetically isolated $J = 1/2 \rightarrow J' = 1/2$ transition, where the spin-up state sees only σ_- light and vice versa. Dy is even more ideal than the $J = 1/2$ case in which spin-up and down states are directly connected by possible one- or two-body couplings (e.g., transverse magnetic fields, dipolar relaxation), whereas those couplings act only in 16th or 8th order in our Dy scheme. The robustness of the scheme comes from the ac Stark shifts that stem from the tensor polarizability.

Experimental protocol

Experimentally, we created a stack of bilayers by superimposing red-detuned optical standing waves with σ_+ and σ_- polarizations operating near the Dy narrowline transition at 741 nm (linewidth $\Gamma/2\pi = 1.78$ kHz) (*39*). The two optical beams were delivered through the same polarization-maintaining fiber, such that they shared the same transverse Gaussian mode. The frequency of the σ_- standing wave can be dynamically tuned using a double-passed phased-array acousto-optic deflector, leading to a precise control of the interlayer distance s with a sensitivity of 4.7 nm MHz^{-1} (*40*).

The ground state of the bilayer was loaded using an adiabatic transfer method, as depicted in Fig. 1D. First, $m_J = -8$ atoms were prepared in a magnetic field with a transverse component $B_x = 200$ mG and an axial component B_z around 10 mG. We then ramped up the σ_+ and σ_- standing waves in the interlaced configuration with $s = \lambda/4$ in 100 ms, loading all layers with atoms aligned with the x axis (Fig. 1D, i). By ramping down B_x in

15 ms, the potential depth increased while a bilayer array was formed with dipoles aligned head to head (Fig. 1D, ii and iii). We ensured balanced loading by making sure that the energy offset (including Zeeman energies) between the minima of the σ_+ and σ_- potentials was zero. It was crucial that the atoms stayed in their local ground state throughout the experiment to prevent losses and heating caused by dipolar relaxation. Therefore, the Zeeman shifts caused by the external magnetic field B_z had to be smaller than the differential ac Stark shift between the $m_J = -8$ and $m_J = -7$ states.

After loading a balanced bilayer array, the powers of the two optical standing waves were ramped up, ensuring that the two layers had the same trap frequencies of typically ($\omega_x, \omega_y, \omega_z$) = $2\pi \times$ (0.5, 0.5, 140) kHz. The strong axial confinement resulted in a harmonic oscillator length $a_{HO} = \sqrt{\hbar/m\omega_z}$ of 21.1 nm, where $\hbar = h/2\pi$ and m is the atomic mass. We loaded 4.2×10^4 ultracold ^{162}Dy atoms into an array of 42 bilayers, with a temperature of 1.7 µK determined from the cloud size after ballistic expansion (*40*, *41*). Subsequently, the interlayer distance s was ramped from $\lambda/4$ to different designated values in 0.5 ms by changing

Fig. 2. Subwavelength control of the interlayer distance, as demonstrated by recording atom loss as a function of layer separation. (**A**) Evolution of the population in σ_+ layers at two different interlayer distances s of 185 and 0 nm. The loss is much faster when the layers are overlapped. Initial loss rates Γ_{3b} are obtained from the fits to the decay curves. (**B**) Gaussian fits of the initial loss rates Γ_{3b} to the interlayer distances s according to Eq. 1 (solid lines) provide a value of $\sigma_z = 19 \pm 1$ nm for the layer thickness.
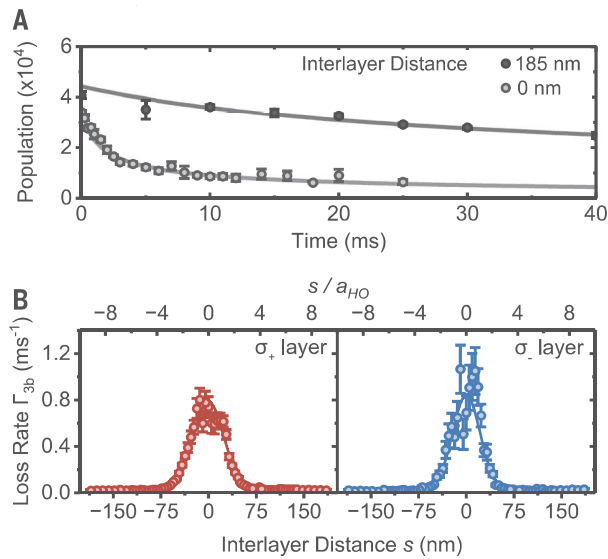

Fig. 3. Observation of interlayer thermalization. (**A**) Interlayer elastic scattering cross sections as functions of separation s calculated using the Born approximation. The gray curves correspond to dipolar cross sections for infinitely thin $\sigma_z = 0$ layers (thin gray) along with its large interlayer distance limit $ks \gg 1$ (dashed gray, following Eq. 2) and for layers with finite thickness $\sigma_z = 14.9$ nm (quasi-2D, solid gray). The red curve is for simple contact interactions at the background scattering length (red, quasi 2D), and the shaded area corresponds to a 10-times-enhanced cross section. (**B**) Observed thermalization rates Γ_0 obtained from the pseudo-exponential fits. The black and red solid lines show the expected thermalization rate from dipolar and contact interactions (40). The dashed line is for reference and is proportional to $1/s^3$. Error bars represent the standard errors of the rates obtained from the pseudo-exponential fits.
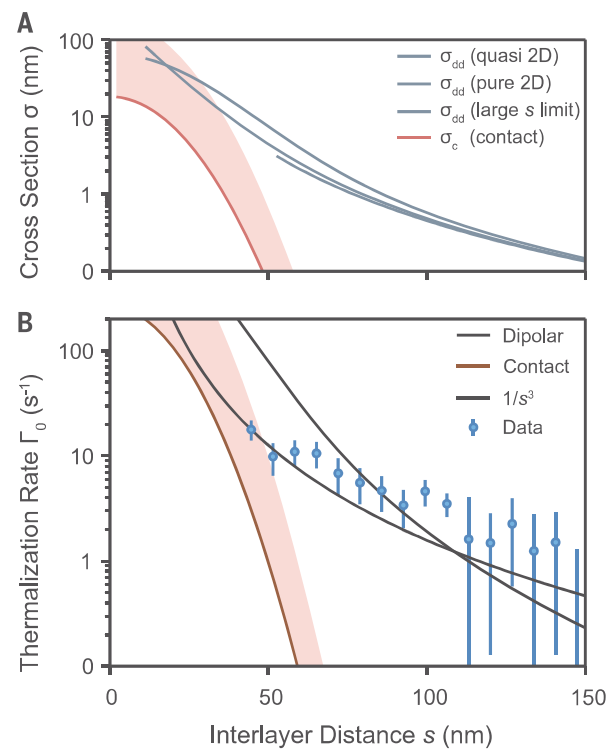
the frequency of the σ_- standing wave. The interlayer distance s was calibrated with Kapitza-Dirac diffraction measurements (40). At the end of each experimental sequence, the atoms were released from the bilayer array within 1 μs and were imaged after ballistic expansion. With the small axial magnetic field B_z serving as a guiding field, atoms remained in the $m_J = \pm 8$ states and were imaged by a spin-resolved absorption imaging technique (40). This meth-

od allowed us to measure the population in each of the two layers simultaneously.

Demonstration of spatial control

We demonstrated the subwavelength spatial control over the bilayer geometry by measuring the lifetime of atomic samples at different layer separations. The sharp peak in the loss rate as a function of interlayer distance s in Fig. 2 is essentially the convolution between

the density profiles of the two layers. Assuming that loss processes occur at short range, we derived a rate equation for the total loss rate Γ_{3b} of each layer

$$\Gamma_{3b} = \Gamma_{intra} + \Gamma_{inter} e^{-\frac{1}{3}\left(\frac{s}{\sigma_z}\right)^2} = \frac{\dot{N}_{tot}}{N_{tot}} \quad (1)$$

where N_{tot} is the total number of atoms in a layer and σ_z is the root-mean-square thickness of each layer. The loss rate contains both an intra- and interlayer contribution characterized by Γ_{intra} and Γ_{inter}. The factor of one-third in the exponent of the interlayer term reflects that the loss is caused by three-body recombination (40). For spin-independent three-body collisions and thermal clouds, we expect that $\Gamma_{intra} = \Gamma_{inter}$. Unexpectedly, we observed about a 50-fold increase in the loss rate when the two layers were overlapped, which implies that three-body recombination involving mixed spin states is much faster than recombination of three atoms that are all in the same spin state. This strongly enhanced loss feature serves as a highly sensitive monitor for the density overlap between the two layers; fitting the loss curve determines the thickness of each layer $\sigma_z = 19 \pm 1$ nm, consistent with the calculated value of $1.31 a_{HO}/\sqrt{2} \approx 18.8 \pm 0.1$ nm that we obtained from trap frequency and temperature measurements (41). The observed losses in the two layers are almost equal, which implies equal loss rates for three-body collisions involving one spin-up and two spin-down atoms, or vice versa. This measurement of the atomic density distribution has no discernible broadening: The measured and calculated widths agreed to within 1 nm. Expressing this as an instrumental point spread function gives an upper limit to the Gaussian width of the point-spread function of 6 nm. This result can be compared with what was achieved in dark-state super-resolution microscopy. McDonald et al. (22) measured an atom cloud size of 55 nm with a broadening of 32 nm due to the width of the dark-state probe. A similar experiment reported by Subhankar et al. (42) measured a size of 26 nm with a broadening of 11 nm from the probe.

We conclude from the loss measurement that the two layers can be regarded as coupled predominantly by long-range dipolar forces for $s \gtrsim 50$ nm. The dipolar energy U_{dd}/h between two Dy atoms with opposite spins at this separation is 20 kHz. This geometry now allows us to study physics with strong interlayer dipole-dipole interactions.

Interlayer thermalization

We applied our technique to study energy transfer through interlayer dipolar interactions, or sympathetic cooling between two atomic systems separated by vacuum (43, 44). Each layer receives heat through the fluctuating magnetic field created by the dipoles in the other layer. For equal temperatures, in detailed
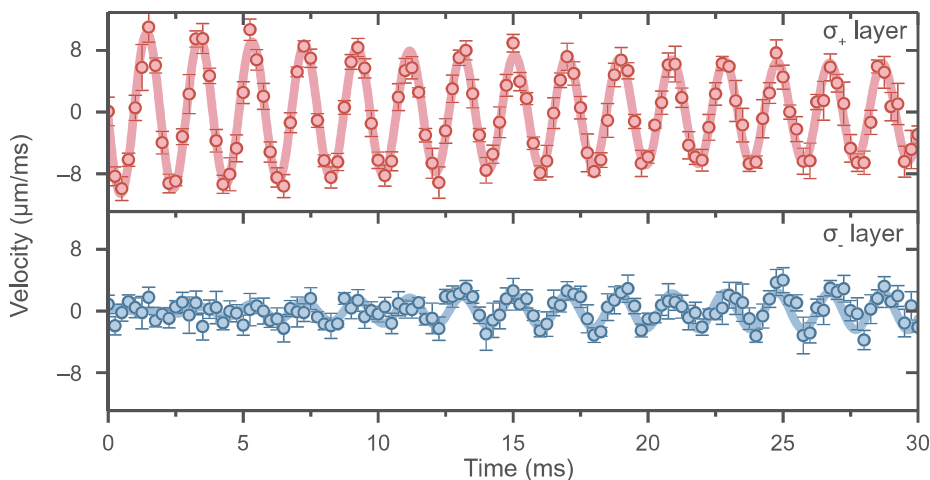
Fig. 4. Observation of coupled oscillations of the two layers at a 62-nm interlayer distance. The center-of-mass oscillation of the σ_+ layer is excited by suddenly switching off a displacement force. The σ_- layer oscillates because of dipolar coupling. Error bars represent the standard errors of the means of independent measurements.

balance, the heat flows cancel. For unequal temperatures, the dipolar fluctuations cause thermalization. Figure 3B shows the experimental results.

We experimentally created a controlled temperature difference between the two layers by heating up the σ_+ layer using a parametric drive by modulating the σ_+ light intensity at twice the transverse trap frequency for 30 ms, followed by a 5-ms hold to ensure any residual breathing motion is damped out. This procedure prepares the σ_+ layer at 3.9 μK and leaves the σ_- layer at 1.7 μK. We then adjusted the interlayer distance over 0.5 ms and monitored the temperature evolution. We fit the temperature difference between two layers to a pseudo-exponential decay $\frac{d\Delta T}{dt} = -\Gamma_0 \frac{N(t)}{N(0)} \Delta T$ to obtain the interlayer thermalization rate Γ_0, where $N(t)$ accounts for the measured particle number decay caused by inelastic collisions (40). Figure 3B shows that the thermalization rate strongly drops with interlayer distance.

We could estimate the interlayer collision rate as $n_{2D}\sigma_{dd}v_{rel}$, where n_{2D} is the 2D density distribution and σ_{dd} is the cross section for two dipolar atoms passing each other at a separation s. Using the Born approximation (45–48), we calculated the elastic cross section between two atoms in thin layers separated by a distance s (40), and the analytic large-s limit is

$$\sigma_{dd}^{2D} = a_{dd}^2 \frac{\pi}{k^2 s^3} \quad (2)$$

Here, a_{dd} = 10.2 nm is the dipolar length and k is the relative momentum between the colliding particles. For s = 75 nm, the quasi-2D cross section σ_{dd} is 0.38 nm (see Fig. 3A). With a typical 2D peak density of $n_{2D} \approx 1.3 \times 10^9$ cm^{-2} and a thermal velocity of 2.1 cm s^{-1} one obtains

an interlayer collision rate of 100 s^{-1}. The observed thermalization times are much slower, around 160 ms (rate of 6 s^{-1}). This can be fully accounted for by the anisotropy of dipolar scattering peaked in the forward direction, which reduces the effective cross section by a factor of six, and by multiple averaging arising from the inhomogeneity of our sample (40). In Fig. 3B, we compare the observed thermalization rates to calculations (40). They do not have any adjustable parameters and fully take into account the momentum and angular dependence of dipolar scattering and the finite thickness of the layer. The calculations are in semiquantitative agreement with the observations. The drop-off of the thermalization rate is much weaker than the steep exponential decrease in density overlap and, therefore, in the contact interactions between the two layers. This is clear evidence for purely dipolar couplings in the range of 50- to 100-nm interlayer distances.

The observed dependence on s roughly follows a $1/s^3$ dependence, which is less steep than predicted. This is possibly a consequence of the assumption of purely dipolar binary collisions. For small s, there can be an interference term with s-wave contact interactions and a contribution from nonuniversal short-range dipolar s-wave scattering (49), which is not included in the Born approximation. The largest separations s studied are comparable to the interparticle separation, and the binary collision approximation may no longer be accurate; that is, there are now more than two particles interacting with each other.

Coupled collective oscillations

In the second experiment, we looked for coupled collective oscillations of the bilayer system.

Several theoretical papers (50, 51) predicted the coupling of transverse oscillations by the mean dipolar field between the layers. Indeed, when we excited transverse oscillations in one layer, we found that they caused oscillations in the other layer (Fig. 4). Experimentally, after loading a balanced bilayer array and adjusting the interlayer distance to a designated value in 0.5 ms, we adiabatically displaced the σ_+ layer along the transverse direction y in 10 ms using an extra laser beam with σ_+ polarization. This beam, blue-detuned from the 626-nm transition by 458 MHz, is misaligned from the atoms by about one beam waist and displaces the atoms only in the σ_+ layer (40). A sudden switch-off of this beam hence creates a center-of-mass oscillation of the σ_+ layer at the transverse trap frequency with an adjustable amplitude ranging from 0 to 8 μm, depending on the final power of the beam. As a function of hold time, we obtained the in-trap velocity of each layer from time-of-flight images to reveal how momentum is transferred between layers.

Figure 4 shows the time evolution of the velocity of each layer at s = 62 nm, as obtained from ballistic expansion images. The harmonic oscillation of the σ_+ layer shows damping, whereas the σ_- layer starts at rest and shows a growing in-phase oscillation. Our observation contrasts with the theoretical treatments (50, 51), where the mean-field coupling potential would cause a beat note, which is initially an oscillation 90° out of phase. Furthermore, the predicted mean-field coupling (50, 51) resulted in a normal-mode splitting of less than 1 Hz, which is too slow to be observed on the experimental timescale. Our observation is fully consistent with a friction force caused by dipolar collisions: The time constant for the damping of the relative motion between the two layers of 25 ms is similar to the observed interlayer thermalization times. These observations establish dipolar drag between two physically separated layers, which have features in common with Coulomb drag studied in bilayer semiconductors (52).

Discussion and outlook

We expect that the technique we developed here should work for all atoms that have electronic orbital angular momentum in the ground state and allow strong vector and tensor ac Stark shifts at sufficiently far detuning. Although it requires the two layers to be in different spin states, those states can be tilted by a transverse magnetic field to angles within 20°. A modified scheme with an in-plane quantization axis could realize attractive interactions and interlayer pairing (47, 53).

Looking ahead, lower temperatures should lead to strong correlations between the layers beyond a mean-field description. Adding transverse optical lattices to the layers will create large repulsive interaction energies between

pairs on the same lattice site (*7*) but can also realize a system described by attractive interactions between particles and holes analogous to electron-hole pairs in bilayer excitons (*54*). It is possible to project separate arbitrary potentials into the σ_+ and σ_- layers, which could realize twisted bilayer potentials (*55*) and more general geometries, including quasi-crystals. These geometries should allow the study of many phenomena that have been predicted for interacting bilayers (*7, 50, 51, 56–62*). Applying the super-resolution technique to optical tweezers will allow the study of super-radiance and radiative shifts at separations much smaller than the optical wavelength as well as the study of magnetic interactions and spin exchange between two isolated atoms, which was done recently with polar molecules (*63–66*). The tweezer setup can be generalized to a linear array of atoms alternating in spin-up and spin-down states. Moving the spin-up atoms back and forth would provide full connectivity along the chain and realize a spin chain with strong magnetic coupling between nearest neighbors. These ideas can be generalized to higher dimensions.

REFERENCES AND NOTES

1. B. Keimer, J. Moore, *Nat. Phys.* **13**, 1045–1055 (2017).
2. E. Y. Andrei, A. H. MacDonald, *Nat. Mater.* **19**, 1265–1275 (2020).
3. M. Lewenstein, A. Sanpera, V. Ahufinger, *Ultracold Atoms in Optical Lattices: Simulating Quantum Many-Body Systems* (Oxford Univ. Press, 2012).
4. I. Bloch, J. Dalibard, W. Zwerger, *Rev. Mod. Phys.* **80**, 885–964 (2008).
5. L. Chomaz *et al.*, *Rep. Prog. Phys.* **86**, 026401 (2022).
6. T. Lahaye, C. Menotti, L. Santos, M. Lewenstein, T. Pfau, *Rep. Prog. Phys.* **72**, 126401 (2009).
7. M. A. Baranto, M. Dalmonte, G. Pupillo, P. Zoller, *Chem. Rev.* **112**, 5012–5061 (2012).
8. S. Müller *et al.*, *Phys. Rev. A* **84**, 053601 (2011).
9. S. Baier *et al.*, *Science* **352**, 201–205 (2016).
10. B. Gadway, B. Yan, *J. Phys. At. Mol. Opt. Phys.* **49**, 152002 (2016).
11. S. A. Moses, J. P. Covey, M. T. Miecnikowski, D. S. Jin, J. Ye, *Nat. Phys.* **13**, 13–20 (2017).
12. A. Browaeys, T. Lahaye, *Nat. Phys.* **16**, 132–142 (2020).
13. R. Gupta, J. J. McClelland, R. J. Celotta, P. Marte, *Phys. Rev. Lett.* **76**, 4689–4692 (1996).
14. T. Schulze *et al.*, *Microelectron. Eng.* **46**, 105–108 (1999).
15. C. C. Bradley, W. R. Anderson, J. J. McClelland, R. J. Celotta, *Appl. Surf. Sci.* **141**, 210–218 (1999).
16. L. Caldwell, M. R. Tarbutt, *Phys. Rev. Lett.* **125**, 243201 (2020).
17. L. Caldwell, M. Tarbutt, *Phys. Rev. Res.* **3**, 013291 (2021).
18. M. Łącki, M. A. Baranov, H. Pichler, P. Zoller, *Phys. Rev. Lett.* **117**, 233001 (2016).
19. S. Nascimbene, N. Goldman, N. R. Cooper, J. Dalibard, *Phys. Rev. Lett.* **115**, 140401 (2015).
20. A. Kruckenhauser *et al.*, *Phys. Rev. A* **102**, 023320 (2020).
21. Y. Wang *et al.*, *Phys. Rev. Lett.* **120**, 083601 (2018).
22. M. McDonald, J. Trisnadi, K.-X. Yao, C. Chin, *Phys. Rev. X* **9**, 021001 (2019).
23. N. Lundblad *et al.*, *Phys. Rev. Lett.* **100**, 150401 (2008).
24. T.-C. Tsui, Y. Wang, S. Subhankar, J. V. Porto, S. L. Rolston, *Phys. Rev. A* **101**, 041603 (2020).
25. G. Ritt, C. Geckeler, T. Salger, G. Cennini, M. Weitz, *Phys. Rev. A* **74**, 063622 (2006).
26. R. P. Anderson *et al.*, *Phys. Rev. Res.* **2**, 013149 (2020).
27. L. Förster *et al.*, *Phys. Rev. Lett.* **103**, 233001 (2009).
28. A. M. Kaufman, B. J. Lester, C. A. Regal, *Phys. Rev. X* **2**, 041014 (2012).
29. Spin-1/2 atoms and alkalis for detunings larger than the excited-state hyperfine splitting share the property that they have only a scalar and vector polarizability. In general, atoms have a vector or tensor polarizability when light scattering can change their angular momentum by $\hbar$ or $2\hbar$, respectively (*67, 68*).
30. O. Mandel *et al.*, *Phys. Rev. Lett.* **91**, 010407 (2003).
31. B.-B. Yang *et al.*, *Phys. Rev. A* **96**, 011602 (2017).
32. P. Soltan-Panahi *et al.*, *Nat. Phys.* **7**, 434–440 (2011).
33. J. de Hond *et al.*, *Phys. Rev. Lett.* **128**, 093401 (2022).
34. B. Gadway, D. Pertot, R. Reimann, D. Schneble, *Phys. Rev. Lett.* **105**, 045303 (2010).
35. N. Belmechri *et al.*, *J. Phys. At. Mol. Opt. Phys.* **46**, 104006 (2013).
36. D. McKay, B. DeMarco, *New J. Phys.* **12**, 055013 (2010).
37. If the Raman couplings are eliminated using an external magnetic field, it breaks the symmetry of the $m_J = \pm 8$ states and causes rapid dipolar relaxation in the $m_J = \pm 8$ layer.
38. Depending on detuning, this contrast does not fully translate into the ac Stark shift because of the scalar background polarizability that is due to the strong transition triplet at 421, 419, and 405 nm.
39. M. Lu, S. H. Youn, B. L. Lev, *Phys. Rev. A* **83**, 012510 (2011).
40. Materials and methods are available as supplementary materials.
41. For technical reasons, the lifetime measurements presented in Fig. 2 are done at trap frequencies of $(\omega_x, \omega_y, \omega_z) = 2\pi \times (0.7, 0.7, 153)$ kHz and temperature of $T = 5.5\ \mu$K. This leads to an oscillator length of $a_{HO} = 20.2$ nm and a layer thickness of
$$\sqrt{\frac{\sum_{n=0}^{\infty}(2n+1)e^{-n\hbar\omega_z/k_BT}}{\sum_{n=0}^{\infty}e^{-n\hbar\omega_z/k_BT}}}\frac{a_{HO}}{\sqrt{2}} = \sqrt{\coth\left(\frac{\hbar\omega_z}{2k_BT}\right)}\frac{a_{HO}}{\sqrt{2}} \approx$$
$1.31 a_{HO}/\sqrt{2} \approx 18.8 \pm 0.1$ nm, where k_B is the Boltzmann constant, owing to thermal excitation into the higher axial vibrational levels.
42. S. Subhankar, Y. Wang, T.-C. Tsui, S. L. Rolston, J. V. Porto, *Phys. Rev. X* **9**, 021002 (2019).
43. B. Renklioglu, B. Tanatar, M. Oktel, *Phys. Rev. A* **93**, 023620 (2016).
44. C. Charalambous, M. A. Garcia-March, M. Mehboudi, M. Lewenstein, *New J. Phys.* **21**, 083037 (2019).
45. S. Hensler *et al.*, *Appl. Phys. B* **77**, 765–772 (2003).
46. J. L. Bohn, D. S. Jin, *Phys. Rev. A* **89**, 022702 (2014).
47. M. A. Baranov, A. Micheli, S. Ronen, P. Zoller, *Phys. Rev. A* **83**, 043602 (2011).
48. B. Pasquiou *et al.*, *Phys. Rev. A* **81**, 042716 (2010).
49. S. Ronen, D. C. Bortolotti, D. Blume, J. L. Bohn, *Phys. Rev. A* **74**, 033611 (2006).
50. N. Matveeva, A. Recati, S. Stringari, *Eur. Phys. J. D* **65**, 219–222 (2011).
51. C.-C. Huang, W.-C. Wu, *Phys. Rev. A* **82**, 053612 (2010).
52. J. A. Seamons, C. P. Morath, J. L. Reno, M. P. Lilly, *Phys. Rev. Lett.* **102**, 026804 (2009).
53. A. Pikovski, M. Klawunn, G. V. Shlyapnikov, L. Santos, *Phys. Rev. Lett.* **105**, 215302 (2010).
54. J. P. Eisenstein, A. H. Macdonald, *Nature* **432**, 691–694 (2004).
55. Z. Meng *et al.*, *Nature* **615**, 231–236 (2023).
56. C. Trefzger, C. Menotti, M. Lewenstein, *Phys. Rev. Lett.* **103**, 035304 (2009).
57. A. Argüelles, L. Santos, *Phys. Rev. A* **75**, 053613 (2007).
58. D.-W. Wang, M. D. Lukin, E. Demler, *Phys. Rev. Lett.* **97**, 180413 (2006).
59. P. Köberle, G. Wunner, *Phys. Rev. A* **80**, 063601 (2009).
60. A. Macia, G. Astrakharchik, F. Mazzanti, S. Giorgini, J. Boronat, *Phys. Rev. A* **90**, 043623 (2014).
61. D. Hufnagl, R. E. Zillich, *Phys. Rev. A* **87**, 033624 (2013).
62. A. Safavi-Naini, Ş. G. Söyler, G. Pupillo, H. R. Sadeghpour, B. Capogrosso-Sansone, *New J. Phys.* **15**, 013036 (2013).
63. C. M. Holland, Y. Lu, L. W. Cheuk, *Science* **382**, 1143–1147 (2023).
64. Y. Bao *et al.*, *Science* **382**, 1138–1143 (2023).
65. L. Christakis *et al.*, *Nature* **614**, 64–69 (2023).
66. B. Yan *et al.*, *Nature* **501**, 521–525 (2013).
67. F. Le Kien, P. Schneeweiss, A. Rauschenbeutel, *Eur. Phys. J. D* **67**, 92 (2013).
68. X. Cui, B. Lian, T.-L. Ho, B. L. Lev, H. Zhai, *Phys. Rev. A* **88**, 011601 (2013).
69. L. Du *et al.*, Data for "Atomic physics on a 50 nm scale: Realization of a bilayer system of dipolar atoms." Zenodo (2023); https://doi.org/10.5281/zenodo.10689742.

Appendix D

Suppressing dipolar relaxation in thin layers of dysprosium atoms

This appendix contains a reprint of Ref. [12]: Pierre Barral, Michael Cantara, Li Du, William Lunden, Julius de Hond, Alan O. Jamison, and Wolfgang Ketterle *Suppressing dipolar relaxation in thin layers of dysprosium atoms* Nature Communications, 2024, 15(1): 3566.

Suppressing dipolar relaxation in thin layers of dysprosium atoms

Pierre Barral [1,2] ✉, Michael Cantara[1,2], Li Du [1,2], William Lunden[1], Julius de Hond [1], Alan O. Jamison[1] & Wolfgang Ketterle [1]

The dipolar interaction can be attractive or repulsive, depending on the position and orientation of the dipoles. Constraining atoms to a plane with their magnetic moment aligned perpendicularly leads to a largely side-by-side repulsion and generates a dipolar barrier which prevents atoms from approaching each other. We show experimentally and theoretically how this can suppress dipolar relaxation, the dominant loss process in spin mixtures of highly magnetic atoms. Using dysprosium, we observe an order of magnitude reduction in the relaxation rate constant, and another factor of ten is within reach based on the models which we have validated with our experimental study. The loss suppression opens up many new possibilities for quantum simulations with spin mixtures of highly magnetic atoms.

Experiments with ultracold atoms or molecules are often limited by unfavorable inelastic collision rates. Several methods have been developed to control collisions such as isolating atoms in deep lattices[1], reducing collisional channels via confinement[2], or by mitigating their effects through the enhancement of elastic collisions via Feshbach resonances[3]. Polar molecules with electric or magnetic dipoles have been shielded from chemical reactions at short range by using repulsive interactions between dipoles, either in two dimensions or via microwave dressing[4–6].

Using dipolar shielding[7–9] with highly magnetic atoms is more challenging than with polar molecules as the dipolar interaction of the former is two orders of magnitude smaller than for the latter. Magnetic atoms have a simpler structure than molecules, allowing them to achieve lower temperatures while providing a controlled, tunable, and relatively simple platform for exploring novel forms of matter with long-range forces[10–16]. Dysprosium, with a magnetic moment of $10\mu_B$, has a magnetic dipole-dipole interaction that is 100 times larger than that of alkali atoms. However, dipolar relaxation – an inelastic spin-flip process that converts Zeeman energy into kinetic energy – occurs at a rate that scales as the square of the dipolar interaction, severely limiting the lifetime of any cloud with population in an excited Zeeman level. The dominance of dipolar relaxation has, thus far, precluded the experimental realization of many proposed new phenomena in spin mixtures of highly magnetic atoms[17–19]. Using dipolar shielding to prevent the atoms from undergoing dipolar relaxation requires a deep

understanding of the dipolar interaction as it drives both the elastic and inelastic processes.

In this work we show that suppression of dipolar relaxation is possible since it occurs mainly at specific interatomic separations, where the dipolar potential reduces the wave function amplitude. It proves that confinement can not only affect the collisional channels between atoms[2], but also modify the interaction potential and provide shielding, as it was original proposed for molecules[7–9]. We observe an order of magnitude suppression of the dipolar relaxation rate, and, supported by comprehensive simulations of the decay rate[2], we show that another order of magnitude is within reach given reasonable parameters. In the limit of high magnetic fields, or for very low temperatures, the amount of suppression can be made arbitrary large. We first describe qualitatively the interplay of magnetic field, temperature, and shielding, then present our experimental results, followed by theoretical simulations.

Results

Basic principles of dipolar shielding

As mentioned, the dipole-dipole interaction is attractive in the case of a tip-to-tail orientation and repulsive for the side-by-side one. Constraining atoms to an xy plane, with a magnetic moment aligned perpendicularly along z, leads to a largely side-by-side repulsion and generates a dipolar barrier. The dipolar length $a_{dd} = \frac{\mu_0}{4\pi}\frac{\mu(10\mu_B)^2}{\hbar^2}$ represents the strength of the interaction and the two-particle oscillator

[1]Research Laboratory of Electronics, MIT-Harvard Center for Ultracold Atoms, and Department of Physics, Massachusetts Institute of Technology, Cambridge, MA 02139, USA. [2]These authors contributed equally: Pierre Barral, Michael Cantara, Li Du. ✉e-mail: pbarral@mit.edu

length $a_z = \sqrt{\hbar/\mu\omega_z}$ the extension of the cloud in the z direction. We denoted μ and ω_z the reduced mass and the trap frequency respectively. A dipolar barrier appears when the dipolar length $a_{dd} > 0.34 a_z$[9], which we refer to as the quasi-2D regime. Thus, experiments with dysprosium require 10,000 times higher axial frequencies than polar molecules to compensate for the 100 times smaller dipolar length. Our experiments have reached this regime with $a_z = 20$ nm and $a_{dd} = 10$ nm.

Three parameters determine the loss rate in quasi-2D: the ratio a_{dd}/a_z set by the confinement, the temperature T, and the magnetic field B. The potential barrier increases with confinement, ultimately reaching the pure-2D limit as $a_z \to 0$ as shown Fig. 1a. As the temperature decreases, the wave function of an incoming pair is suppressed by
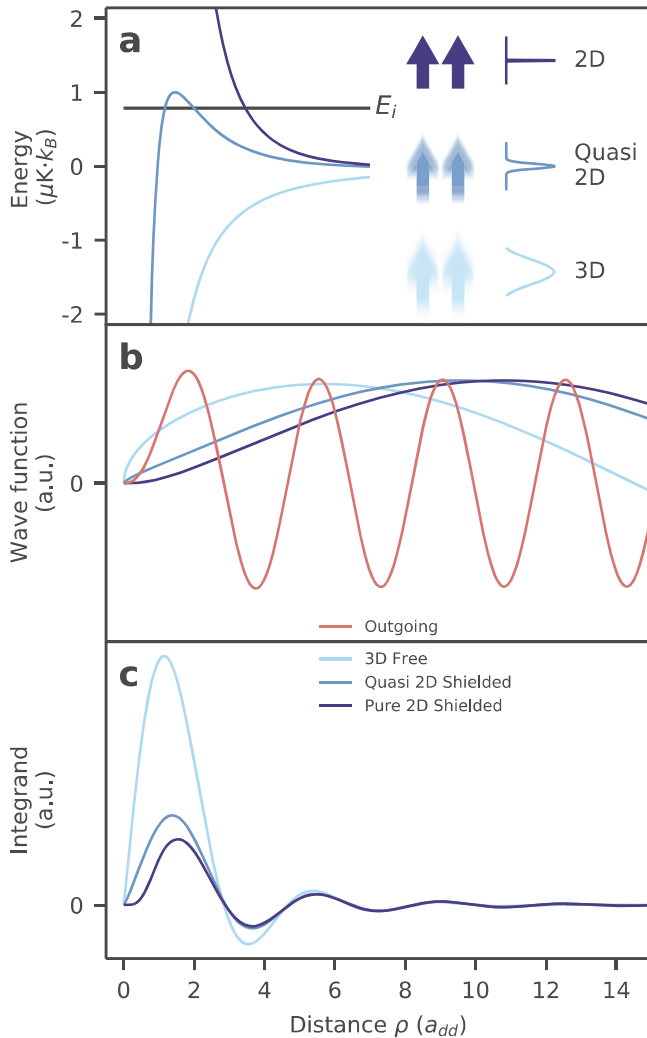

Fig. 1 | Principle of dipolar shielding. a Effective radial potential between two atoms from equation (6) for: no confinement (light blue, 3D), quasi-2D with $\omega_z/2\pi = 300$ kHz (steel blue) and pure-2D (dark blue). The incoming energy is given by the temperature $T = 1\,\mu$K. **b** Wave function solutions of equation (6) with $n = 0$ and initial orbital momentum $m_i = 0$ for the three confinement strengths described above, and in red the spin-flipped outgoing wave function to $m_f = 2$ and $B = 500$ mG. The effect of shielding of the outgoing wave function is negligible for these parameters. **c** Integrand of Fermi's golden rule (equation (2) and see equation (SI-10) in Supplementary Information Note 2). Each curve is the product of the respective wave function in **b**, the outgoing wave function, and the double spin-flip operator from equation (4) integrated with the harmonic oscillator wave functions in the z-direction. The shielding we implement here corresponds to the difference between the light blue and steel blue curves. The minimum attainable decay rate for this incoming energy corresponds to the dark blue curve. See Supplementary Information Note 5 for insights on the behavior of the integrand.

the barrier over a longer range, thereby decreasing the chance of two atoms reaching close range. This shielding effect on the wave function is illustrated in Fig. 1b. As the magnetic field increases, the range where dipolar relaxation occurs is shortened and the shielding increases. Indeed, a higher magnetic field leads to a higher released energy, and correspondingly a more rapidly oscillating outgoing wave function (see red curve Fig. 1b). Since the dipolar potential falls off as $1/r^3$, the majority of the decay will come from the first oscillating lobe of the outgoing wave function, as seen in Fig. 1c. The range of dipolar relaxation, therefore, decreases as the magnetic field increases. This can also be explained in a semi-classical picture: the Franck-Condon principle predicts spin flips to occur at the classical turning point of the outgoing wave function[2,20], i.e. when the released Zeeman energy equals the energy of the centrifugal barrier. Correspondingly, higher magnetic fields cause spin-flips to occur at a shorter range, ultimately behind the barrier felt by the incoming atoms, where they are strongly suppressed. In addition to increasing shielding, magnetic fields affect dipolar relaxation rates via the density of final states. Without shielding in 3D and 2D[2,19,21], this leads to an increasing rate (for bosons). Shielding qualitatively changes the magnetic field dependence of the dipolar relaxation rate which now decreases with magnetic field (see Supplementary Information Note 4).

Experiment

Here we study these principles experimentally. We load ~8×10^4 spin-polarized ^{162}Dy atoms in the excited $|J = 8, m_J = 8\rangle$ Zeeman level (see Methods for details) in an optical lattice and get a stack of about 45 thin pancakes ('crêpes'). The crêpes reach an $a_z/2 = 10$ nm root-mean-square (RMS) width and a 5.7 μm radius. The peak density is 2.9×10^9 cm^{-2}. The experiment is performed at $T \approx 1.6\,\mu$K, above the BEC transition temperature (300 nK), to prevent convolving our results with changes in the two-particle correlation function[22,23]. The quantization axis is set by an external magnetic field along the z direction. The lattice beam is blue detuned, with its radial repulsion compensated by a coaxial red-detuned optical dipole trap, as shown in Fig. 2a. Axial trap frequencies are limited to $\omega_z/2\pi = 260$ kHz by the maximum laser power of the compensation beam.

By measuring the atom losses we determine the inelastic decay coefficient, β_{3D}, as defined by the differential equation for the 3D density n:

$$\frac{dn}{dt} = -\beta_{3D} n^2. \tag{1}$$

We obtain densities from the measured atom number, temperature and trap frequencies, and average over the stack of crêpes (also see the Methods section). We sometimes refer to the 2D loss rate β_{2D} in cm^2/s, which uses the 2D density instead. It is related to β_{3D} through the axial harmonic confinement via $\beta_{2D} = \beta_{3D}/(a_z\sqrt{\pi})$.

Our experimental results are shown in Fig. 2b, c. We also compare the theoretical shielded decay rate (solid blue) with the one we would expect in the same crêpe geometry if there was no elastic dipolar potential to repel the atoms (dashed blue). In contrast to the loss rate in a 3D geometry (red), which increases with $\sqrt{B}$ (see Supplementary Information Note 5), we observe the signature of shielding in Fig. 2b: a much weaker dependence on magnetic fields (solid blue). Our results are also qualitatively different from those presented in[2], represented by the dash-blue curve. Their approach relies solely on shaping the trap to modify the available outgoing channels, whereas we go further by altering the interaction potential experienced by the atoms.

We operate in the quasi-2D regime which differs from the pure-2D one in several aspects. Compared to pure-2D, the finite axial extent of the quasi-2D geometry softens the radial barrier, reducing the barrier height to energies comparable to typical temperatures in the experiment. Furthermore, for Zeeman energies that are larger than the axial
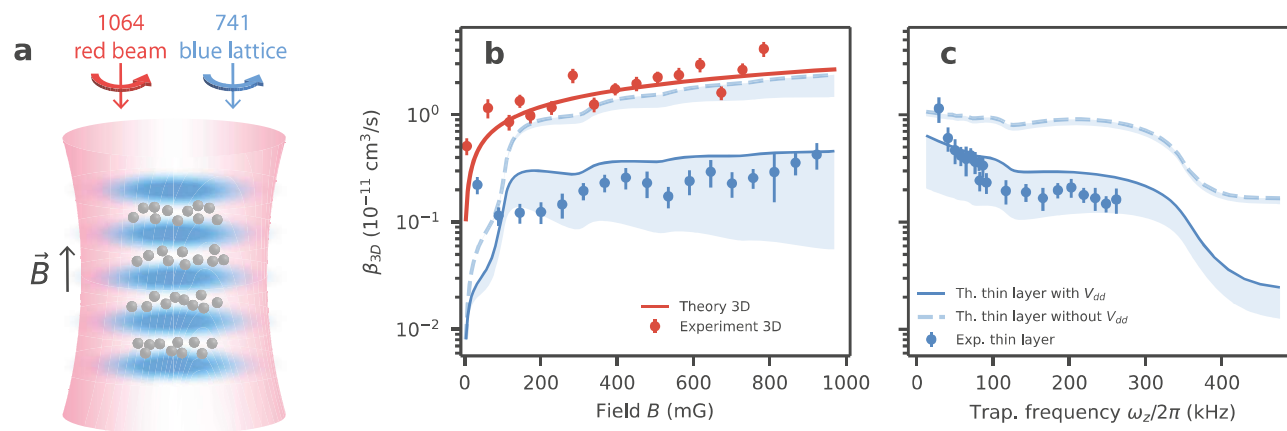
Fig. 2 | Experiment scheme and results. a Trap geometry. A blue-detuned 741 nm retroreflected beam repels the atoms to create a 1D lattice. The finite contrast of the lattice and the zero-point motion of the atoms in the ground state create a repulsive transverse potential, which is compensated by a 1064 nm red-detuned beam to create an adjustable transverse harmonic confinement. **b, c** Experimentally measured β_{3D} in a large volume trap (red) and in a thin layer (blue). The lines are theory curves obtained by using Fermi's golden rule (see Supplementary Information Note 2 for derivations). The red curve shows the decay rate in 3D[19,21], the dashed blue curve is for non-shielded atoms in a lattice[2]. The solid blue line takes into account the shielding induced by the elastic dipole-dipole interaction. All theoretical curves are thermally averaged over the incoming momenta. The shaded blue region corresponds to the inclusion of contact interactions (see an extended discussion of the short-range physics in Methods). **b** Measurement of β_{3D} as a function of magnetic field. The axial trap frequency is $\omega_z/2\pi = 185$ kHz which corresponds to $a_z/2 = 13$ nm. **c** Measurement of β_{3D} in a constant magnetic field of 200 mG while varying the trap frequency. The uncertainties are set by the atom number stability, cloud temperature measurement and trap frequency measurements (see Methods section). The relaxation rates measured at very low fields deviate from the theoretical values, most likely because the imperfect circular polarization of the lattice and compensating beams changes the orientation of the dipoles (see Methods section).
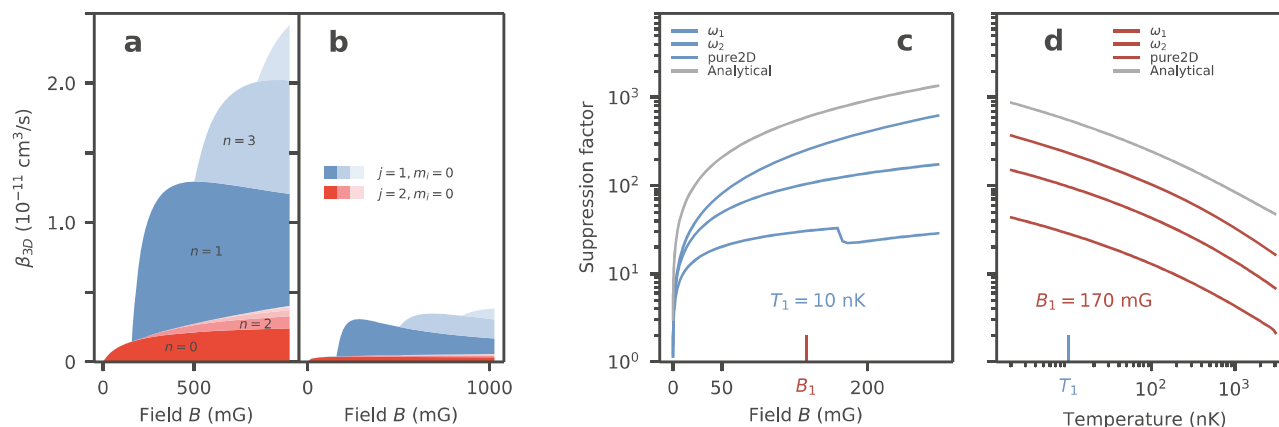

Fig. 3 | Theoretical loss rate coefficients. Channel-by-channel decomposition of the dipolar relaxation rates of the $m_i = 0$ incoming state (valid when $\mu_B B \gg k_B T$, see Supplementary Information Note 3) in a 300 kHz trap, both for free wave functions (**a**) and shielded ones (**b**). The blue and red colors correspond to single and double spin flips, respectively. The different shades correspond to different harmonic oscillator states as they open up with increasing magnetic field. The suppression factor defined as the ratio of β_{3D} obtained from shielded and free wave functions, both at fixed temperature T_1 (**c**), and at fixed magnetic field B_1 (**d**). For each of the graphs we present curves for $\omega_1/2\pi = 300$ kHz (dotted), $\omega_2/2\pi = 1.8$ MHz (dashed dotted), the pure-2D case (solid line) as well as the analytical approximation (grey dotted) from equations (SI-17) and (SI-22) detailed in Supplementary Information Note 4.

trapping frequency, new collisional channels open, with a portion of the released energy converted into axial excitation and the remainder into radial motion. As a result, the relaxation for these processes is shifted to larger distances, thereby weakening the shielding. The first channel opening is visible in Fig. 2b around 100 mG as well as in Fig. 3a, b. The aforementioned factors lead to a relaxation rate that does not decrease with magnetic field, as it would in the pure-2D case, but instead shows a weaker increase compared to the case without a dipolar barrier (dashed blue). Figure 2c shows the loss rate coefficient as a function of axial confinement. The loss rate decreases with confinement due to enhanced shielding by the dipolar repulsion and closing axially excited states channels.

We have reduced the loss rate coefficient to approximately 1×10^{-12} cm^3/s. Over a large range of magnetic fields in a lattice, we achieved more than an order of magnitude reduction in the dipolar relaxation rate coefficient compared to the unshielded case. The agreement between the numerical calculations and the experiment enables extrapolation beyond the current limitation of the experiment: very favorable loss rate coefficients of 2×10^{-13} cm^3/s can be achieved at 200 mG with an axial confinement of 500 kHz at 1 μK. This matches the lowest rate obtained with fermions through Pauli suppression in reference[19]. Under such conditions, axial excitations are energetically forbidden and the 2D decay rate is less than a factor of 3 above the pure-2D limit. By lowering the temperature to 100 nK, the relaxation rate would be suppressed by an additional factor of three and reach the 10^{-14} cm^3/s regime. To further understand how these numbers are computed, we describe our theoretical model in the following paragraphs.

Theoretical model

Dipolar relaxation rates can be calculated from Fermi's golden rule. The decay rate Γ of 2 particles is given by

$$\hbar\Gamma = 2\pi|\langle\Psi_{\text{out}}|\hat{V}_{\text{dd}}|\Psi_{\text{in}}\rangle|^2\rho(E), \tag{2}$$

where $\rho(E)$ is the final density of states at energy E. The incoming wave function is an excited Zeeman state with transverse momentum $\boldsymbol{k}_i$ in the lowest harmonic oscillator state, $n_i = 0$. The outgoing wave function is a lower Zeeman state with momentum $\boldsymbol{k}_f$ in the harmonic oscillator state n_f. The loss rate coefficient β_{2D} is related to Γ through $\beta_{2D} = \pi L^2\Gamma$, with L being the radius of the transverse box used to normalize the wave functions. The atoms are coupled by the magnetic dipole-dipole interaction:

$$\hat{V}_{\text{dd}} = \frac{\mu_0}{4\pi}(g_J\mu_B)^2\frac{\hat{\boldsymbol{J}}_1\cdot\hat{\boldsymbol{J}}_2 - 3(\hat{\boldsymbol{J}}_1\cdot\boldsymbol{u}_r)(\hat{\boldsymbol{J}}_2\cdot\boldsymbol{u}_r)}{r^3}, \tag{3}$$

where $\boldsymbol{r}$ is the interatomic separation (with corresponding unit vector $\boldsymbol{u}_r$). The magnetic field points along z. Atoms in the initial spin state $|j_0\rangle = |m_{J_1} = 8, m_{J_2} = 8\rangle$ can collide and remain in the same spin state, or relax to either $|j_1\rangle = (|7,8\rangle + |8,7\rangle)/\sqrt{2}$ or $|j_2\rangle = |7,7\rangle$. The dipole-dipole operator acting on $|j_0\rangle$ is:

$$\hat{V}_{\text{dd}}|j_0\rangle = \frac{\mu_0(Jg_J\mu_B)^2}{4\pi r^3}\left[(1-3\bar{z}^2)|j_0\rangle - \frac{3\bar{z}\bar{r}_+}{J^{1/2}}|j_1\rangle - \frac{3\bar{r}_+^2}{2J}|j_2\rangle\right] \tag{4}$$

$$= V_{\text{dd},0}|j_0\rangle + V_{\text{dd},1}|j_1\rangle + V_{\text{dd},2}|j_2\rangle \tag{5}$$

with $\bar{z} = z/r$ and $\bar{r}_+ = (x+iy)/r$. Equation (4) shows the three effects of the dipolar interaction: an elastic scattering process, a single spin-flip proportional to $\bar{z}$, and a double spin-flip which implicitly depends on z through r.

In the two-dimensional limit where $z = 0$, the single spin-flip term vanishes and the elastic term is a purely repulsive $1/\rho^3$ potential (where $\rho = \sqrt{x^2 + y^2}$). This potential has an analytic solution at zero temperature ($k_i = 0$)[24], while other cases have to be solved numerically.

We assume a quasi-2D geometry where we ignore the effect of $V_{\text{dd},0}$ on the z motion, which is then factorized and described by harmonic oscillator wave functions (see Methods for a discussion on this approximation). The elastic portion of the operator in equation (4) is averaged over the z direction. This leads to an effective repulsive potential (see Fig. 1a) in the one-dimensional radial Schrödinger equation:

$$\left\{\frac{\hbar^2}{2\mu}\left(-\frac{d^2}{d\rho^2} + \frac{m^2-1/4}{\rho^2}\right) + \langle n|V_{\text{dd},0}|n\rangle\right\}\phi = \frac{\hbar^2k_i^2}{2\mu}\phi. \tag{6}$$

Here, the state $|n\rangle$ is the nth harmonic oscillator's state along z. We focus on incoming states with zero projection of orbital angular momentum, $m_i = 0$, as this channel dominates for any reasonable magnetic field (see Supplementary Information Note 3).

We solve the Schrödinger equation for the radial wave function using numerical techniques, and use it to perturbatively calculate the dipolar relaxation rate with Fermi's golden rule (2). In Fig. 1 we show how dipolar repulsion (Fig. 1a) modifies the incoming wave function (Fig. 1b) and reduces the integral of the transition matrix element (Fig. 1c).

Without axial excitation, only double spin flips to the final spin state $|j_2\rangle = |7,7\rangle$ and orbital state $m_f = 2$ are allowed. At sufficiently high magnetic field the energy released during the collision can exceed $\hbar\omega_z$, thereby opening up new collisional channels resulting in axial excitations. Energy conservation requires

$$\frac{\hbar^2k_f^2}{2\mu} = \frac{\hbar^2k_i^2}{2\mu} + \Delta j\mu_B g_J B - \Delta n\hbar\omega_z. \tag{7}$$

The single spin-flip channel ($\Delta j = 1$) requires odd Δn due to the odd symmetry of the $\bar{z}$ term in equation (4), whereas double spin flips ($\Delta j = 2$) require even Δn. Newly opened channels increase the decay rate, as shown in Fig. 3a, b. Furthermore, as previously explained, they also decrease the shielding factor, as visible in the small notch in Fig. 3c.

Remaining in the ground state of the harmonic oscillator is therefore necessary for obtaining extremely low relaxation rates, but that requires working at low enough fields. Unfortunately, the relaxation rates we measure at very low fields deviate from the theoretical values in Fig. 2b, most likely because of imperfect circular polarization of the lattice and compensating beams. The mixture of σ^+ and σ^- light induces Raman couplings between $|m_J = +8\rangle$ and other even $|m_J\rangle$ states, thereby opening additional relaxation channels via spin exchange[21]. With a > 95% circular polarization purity, we find agreement between experimental decay rates and calculated dipolar relaxation rates for fields > 100mG, where the Raman coupling is suppressed by Zeeman detuning.

Discussion

We have shown that confinement in thin layers not only reduces the number of available collisional channels, but additionally provides dipolar shielding, thereby strongly suppressing dipolar relaxation between atoms. In principle, arbitrarily low loss rates and infinite shielding factors are possible at very low temperatures. Strong magnetic fields are also predicted to reduce the shielded collision rate to arbitrary low values if strong axial confinement suppresses the opening of collision channels. As we have discussed above, rather straightforward improvements in axial confinement, purity of polarization and temperature should result in rate coefficients in the 10^{-14}cm³/s regime.

Our simulations and experiments show that there is already substantial shielding at thermal energies comparable to the barrier height. Lowering the temperature well below the barrier eventually results in exponential suppression[8]. For our experimental parameters, going from 1 μK to 100 nK would increase the suppression by a factor of three.

In this work, we have discussed the interplay between the elastic and inelastic aspects of dipolar interactions. Both scale with the dipolar length, which could be 10,000 times larger for polar molecules. Yet the large total angular momentum $J = 8$ works in favors of dysprosium over molecules, as the elastic part of the dipole-dipole potential scales as J^4 in a stretched state, while the relaxation rate scales as J^3 for single spin-flips and J^2 for double spin-flips.

An important point of comparison is the elastic scattering rate. At 1 Gauss in a trap with a 2 MHz axial frequency, the inelastic 2D cross-section would be 20 nm without shielding. Shielding drops this number to 0.3 nm, while the semi-classical dipolar elastic collisional cross section is $\sigma_{\text{SC}} = 180$ nm[24]. Shielding is necessary to obtain a ratio of good to bad collisions in excess of 100. Shielding is also necessary to study dipolar exchange. Given our density $n_{2D} = 2.9 \times 10^9$ cm⁻², an estimated spin exchange rate is 200/s, which is comparable to the observed shielded dipolar decay rates.

Dipolar shielding has previously been observed in polar molecules with fermionic statistics[5], for which the shielding is qualitatively different. Since identical fermions already have an isotropic p-wave barrier, adding moderate dipolar interactions in a confined geometry will first strengthen this barrier in the radial direction but also weaken it in the axial one. As a result, the inelastic collision rate will first decrease with the dipole moment and then increase[25]. This cannot be seen with
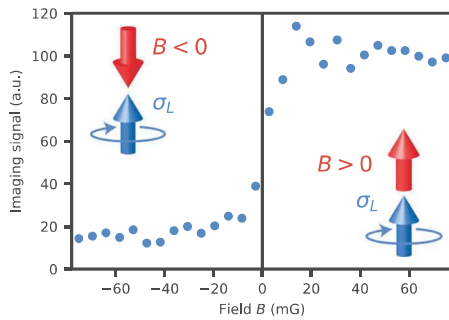
Fig. 4 | Determining the zero of the magnetic field. For spin-polarized $m_J = -8$ dysprosium atoms and left-circularly polarized imaging light, the drastic difference in Clebsch-Gordan coefficients for σ_+ and σ_- transitions produces a step-like change in imaging signal as the magnetic field traverses through zero.

bosons. For both particle types, the inelastic collision rate will eventually decrease when entering more deeply into the 2D regime, as we have explored in this work. Our technique would be crucial to study spin mixtures of bulk gases of bosonic dipolar species.

In conclusion, we have demonstrated a way to realize long-lived spin mixtures in dense bosonic lanthanide clouds, opening up new possibilities for quantum simulation experiments in two dimensions. With such technique, dysprosium can be used to study quantum materials with dipolar interactions in regimes different from those currently possible for polar molecules[7] and Rydberg atoms[26]. Stable spin mixtures are important for implementing spin-orbit coupling and artificial gauge potentials via Raman coupling of spin states[27,28]. By suppressing dipolar relaxation, one can take advantage of the ground state orbital angular momentum of lanthanides to avoid the substantial photon scattering rates of the Raman beams for alkali atoms[29].

Methods
Sample preparation
The samples are obtained after evaporative cooling in a crossed optical-dipole trap (ODT) which is loaded from the narrow-line magneto-optical trap described in reference[30]. The ODT consists of three 1064 nm laser beams: two beams with $40\,\mu m$ beam waists crossed at 8° in the horizontal plane, and a beam with a $64\,\mu m$ waist propagating along the (vertical) z direction. We prepare spin-polarized samples of $\sim 8 \times 10^4$ ^{162}Dy atoms in the $|J=8, m_J = -8\rangle$ state in an optical dipole trap just above the transition temperature. Working with a thermal gas makes it easier to determine dipolar relaxation rate coefficients without accounting for a varying condensate fraction.

The highest spin state $|m_J = +8\rangle$ is populated via adiabatic rapid passage using an RF sweep in a magnetic field of 3.5 G along the z direction. A stack of quasi-2D layers, which we refer to as crêpes due to their extreme aspect ratio, is created using a 1D optical lattice formed by retroreflecting a 741 nm laser beam along the z axis. We use a Ti:Sapph laser focused down to a waist of $50\,\mu m$ to the atoms. It can deliver about 300 mW of light after fiber coupling and intensity stabilization. It is typically detuned by 14.25 to 2.25 GHz to the blue side of the narrow 1.8 kHz transition[31], thus providing frequency-controllable tight axial confinement. During the dipolar relaxation experiment, the horizontal beams are switched off, and the vertical 8 W ODT beam serves to compensate for the deconfinement of the blue-detuned lattice. We verified with in-situ images (obtained with detuned imaging light due to the high optical densities) that the blue-detuned lattice is correctly compensated without displacement of the cloud. The lattice and the vertical dipole trap are turned on using exponential ramps with a 50ms time constant to adiabatically load the atoms into the lowest vibrational level of the 2D layers. During the first 40 ms of the lattice ramp, the magnetic field is rapidly reduced to 40mG to minimize the dipolar relaxation losses. The magnetic field is then ramped

up to its final value during the last 10ms of the lattice loading ramp, after which the decay of the sample due to inelastic collisions is measured.

The RMS extension of the cloud along the lattice direction before loading is $\sigma_{ODT} \simeq 4.7\,\mu m$. Given the layer separation of $\lambda/2 \simeq 371$ nm, around $4\sqrt{\pi}\sigma_{ODT}/\lambda = 45$ crêpes are loaded with initially 3×10^4 atoms and a central density of $n_0 = 2.9 \times 10^9$ cm^{-2}. The density distribution in the ith pancake is described by (see Fig. 5)

$$n_i(t,\rho,z) = n_0(t) \exp\left(-z_i^2/(2\sigma_{ODT}^2)\right) \exp\left(-\rho^2/(2\sigma_\perp^2)\right) \tag{8}$$

with $z_i = i\frac{\lambda}{2}$ and $\sigma_\perp = \sqrt{\frac{k_B T_{\text{lattice}}}{2\mu\omega_\perp^2}}$, $\sigma_{ODT} = \sqrt{\frac{k_B T_{ODT}}{2\mu\omega_{ODT}^2}}$. The parameters $\omega_{ODT} = 2\pi \cdot 94$ Hz and $T_{ODT} = 150$ nK describe the cloud before the lattice is ramped up whereas $\omega_\perp = 2\pi \cdot 200$ Hz and $T_{\text{lattice}} \simeq 1\,\mu K$ characterize the conditions after lattice ramp up. The central crêpe contains about 900 atoms. The RMS width of the crêpes is typically $\sigma_z \simeq 10$ nm while the radial one is $\sigma_\perp = 5.7\,\mu m$.

Zeroing the magnetic field
Achieving control of low magnetic fields is critical for minimizing dipolar suppression by preventing higher outgoing vibrational channels from opening. We have devised a method to zero the magnetic field that relies on the large disparity of Clebsch-Gordan coefficients for dysprosium. When an atom's magnetic moment is aligned along the propagation of a circularly polarized imaging beam, the amount of scattered light strongly differs whether the magnetic dipole moment is oriented parallel or anti-parallel to the propagation of the imaging beam. By using absorption imaging for various external magnetic fields, as shown in Fig. 4, one can observe when the dipole moment has flipped, which determines the zero of the external magnetic field.

More specifically, in a spin-polarized ($m_J = -8$) sample of bosonic dysprosium, the Clebsch-Gordan coefficients for σ_-, π and σ_+ transitions are 1, 1/9 and 1/153 respectively. We perform absorption imaging of a spin-polarized sample with left-circularly polarized (σ_L) light along the magnetic field quantization axis z. We work with low enough light intensity and imaging time to prevent optical pumping. At large positive magnetic field bias, the atoms see σ_- light with a corresponding Clebsch-Gordan coefficient of 1, resulting in a large atom count. At large negative magnetic field bias, the atoms see σ_+ light with a corresponding Clebsch-Gordan coefficient of 1/153 leading to a low atom count. The lower the transverse magnetic field, the sharper is the transition when the longitudinal field is varied. In this way, the zero settings for all components of the magnetic field are determined.

Lattice light choice
The need for deep optical lattices requires a tightly focused lattice beam, which causes undesirably strong radial confinement if one uses a red-detuned beam. By choosing a blue-detuned lattice we avoid adiabatic compression of the cloud in the transverse direction and the substantial corresponding increase in temperature when ramping up the optical lattice. The choice of a blue-detuned lattice also exposes the atoms to lower light intensities and reduces the unwanted Raman transitions due to imperfect circular polarization. However, the radial deconfinement created by the lattice needs to be compensated, which we achieve with a red-detuned optical dipole trap that enables independent control of the axial and transverse trap frequencies (see Fig. 5 left).

Lifetime analysis
The decay of the cloud can be described via equation (1) for the 3D densities

$$\frac{dn_{3D}}{dt} = -\beta_{3D} n_{3D}^2. \tag{9}$$

or by using a 2D equation

$$\frac{dn_{2D}}{dt} = -\beta_{2D} n_{2D}^2.$$ (10)

The densities in each pancake are related by

$$n_{3D} = n_{2D} \frac{1}{\sqrt{2\pi}\sigma_z} \exp(-z^2/(2\sigma_z^2))$$ (11)

with $\sigma_z = \sqrt{\frac{\hbar}{4\mu\omega_z}} = a_z/2 \simeq 10$ nm. Our 2D density of $n_{2D} = 2.9 \times 10^9$ cm^{-2} corresponds to a 3D density of $n_{3D} = 1.1 \times 10^{15}$ cm^{-3}. When integrating equation (9) and equating it to (10), we obtain

$$\beta_{3D} = 2\sqrt{\pi}\sigma_z\beta_{2D}.$$ (12)

In the main paper, we are using β_{3D} to characterize the decay.

We will omit the 2D subscript for the densities in the rest of the manuscript. Equation (10) – in a local-density approximation – needs to be integrated over the cloud volume to relate to the observed quantity
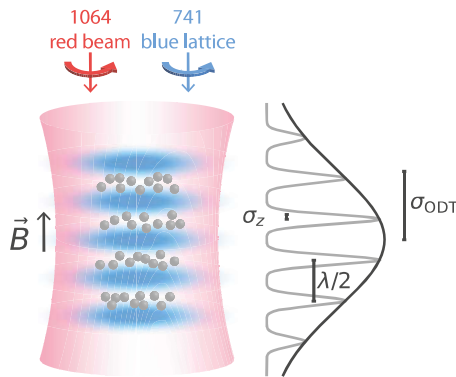

Fig. 5 | Trap geometry and relevant length scales. Left: Reproduction of Fig. 2a of the main text. Right: The spatial density of the cloud in the longitudinal direction is characterized by the axial RMS width $\sigma_z = a_z/2$, the lattice spacing $\lambda/2$ and the initial width of the loaded thermal cloud σ_{ODT}.

N, the number of atoms:

$$\frac{dN}{dt} = -\beta_{2D} \int_{\mathcal{S}} n^2 d\tau = -\beta_{2D} \langle n \rangle \equiv -\beta_{2D} \frac{N^2}{V_{eff}}.$$ (13)

The effective volume V_{eff} is determined as follows. After integration of equation (8), one gets $N = \sum_i N_i = \sum_i \int n_i d\tau = n_0 2\pi\sigma_\perp^2 \sqrt{2\pi}\sigma_{ODT}/(\lambda/2)$ and

$$\frac{dN}{dt} = \sum_i \frac{dN_i}{dt} = -\beta_{2D} \sum_i \int_{\mathcal{S}} n_i^2 2\pi\rho \, d\rho = -\beta_{2D} n_0^2 \pi\sigma_\perp^2 \sum_i e^{-\frac{z_i^2}{2\sigma_{ODT}^2}}$$

$$= -\beta_{2D} n_0^2 \pi\sigma_\perp^2 \frac{\sqrt{\pi}\sigma_{ODT}}{\lambda/2}.$$ (14)

Identifying V_{eff} in equation (13) gives

$$V_{eff} = 4\pi\sigma_\perp^2 \frac{2\sqrt{\pi}\sigma_{ODT}}{\lambda/2}.$$ (15)

We note that $\langle n \rangle = \frac{N}{2^{3/2} V_{eff}}$, where each $\sqrt{2}$ factor comes from the Gaussian averaging along one axis. To take into account the moderate heating during the experiment, we perform a linear fit of the temperature $T(t) = T_0 + \nu_T t$ for each measurement of the decay rate, which is used to scale the effective volume $V_{eff}(t)$. The solution of the differential equation (13) that we fit is $N(t) = \frac{N_0}{1 + \frac{\beta_{2D}}{V_{eff}} N_0 \frac{\ln(1+\nu_T t)}{\nu_T}}$ from which we determine β_{2D}. A comparison of this fit with one ignoring the temperature increase is shown in Fig. 6. The atom number $N(t)$ is measured as a function of hold time (typically tens of ms) using time of flight imaging.

Here we have assumed that every dipolar relaxation event leads to the loss of both atoms. This is justified since the effective trap depth of a few micro-kelvins is negligible compared to the kinetic energy gained by the spin-flip for magnetic fields larger than a few tens of milligauss. Note that the trap depth is much lower than the axial excitation energy $\hbar\omega_z$. This is due to the compensated blue lattice which provides a very weak trap in the transverse direction compared to the tight axial confinement. The experiment is sufficiently fast (tens of ms) such that photon scattering in the lattice, background collisions and residual evaporation are not important.
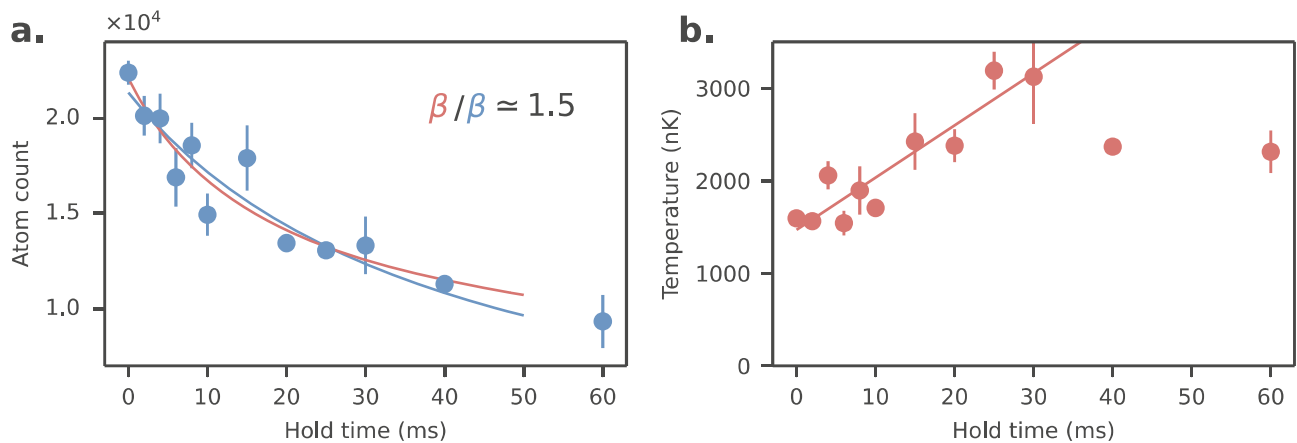

Fig. 6 | Typical dipolar relaxation decay curve. The atom number decay is shown in panel **a** and the temperature increase is shown in **b**. Two different decay fit are shown. Either the pure two-body decay (blue) or the one incorporating a linear increase in the temperature, which modifies the density (in red). The difference in the extracted β coefficient is here about 50% as incorporating the temperature increase prevents under-fitting the initial fast decay. The loss rate coefficient β is systematically 20 to 50% larger with this method. Only the initial part of the temperature increase is used in the fit, as temperature measurements at later times were not reliable. The uncertainty is the statistical standard deviation of the mean of three measurements.

Error bars

The uncertainties represented by the errorbars in the plots are one standard deviation coming from the statistical error due to the curve fitting, as well as our best estimate in the uncertainties of ω_{ODT}, T_{ODT}, $\omega_\perp$, ω_z and T_{lattice} added in quadrature. ω_{ODT} is measured in the ODT by observing the oscillation of the cloud after suddenly applying a magnetic force. $\omega_\perp$ is measured by modulating the intensity of the vertical trapping beam and observing the parametric heating resonance. Axial trap frequencies ω_z (which go up to several hundreds of kHz) are also measured via parametric heating. Due to the bandwidth of the drive electronics, this was done only in shallow lattices and extrapolated to deeper lattices. Temperatures are observed in time of flight.

Theoretical decay rate

We summarize here the main equations to produce the theoretical predictions in Figs. 1–3. Detailed derivations are given in Supplementary Information Note 2 and ref. 32.

We recall equation (4)

$$\hat{V}_{\mathrm{dd}}|j_0\rangle = \frac{\mu_0(Jg_J\mu_B)^2}{4\pi r^3}\left[(1-3\bar{z}^2)|j_0\rangle - \frac{3\bar{z}\bar{r}_+}{J^{1/2}}|j_1\rangle - \frac{3\bar{r}_+^2}{2J}|j_2\rangle\right] \quad (16)$$

which is used to compute the potential used in equation (6):

$$\left\{\frac{\hbar^2}{2\mu}\left(-\frac{d^2}{d\rho^2} + \frac{m^2-1/4}{\rho^2}\right) + \langle n|V_{\mathrm{dd},0}|n\rangle\right\}\phi = \frac{\hbar^2 k_i^2}{2\mu}\phi. \quad (17)$$

This is the equation that we solve numerically for both the incoming ($m = 0$, $n = 0$) and outgoing ($m = 2$, n even or $m = 1$, n odd) wave functions. The code we developed combines grids of multiple step-sizes to account for the need to appropriately average the potential along z, describe the short-range shielding at small ρ and normalize correctly the wave functions at large distances. Given the temperature, magnetic fields, z trapping frequencies and desired precision, the code determines an appropriate grid, and computes the incoming wave function and the harmonic oscillator states on this specific grid. It then distributes those results on multiple cores, computing the outgoing wave function for each of the different decay channels and the respective integral of Fermi's golden rule. This method enables the code to produce the plots presented in this paper on a simple laptop in a reasonable time.

The normalization condition reads: $\int_0^L d\rho\, \phi_{n,m}(\rho)^2 = 1$ for a cylinder of radius L. Our model accounts for the modification of both incoming and outgoing wave functions by the dipolar interaction. The free radial wave function solution with momentum k is $\phi_{n,m}^{(\mathrm{free})}(\rho) = \sqrt{\frac{\pi k \rho}{L}}J_m(k\rho)$, which does not depend on n.

The 2D loss rate coefficient for the channel $|j_0\rangle \rightarrow |j_f\rangle, |0\rangle \rightarrow |n_f\rangle$ reads

$$\beta_{\mathrm{2D}}^{j_f,n_f} = \frac{8\mu}{k_i k_f \hbar^3}\left|L\int_{-\infty}^{+\infty}dz\int_0^L d\rho\,\phi_{n_f,j_f}(\rho)\chi_{n_f}(z)V_{\mathrm{dd},j_f}(\rho,z)\chi_0(z)\phi_0(\rho)\right|^2 \quad (18)$$

with χ_n being the nth harmonic oscillator's state wave function:

$$\chi_n(z) = \frac{1}{\sqrt{2^n n!}}\left(\frac{1}{\pi a_z^2}\right)^{1/4}H_n(z/a_z)e^{-\frac{z^2}{2a_z^2}}. \quad (19)$$

The total rate is then the sum over all channels:

$$\beta_{\mathrm{2D}} = \sum_{j_f,n_f}\beta_{\mathrm{2D}}^{j_f,n_f}. \quad (20)$$

and relates to the 3D rate as $\beta_{\mathrm{3D}} = \sqrt{\pi}a_z\beta_{\mathrm{2D}}$.

The rate is eventually averaged over the thermal distribution of incoming momenta (see Supplementary Information Note 2) for the Fig. 2b, c, and computed at the mean momentum for all of the other figures.

Pure-2D limit

In pure-2D the double spin-flip potential is $V_{\mathrm{dd},2}(\rho) \propto 1/\rho^3$. If we ignore the shielding, in the low-temperature limit, we find that the 2D decay rate is

$$\beta_{\mathrm{free}}^{\mathrm{pure-2D}} = 4\pi^2\frac{1}{J^2}\frac{E_{\mathrm{dd}}}{\hbar}a_{\mathrm{dd}}^4 k_f^2. \quad (21)$$

So $\beta_{\mathrm{free}}^{\mathrm{pure-2D}} \propto B$. If we incorporate shielding we find that

$$\beta_{\mathrm{shielded}}^{\mathrm{pure-2D}} \propto \left(1/\log(k_i)\right)^2 \quad (22)$$

which goes to zero at zero temperature. Under certains assumptions detailed in Supplementary Information Note 4 and noting x_2 the first zero of the Bessel function $J_2(x)$, one can find that the decay rate in a certain field range behaves as

$$\beta_{\mathrm{shielded}}^{\mathrm{pure-2D}} \propto k_f^{1/4}\exp\left(-2\sqrt{\frac{8a_{\mathrm{dd}}k_f}{x_2}}\right), \quad (23)$$

which vanishes at high magnetic fields.

Discussion of various approximations

Unitarity limit. The perturbative results will get modified when the decay rate approaches the unitary limit. However, in our range of parameters, the decay rates are much smaller than the unitary limit. A β_{3D} of high 10^{-12} cm³/s corresponds to a $\beta_{\mathrm{2D}} = \sigma\hbar k/\mu$ in the low 10^{-6}cm²/s. This gives a $\sigma k \simeq 0.1 \ll 4$ which puts us safely in the non-unitary regime. Note that the total cross section in 2D is $\sigma = \frac{4}{k}\sum_m\sin^2\delta$, and is dominated by the s-wave contribution given our magnetic fields.

Wave function substitution approximation. The system is perturbed by two parts of the dipolar potential: one which is diagonal in the spin states basis and therefore elastic, the other part is non-diagonal and causes transitions. Usually, the weakest part of the Hamiltonian should be treated perturbatively. It is the case here since $|\hat{V}_{\mathrm{dd}}^{\mathrm{inelastic}}/\hat{V}_{\mathrm{dd}}^{\mathrm{elastic}}|^2 \simeq 1/J = 1/8$ as shown in equation (16). This is why we evaluate the decay rate on the shielded wave function. Following previous treatments[2,19,21], we have not checked the importance of higher-order terms in the perturbation theory.

Effective potential approximation. To compute the wave functions we assumed an effective potential obtained by averaging V_{dd} in the nth state of the harmonic oscillator. This is the diabatic limit of a coupled channels calculation. There exists a fully adiabatic method to compute the molecular potential of two interacting dipoles in a quasi-2D geometry[9]. It would mix the harmonic oscillator states but we found it would only affect the wave function at short distances, which is important only at high magnetic fields. In our experiment, $k_f a_{\mathrm{dd}}$ remains on the order of 1, and restricting the z-motion to the pre-existing harmonic oscillator states is acceptable.

Fermi's golden rule approximation. The use of Fermi's golden rule with the original density distribution is valid only if the decay rate is smaller than the other time constants of the system. The relaxation rate $\Gamma = \beta_{\mathrm{3D}}n \simeq 10^2$ s⁻¹ is indeed smaller than the collision rate which is around 10^3 s⁻¹, or the trap frequencies of 200 Hz. This assumption is therefore fulfilled. The system will stay in (quasi-) equilibrium when the

loss rates are smaller than the trapping frequencies and smaller than the rate of elastic collisions which provides thermalization.

Neglecting short-range interactions. The background s-wave scattering length of dysprosium $a = 5.9$ nm[33] can modify the wave functions. A previous paper[2] studied extensively its influence on chromium. However, the decay rate we observed in a large volume 3D trap (red curve in Fig. 2) agrees better with the theory which does not take the scattering length into account. Another dysprosium experiment[19] found a similar result in an even wider range of fields. However, it is possible that the short-range molecular potential plays a role in the 2D results, and could possibly explain why we obtain rates a few times smaller than the theory predicts (see shaded areas in Fig. 2). Indeed, a sizeable contribution to the loss comes from interatomic distances smaller than the van der Waals length $a_{vdW} = 4.3$ nm and the scattering length $a = 5.9$ nm. Since the real wave function rapidly oscillates at short-range, the contribution to the overlap matrix element should vanish. To get a sense of the sensitivity of our model to contact interactions we also used simulated wave functions with a hard-core potential at $a_s = 5.9$ nm, while keeping the dipolar potential elsewhere. We put a node in the incoming and outgoing radial wave functions ϕ at this position, and integrated from this distance outward. This produced the lower bound of the shaded areas in Fig. 2. It would be interesting to use a more realistic interaction potential to study the impact of short-range interactions, however this goes beyond the scope of this paper.

Data availability
The data that support the findings of this study are available from the corresponding author upon request.

Code availability
The code that supports the findings of this study is available from the corresponding author upon request.

References
1. Wilpers, G. et al. Optical clock with ultracold neutral atoms. *Phys. Rev. Lett.* **89**, 230801 (2002).
2. Pasquiou, B. et al. Control of dipolar relaxation in external fields. *Phys. Rev. A* **81**, 042716 (2010).
3. Cornish, S. L., Claussen, N. R., Roberts, J. L., Cornell, E. A. & Wieman, C. E. Stable ^{85}Rb Bose-Einstein condensates with widely tunable interactions. *Phys. Rev. Lett.* **85**, 1795–1798 (2000).
4. Frisch, A. et al. Ultracold dipolar molecules composed of strongly magnetic atoms. *Phys. Rev. Lett.* **115**, 203201 (2015).
5. Valtolina, G. et al. Dipolar evaporation of reactive molecules to below the fermi temperature. *Nature* **588**, 239–243 (2020).
6. Anderegg, L. et al. Observation of microwave shielding of ultracold molecules. *Science* **373**, 779–782 (2021).
7. Micheli, A., Pupillo, G., Büchler, H. P. & Zoller, P. Cold polar molecules in two-dimensional traps: Tailoring interactions with external fields for novel quantum phases. *Phys. Rev. A* **76**, 043604 (2007).
8. Micheli, A. et al. Universal rates for reactive ultracold polar molecules in reduced dimensions. *Phys. Rev. Lett.* **105**, 073202 (2010).
9. Ticknor, C. Quasi-two-dimensional dipolar scattering. *Phys. Rev. A* **81**, 042708 (2010).
10. Chomaz, L. et al. Dipolar physics: A review of experiments with magnetic quantum gases. *Rep. Prog. Phys.* **86**, 026401 (2022).
11. Lahaye, T., Menotti, C., Santos, L., Lewenstein, M. & Pfau, T. The physics of dipolar bosonic quantum gases. *Rep. Prog. Phys.* **72**, 126401 (2009).
12. Lian, B., Ho, T.-L. & Zhai, H. Searching for non-Abelian phases in the bose-einstein condensate of dysprosium. *Phys. Rev. A* **85**, 051606 (2012).
13. Deng, Y., Cheng, J., Jing, H., Sun, C.-P. & Yi, S. Spin-orbit-coupled dipolar Bose-Einstein condensates. *Phys. Rev. Lett.* **108**, 125301 (2012).
14. Lian, B. & Zhang, S. Singlet mott state simulating the bosonic laughlin wave function. *Phys. Rev. B* **89**, 041110 (2014).
15. Cui, X., Lian, B., Ho, T.-L., Lev, B. L. & Zhai, H. Synthetic gauge field with highly magnetic lanthanide atoms. *Phys. Rev. A* **88**, 011601 (2013).
16. Babik, D., Roell, R., Helten, D., Fleischhauer, M. & Weitz, M. Synthetic magnetic fields for cold erbium atoms. *Phys. Rev. A* **101**, 053603 (2020).
17. Gopalakrishnan, S., Martin, I. & Demler, E. A. Quantum quasicrystals of spin-orbit-coupled dipolar bosons. *Phys. Rev. Lett.* **111**, 185304 (2013).
18. Yi, S. & Pu, H. Spontaneous spin textures in dipolar spinor condensates. *Phys. Rev. Lett.* **97**, 020401 (2006).
19. Burdick, N. Q., Baumann, K., Tang, Y., Lu, M. & Lev, B. L. Fermionic suppression of dipolar relaxation. *Phys. Rev. Lett.* **114**, 023201 (2015).
20. Condon, E. U. The franck-condon principle and related topics. *Am. J. Phys.* **15**, 365–374 (1947).
21. Hensler, S. et al. Dipolar relaxation in an ultra-cold gas of magnetically trapped chromium atoms. *Appl. Phys. B* **77**, 765–772 (2003).
22. Kagan, Y., Svistunov, B., Shlyapnikov, G. Effect of bose condensation on inelastic processes in gases. *JETP Lett.* **42**, 209–212 (1985).
23. Burt, E. A. et al. Coherence, correlations, and collisions: What one learns about bose-einstein condensates from their decay. *Phys. Rev. Lett.* **79**, 337–340 (1997).
24. Ticknor, C. Two-dimensional dipolar scattering. *Phys. Rev. A* **80**, 052702 (2009).
25. Quéméner, G. & Bohn, J. L. Dynamics of ultracold molecules in confined geometry and electric field. *Phys. Rev. A* **83**, 012705 (2011).
26. Browaeys, A. & Lahaye, T. Many-body physics with individually controlled rydberg atoms. *Nat. Phys.* **16**, 132–142 (2020).
27. Lin, Y.-J., Compton, R. L., Jiménez-García, K., Porto, J. V. & Spielman, I. B. Synthetic magnetic fields for ultracold neutral atoms. *Nature* **462**, 628–632 (2009).
28. Lin, Y.-J., Jiménez-García, K. & Spielman, I. B. Spin–orbit-coupled Bose–Einstein condensates. *Nature* **471**, 83–86 (2011).
29. Burdick, N. Q., Tang, Y. & Lev, B. L. Long-lived spin-orbit-coupled degenerate dipolar fermi gas. *Phys. Rev. X* **6**, 031022 (2016).
30. Lunden, W. et al. Enhancing the capture velocity of a Dy magneto-optical trap with two-stage slowing. *Phys. Rev. A* **101**, 063403 (2020).
31. Lu, M., Youn, S. H. & Lev, B. L. Spectroscopy of a narrow-line laser-cooling transition in atomic dysprosium. *Phys. Rev. A* **83**, 012510 (2011).
32. Barral, P. Elastic and inelastic dipolar scattering. PhD thesis, Massachusetts Institute of Technology (2023).
33. Tang, Y., Sykes, A., Burdick, N. Q., Bohn, J. L. & Lev, B. L. s-wave scattering lengths of the strongly dipolar bosons dy 162 and dy 164. *Phys. Rev. A* **92**, 022703 (2015).

Acknowledgements

Author contributions
P.B., M.C, L.D., W.L., A.O.J. and W.K. designed and constructed the experimental setup, P.B., M.C., L.D. and J.d.H carried out the experimental work, P.B., M.C., L.D., J.d.H and W.K. developed the theoretical

models and simulations, all authors contributed to the writing of the manuscript.

Competing interests

The authors declare no competing interests.

Additional information

Bibliography

[1] K Aikawa, A Frisch, M Mark, S Baier, R Grimm, and F Ferlaino. Reaching fermi degeneracy via universal dipolar scattering. *Physical review letters*, 112(1):010404, 2014.

[2] K Aikawa, A Frisch, M Mark, S Baier, A Rietzler, R Grimm, and F Ferlaino. Bose-einstein condensation of erbium. *Physical review letters*, 108(21):210401, 2012.

[3] Loïc Anderegg, Sean Burchesky, Yicheng Bao, Scarlett S Yu, Tijs Karman, Eunmi Chae, Kang-Kuen Ni, Wolfgang Ketterle, and John M Doyle. Observation of microwave shielding of ultracold molecules. *Science*, 373(6556):779–782, 2021.

[4] Mike H Anderson, Jason R Ensher, Michael R Matthews, Carl E Wieman, and Eric A Cornell. Observation of bose-einstein condensation in a dilute atomic vapor. *science*, 269(5221):198–201, 1995.

[5] GE Astrakharchik, D Blume, Stefano Giorgini, and BE Granger. Quasi-one-dimensional bose gases with a large scattering length. *Physical review letters*, 92(3):030402, 2004.

[6] GE Astrakharchik, J Boronat, J Casulleras, and Stefano Giorgini. Beyond the tonks-girardeau gas: Strongly correlated regime in quasi-one-dimensional bose gases. *Physical review letters*, 95(19):190407, 2005.

[7] Simon Baier, Manfred J Mark, Daniel Petter, Kiyotaka Aikawa, Lauriane Chomaz, Zi Cai, M Baranov, P Zoller, and F Ferlaino. Extended bose-hubbard models with ultracold magnetic atoms. *Science*, 352(6282):201–205, 2016.

[8] Sebastien Balibar. The enigma of supersolidity. *Nature*, 464(7286):176–182, 2010.

[9] Mikhail A Baranov, Marcello Dalmonte, Guido Pupillo, and Peter Zoller. Condensed matter theory of dipolar quantum gases. *Chemical Reviews*, 112(9):5012–5061, 2012.

[10] Pierre Barral. *Elastic and inelastic dipolar scattering*. PhD thesis, Massachusetts Institute of Technology, 2023.

[11] Pierre Barral, Michael Cantara, Li Du, William Lunden, Julius de Hond, Alan O Jamison, and Wolfgang Ketterle. Can the dipolar interaction suppress dipolar relaxation? *arXiv preprint arXiv:2303.06281*, 2023.

[12] Pierre Barral, Michael Cantara, Li Du, William Lunden, Julius de Hond, Alan O Jamison, and Wolfgang Ketterle. Suppressing dipolar relaxation in thin layers of dysprosium atoms. *Nature Communications*, 15(1):3566, 2024.

[13] MT Batchelor, Michael Bortz, Xi-Wen Guan, and Norman Oelkers. Evidence for the super tonks–girardeau gas. *Journal of Statistical Mechanics: Theory and Experiment*, 2005(10):L10001, 2005.

[14] Niccolò Bigagli, Weijun Yuan, Siwei Zhang, Boris Bulatovic, Tijs Karman, Ian Stevenson, and Sebastian Will. Observation of bose-einstein condensation of dipolar molecules. *arXiv preprint arXiv:2312.10965*, 2023.

[15] Damien Bloch, Britton Hofer, Sam Roberto Cohen, Maxence Lepers, Antoine Browaeys, and Igor Ferrier-Barbut. Anisotropic polarizability of dy at 532 nm on the intercombination transition. *arXiv preprint arXiv:2404.10480*, 2024.

[16] Immanuel Bloch. Ultracold quantum gases in optical lattices. *Nature physics*, 1(1):23–30, 2005.

[17] Immanuel Bloch, Jean Dalibard, and Wilhelm Zwerger. Many-body physics with ultracold gases. *Reviews of modern physics*, 80(3):885, 2008.

[18] Bose. Plancks gesetz und lichtquantenhypothese. *Zeitschrift für Physik*, 26(1):178–181, 1924.

[19] Fabian Böttcher, Jan-Niklas Schmidt, Matthias Wenzel, Jens Hertkorn, Mingyang Guo, Tim Langen, and Tilman Pfau. Transient supersolid properties in an array of dipolar quantum droplets. *Physical Review X*, 9(1):011051, 2019.

[20] Hans Peter Büchler, Eugene Demler, Mikhail Lukin, Andrea Micheli, N Prokof'Ev, Guido Pupillo, and Peter Zoller. Strongly correlated 2d quantum phases with cold polar molecules: controlling the shape of the interaction potential. *Physical Review Letters*, 98(6):060404, 2007.

[21] Nathaniel Q Burdick, Kristian Baumann, Yijun Tang, Mingwu Lu, and Benjamin L Lev. Fermionic suppression of dipolar relaxation. *Physical review letters*, 114(2):023201, 2015.

[22] Michael Alan Cantara. *Dipolar Shielding and Sub-wavelength Bilayers in a Quantum Gas of Dysprosium*. PhD thesis, Massachusetts Institute of Technology, 2023.

[23] Thomas Chalopin, Tanish Satoor, Alexandre Evrard, Vasiliy Makhalov, Jean Dalibard, Raphael Lopes, and Sylvain Nascimbene. Probing chiral edge dynamics and bulk topology of a synthetic hall system. *Nature Physics*, 16(10):1017–1021, 2020.

[24] Christos Charalambous, Miguel-Angel Garcia-March, Mohammad Mehboudi, and Maciej Lewenstein. Heat current control in trapped bose–einstein condensates. *New Journal of Physics*, 21(8):083037, 2019.

[25] Shu Chen, Liming Guan, Xiangguo Yin, Yajiang Hao, and Xi-Wen Guan. Transition from a tonks-girardeau gas to a super-tonks-girardeau gas as an exact many-body dynamics problem. *Physical Review A*, 81(3):031609, 2010.

[26] L Chomaz, D Petter, P Ilzhöfer, G Natale, A Trautmann, C Politi, G Durastante, RMW Van Bijnen, A Patscheider, M Sohmen, et al. Long-lived and transient supersolid behaviors in dipolar quantum gases. *Physical Review X*, 9(2):021012, 2019.

[27] Lauriane Chomaz, Igor Ferrier-Barbut, Francesca Ferlaino, Bruno Laburthe-Tolra, Benjamin L Lev, and Tilman Pfau. Dipolar physics: A review of experiments with magnetic quantum gases. *Reports on Progress in Physics*, 2022.

[28] Eric A Cornell, Jason R Ensher, and Carl E Wieman. Experiments in dilute atomic bose-einstein condensation. *arXiv preprint cond-mat/9903109*, 1999.

[29] Xiaoling Cui, Biao Lian, Tin-Lun Ho, Benjamin L Lev, and Hui Zhai. Synthetic gauge field with highly magnetic lanthanide atoms. *Physical Review A*, 88(1):011601, 2013.

[30] Kendall B Davis, M-O Mewes, Michael R Andrews, Nicolaas J van Druten, Dallin S Durfee, DM Kurn, and Wolfgang Ketterle. Bose-einstein condensation in a gas of sodium atoms. *Physical review letters*, 75(22):3969, 1995.

[31] Brian DeMarco and Deborah S Jin. Onset of fermi degeneracy in a trapped atomic gas. *science*, 285(5434):1703–1706, 1999.

[32] Davide Dreon, Leonid A Sidorenkov, Chayma Bouazza, Wilfried Maineult, Jean Dalibard, and Sylvain Nascimbene. Optical cooling and trapping of highly magnetic atoms: the benefits of a spontaneous spin polarization. *Journal of Physics B: Atomic, Molecular and Optical Physics*, 50(6):065005, 2017.

[33] Li Du, Pierre Barral, Michael Cantara, Julius de Hond, Yu-Kun Lu, and Wolfgang Ketterle. Atomic physics on a 50 nm scale: Realization of a bilayer system of dipolar atoms. *arXiv preprint arXiv:2302.07209*, 2023.

[34] Li Du, Pierre Barral, Michael Cantara, Julius de Hond, Yu-Kun Lu, and Wolfgang Ketterle. Atomic physics on a 50-nm scale: Realization of a bilayer system of dipolar atoms. *Science*, 384(6695):546–551, 2024.

[35] Albert Einstein and Jakob Grommer. Allgemeine relativitätstheorie und be-
wegungsgesetz. *Albert Einstein: Akademie-Vorträge: Sitzungsberichte der
Preußischen Akademie der Wissenschaften 1914–1932*, pages 282–294, 2005.

[36] JP Eisenstein and Allan H MacDonald. Bose–einstein condensation of excitons
in bilayer electron systems. *Nature*, 432(7018):691–694, 2004.

[37] AK Fedorov, SI Matveenko, VI Yudson, and GV Shlyapnikov. Novel p-wave
superfluids of fermionic polar molecules. *Scientific reports*, 6(1):27448, 2016.

[38] Albert Frisch, Michael Mark, Kiyotaka Aikawa, Francesca Ferlaino, John L
Bohn, Constantinos Makrides, Alexander Petrov, and Svetlana Kotochigova.
Quantum chaos in ultracold collisions of gas-phase erbium atoms. *Nature*,
507(7493):475–479, 2014.

[39] Vitaly L Ginzburg, Vitaly Lazarevich Ginzburg, and LD Landau. *On the theory
of superconductivity*. Springer, 2009.

[40] Stefano Giorgini, Lev P Pitaevskii, and Sandro Stringari. Theory of ultracold
atomic fermi gases. *Reviews of Modern Physics*, 80(4):1215, 2008.

[41] Krzysztof Góral, Kazimierz Rzążewski, and Tilman Pfau. Bose-einstein con-
densation with magnetic dipole-dipole forces. *Physical Review A*, 61(5):051601,
2000.

[42] Phillip L Gould, George A Ruff, and David E Pritchard. Diffraction of atoms by
light: The near-resonant kapitza-dirac effect. *Physical review letters*, 56(8):827,
1986.

[43] Axel Griesmaier, Jörg Werner, Sven Hensler, Jürgen Stuhler, and Tilman
Pfau. Bose-einstein condensation of chromium. *Physical Review Letters*,
94(16):160401, 2005.

[44] Mingyang Guo, Fabian Böttcher, Jens Hertkorn, Jan-Niklas Schmidt,
Matthias Wenzel, Hans Peter Büchler, Tim Langen, and Tilman Pfau. The low-
energy goldstone mode in a trapped dipolar supersolid. *Nature*, 574(7778):386–
389, 2019.

[45] Z Hadzibabic, S Gupta, CA Stan, CH Schunck, MW Zwierlein, K Dieckmann,
and W Ketterle. Fiftyfold improvement in the number of quantum degenerate
fermionic atoms. *Physical review letters*, 91(16):160401, 2003.

[46] Elmar Haller, Mattias Gustavsson, Manfred J Mark, Johann G Danzl, Russell
Hart, Guido Pupillo, and Hanns-Christoph Nägerl. Realization of an excited,
strongly correlated quantum gas phase. *Science*, 325(5945):1224–1227, 2009.

[47] Jan Harms, J Peter Toennies, and Franco Dalfovo. Density of superfluid he-
lium droplets. *Physical Review B*, 58(6):3341, 1998.

[48] S Hensler, J Werner, A Griesmaier, PO Schmidt, A Görlitz, T Pfau, S Giovanazzi, and K Rzażewski. Dipolar relaxation in an ultra-cold gas of magnetically trapped chromium atoms. *Applied Physics B*, 77:765–772, 2003.

[49] J Hertkorn, J-N Schmidt, F Böttcher, M Guo, M Schmidt, KSH Ng, SD Graham, HP Büchler, T Langen, M Zwierlein, et al. Density fluctuations across the superfluid-supersolid phase transition in a dipolar quantum gas. *Physical Review X*, 11(1):011037, 2021.

[50] Chao-Chun Huang and Wen-Chin Wu. Center motions of nonoverlapping condensates coupled by long-range dipolar interaction in bilayer and multilayer stacks. *Physical Review A*, 82(5):053612, 2010.

[51] Paul Niklas Jepsen, Jesse Amato-Grill, Ivana Dimitrova, Wen Wei Ho, Eugene Demler, and Wolfgang Ketterle. Spin transport in a tunable heisenberg model realized with ultracold atoms. *Nature*, 588(7838):403–407, 2020.

[52] Shuwei Jin, Jianshun Gao, Karthik Chandrashekara, Christian Gölzhäuser, Joschka Schöner, and Lauriane Chomaz. Two-dimensional magneto-optical trap of dysprosium atoms as a compact source for efficient loading of a narrow-line three-dimensional magneto-optical trap. *Physical Review A*, 108(2):023719, 2023.

[53] Holger Kadau, Matthias Schmitt, Matthias Wenzel, Clarissa Wink, Thomas Maier, Igor Ferrier-Barbut, and Tilman Pfau. Observing the rosensweig instability of a quantum ferrofluid. *Nature*, 530(7589):194–197, 2016.

[54] Wil Kao, Kuan-Yu Li, Kuan-Yu Lin, Sarang Gopalakrishnan, and Benjamin L Lev. Topological pumping of a 1d dipolar gas into strongly correlated prethermal states. *Science*, 371(6526):296–300, 2021.

[55] Yuki Kawaguchi, Hiroki Saito, and Masahito Ueda. Einstein–de haas effect in dipolar bose-einstein condensates. *Physical review letters*, 96(8):080405, 2006.

[56] Yuki Kawaguchi and Masahito Ueda. Spinor bose–einstein condensates. *Physics Reports*, 520(5):253–381, 2012.

[57] Wolfgang Ketterle and Martin W Zwierlein. Making, probing and understanding ultracold fermi gases. *La Rivista del Nuovo Cimento*, 31(5):247–422, 2008.

[58] Duk Y Kim and Moses HW Chan. Absence of supersolidity in solid helium in porous vycor glass. *Physical Review Letters*, 109(15):155301, 2012.

[59] Eunseong Kim and Moses Hung-Wai Chan. Probable observation of a supersolid helium phase. *Nature*, 427(6971):225–227, 2004.

[60] Toshiya Kinoshita, Trevor Wenger, and David S Weiss. A quantum newton's cradle. *Nature*, 440(7086):900–903, 2006.

[61] Masaaki Kitagawa, Katsunari Enomoto, Kentaro Kasa, Yoshiro Takahashi, Roman Ciuryło, Pascal Naidon, and Paul S Julienne. Two-color photoassociation spectroscopy of ytterbium atoms and the precise determinations of s-wave scattering lengths. *Physical Review A*, 77(1):012719, 2008.

[62] A Kramida, Yu Ralchenko, and J Reader. Team 2020 nist atomic spectra database (version 5.8).

[63] Fam Le Kien, Philipp Schneeweiss, and Arno Rauschenbeutel. Dynamical polarizability of atoms in arbitrary light fields: general theory and application to cesium. *The European Physical Journal D*, 67:1–16, 2013.

[64] Julian Léonard, Andrea Morales, Philip Zupancic, Tilman Esslinger, and Tobias Donner. Supersolid formation in a quantum gas breaking a continuous translational symmetry. *Nature*, 543(7643):87–90, 2017.

[65] S Lepoutre, K Kechadi, B Naylor, B Zhu, L Gabardos, L Isaev, P Pedri, AM Rey, L Vernac, and B Laburthe-Tolra. Spin mixing and protection of ferromagnetism in a spinor dipolar condensate. *Physical Review A*, 97(2):023610, 2018.

[66] Steven Lepoutre, Joahnnes Schachenmayer, Lucas Gabardos, Bihui Zhu, Bruno Naylor, Etienne Maréchal, Olivier Gorceix, Ana Maria Rey, Laurent Vernac, and Bruno Laburthe-Tolra. Out-of-equilibrium quantum magnetism and thermalization in a spin-3 many-body dipolar lattice system. *Nature Communications*, 10(1):1714, 2019.

[67] Tsz-Him Leung, Malte N Schwarz, Shao-Wen Chang, Charles D Brown, Govind Unnikrishnan, and Dan Stamper-Kurn. Interaction-enhanced group velocity of bosons in the flat band of an optical kagome lattice. *Physical Review Letters*, 125(13):133001, 2020.

[68] Barbara G Levi. Cornell, ketterle, and wieman share nobel prize for bose–einstein condensates. *Physics Today*, 54(12):14–16, 2001.

[69] Hui Li, Jean-Francois Wyart, Olivier Dulieu, Sylvain Nascimbene, and Maxence Lepers. Optical trapping of ultracold dysprosium atoms: transition probabilities, dynamic dipole polarizabilities and van der waals c6 coefficients. *Journal of Physics B: Atomic, Molecular and Optical Physics*, 50(1):014005, 2016.

[70] Jun-Ru Li, Jeongwon Lee, Wujie Huang, Sean Burchesky, Boris Shteynas, Furkan Çağrı Top, Alan O Jamison, and Wolfgang Ketterle. A stripe phase with supersolid properties in spin–orbit-coupled bose–einstein condensates. *Nature*, 543(7643):91–94, 2017.

[71] Biao Lian, Tin-Lun Ho, and Hui Zhai. Searching for non-abelian phases in the bose-einstein condensate of dysprosium. *Physical Review A*, 85(5):051606, 2012.

[72] Mingwu Lu, Nathaniel Q Burdick, and Benjamin L Lev. Quantum degenerate dipolar fermi gas. *Physical Review Letters*, 108(21):215301, 2012.

[73] Mingwu Lu, Nathaniel Q Burdick, Seo Ho Youn, and Benjamin L Lev. Strongly dipolar bose-einstein condensate of dysprosium. *Physical review letters*, 107(19):190401, 2011.

[74] Mingwu Lu, Seo Ho Youn, and Benjamin L Lev. Spectroscopy of a narrow-line laser-cooling transition in atomic dysprosium. *Physical Review A*, 83(1):012510, 2011.

[75] William Lunden. *Development of a new Dy quantum gas experiment*. PhD thesis, Massachusetts Institute of Technology, 2020.

[76] William Lunden, Li Du, Michael Cantara, Pierre Barral, Alan O Jamison, and Wolfgang Ketterle. Enhancing the capture velocity of a dy magneto-optical trap with two-stage slowing. *Physical Review A*, 101(6):063403, 2020.

[77] Thomas Maier. *Interactions in a quantum gas of dysprosium atoms*. Verlag Dr. Hut, 2016.

[78] Thomas Maier, Igor Ferrier-Barbut, Holger Kadau, Matthias Schmitt, Matthias Wenzel, Clarissa Wink, Tilman Pfau, Krzysztof Jachymski, and Paul Sebastian Julienne. Broad universal feshbach resonances in the chaotic spectrum of dysprosium atoms. *Physical Review A*, 92(6):060702, 2015.

[79] William Clyde Martin, Romuald Zalubas, and Lucy Hagan. Atomic energy levels-the rare-earth elements. *(No Title)*, 1978.

[80] Kyle Matsuda, Luigi De Marco, Jun-Ru Li, William G Tobias, Giacomo Valtolina, Goulven Quéméner, and Jun Ye. Resonant collisional shielding of reactive molecules using electric fields. *Science*, 370(6522):1324–1327, 2020.

[81] Natalia Matveeva, Alessio Recati, and Sandro Stringari. Dipolar drag in bilayer harmonically trapped gases. *The European Physical Journal D*, 65(1-2):219–222, 2011.

[82] Anton Mazurenko, Christie S Chiu, Geoffrey Ji, Maxwell F Parsons, Márton Kanász-Nagy, Richard Schmidt, Fabian Grusdt, Eugene Demler, Daniel Greif, and Markus Greiner. A cold-atom fermi–hubbard antiferromagnet. *Nature*, 545(7655):462–466, 2017.

[83] Zengming Meng, Liangwei Wang, Wei Han, Fangde Liu, Kai Wen, Chao Gao, Pengjun Wang, Cheng Chin, and Jing Zhang. Atomic bose–einstein condensate in twisted-bilayer optical lattices. *Nature*, 615(7951):231–236, 2023.

[84] G Natale, RMW van Bijnen, A Patscheider, D Petter, MJ Mark, L Chomaz, and F Ferlaino. Excitation spectrum of a trapped dipolar supersolid and its experimental evidence. *Physical review letters*, 123(5):050402, 2019.

[85] B Pasquiou, G Bismut, Q Beaufils, A Crubellier, E Maréchal, P Pedri, L Vernac, O Gorceix, and B Laburthe-Tolra. Control of dipolar relaxation in external fields. *Physical Review A*, 81(4):042716, 2010.

[86] B Pasquiou, E Maréchal, L Vernac, O Gorceix, and B Laburthe-Tolra. Thermodynamics of a bose-einstein condensate with free magnetization. *Physical Review Letters*, 108(4):045307, 2012.

[87] Benjamin Pasquiou, Etienne Maréchal, Gabriel Bismut, Paolo Pedri, Laurent Vernac, Olivier Gorceix, and Bruno Laburthe-Tolra. Spontaneous demagnetization of a dipolar spinor bose gas in an ultralow magnetic field. *Physical Review Letters*, 106(25):255303, 2011.

[88] Niels Petersen, Marcel Trümper, and Patrick Windpassinger. Spectroscopy of the 1001-nm transition in atomic dysprosium. *Physical Review A*, 101(4):042502, 2020.

[89] D Petter, G Natale, RMW van Bijnen, A Patscheider, MJ Mark, L Chomaz, and F Ferlaino. Probing the roton excitation spectrum of a stable dipolar bose gas. *Physical Review Letters*, 122(18):183401, 2019.

[90] B Renklioglu, Bilal Tanatar, and MÖ Oktel. Heat transfer through dipolar coupling: Sympathetic cooling without contact. *Physical Review A*, 93(2):023620, 2016.

[91] Shai Ronen, Daniele CE Bortolotti, D Blume, and John L Bohn. Dipolar bose-einstein condensates with dipole-dependent scattering length. *Physical Review A*, 74(3):033611, 2006.

[92] L Santos and T Pfau. Spin-3 chromium bose-einstein condensates. *Physical review letters*, 96(19):190404, 2006.

[93] Matthias Schmitt, Matthias Wenzel, Fabian Böttcher, Igor Ferrier-Barbut, and Tilman Pfau. Self-bound droplets of a dilute magnetic quantum liquid. *Nature*, 539(7628):259–262, 2016.

[94] Ruwan Senaratne, Shankari V Rajagopal, Zachary A Geiger, Kurt M Fujiwara, Vyacheslav Lebedev, and David M Weld. Effusive atomic oven nozzle design using an aligned microcapillary array. *Review of Scientific Instruments*, 86(2), 2015.

[95] Dan M Stamper-Kurn and Masahito Ueda. Spinor bose gases: Symmetries, magnetism, and quantum dynamics. *Reviews of Modern Physics*, 85(3):1191, 2013.

[96] Daniel A Steck. *Quantum and atom optics*. 2007.

[97] Dominik Studer, Lena Maske, Patrick Windpassinger, and Klaus Wendt. Laser spectroscopy of the 1001-nm ground-state transition in dysprosium. *Physical Review A*, 98(4):042504, 2018.

[98] Lin Su, Alexander Douglas, Michal Szurek, Robin Groth, S Furkan Ozturk, Aaron Krahn, Anne H Hébert, Gregory A Phelps, Sepehr Ebadi, Susannah Dickerson, et al. Dipolar quantum solids emerging in a hubbard quantum simulator. *arXiv preprint arXiv:2306.00888*, 2023.

[99] Y Takasu, K Komori, K Honda, M Kumakura, T Yabuzaki, and Y Takahashi. Photoassociation spectroscopy of laser-cooled ytterbium atoms. *Physical review letters*, 93(12):123202, 2004.

[100] Yijun Tang, Wil Kao, Kuan-Yu Li, Sangwon Seo, Krishnanand Mallayya, Marcos Rigol, Sarang Gopalakrishnan, and Benjamin L Lev. Thermalization near integrability in a dipolar quantum newton's cradle. *Physical Review X*, 8(2):021030, 2018.

[101] L Tanzi, SM Roccuzzo, E Lucioni, F Famà, A Fioretti, C Gabbanini, G Modugno, A Recati, and S Stringari. Supersolid symmetry breaking from compressional oscillations in a dipolar quantum gas. *Nature*, 574(7778):382–385, 2019.

[102] Luca Tanzi, Eleonora Lucioni, Francesca Famà, Jacopo Catani, Andrea Fioretti, Carlo Gabbanini, Russell N Bisset, Luis Santos, and Giovanni Modugno. Observation of a dipolar quantum gas with metastable supersolid properties. *Physical review letters*, 122(13):130405, 2019.

[103] Christopher Ticknor. Two-dimensional dipolar scattering. *Physical Review A*, 80(5):052702, 2009.

[104] Christopher Ticknor. Quasi-two-dimensional dipolar scattering. *Physical Review A*, 81(4):042708, 2010.

[105] Satoshi Tojo, Masaaki Kitagawa, Katsunari Enomoto, Yutaka Kato, Yosuke Takasu, Mitsutaka Kumakura, and Yoshiro Takahashi. High-resolution photoassociation spectroscopy of ultracold ytterbium atoms by using the intercombination transition. *Physical review letters*, 96(15):153201, 2006.

[106] Giacomo Valtolina, Kyle Matsuda, William G Tobias, Jun-Ru Li, Luigi De Marco, and Jun Ye. Dipolar evaporation of reactive molecules to below the fermi temperature. *Nature*, 588(7837):239–243, 2020.

[107] Vijin Venu, Peihang Xu, Mikhail Mamaev, Frank Corapi, Thomas Bilitewski, Jose P D'Incao, Cora J Fujiwara, Ana Maria Rey, and Joseph H Thywissen. Unitary p-wave interactions between fermions in an optical lattice. *Nature*, 613(7943):262–267, 2023.

[108] Martin W Zwierlein. *High-temperature superfluidity in an ultracold Fermi gas.* PhD thesis, Massachusetts Institute of Technology, 2006.